

THE NONLINEAR  $g$  MODE IN

THE REVERSE FIELD PINCH

by

Timothy C. Hender B.Sc.

A thesis submitted for the degree  
of Doctor of Philosophy of  
the University of London

Department of Physics,  
Royal Holloway College,  
Egham, Surrey.

RHC

603224 8



a30214 006032248b

ProQuest Number: 10097498

All rights reserved

INFORMATION TO ALL USERS

The quality of this reproduction is dependent upon the quality of the copy submitted.

In the unlikely event that the author did not send a complete manuscript and there are missing pages, these will be noted. Also, if material had to be removed, a note will indicate the deletion.



ProQuest 10097498

Published by ProQuest LLC(2016). Copyright of the Dissertation is held by the Author.

All rights reserved.

This work is protected against unauthorized copying under Title 17, United States Code.  
Microform Edition © ProQuest LLC.

ProQuest LLC  
789 East Eisenhower Parkway  
P.O. Box 1346  
Ann Arbor, MI 48106-1346

## ABSTRACT

A primarily numerical investigation of the nonlinear  $g$  mode in the reverse field pinch is presented.

A two dimensional study of the nonlinear  $m=0$   $g$  mode is made using two computer codes. One code solves the resistive incompressible MHD equations, for the  $m=0$  mode, using a mixed explicit/alternating direction implicit scheme. Whilst for the second code a truncated Fourier expansion is used to reduce the two dimensional  $m=0$  equations to a larger one dimensional set, which are then solved using a mixed explicit/Crank-Nicholson scheme. A stabilising mechanism has been found in which the  $g$  mode acts to flatten the pressure in the vicinity of its singular surface. A quasi-linear scaling argument is given to explain this pressure flattening mechanism. Ohmic heating is found to counteract this stabilising effect by increasing the gross pressure in the pinch. The final nonlinear state of the  $g$  mode depends on the competition between the pressure flattening and ohmic heating mechanisms.

To study modes of any helicity a spectral code is developed to solve the compressible resistive MHD equations in a periodic cylindrical system. Simulating energy loss processes by removing the ohmic heating terms is shown to lower the final nonlinear growth rate of the  $m=0$   $g$  mode. The  $m=1$  mode is examined and the same dominant nonlinear mechanisms are found to apply. Some tentative mixed helicity calculations are also presented, but these studies are far from complete.

PLIC  
LIBRARY

The two dimensional studies allow the magnitudes of typical magnetic fluctuations due to the g mode to be estimated. Using a field line tracing code these fluctuations are shown to give rise to ergodic field line behaviour. Estimates of the enhanced electron transport which occurs because of this behaviour are given. The relevance of these results to experimentally observed phenomena is discussed.

ORIGINAL WORK IN THESIS OF T C HENDER

Chapter 2 (pp 14 - 41)

This is a review chapter and so contains no original work.

Chapter 3 (pp 42 - 70)

The derivation of the reduced  $m=0$  mode equations and associated boundary conditions is original work by T C Hender and so too is the description of the two  $m=0$  codes that are developed.

Chapter 4 (pp 71 - 100)

All the work described in Sections 4.4 and 4.5 is original work by T C Hender (numerous helpful comments from Dr D C Robinson are gratefully acknowledged).

Chapter 5 (pp 101 - 121)

All the work in this chapter is original work done by T C Hender.

Chapter 6 (pp 122 - 155)

The work described in Sections 6.1 to 6.4 is original work by T C Hender. The work on ergodicity in Section 6.5 was done in conjunction with Dr D C Robinson, but with the majority of work presented being performed by T C Hender.

Published papers (pp 165)

Paper 1 and 2

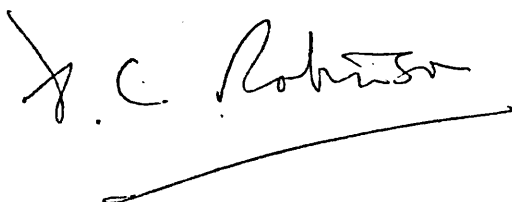
These describe work done by T C Hender under the guidance of Dr D C Robinson.

Paper 3

The contribution of T C Hender to this paper was the development of the anisotropic heat conduction and field diffusion code and the prediction of the anomalous conductivity required (cf Fig.3 this paper).

Paper 4

The work in Section 2 is that of D C Robinson. The remainder of work on nonlinear 'g' modes was done by T C Hender under the guidance of D C Robinson.

A handwritten signature in black ink, reading "D. C. Robinson". The signature is written in a cursive style and is underlined with a long horizontal stroke.

## ACKNOWLEDGEMENTS

First and foremost I should like to thank my Culham supervisor Dr Derek Robinson who has been a constant source of help and encouragement throughout my three years at Culham. Also I must thank my Royal Holloway supervisor Dr Eric Wooding for his help during the past three years and particularly for his many helpful comments during the preparation of this thesis.

I am very grateful to Chris Shepherd who typed all the equations in thesis including the horrific multi-level subscript expressions of chapter 5. Victor Piotrowicz, and Linda my fiancée, whose proof reading of this thesis have eradicated numerous errors, have my thanks.

Finally I must thank the U.K.A.E.A for their financial support and the facilities extended to me at Culham laboratory.

## Table of Contents

CHAPTER 1	INTRODUCTION.....	8
1.1	MOTIVATION.....	8
1.2	PLASMA INSTABILITIES.....	10
1.3	OUTLINE OF THIS THESIS.....	11
CHAPTER 2	MAGNETO-HYDRO-DYNAMIC THEORY.....	14
2.1	INTRODUCTION.....	14
2.2	THE MHD EQUATIONS.....	14
2.2.1	THE EM EQUATIONS FOR A CONTINUOUS MEDIUM.....	15
2.2.2	THE FLUID EQUATIONS.....	17
2.2.3	SUMMARY AND DISCUSSION OF THE M.H.D EQUATIONS.....	19
2.3	INSTABILITIES OF AN IDEAL PLASMA.....	20
2.3.1	FIXED BOUNDARY INSTABILITIES.....	22
2.3.2	FREE BOUNDARY INSTABILITIES.....	27
2.4	RESISTIVE INSTABILITIES.....	29
2.4.1	MAGNETIC ISLANDS.....	29
2.4.2	THE RESISTIVE INTERCHANGE MODE.....	35
CHAPTER 3	NUMERICAL METHODS FOR THE $m=0$ g MODE.....	42
3.1	INTRODUCTION.....	42
3.2	REDUCED FORMULATION.....	42
3.2.1	MATHEMATICAL FORMULATION.....	43
3.2.2	BOUNDARY CONDITIONS.....	45
3.2.3	NON DIMENSIONAL FORM.....	49
3.3	NUMERICAL METHODS.....	50
3.4	THE $m=0$ CODE.....	55
3.4.1	THE ALGORITHM.....	56
3.4.2	TESTING THE CODE.....	63
3.5	THE FOURIER HARMONIC CODE.....	66
3.5.1	FOURIER HARMONIC EQUATIONS.....	66
3.5.2	NUMERICAL ALGORITHM.....	68

CHAPTER 4	m=0 MODE RESULTS AND DISCUSSION.....	71
4.1	INTRODUCTION.....	71
4.2	THE EQUILIBRIUM.....	71
4.3	LINEAR RESULTS.....	75
4.4	DIAGNOSTICS FROM THE CODE.....	77
4.5	NONLINEAR RESULTS AND DISCUSSION.....	79
4.6	CONCLUSIONS.....	100
CHAPTER 5	THE FOURIER HARMONIC CODE.....	101
5.1	INTRODUCTION.....	101
5.2	THE MHD FORMULATION.....	102
5.3	THE FOURIER COMPONENT EQUATIONS.....	103
5.4	BOUNDARY CONDITIONS.....	110
5.5	NUMERICAL ALGORITHM.....	112
5.6	TESTING THE CODE.....	118
CHAPTER 6	COMPRESSIBLE g MODE RESULTS.....	122
6.1	INTRODUCTION.....	122
6.2	m=0 MODE RESULTS.....	122
6.3	m=1 MODE RESULTS.....	128
6.4	MIXED HELICITY RESULTS.....	129
6.5	ERGODICITY.....	135
6.5.1	THE FIELD LINE TRACING CODE.....	135
6.5.2	ERGODIC BEHAVIOUR IN THE RFP.....	136
6.5.3	ERGODICITY AND EXPERIMENT.....	147
6.6	CONCLUSIONS.....	154
CHAPTER 7	CONCLUSIONS.....	156
7.1	SUMMARY OF THESIS AND CONCLUSIONS.....	156



7.2 FUTURE WORK.....158

REFERENCES.....161

APPENDIX PUBLISHED PAPERS.....165

1.1 MOTIVATION

Throughout the entire industrialised world the single most important "raw material" is energy. For the past century the primary sources of energy have been the fossil fuels - coal and to an increasing extent oil. However the accessible reserves of these fuels are unlikely to keep abreast of world demand for more than a few decades. It has therefore become increasingly important to develop alternative energy sources. To this end increasing importance is being attached to existing but under exploited methods of electricity generation, notably fission power, wind power, and hydro-electric power. Also new possibilities such as solar energy, geo-thermal energy and controlled thermo-nuclear fusion are being examined.

Controlled nuclear fusion has several advantages over its rivals. Deuterium, one of the hydrogen isotopes capable of fueling a fusion reactor exists in and is extractable from sea water, thus providing a cheap and virtually limitless supply of fuel. Also the fusion reactor has no geographical or climatic dependence, unlike many of its rivals.

Fusion is the process of coalescing the nuclei of light elements to form heavier ones; a process which yields a nett energy gain. In order to achieve fusion a criterion given by Lawson must be satisfied [1]

$$n\tau > 10^{14} \text{ cm}^{-3} \text{ s}$$

where  $n$  is the plasma particle density ( $\text{cm}^{-3}$ )

and  $\tau$  is the energy containment time in seconds.

Two basic alternative methods of achieving controlled nuclear fusion are currently under investigation. One method involves irradiating the surface of a high density pellet of fuel (eg. deuterium) with laser or ion beams. As the surface of the pellet melts and expands so its fuel contents are compressed. Thus producing a very high density plasma, but for a very short time. The other method involves containing a rather less dense plasma in a magnetic field for a relatively long period of time. Since the plasma is a good electrical conductor at typical temperatures ( $>10^6$ °C), it is not free to move across the magnetic field and so the plasma is magnetically trapped. Early experiments on magnetic containment were conducted using cylindrical configurations. These however suffered from high plasma losses at their ends. Therefore practically all present experiments are conducted using toroidal configurations to circumvent this problem. Within the toroidal containment devices a further sub-division exists depending on the shape and magnitudes of the magnetic fields. Currently the most promising toroidal device appears to be the tokamak [2], which is characterised by a very strong toroidal magnetic field. There are several alternatives to the tokamak of which the reverse field pinch (RFP) is one [3]. The chief attraction of the RFP over the tokamak is that it can achieve higher ratios of plasma pressure to containing magnetic pressure - a quantity known as beta ( $\beta$ ). Since the magnetic field is energetically expensive to provide,  $\beta$  is essentially a measure of efficiency.

## 1.2 PLASMA INSTABILITIES

One of the major problems from which all magnetic containment systems suffer is that of large scale instabilities. These instabilities manifest themselves as large scale plasma flows and as perturbations to the magnetic field. Such instabilities can have very detrimental effects on the plasma containment. They may cause the plasma to come into contact with the wall in which case sputtering of heavy impurities will occur. These heavy impurities can dramatically increase the radiative loss from the plasma. Also the instabilities can enhance convective and conductive losses of energy. Indeed if the instabilities are sufficiently wide spread throughout a volume they may cause the magnetic field lines in that volume to wander randomly - a process known as ergodic field line behaviour. Since the thermal conductivity parallel to the magnetic field is very high, ergodic field line behaviour seriously degrades the energy containment [4]. Another consequence of gross instabilities occurs in tokamaks where the interaction of tearing instabilities is thought to lead to the major disruption, which totally destroys the discharge [5].

During the late 1950's and 1960's virtually all research on instabilities concentrated on linear behaviour. Such research on the effects of a small perturbation to an equilibrium revealed much useful information on the avoidance of instabilities. However nonlinear studies which have been conducted during the last decade have shown that many instabilities saturate at a tolerably small level. For this reason and because the nonlinear instability phase is far longer than the linear phase, the study of nonlinear instabilities is of utmost

importance.

The vast majority of nonlinear instability studies are conducted numerically, primarily because the equations are analytically intractable. However the numerical studies often reveal simplifying assumptions which render analytic solutions possible. Such analytic explanations are important in establishing the validity of the numerical results.

The primary magneto-hydro-dynamic (MHD) instability which afflicts an established RFP field configuration is the g mode [6]. The g mode is driven by the interaction of pressure and curvature and is an analogue of the Rayleigh-Taylor instability. In their review paper Bodin and Newton [3] state that the g mode may well determine an upper limit on the attainable  $\beta$  in an RFP. It is therefore extremely important to investigate the nonlinear behaviour of the g mode. Such an investigation is pursued in this thesis.

### 1.3 OUTLINE OF THIS THESIS

A brief review of the MHD equations and instability theory is given in chapter 2, particular emphasis being placed on the pressure driven Suydam and g modes. Numerical methods applicable to resistive instabilities are examined in chapter 3 and two algorithms to study the nonlinear g mode are developed. These algorithms solve specifically for the g mode which occurs about the toroidal field reversal point. Using the FORTRAN codes developed from these algorithms, an extensive

study has been made of a particular RFP equilibrium developed by Robinson [7]. These results are presented in chapter 4, where a potential saturation mechanism for the g mode is exhibited. A scaling argument is given to explain this saturation mechanism. A second important nonlinear effect is shown to be the ohmic heating which increases the gross pressure in the pinch. Since the g mode is pressure driven this gross pressure increase tends to negate the effects of the saturation mechanism. The final nonlinear state depends on the competition between these two mechanisms and a scaling argument is again given in chapter 4 to explain this facet of the behaviour.

Having completed the studies described in chapter 4 it was desired to extend the studies to g modes which occur in other places than about the field reversal point. It was also desired to be able to study interactions between g modes. An algorithm which fulfils these requirements is developed in chapter 5. The algorithm employs a Fourier resolution in two spatial dimensions; a technique which has only just begun to be used in plasma physics [8]. The results of using this algorithm to study the nonlinear behaviour of the  $m=0$  g mode are given in chapter 6. These results are found to be qualitatively in agreement with those given in chapter 4. The nonlinear  $m=1$  g mode is also examined in chapter 6 and the same dominant nonlinear processes are found as for the  $m=0$  mode. The interaction between an  $m=0$  g mode and an  $m=1$  g mode, in the core, is studied in chapter 6. This interaction is shown to lead to very rapid growth which gives rise to ergodic field line behaviour. This ergodic behaviour is studied in detail in chapter 6 where it is shown that such behaviour will always occur due to the g mode. Ergodicity has important consequences in relation to the pinches ability to contain energy. The enhanced

electron transport due to ergodic behaviour is discussed and comparisons are made with contemporary RFP results. Lastly the experimental RFP phenomenon known as pump out, in which a very rapid decrease in density occurs, is explained as a consequence of ergodic behaviour. Finally in chapter 7 the conclusions of the preceding chapters are re-emphasised and future extensions to this work are indicated.

## 2.1 INTRODUCTION

In this chapter some topics of relevance to this thesis are briefly reviewed. Firstly in section 2.2 the magneto-hydro-dynamic (MHD) equations are examined. The conditions of applicability and the utility of the MHD equations are dwelt upon at some length because of the central role they play in this thesis. In section 2.3 the instabilities of an infinitely conducting plasma are reviewed. Particular emphasis here is placed on the properties of a localised pressure driven mode, known as the Suydam mode. Finally in section 2.4 resistive instabilities are discussed. The formation of magnetic islands as a consequence of resistive instabilities is explained and the linear theory of the resistive interchange or g mode is examined.

## 2.2 THE MHD EQUATIONS

In order to study the behaviour of a plasma we require a closed set of equations describing the time evolution of a moving plasma interacting with an electromagnetic (EM) field. The MHD equations constitute such a set.



### 2.2.1 THE EM EQUATIONS FOR A CONTINUOUS MEDIUM

In an inertial frame of reference Maxwell's equations are [ 9 ]

$$\nabla \times \underline{H} = \underline{J} + \frac{\partial \underline{D}}{\partial t} \quad 2.2.1$$

$$\nabla \times \underline{E} = - \frac{\partial \underline{B}}{\partial t} \quad 2.2.2$$

$$\nabla \cdot \underline{D} = \rho_c \quad 2.2.3$$

$$\nabla \cdot \underline{B} = 0 \quad 2.2.4$$

where  $\underline{D}$  is the electric displacement

$\underline{E}$  is the electric field

$\underline{H}$  is the magnetic intensity

$\underline{B}$  is the magnetic field

$\underline{J}$  is the current density

&  $\rho_c$  is the charge density

Examination of the orderings in eqn 2.2.2 shows that

$$\frac{|\underline{E}|}{\ell_c} \sim \frac{|\underline{B}|}{t_c} \quad 2.2.5$$

where  $\ell_c$  and  $t_c$  are respectively, typical length and time scales. If it is now assumed that typical speeds in our system are very much smaller than the speed of light, i.e.  $\ell_c/t_c \ll C$  then using eqn 2.2.5

$$\frac{\left| \frac{\partial \underline{D}}{\partial t} \right|}{|\nabla \times \underline{H}|} \sim \frac{\epsilon \frac{|\underline{E}|}{t_c}}{|\underline{B}|/\mu \ell_c} = \frac{\ell_c}{t_c C^2} \frac{|\underline{E}|}{|\underline{B}|} \ll 1 \quad 2.2.6$$

where the constitutive relations have been used :-

$$\underline{B} = \mu \underline{H} \quad \text{and} \quad \underline{D} = \epsilon \underline{E}$$

$\epsilon$ ,  $\mu$ , being the permittivity and permeability of the plasma, respectively. Relation 2.2.6 allows us to rewrite eqn 2.2.1 in reduced form.

$$\nabla \times \underline{H} = \underline{J} \quad 2.2.7$$

We require one more equation to close our set, namely Ohm's law. For a stationary conductor this is

$$\eta \underline{J} = \underline{E} \quad 2.2.8$$

where  $\eta$  is the electrical resistivity. Since this is valid only in a stationary conductor we must derive a form applicable to our continuous medium. We consider a typical fluid element of our plasma moving with velocity  $\underline{V}$  relative to the inertial frame of reference in which we stated Maxwell's equations. Then using the above assumption that  $V^2/C^2 \ll 1$ , the Lorentz transformations of special relativity yield [10]

$$\underline{E}' = \underline{E} + \underline{V} \times \underline{B} \quad 2.2.9$$

$$\underline{J}' = \underline{J} - \rho_c \underline{V} \quad 2.2.10$$

where primed quantities are in a frame of reference moving with the fluid and unprimed quantities are in our inertial frame of reference. We may now write eqn 2.2.8 as

$$\eta(\underline{J} - \rho_c \underline{V}) = \underline{E} + \underline{V} \times \underline{B} \quad 2.2.11$$

Now in the situations relevant to thermonuclear fusion the plasmas are very good conductors and so  $\eta \approx 0$ . Eqn 2.2.9 then shows us that

$$\underline{E} \approx -\underline{V} \times \underline{B} \quad 2.2.12$$

since otherwise we would drive nearly infinite currents; a condition which is physically unacceptable. Eqns 2.2.12 and 2.2.7 then give

$$\frac{|\rho_c \underline{V}|}{|\underline{J}|} \sim \frac{|\nabla \cdot \underline{D}| |\underline{V}|}{|\nabla \times \underline{H}|} \sim \epsilon \frac{|\underline{V} \times \underline{B}| |\underline{V}|}{|\underline{H}|} \sim \frac{V^2}{C^2} \ll 1$$

Hence eqn 2.2.11 may be simplified to give

$$\underline{\eta J} = \underline{E} + \underline{V} \times \underline{B} \quad 2.2.13$$

Summarising, the EM equations valid in the limit  $V^2/C^2 \rightarrow 0$ , are in rationalised M.K.S. units ( $\epsilon = \mu = 1$ )

$$\underline{J} = \nabla \times \underline{B} \quad 2.2.14$$

$$\frac{\partial \underline{B}}{\partial t} = -\nabla \times \underline{E} \quad 2.2.15$$

$$\nabla \cdot \underline{E} = \rho_c \quad 2.2.16$$

$$\nabla \cdot \underline{B} = 0 \quad 2.2.17$$

$$\underline{\eta J} = \underline{E} + \underline{V} \times \underline{B} \quad 2.2.18$$

## 2.2.2 THE FLUID EQUATIONS

By analogy with ordinary fluid mechanics, equations describing the conservation of mass, momentum, and energy are expected. This is generally the case, however in many MHD formulations various other equations of state are often used to replace or make the energy equation redundant. The MHD fluid equations may be obtained by taking moments of the Boltzmann equation [11]. However here it is chosen to present the equations and then give physical insight into their various terms.

$$\frac{\partial \rho}{\partial t} + \nabla \cdot (\rho \underline{V}) = 0 \quad 2.2.19$$

$$\rho \left( \frac{\partial \underline{V}}{\partial t} + \underline{V} \cdot \nabla \underline{V} \right) = \underline{J} \times \underline{B} - \nabla P \quad 2.2.20$$

$$\frac{\partial P}{\partial t} + \underline{V} \cdot \nabla P = -\gamma P \nabla \cdot \underline{V} + (\gamma - 1) \eta |\underline{J}|^2 \quad 2.2.21$$

where  $\rho$  is the mass density

$P$  is the pressure

&  $\gamma$  is the ratio of specific heats (usually taken to be 5/3)

Eqn 2.2.19 is a statement of mass conservation which may be derived by applying the divergence theorem.

Eqn 2.2.20 is an expression relating the acceleration to the local forces (i.e. Newton's second law). The  $\frac{\partial \underline{V}}{\partial t} + \underline{V} \cdot \nabla \underline{V}$  term, often known as the convective derivative of  $\underline{V}$ , is the acceleration of an element moving with the fluid. The  $\underline{J} \times \underline{B}$  term is an approximation of the Lorentz force equation

$$\underline{F}_{em} = \rho_c \underline{E} + \underline{J} \times \underline{B} \quad 2.2.22$$

where  $\underline{F}_{em}$  is the EM force. Using the assumption  $v^2/c^2 \ll 1$  together with eqns 2.2.3 & 2.2.12

$$\frac{|\rho_c \underline{E}|}{|\underline{J} \times \underline{B}|} \sim \mu \epsilon \frac{|\nabla \cdot \underline{E}| |\underline{E}|}{|\nabla \times \underline{B}| |\underline{B}|} \sim \frac{1}{c^2} \frac{|\underline{E}|^2}{|\underline{B}|^2} \sim \frac{1}{c^2} \frac{|\underline{V} \times \underline{B}|^2}{|\underline{B}|^2} \ll 1$$

Eqn 2.2.22 becomes

$$\underline{F}_{em} = \underline{J} \times \underline{B} \quad 2.2.23$$

The final term on the R.H.S. of the eqn 2.2.20 is the hydrodynamic

pressure. The inclusion of viscosity would of course require the use of a stress tensor form for P. The general stress tensor for a plasma is greatly complicated by the anisotropy introduced by the magnetic field. A full form for it is given by Braginskii [12].

Finally eqn 2.2.21 says that the rate of change of pressure for a fluid element, moving with the fluid, is equal to the effects of compression,  $-\gamma P \nabla \cdot \underline{V}$ , plus the ohmic heating  $(\gamma-1) \eta |\underline{J}|^2$ . Some authors choose to ignore the ohmic heating contribution, in which case eqn 2.2.21 then becomes an expression of the adiabatic gas law for a given fluid element. Additionally, the need for an energy equation may be removed by the approximation of incompressibility i.e.  $\nabla \cdot \underline{V} = 0$ . This approximation lowers the number of dependent variables and so renders the equations more tractable both analytically and numerically.

### 2.2.3 SUMMARY AND DISCUSSION OF THE M.H.D EQUATIONS

The MHD equations are summarised in Table 2.2.1 below

Table 2.2.1

$$\frac{\partial \underline{B}}{\partial t} = -\nabla \times \underline{E} \quad 2.2.24$$

$$\underline{J} = \nabla \times \underline{B} \quad 2.2.25$$

$$\nabla \cdot \underline{B} = 0 \quad 2.2.26$$

$$\eta \underline{J} = \underline{E} + \underline{V} \times \underline{B} \quad 2.2.27$$

$$\frac{\partial \rho}{\partial t} + \nabla \cdot (\rho \underline{V}) = 0 \quad 2.2.28$$

Table 2.2.1 (Cont.)

$$\rho \left( \frac{\partial \underline{V}}{\partial t} + \underline{V} \cdot \nabla \underline{V} \right) = \underline{J} \times \underline{B} - \nabla P \quad 2.2.29$$

$$\frac{\partial P}{\partial t} + \underline{V} \cdot \nabla P = -\gamma P \nabla \cdot \underline{V} + (\gamma-1)\eta |\underline{J}|^2 \quad 2.2.30$$

Eqns 2.2.24 to 2.2.27 may be combined to give

$$\frac{\partial \underline{B}}{\partial t} = \nabla \times (\underline{V} \times \underline{B}) - \nabla \times (\eta \nabla \times \underline{B}) \quad 2.2.31$$

The MHD equations represent only a first approximation to reality. However, as such, they provide a useful insight into the behaviour of a plasma. Their use in the study of instabilities has provided a wealth of information on the attainment of stable operating regimes in containment devices. Although, even after all MHD stability requirements have been satisfied one may still be plagued by micro-instabilities [13]. Satisfying the MHD stability requirements does however remove one of the major possible sources of plasma loss. Conversely, it will prove extremely difficult to contain a plasma if these requirements are not satisfied.

### 2.3 INSTABILITIES OF AN IDEAL PLASMA

In this section we shall use the ideal, or infinitely conducting MHD equations, to study the stability of equilibria. An equilibrium may be defined as the situation when forces are balanced at every point in space. At equilibrium, the equation of motion, eqn 2.2.20 becomes

the familiar equilibrium relation

$$\nabla p = \underline{J} \times \underline{B} \quad 2.3.1$$

An equilibrium is said to be unstable to a given perturbation, if that perturbation grows in time. Conversely an equilibrium is stable if the perturbation decays. As pointed out by Bateman [14] we should strictly use a velocity perturbation to study stability, otherwise we do not initially have an equilibrium.

We shall look at the instabilities of a periodic cylindrical system. A cylinder is often chosen to model a toroidal system as the algebra is simple enough not to mask the physics, and yet the approximation is still good enough to exhibit most toroidal instabilities. It should be noted however, that one important class of instabilities, the ballooning modes [15] occur in a toroidal system but are precluded in cylindrical geometry.

By linearisation to first order in perturbed quantities it is possible to Fourier analyse in space and time, taking the  $\theta, z$  and  $t$  dependence of all perturbed quantities to be:-

$$e^{i(\omega t + m\theta + nkz)}$$

Where  $\omega$  is referred to as the growth rate,  $m$  the poloidal mode number,  $n$  the toroidal mode number, and  $k$  the wavenumber. The ratio of  $m$  to  $n$  is referred to as the helicity of that mode.

We divide our MHD instabilities into two classes :-

(i) Those with fixed boundaries - often a conducting wall. Here the

instabilities appear as an internal motion of the plasma.

(ii) Those with a vacuum region surrounding the plasma. Here free boundary modes representing gross motions of the plasma may occur.

### 2.3.1 FIXED BOUNDARY INSTABILITIES

The linearised MHD equations may be combined into a single relation [16].

$$\rho_0 \frac{\partial^2 \underline{\xi}}{\partial t^2} = \nabla \cdot (\gamma P_0 \nabla \cdot \underline{\xi} + \underline{\xi} \cdot \nabla P_0) + (\nabla \times \underline{B}_0) \times (\nabla \times (\underline{\xi} \times \underline{B}_0)) + (\nabla \times (\nabla \times (\underline{\xi} \times \underline{B}_0))) \times \underline{B}_0 \quad 2.3.2$$

where "0" subscripts indicate equilibrium quantities and "1" subscripts perturbation quantities and  $\underline{\xi}$  is the displacement defined as

$$\underline{\xi}(r, t) = \int_0^t v_1(r, t') dt'$$

Writing eqn 2.3.2 symbolically

$$\rho_0 \frac{\partial^2 \underline{\xi}}{\partial t^2} = F(\underline{\xi}) \quad 2.3.3$$

where F may be shown to be Hermitian [16], hence

$$\begin{aligned} \int \rho_0 \frac{\partial^2 \underline{\xi}}{\partial t^2} \cdot \frac{\partial \underline{\xi}}{\partial t} dV &= \frac{\partial}{\partial t} \left( \frac{1}{2} \int \rho_0 \left( \frac{\partial \underline{\xi}}{\partial t} \right)^2 dV \right) = \int \frac{\partial \underline{\xi}}{\partial t} \cdot F(\underline{\xi}) dV \\ &= \frac{1}{2} \int \left( \frac{\partial \underline{\xi}}{\partial t} \cdot F(\underline{\xi}) + \underline{\xi} \cdot F \left( \frac{\partial \underline{\xi}}{\partial t} \right) \right) dV = \frac{1}{2} \frac{\partial}{\partial t} \int \underline{\xi} \cdot F(\underline{\xi}) dV \end{aligned}$$

where integrals are taken over the entire plasma volume.

$$\text{So } \frac{\partial}{\partial t} \left( \frac{1}{2} \int \rho_0 \left( \frac{\partial \underline{\xi}}{\partial t} \right)^2 dV - \frac{1}{2} \int \underline{\xi} \cdot F(\underline{\xi}) dV \right) = 0 \quad 2.3.4$$



Now the first term is the kinetic energy (K.E.) of the perturbation so we may identify the second term as the change in the potential energy (P.E.) due to the perturbation. Now in any physical system, if there exists any perturbation which lowers its P.E., then that perturbation grows in time. If we use  $\delta w$  to denote the change in P.E. then we may state an energy principle :-

If  $\delta w > 0$  for all  $\underline{\xi}$  then the equilibrium is stable and conversely if there exists an  $\underline{\xi}$  such that  $\delta w < 0$  then the equilibrium is unstable.

This gives us a very powerful tool with which to study the stability of equilibria to ideal modes.

Much physical insight into the possible sources of instability and their stabilisation may be gained by careful formulation of  $\delta w$ , a particularly informative form is given by Furth et al [17]

$$\delta w = \frac{1}{2} \int \left[ |\underline{B}_\perp|^2 + \left| \underline{B}_\parallel - \underline{B}_0 \frac{\underline{\xi} \cdot \nabla P_0}{|\underline{B}_0|^2} \right|^2 + \gamma P_0 |\nabla \cdot \underline{\xi}|^2 \right. \\ \left. + \frac{\underline{J}_0 \cdot \underline{B}_0}{|\underline{B}_0|^2} \underline{B}_0 \times \underline{\xi} \cdot \underline{B}_1 - 2 \underline{\xi} \cdot \nabla P_0 \underline{\xi} \cdot \underline{K} \right] dV \quad 2.3.5$$

where  $\underline{B}_\perp$  and  $\underline{B}_\parallel$  are the components of  $\underline{B}_1$  perpendicular and parallel to  $\underline{B}_0$  respectively and  $\underline{K}$  is the normal curvature to  $\underline{B}_0$ .

The first three terms of eqn 2.3.5 are positive definite and hence represent stabilising terms. The first term is the energy stored in the Alfvén waves, the second is that stored in the fast magneto-sonic waves, and the third that stored in sound waves. The final two terms

may be negative and hence represent possible sources of instability. The penultimate term is associated with unstable modes (instabilities) driven by parallel current and known as kink modes. The final term represents modes driven by the interaction of pressure and curvature and known as interchange or Suydam modes.

If we now apply our energy principle to a single Fourier harmonic the calculus of variations allows us to minimise  $\delta w$  with respect to  $\xi_\theta$  and  $\xi_z$ . The result is that  $\delta w$  is minimised by incompressible velocity perturbations [18]. This allows us to write down a simplified form for  $\delta w$  in terms of  $\xi_r$  only [18] (for simplicity we denote  $\xi_r$  as  $\xi$  for the rest of this section)

$$\delta w = \frac{\pi}{2} \int_0^{\text{wall}} \left( f \left( \frac{\partial \xi}{\partial r} \right)^2 + g \xi^2 \right) dr \quad 2.3.6$$

where

$$f(r) = \frac{r^3 (nkB_z + \frac{m}{r} B_\theta)^2}{n^2 k^2 r^2 + m^2}$$

and

$$g(r) = \frac{2n^2 k^2 r^2}{n^2 k^2 r^2 + m^2} \frac{\partial P}{\partial r} + r (nkB_z + \frac{m}{r} B_\theta)^2 \frac{n^2 k^2 r^2 + m^2 - 1}{n^2 k^2 r^2 + m^2} \\ + \frac{2n^2 k^2 r^3}{(n^2 k^2 r^2 + m^2)^2} \left( n^2 k^2 B_z^2 - \frac{m^2}{r} B_\theta^2 \right)$$

Now  $f$  is positive definite and so if we are to have instability ( $\delta w < 0$ ) it must come from the  $g$  term being negative. Further, the range over which the  $g$  term is negative will give us a fair indication of the range of the instability, because  $\xi$  must be larger in this region to render  $\delta w < 0$ . For  $m=0$  the expression for  $g$  reduces to

$$g(r) = 2 \frac{\partial P}{\partial r} + \frac{B_z^2}{r} (n^2 k^2 r^2 + 1) \quad 2.3.7$$

Most pinches have higher pressure in the core decreasing towards the wall. Hence the pressure generally has a negative gradient and may be a source of instability. Also from eqn 2.3.7 we observe that increasing  $k$  increases the size of a positive definite term in  $g$ . Thus the shorter the wavelength, the narrower the range of the instability. For  $m=0$  we may conclude that the instability is fairly localised provided  $\left| \frac{\partial P}{\partial r} \right|$  is not large. For modes with poloidal mode number  $m \geq 1$  we refer to an analysis by Shafranov [19], who showed  $g$  to be quadratic in the variable  $\chi = \frac{-nkr B_z}{B_\theta} = -nq$ , where  $q$  is known as the safety factor. In the limit that  $\frac{nkr}{m} \ll 1$ , which is true of all tokamaks but not necessarily of other confinement devices, Shafranov shows the  $m \geq 2$  modes to be similar in character to the  $m=0$  mode with a fairly localised structure provided the pressure is not too high. For  $m=1$  modes the situation is very different with the two roots in  $\chi$  being given by

$$\chi_{1,2} = \frac{1 \pm 2\sqrt{\left(1 - \frac{3}{2} \frac{rP'}{B_\theta^2}\right)}}{3} \quad 2.3.8$$

Here, given that  $P' < 0$ , the instability is global in character being contained within the entire region  $-nq < 1$ . In Tokamaks  $q$  is generally a monotonic increasing function and hence  $q > 1$  on axis is a prerequisite for stability to the  $m=1$  mode.

If we assume the modes to be spatially localised in nature then we can derive a general stability criterion. Again referring to Shafranov's analysis it is shown that a given  $(m,n)$  mode will localise about a surface of radius  $r_s$  where  $\frac{m}{r_s} B_\theta(r_s) + nk B_z(r_s) = 0$ . This surface

represents a regular singularity of the ideal MHD equations and is thus often known as the singular surface. At this surface the perturbations produce least bending of the field lines and so this surface is energetically the most favourable for the given Fourier harmonic to occur at. If we define  $x=r-r_s$  then we may expand  $f$  for localised modes as

$$f(x) = \frac{x^2}{2} \frac{\partial^2 f}{\partial x^2} \Big|_{r_s} \quad 2.3.9$$

Then noting that the Schwartz inequality yields the inequality (which is valid for any  $\xi$  such that  $\xi|_{x=a} = \xi|_{x=b} = 0$ )

$$\int_a^b x^2 \left( \frac{\partial \xi}{\partial x} \right)^2 dx \geq \frac{1}{4} \int_a^b \xi^2 dx \quad 2.3.10$$

we see that our stability criterion  $\delta w > 0$  is definitely satisfied if

$$\int_a^b \xi^2 \left( \frac{1}{8} \frac{\partial^2 f}{\partial x^2} \Big|_{r_s} + g(r_s) \right) dx > 0$$

where since we are considering localised modes  $a$  and  $b$  are taken to be arbitrarily close to  $r_s$  ( $a < r_s < b$ ). This integral in turn is satisfied if the term of the integrand inside the bracket is positive. After some simple algebra, this gives us a necessary condition for stability

$$\frac{-2}{r B_z^2} \frac{\partial P}{\partial r} \left( \frac{q}{q'} \right)^2 < \frac{1}{4} \quad 2.3.11$$

This result was first derived by Suydam [20] and is known as Suydam's Criterion. Physically its interpretation is that for a given  $\frac{\partial P}{\partial r}$ , the localised mode may be stabilised by raising the shear in the region of the singular surface.

### 2.3.2 FREE BOUNDARY INSTABILITIES

If the plasma is surrounded by a vacuum then the plasma column is free to bend and contort. These modes were often observed by early experimentalists [21] and were given graphic names relating to the shape they produce.

For surface modes of poloidal mode number,  $m=0$  the instability is known as a sausage mode (fig 2.3.1). This mode is stabilised by the application of a longitudinal field,  $B_z$ , satisfying  $B_z^2 > B_\theta^2/2$  [22]. On being forced to compress  $B_z$  the mode becomes energetically unfavourable.

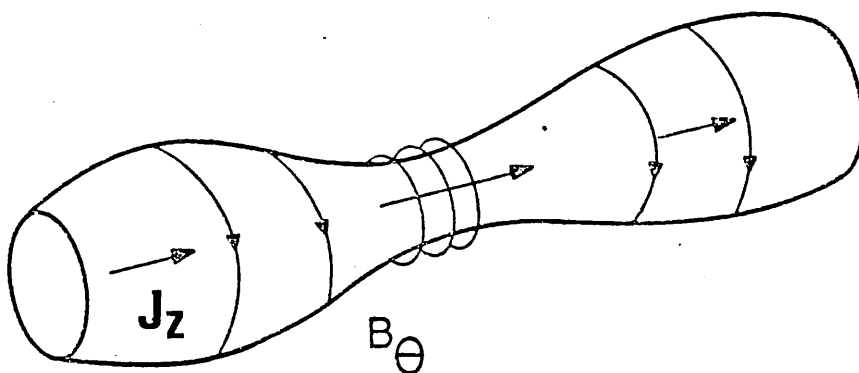


FIG.2.3.1  $m=0$  Sausage Mode

Modes with poloidal wavenumber,  $m \geq 1$ , contort the plasma into corkscrew shapes and are known as kink modes (fig 2.3.2). They may be stabilised by surrounding the plasma by a conducting wall. The image currents generated in the wall oppose the plasma motion and stabilise it.

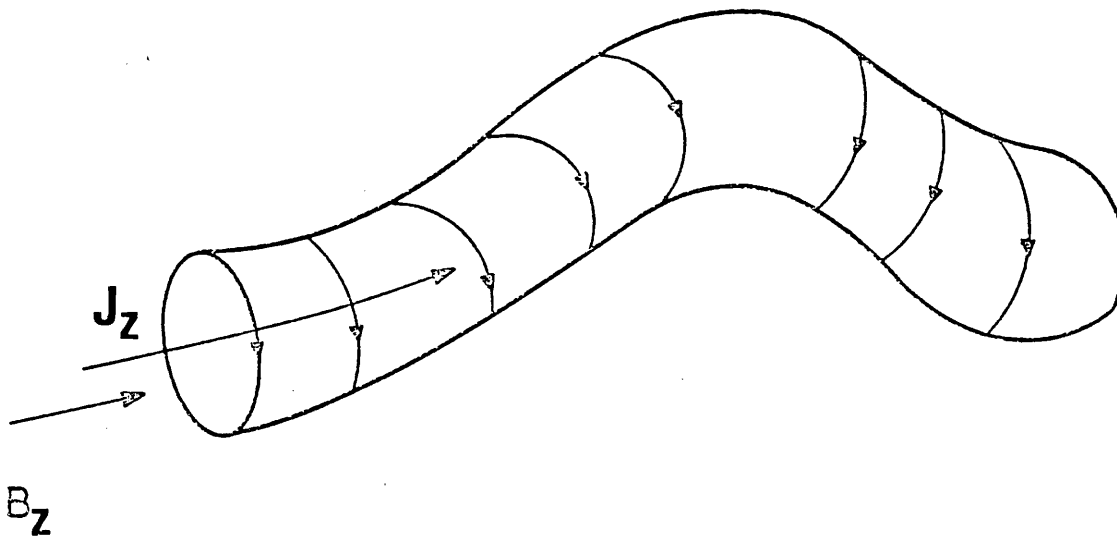


FIG. 2.3.2  $m=1$  Kink Mode

For higher poloidal mode numbers the distorted plasma takes on the appearance of a fluted column and these modes are known as flute modes.

An  $m=4$  flute mode is illustrated in fig 2.3.3.

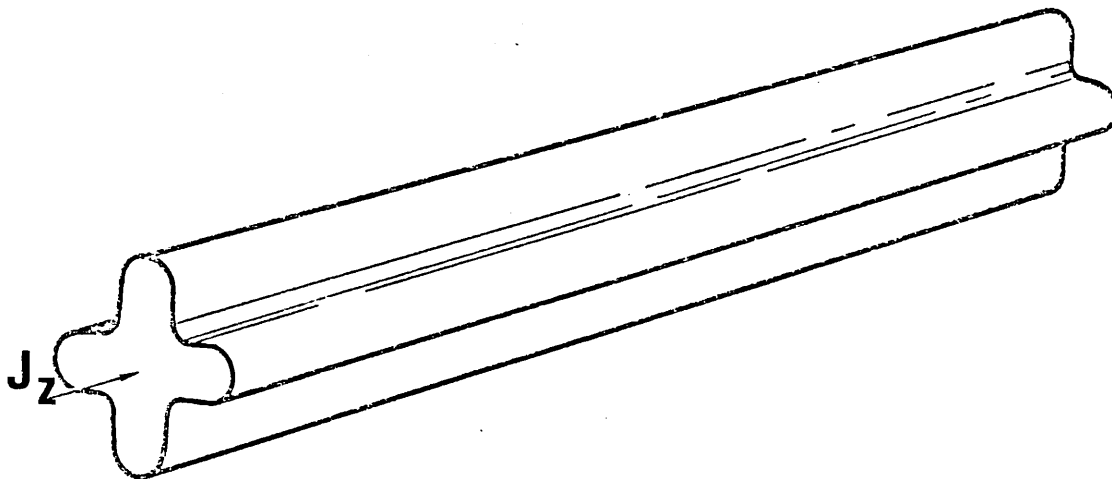


FIG.2.3.3  $m=4$  Flute Mode

## 2.4 RESISTIVE INSTABILITIES

It might be thought that the inclusion of resistivity into the ideal MHD framework, discussed in the last section, would merely provide a slight damping factor in their growth rates. This was shown to be a fallacious assumption by Furth, Killeen, and Rosenbluth in their classic paper [23].

The resistivity allows  $B_r$  to vary in time at the singular surface and permits the formation of structures known as magnetic islands. These will be discussed in detail in section 2.4.1. In the case of Suydam modes the inclusion of resistivity allows instability to occur even when Suydam's stability criterion is satisfied [24]. These new resistive counterparts of the Suydam mode are known as resistive interchange or g modes. They will be discussed in detail in section 2.4.2.

### 2.4.1 MAGNETIC ISLANDS

In order to establish the importance of resistivity the constraints imposed by infinite conductivity must first be examined. For  $\eta=0$  the first order Ohm's law is

$$\underline{E}_1 + \underline{V}_1 \times \underline{B}_0 = 0 \quad 2.4.1$$

So considering a singular surface defined by  $\underline{k} \cdot \underline{B}_0 |_{r_s} = 0$  and taking the r component of the vector product of  $\underline{k}$  and eqn.2.4.1 we obtain

$$i \underline{k} \cdot \underline{B}_0 \xi_r - B_{r_1} = 0 \quad 2.4.2$$

Hence at  $\underline{k} \cdot \underline{B}_0 = 0$  .

$$B_{r_1} = 0$$

The inclusion of resistivity introduces an  $\eta \underline{J}$  term to the R.H.S. of eqn 2.4.1 and relaxes the constraint on  $B_{r_1}$  at  $r_s$  .

If we restrict attention to the singular surface associated with a given  $\underline{k} = (0, \frac{m}{r}, nk)$  , then we may define a flux function,  $\psi$  as:-

$$B_r = - \frac{1}{r} \frac{\partial \psi}{\partial \tau} \quad \underline{k} \cdot \underline{B} = \frac{1}{r} \frac{\partial \psi}{\partial r}$$

where

$$\tau = m\theta + nkz$$

$\psi$  has the property that  $\underline{B} \cdot \nabla \psi = 0$ , hence field lines are constrained to lie on surfaces where  $\psi$  is constant. For an equilibrium situation,  $\underline{k} \cdot \underline{B}_0$ , by definition has a root at  $r_s$  and hence  $\psi_0$  has the form shown in fig 2.4.1.

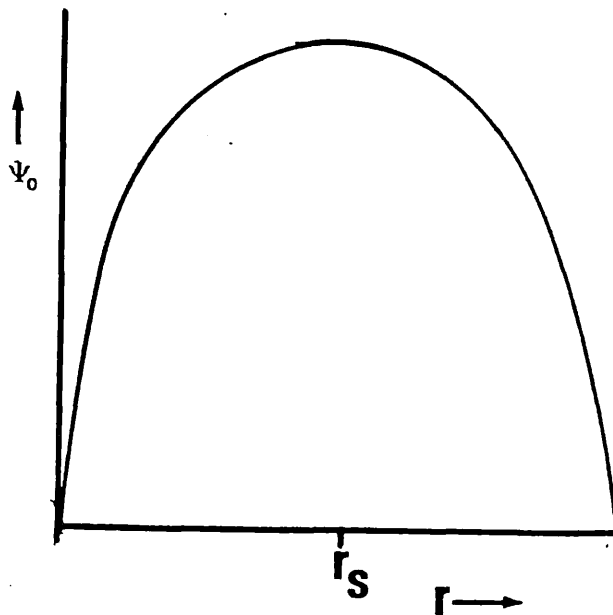


FIG.2.4.1 Typical form for  $\psi_0$  (note that in general value of  $\psi_0|_{r=0} \neq \psi|_{r=\text{wall}}$ )



Applying a small sine phased perturbation to  $B_r$ ,  $\psi = (\psi_0 - \psi_1 \cos \tau)$  takes the form shown in fig 2.4.2. Since field lines are constrained to surfaces of constant  $\psi$ , a contour plot of  $\psi$  reveals the island structure that a given field line will form (fig 2.4.3).

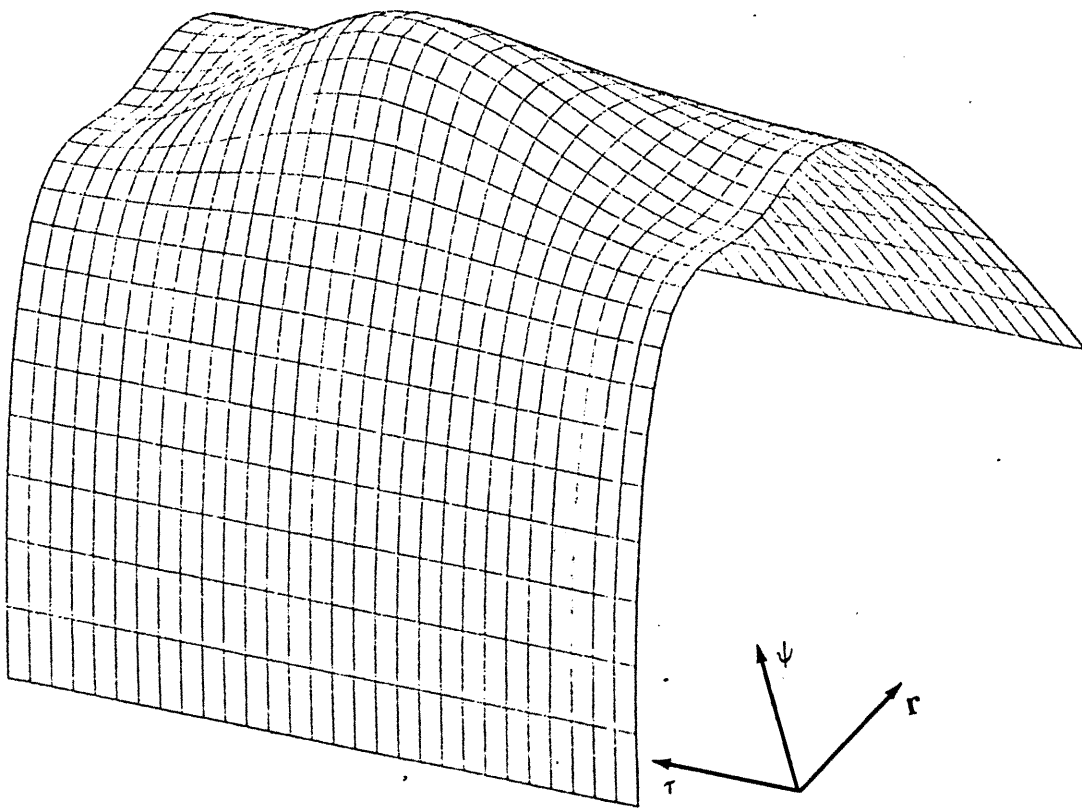


FIG.2.4.2 Effect of  $b_r$  perturbation on  $\psi_0$  (exaggerated for clarity).

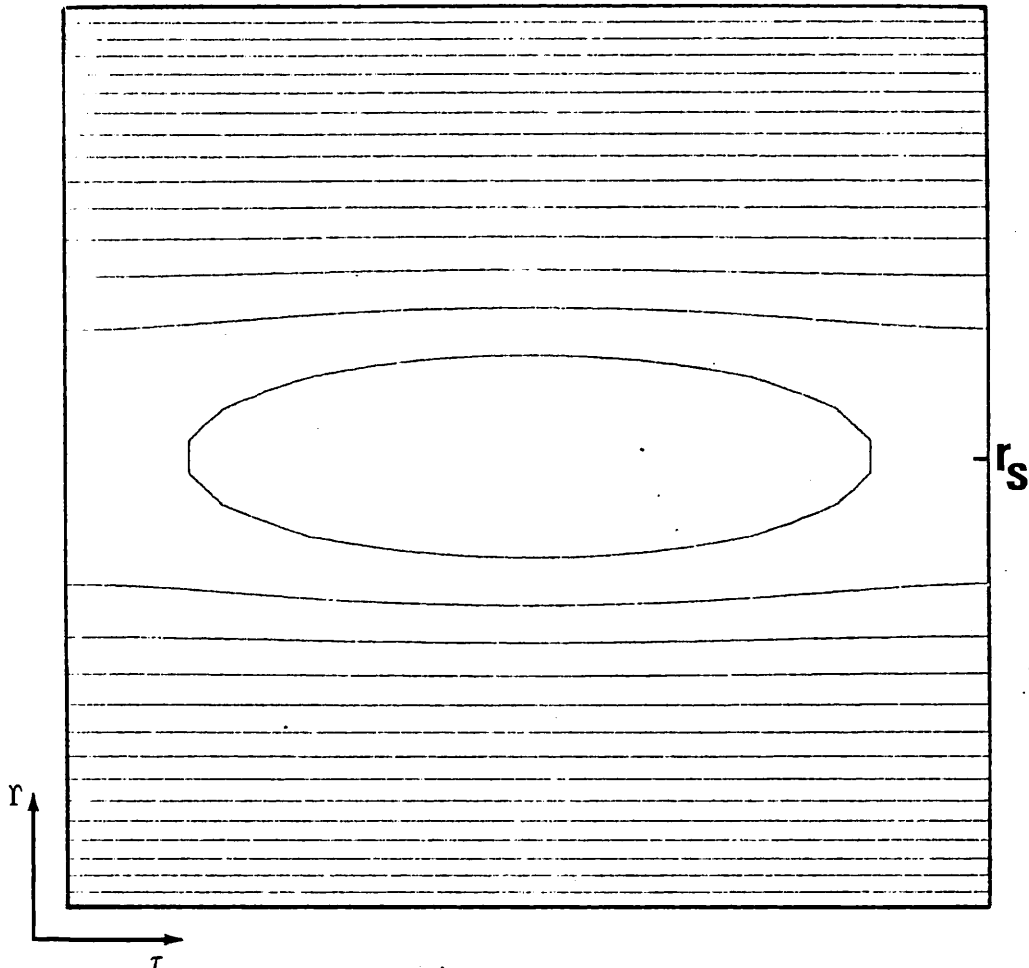


FIG.2.4.3 Magnetic Island Structure

The outermost flux surface of the island structure is known as the separatrix, the point where it crosses the singular surface is known as the x-point and the point at the centre of the island as the o-point. In a torus these island flux surfaces join onto themselves after traversing the torus  $m$  times toroidally and  $n$  times poloidally. Applying a field line following code to a suitably perturbed equilibrium we do indeed find these island structures. Fig 2.4.4 shows the intersection of a single field line with the azimuthal plane as that field line spirals round and round the torus.

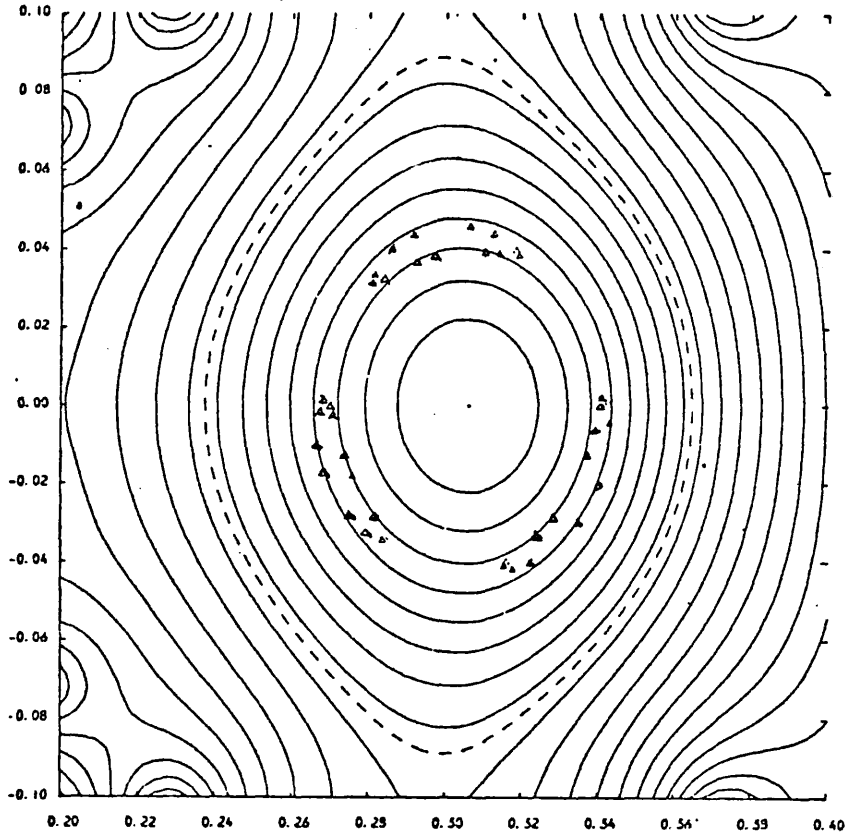


FIG.2.4.4 Azimuthal cross section of torus. The unbroken lines are flux contours of equilibrium obtained from a 2D code and the ' $\Delta$ ' the intersection of a field with the azimuthal plane as it spirals around the torus after the equilibrium has been perturbed to form  $m=3, n=2$  islands. The dotted line is the separatrix of the equilibrium flux surfaces.

A simple formula may be derived for the width of the island.

Examination of figs 2.4.2 and 2.4.3 shows

$$\psi|_{\text{x-point}} = \psi_0 - \psi_1$$

Expanding  $\psi_0$  as a Taylor series

$$\psi_0|_r = \psi_0|_{r_s} + \frac{(r-r_s)^2}{2} \left. \frac{\partial^2 \psi_0}{\partial r^2} \right|_{r_s}$$

since  $\frac{\partial \psi_0}{\partial r} \Big|_{r_s} = r_s k \cdot \underline{B}_0 \Big|_{r_s} = 0$ . At the farthest point on the separatrix from the singular surface

$$\psi = \psi_0 \Big|_{r_s} + \frac{w^2}{8} \frac{\partial^2 \psi_0}{\partial r^2} \Big|_{r_s} + \psi_1$$

where  $w$  is the island width. Now both this point and the x-point lie on the separatrix, hence their fluxes must be equal. Equating and rearranging gives a formula for the island width

$$w = 4 \sqrt{\left( \frac{-\psi_1}{\frac{\partial^2 \psi_0}{\partial r^2}} \right)}$$

where the minus sign is necessary since in this case  $\frac{\partial^2 \psi_0}{\partial r^2} < 0$ . Repeating the argument for  $\frac{\partial^2 \psi_0}{\partial r^2} > 0$  removes this minus sign. Hence in general

$$w = 4 \sqrt{\left( \frac{|\psi_1|}{\left| \frac{\partial^2 \psi_0}{\partial r^2} \right|} \right)} \quad 2.4.3$$

Bateman has found this formula provides a good estimate of island width even for large islands occupying as much as 30% of the minor radius [25].

The importance of these island structures is that the thermal conductivity parallel to  $\underline{B}$  is very large and hence there exists very good thermal conductivity across islands. This can result in detrimental effects to the heat containment of the pinch, particularly when a series of islands are nested side by side. Furthermore in tokamaks the interaction of islands of different helicity is thought to lead to random field line behaviour and cause the major disruption

which totally destroys the containment [26].

#### 2.4.2 THE RESISTIVE INTERCHANGE MODE

At the singular surface a second order pole occurs in the ideal M.H.D equations. The inclusion of resistivity however introduces higher order derivatives into the system and thus removes the singularity. Since, as mentioned previously the resistance of typical thermonuclear plasmas is very low, we can ignore the higher derivatives in all but a narrow layer about the singularity. Near the singularity the ideal and resistive solutions may differ dramatically; in particular as proved previously  $B_r$  is free to vary in time, at the singular surface for the resistive case.

The situation described in the last paragraph, where a higher order derivative may be ignored in all but a narrow layer, where a singularity of the reduced equations occurs, defines a boundary layer problem. Using the techniques of boundary layer analysis Coppi, Greene, & Johnson analysed the resistive stability of a cylindrical system [24]. Their results relating to the resistive interchange mode will now be briefly reviewed.

Central to any boundary layer analysis is the introduction of an expansion parameter which allows the relative magnitudes of the terms of the equations to be assessed in the boundary layer. The choice of expansion parameter relies on some a priori knowledge of which terms in the equations must be of equal magnitude. Coppi et al introduce an ordering such that:-

(i) The resistive layer thickness is comparable with the resistive skin

depth [27].

(ii) The inertia perpendicular to the magnetic field is comparable to the restoring force resulting from the bending of the magnetic field (evaluated at the boundary layer edge).

For low poloidal mode numbers these two assumptions yield a consistent ordering known as the slow interchange ordering [28]. Under this ordering Coppi et al reduce the resistive MHD equations within the boundary layer to the following:-

$$B^2 B_{B_1} = P' \xi_r + \gamma P \nabla \cdot \underline{\xi} \quad 2.4.4$$

$$\rho \omega^2 B^2 \xi_B = -P' b_r + \frac{imk B_z \ell' B^2}{2\pi} \times B_{B_1} \quad 2.4.5$$

$$\rho \omega^2 \xi_r'' = \frac{2m^2 B^2 B_\theta^2 B_{B_1}}{r_s^3 B_z^2} + \frac{imB_z \ell' k}{2\pi} \times B_{r_1}'' \quad 2.4.6$$

$$B_{r_1} - \frac{\eta}{\omega} B_{r_1}'' = \frac{imk B_z \ell' x}{2\pi} \xi_r \quad 2.4.7$$

$$B_{B_1} - \frac{\eta}{\omega} B_{B_1}'' = \frac{imk B_z \ell' x}{2\pi} \xi_B - \nabla \cdot \underline{\xi} - \frac{(P+B^2)'}{B^2} \xi_r \quad 2.4.8$$

where subscripts B relate to quantities parallel to the equilibrium magnetic field, and  $\ell = \frac{2\pi B_\theta}{kr B_z}$  is the rotational transform (all other quantities being as previously defined). All equilibrium quantities here being evaluated at the singular surface,  $r_s$ .

Implicit in the above ordering is the assumption that the growth rate scales as a fractional power of the resistivity, namely  $\eta^{1/3}$ . Thus outside the boundary layer not only do the MHD equations reduce to the ideal MHD equations but also to lowest order we may discard all time

derivatives. The result is that outside the boundary layer we are left to solve the marginal ideal MHD stability equation.

$$\frac{d}{dr} \left( \frac{d\xi_r}{f} \right) - g\xi_r = 0 \quad 2.4.9$$

Where  $f$  and  $g$  are as defined for eqn 2.3.6. Defining  $x = r - r_s$  and  $D = \lim_{x \rightarrow 0} \frac{-x^2 g(x)}{f(x)}$  the small  $x$  solution of eqn 2.4.9 is [18]

$$\xi_r = C1 \left| \frac{x}{r_s} \right|^h + C2 \left| \frac{x}{r_s} \right|^{-1-h} \quad 2.4.10$$

where

$$h = \frac{1}{2} \left( (1-4D)^{\frac{1}{2}} - 1 \right)$$

After some simple algebra we find

$$D = \frac{-2}{rB_z^2} \left. \frac{dP}{dr} \left( \frac{q}{q'} \right)^2 \right|_{r=r_s} \quad 2.4.11$$

where  $q$  is the safety factor.

Thus  $D < \frac{1}{4}$  is the Suydam stability criterion (eqn 2.3.11).

Returning now to the equations within the boundary layer, for convenience Coppi et al recast eqns 2.4.4-2.4.8 in dimensionless form.

Defining

$$B = \frac{|B|}{B_s} \quad F' = \frac{kr_s B_z(r_s) \ell'(r_s)}{2\pi B_s}$$

$$\beta = \frac{2P(r_s)}{B_s^2} \quad S = \frac{-2B_\theta^2(r_s) D}{r_s P'(r_s)}$$

and introducing a scale length and frequency

$$L_R = \left( \frac{\rho \eta^2 r_s^2}{m^2 F'^2 B^2} \right)^{1/6} \quad Q_R = \left( \frac{m^2 \eta F'^2 B^2}{\rho r_s^2} \right)^{1/3}$$

we can define new variables

$$X = x/L_R \quad Q = q/Q_R \quad \theta = \xi_r$$

$$\psi = (ia/L_R m F' B) B_{r1} \quad \nu = (DB^2/P') B_{B1}$$

Eqns 2.4.4-2.4.8 then yield

$$\psi'' = Q(\psi + X\theta) \quad 2.4.12$$

$$\theta'' = \frac{X^2}{Q} \theta + \frac{X}{Q} \psi - \frac{v}{Q^2} \quad 2.4.13$$

$$v'' = Q \left( 1 + \frac{X^2}{Q^2} + \frac{2}{\gamma\beta} \right) v + Q \left( S-D - \frac{2D}{\gamma\beta} \right) \theta + \frac{DX\psi}{Q} \quad 2.4.14$$

The large X solution of these equations is (X>0)

$$\begin{aligned} \theta = & (A1 X^{-\frac{1}{2}(1-s)} + A2 X^{-\frac{1}{2}(1-t)}) e^{x^2/2P} \\ & + A3 X^h + A4 X^{-1-h} \\ & + (A5 X^{-\frac{1}{2}(1+t)} + A6 X^{-\frac{1}{2}(1+s)}) e^{-x^2/2P} \end{aligned} \quad 2.4.15$$

where  $P=Q^{\frac{1}{2}}$ . Since s,t do not figure further they will not be defined. (Their definition may be found in Coppi et al [24])

Since eqns 2.4.12-2.4.14 constitute a sixth order set of differential equations, we shall require six matching conditions at the boundary layer edges. Two of these are implied by requiring that  $\theta$  remains bounded as  $X \rightarrow \infty$ , this requirement gives  $A1=A2=0$ . Two more matching conditions follow from similar considerations as  $X \rightarrow -\infty$ . Matching to the solutions exterior to the boundary layer yields the final two matching conditions by giving a value for  $A3/A4$  as  $X \rightarrow \infty$  and similarly as  $X \rightarrow -\infty$ . We thus have a well defined eigenvalue problem which we may in principle solve for Q.

We can simplify the problem by noting a particular property of the eqns 2.4.12-2.4.14; if we have a solution  $\psi, \theta, v$  valid for  $X>0$  then we



can construct solutions valid for  $X < 0$  by

$$\begin{aligned} \psi(X) &= -\psi(-X) & ; & & \theta(X) &= \theta(-X) & ; & & v(X) &= v(-X) \text{ for } X < 0 \\ \text{or } \psi(X) &= \psi(-X) & ; & & \theta(X) &= -\theta(-X) & ; & & v(X) &= -v(-X) \text{ for } X < 0 \end{aligned}$$

these correspond to the odd and even boundary conditions of Coppi et al:-

EVEN	$\theta=1$	$\theta'=0$	$\psi=0$	$v'=0$
ODD	$\theta=0$	$\psi=1$	$\psi'=0$	$v=0$

In general these modes are non-degenerate and so one will dominate by having a faster growth rate. The problem has thus been reduced to solving for  $X > 0$  (or  $X < 0$ ) and using either the odd or even boundary conditions at  $X=0$ .

To make further progress Coppi et al use a so called low  $\beta$  approximation. They reduce  $\beta$  and the shear to zero such that  $D$  remains finite. Eqn 2.4.14 then reduces to

$$v = D\theta \tag{2.4.16}$$

Using this eqn 2.4.13 becomes

$$\theta'' = \frac{X^2}{Q} \theta + \frac{X}{Q} \psi - \frac{D\theta}{Q^2} \tag{2.4.17}$$

Defining Fourier transforms of the functions  $\theta$  and  $\psi$  by

$$\lambda = \int_{-\infty}^{\infty} \theta(X) e^{-i\mu X} dX \quad \phi = \int_{-\infty}^{\infty} \psi(X) e^{-i\mu X} dX$$

eqns 2.4.12 and 2.4.17 yield

$$\left( \frac{\mu^2 \lambda'}{\mu^2 + Q} \right)' - \left( \mu^2 - \frac{D}{Q^2} \right) Q \lambda = 0 \tag{2.4.18}$$

One boundary condition arises from the series solution near the origin

$$D1 |\mu|^h + D2 |\mu|^{-1-h}$$

the ratio  $D1/D2$  being fairly simply related to  $C1, C2$  of eqn 2.4.10

(Coppi et al Appendix B) and the other boundary condition arises by requiring boundedness at infinity.

A particular set of solutions of eqn. 2.4.18 is

$$\lambda = \mu^h \exp\left(-\frac{1}{2} Q^{\frac{1}{2}} u^2\right) \sum_{j=0}^n a_j \mu^{2j}$$

where  $Q^{\frac{3}{2}} \frac{D}{h+2n+\frac{1}{2}+(4hn+(2n+\frac{1}{2})^2)^{\frac{1}{2}}}$  and  $n$  is an integer.

It should be noted that although this solution only satisfies a particular set of boundary conditions at the origin it does exhibit the important property that resistive interchange modes may grow in situations that are Suydam stable (i.e. satisfying eqn 2.3.11). Coppi et al numerically solve eqn 2.4.18 for the complete spectrum of  $A3/A4$  ratios (ie  $D1/D2$  ratios). Their results are shown in fig 2.4.5.

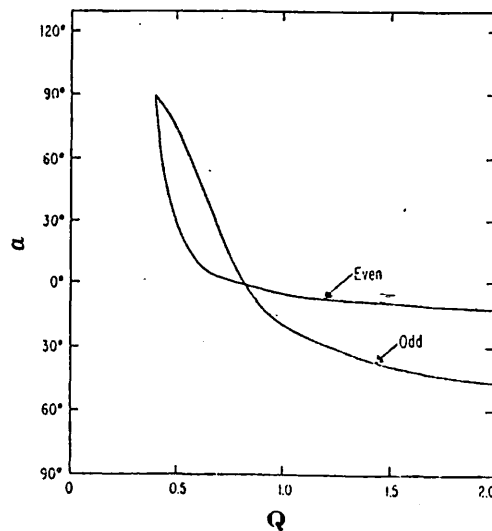


FIG.2.4.5  $\alpha = \text{Cot}^{-1} (A3/A4) v$  growth rate ( $Q$ ) for numerical solution of eqn 2.4.18 with odd and even boundary conditions. ( $D=0.1875$ )

It can be seen that at and beyond marginal ideal MHD stability ( $\alpha \leq 0$ ) the even mode dominates. Hence for ideally stable cases the odd mode

will dominate and further the odd mode has  $\psi|_{r_s} \neq 0$  (i.e.  $b_r|_{r_s} \neq 0$ ) hence the existence of islands is predicted by this theory.

In conclusion it must be noted that other valid boundary layer orderings exist; notably the tearing ordering and the fast interchange ordering [24]. In practice the solution is not purely a single ordering but a mixture in which one ordering is generally dominant. An analysis has been given by Glasser et al [29] which includes both the tearing and slow interchange orderings in various limits, for a system with toroidal geometry. The effects of including a non-hydrostatic stress tensor have also been investigated by various authors. For a curved geometry system parallel viscosity [30] is the lowest order term and represents the most important effect. Hosking and Robinson [31] have found that the inclusion of parallel viscosity can stabilise the  $m=1$  resistive g mode at modest beta. In a straight (slab) geometry the higher order perpendicular viscosity terms dominate and provide a stabilising effect [32]. Another effect of including resistivity is to cause a radial equilibrium flow [23], whose effects have been ignored in the above analysis. Dobrott et al [33] have found this effect reduces the growth rate of the tearing mode but has no effect on the resistive g mode. The nonlinear theory of the tearing mode has been studied in great detail over the last decade. Notable contributions being made analytically by Rutherford [34] and both numerically and analytically by White et al [35]. Numerical analyses have now been extended into 3D for the tearing mode. The most notable work here being done by the Oak Ridge Group [36].

3.1 INTRODUCTION

In order to gain some insight into the behaviour of the nonlinear g mode, it was decided to initially study a reduced and simplified problem. The particular assumptions and resulting equations are discussed in section 3.2. A brief review of the numerical methods applicable to such equations is given in section 3.3 and the  $m=0$  mode code developed to use these methods is discussed in section 3.4. Use of this code revealed that an efficient Fourier harmonic formulation is applicable to the g mode problem. This alternate formulation is described in section 3.5.

3.2 REDUCED FORMULATION

In the vicinity of the surface where the longitudinal field reverses in a Reverse Field Pinch (RFP), an  $m=0$  g mode may occur. It is known from previous work that the  $m=0$  mode is least likely to be stabilised by finite Larmor radius (FLR) effects, such as parallel viscosity [31]. Also the work of Schnack indicates that this mode may continue growing far into the nonlinear regime [37]. With these points in mind it was chosen to initially focus attention on the  $m=0$  mode only. To achieve this a 2D approximation is made in which all

variables are taken to be functions of  $r$  and  $z$  only, so that  $\frac{\partial}{\partial \theta} \equiv 0$ . To further simplify the problem the plasma is assumed to be incompressible. This assumption does affect the growth of the mode but in no way does it alter the basic character of it [38].

### 3.2.1 MATHEMATICAL FORMULATION

If one is not to impose a fictitious gravitational term to drive the  $g$  mode [23] it is necessary to study it in some curved geometry system. As the RFP is a toroidal containment system, toroidal co-ordinates might seem the obvious choice. However, a periodic cylindrical system produces a much simpler formulation, and because contemporary RFP's do not have tight aspect ratios, represents a fairly good approximation.

The conditions of incompressibility,  $\nabla \cdot \underline{V} = 0$ , and Maxwell's equation,  $\nabla \cdot \underline{B} = 0$ , permit the definition of a velocity stream function  $\phi$  and a magnetic stream function  $\psi$ , for our 2D system:-

$$\underline{V} = \left( -\frac{1}{r} \frac{\partial \phi}{\partial z}, \quad V_{\theta}, \quad \frac{1}{r} \frac{\partial \phi}{\partial r} \right) \quad 3.2.1$$

$$\underline{B} = \left( -\frac{1}{r} \frac{\partial \psi}{\partial z}, \quad B_{\theta}, \quad \frac{1}{r} \frac{\partial \psi}{\partial r} \right) \quad 3.2.2$$

The  $r$  and  $z$  components of Faraday's law

$$\frac{\partial \underline{B}}{\partial t} = -\nabla \times \underline{E}$$

may be integrated with respect to  $z$  and  $r$  respectively to give:-

$$rE_{\theta} = -\frac{\partial \psi}{\partial t} + C(t) \quad 3.2.3$$

where  $C(t)$  is as yet an arbitrary function of time. We impose a perfectly conducting wall as a boundary condition, hence the tangential

component of  $\underline{E}$  at the wall must be zero [39], and in particular  $E_\theta|_{\text{wall}}=0$ . We are also free to apply a gauge constraint which is taken to be  $\psi = \text{constant}$  at the wall for all time. Evaluating eqn 3.2.3 at the wall we find  $C(t)=0$ . Hence

$$rE_\theta = - \frac{\partial\psi}{\partial t} \quad 3.2.4$$

Using the  $\theta$ -component of Ohm's law (eqn 2.2.27) to substitute for  $E_\theta$  in eqn 3.2.4 we obtain

$$\frac{\partial\psi}{\partial t} + v_r \frac{\partial\psi}{\partial r} + v_z \frac{\partial\psi}{\partial z} = \eta \left( r \frac{\partial}{\partial r} \left( \frac{1}{r} \frac{\partial\psi}{\partial r} \right) + \frac{\partial^2\psi}{\partial z^2} \right) \quad 3.2.5$$

The  $\theta$ -component of the resistive diffusion equation (eqn 2.2.31) yields

$$\begin{aligned} \frac{\partial B_\theta}{\partial t} &= \frac{\partial}{\partial z} \left( \frac{v_\theta}{r} \frac{\partial\psi}{\partial r} - v_z B_\theta \right) - \frac{\partial}{\partial r} \left( v_r B_\theta + \frac{v_\theta}{r} \frac{\partial\psi}{\partial z} \right) \\ &+ \eta \left( \frac{1}{r} \frac{\partial}{\partial r} \left( r \frac{\partial B_\theta}{\partial r} \right) + \frac{\partial^2 B_\theta}{\partial z^2} - \frac{B_\theta}{r^2} \right) (\eta = \text{const}) \end{aligned} \quad 3.2.6$$

and the  $\theta$ -component of the equation of motion (eqn 2.2.29) yields

$$\rho \left( \frac{\partial v_\theta}{\partial t} + v_r \frac{\partial v_\theta}{\partial r} + v_z \frac{\partial v_\theta}{\partial z} + \frac{v_\theta v_r}{r} \right) = \frac{1}{r} \frac{\partial\psi}{\partial r} \frac{\partial B_\theta}{\partial z} - \frac{1}{r^2} \frac{\partial(rB_\theta)}{\partial r} \frac{\partial\psi}{\partial z} \quad 3.2.7$$

The  $\theta$ -component of the vorticity equation yields

$$\begin{aligned} &\rho \left( \frac{\partial\omega}{\partial t} + \frac{\partial}{\partial r} (v_r \omega) + \frac{\partial}{\partial z} (v_z \omega) \right) \\ &= \frac{\partial}{\partial r} (B_r J_\theta) + \frac{\partial}{\partial z} (B_z J_\theta) + \frac{1}{r} \left( \rho \frac{\partial v_\theta^2}{\partial z} - \frac{\partial B_\theta^2}{\partial z} \right) \end{aligned} \quad 3.2.8$$

where  $\omega$  is defined as  $\omega = (\nabla \times \underline{V})_\theta$ .

The system to be solved is closed by the relation

$$\omega = - \frac{1}{r} \frac{\partial^2\psi}{\partial z^2} - \frac{\partial}{\partial r} \left( \frac{1}{r} \frac{\partial\psi}{\partial r} \right) \quad 3.2.9$$

which follows directly from the definition of  $\omega$ .

### 3.2.2 BOUNDARY CONDITIONS

#### At the wall

At the perfectly conducting outer wall we choose, as mentioned above, the gauge constraint that  $\psi = \text{constant}$ .

If we also take the wall to be non-porous then we must have

$$v_r|_{\text{wall}} = 0$$

Hence

$$\frac{\partial \phi}{\partial z} = 0 \quad \rightarrow \quad \phi = \text{fn}(t) \text{ at wall}$$

As  $\phi$  is not time advanced we are free to choose any constraint which is in accordance with this equation. We choose the simplest

$$\phi|_{\text{wall}} = 0$$

As mentioned previously in section 3.2.1 the tangential component of  $\underline{E}$ , at the wall, is zero and hence in particular  $E_z = 0$ . This together with the z-component of Ohm's law gives

$$\frac{\partial r B_\theta}{\partial r} = 0$$

The final two boundary conditions required on  $\omega$  and  $v_\theta$  are rather more arbitrary. We choose those given by Schnack [40].

$$\frac{\partial r v_\theta}{\partial r} = 0$$

and

$$\frac{\partial v_z}{\partial r} = 0$$

This latter condition together with  $V_r|_{\text{wall}}=0$  gives

$$\omega|_{\text{wall}} = 0$$

So in summary, at the wall, we take the boundary conditions as

$$\phi = \frac{\partial r B_\theta}{\partial r} = \frac{\partial r V_\theta}{\partial r} = \omega = 0 \text{ and } \psi = \text{const.}$$

At the origin (r=0)

Here the boundary conditions are governed by symmetry considerations. We take those given by Dibiase [38]

$$V_r = B_r = V_\theta = B_\theta = \frac{\partial V_z}{\partial r} = \frac{\partial B_z}{\partial r} = 0$$

all variables being evaluated at r=0.

Using these relations and eqn 3.2.5 we find that

$$\left. \frac{\partial \psi}{\partial t} \right|_{r=0} = 0$$

hence

$$\psi|_{r=0} = \text{const.}$$

Also the above relations give

$$\omega|_{r=0} = 0$$

The final boundary condition required is that on  $\phi$  at r=0. This is by far the most difficult boundary condition to derive. First we shall present physical arguments to justify it and then support this with some mathematical detail.

The code developed to solve the above equations is primed by introducing a solution from a linear code. Thus initially the solution



is symmetric about the X-point in the z-direction and there is no reason why, as it evolves, either z-direction should be preferred. Hence  $V_z$  will always remain zero along a radius passing through the X-point. Thus

$$\int_0^{\text{wall}} r V_z \Big|_{z=X_{\text{pt}}} dr = \left[ \phi \Big|_{z=X_{\text{pt}}} \right]_0^{\text{wall}} = 0$$

Hence

$$\phi \Big|_{r=0, z=X_{\text{pt}}} = 0$$

and since  $\frac{\partial \phi}{\partial z} \Big|_{r=0} = 0$  we have  $\phi \Big|_{r=0} = 0$ .

The above argument is not wholly valid because a solution of any phase is free to arise from noise. However these perturbations will remain negligible as we follow the evolution of the solution for only a few e-folding times. Thus if any asymmetry arises in the solution, it must come from the convolutions that occur in the nonlinear terms. Taking an initially symmetric solution it is easy, though tedious, to show that it remains symmetrical. Choosing a symmetric solution with its X-point at  $z=0$ , we have

$$\psi = \sum_{n=0}^{\infty} \psi_n \cos nkz$$

$$v_{\theta} = v_{\theta_0} + \sum_{n=1}^{\infty} v_{\theta_n} \sin nkz$$

$$B_{\theta} = \sum_{n=0}^{\infty} B_{\theta_n} \cos nkz$$

$$\omega = \omega_0 + \sum_{n=1}^{\infty} \omega_n \sin nkz$$

now  $v_r = -\frac{1}{r} \frac{\partial \phi}{\partial z}$  and so  $v_r = 0$  thus

$$V_r = \sum_{n=1}^{\infty} V_{r_n} \cos nkz$$

examining the first nonlinear term of eqn 3.2.5

$$\begin{aligned} V_r \frac{\partial \psi}{\partial r} &= \sum_{m=1}^{\infty} V_{r_m} \cos mkz \sum_{n=0}^{\infty} \frac{\partial \psi_n}{\partial r} \cos nkz \\ &= \frac{1}{2} \sum_{n,m=0}^{\infty} V_{r_m} \frac{\partial \psi_n}{\partial r} (\cos(m-n)kz + \cos(n+m)kz) \end{aligned}$$

and so no asymmetry (sine phased terms) can be generated by this term. Similar reasoning shows the same to be true for all nonlinear terms in eqns 3.2.5-3.2.8. Thus

$$V_z = V_{z_0} + \sum_{n=1}^{\infty} V_{z_n} \sin nkz$$

It now remains to show that  $V_{z_0} = 0$ , in order to prove that  $V_z|_{z=Xpt} = 0$ .

The zeroth harmonic of the z-component of the equation of motion is

$$\rho_0 \left( \frac{\partial V_{z_0}}{\partial t} + \frac{1}{r} \frac{\partial}{\partial r} r (V_r V_z)_0 \right) = \frac{1}{r} \frac{\partial}{\partial r} r (B_r B_z)_0 \quad (\rho_0 = \text{const})$$

But

$$\begin{aligned} V_r V_z &= \left( \sum_{m=1}^{\infty} V_{r_m} \cos mkz \right) \left( V_{z_0} + \sum_{n=1}^{\infty} V_{z_n} \sin nkz \right) \\ &= V_{z_0} \sum_{m=1}^{\infty} V_{r_m} \cos mkz + \frac{1}{2} \sum_{m,n=1}^{\infty} V_{r_m} V_{z_n} (\sin(n-m)kz + \sin(n+m)kz) \end{aligned}$$

hence

$$(V_r V_z)_0 = 0$$

Similarly

$$(B_r B_z)_0 = 0$$

hence the initial condition that  $V_{z_0}|_{t=0} = 0$  implies

$$V_{z_0} = 0$$

Hence the boundary condition  $\phi|_{r=0} = 0$  is proven.

Summarising, the boundary conditions at the origin are

$$V_{\theta} = B_{\theta} = \phi = \omega = 0 \text{ and } \psi = \text{const}$$

At  $Z=0$  ,  $2\pi/k$

Since we are approximating a torus we require periodicity in the z-direction e.g.  $\psi|_{z=0} = \psi|_{z=2\pi/k}$  for all r, where k is the wave number of the first harmonic in the torus (ie.  $k = 1/R$ , R being the major radius).

### 3.2.3 NON DIMENSIONAL FORM

Before proceeding to a numerical solution it is convenient to cast the equations in non-dimensional form. There are two characteristic time scales applicable to the problem. The resistive diffusion time

$$\tau_R = \frac{a^2}{\eta_0} \tag{3.2.10}$$

and the Alfvén transit time

$$\tau_H = \frac{a \rho_0^{1/2}}{B_0} \tag{3.2.11}$$

where 'a' is the characteristic length for the problem and  $B_0$ ,  $\rho_0$  and  $\eta_0$  are typical values of magnetic field, density and resistivity respectively. The ratio of these two times  $S = \tau_R / \tau_H$  is the magnetic Reynolds number.

We choose to normalise to the Alfvén transit time and accordingly define dimensionless variables

$$\begin{aligned}
\hat{\mathbf{r}} &= \mathbf{r}/a & ; & & \hat{t} &= t/\tau_H & ; & & \hat{\eta} &= \eta/\eta_0 \\
\hat{\rho} &= \rho/\rho_0 & ; & & \hat{\mathbf{B}} &= \mathbf{B}/B_0 & ; & & \hat{\omega} &= \tau_H \omega \\
\hat{\phi} &= \tau_H \phi/a^3 & ; & & \hat{\psi} &= \psi/B_0 a^2 & ; & & \hat{J}_\theta &= a J_\theta/B_0 & ; & & \hat{V}_\theta &= \tau_H V_\theta/a
\end{aligned}$$

Because we choose  $\eta, \rho$  constant we set  $\hat{\eta}=\hat{\rho}=1$  and our equations then become

$$\frac{\partial \hat{\psi}}{\partial \hat{t}} + \frac{1}{\hat{r}} \frac{\partial}{\partial \hat{r}} (\hat{r} \hat{V}_r \hat{\psi}) + \frac{\partial}{\partial \hat{z}} (\hat{V}_z \hat{\psi}) = \frac{1}{S} \left( \frac{1}{\hat{r}} \frac{\partial \hat{r}}{\partial \hat{r}} \frac{\partial \hat{\psi}}{\partial \hat{r}} + \frac{\partial^2 \hat{\psi}}{\partial \hat{z}^2} - 2 \frac{\partial \hat{\psi}}{\partial \hat{r}} \right) \quad 3.2.12$$

$$\frac{\partial \hat{B}_\theta}{\partial \hat{t}} = \frac{\partial}{\partial \hat{z}} \left( \frac{\hat{V}_\theta}{\hat{r}} \frac{\partial \hat{\psi}}{\partial \hat{r}} - \hat{V}_z \hat{B}_\theta \right) - \frac{\partial}{\partial \hat{r}} \left( \hat{V}_r \hat{B}_\theta + \frac{\hat{V}_\theta}{\hat{r}} \frac{\partial \hat{\psi}}{\partial \hat{z}} \right) + \frac{1}{S} \left( \frac{\partial}{\partial \hat{r}} \left\{ \frac{1}{\hat{r}} \frac{\partial \hat{r} \hat{B}_\theta}{\partial \hat{r}} \right\} + \frac{\partial^2 \hat{B}_\theta}{\partial \hat{z}^2} \right) \quad 3.2.13$$

$$\frac{\partial \hat{V}_\theta}{\partial \hat{t}} = \frac{\partial}{\partial \hat{z}} \left( \frac{\hat{B}_\theta}{\hat{r}} \frac{\partial \hat{\psi}}{\partial \hat{r}} - \hat{V}_z \hat{V}_\theta \right) - \frac{1}{\hat{r}} \frac{\partial}{\partial \hat{r}} \hat{r} \left( \hat{V}_r \hat{V}_\theta + \frac{\hat{B}_\theta}{\hat{r}} \frac{\partial \hat{\psi}}{\partial \hat{z}} \right) - \frac{1}{\hat{r}} \left( \hat{V}_r \hat{V}_\theta + \frac{\hat{B}_\theta}{\hat{r}} \frac{\partial \hat{\psi}}{\partial \hat{z}} \right) \quad 3.2.14$$

$$\begin{aligned}
\frac{\partial \hat{\omega}}{\partial \hat{t}} &= \frac{\partial}{\partial \hat{z}} \left( \frac{\hat{J}_\theta}{\hat{r}} \frac{\partial \hat{\psi}}{\partial \hat{r}} \right) - \frac{\partial}{\partial \hat{r}} \left( \frac{\hat{J}_\theta}{\hat{r}} \frac{\partial \hat{\psi}}{\partial \hat{z}} \right) - \frac{\partial}{\partial \hat{r}} (\hat{V}_r \hat{\omega}) - \frac{\partial}{\partial \hat{z}} (\hat{V}_z \hat{\omega}) + \frac{1}{\hat{r}} \frac{\partial}{\partial \hat{z}} \left( \hat{V}_\theta \frac{\partial \hat{r} \hat{V}_\theta}{\partial \hat{r}} \right) \\
&\quad - \frac{\partial}{\partial \hat{r}} \left( \hat{V}_\theta \frac{\partial \hat{V}_\theta}{\partial \hat{z}} \right) - \frac{1}{\hat{r}} \frac{\partial}{\partial \hat{z}} \left( \hat{B}_\theta \frac{\partial \hat{r} \hat{B}_\theta}{\partial \hat{r}} \right) + \frac{\partial}{\partial \hat{r}} \left( \hat{B}_\theta \frac{\partial \hat{B}_\theta}{\partial \hat{z}} \right) \quad 3.2.15
\end{aligned}$$

$$\hat{\omega} = - \frac{\partial}{\partial \hat{r}} \left( \frac{1}{\hat{r}} \frac{\partial \hat{\phi}}{\partial \hat{r}} \right) - \frac{1}{\hat{r}} \frac{\partial^2 \hat{\phi}}{\partial \hat{z}^2} \quad 3.2.16$$

### 3.3 NUMERICAL METHODS

The above equations are intractable analytically and so one is virtually forced to solve them numerically. The technique employed in any numerical method for solving systems of differential equations is

to replace that system by a discrete system. One method which has been particularly successful in the study of tearing modes, is finite differences [41]. In a finite difference method the exact differential,  $\frac{\partial y}{\partial x}$ , is replaced by the ratio,  $\frac{\Delta y}{\Delta x}$ , over a finite set of points known as a grid or mesh. This discretisation is used both spatially and temporally in our application.

To elucidate the method the one dimensional diffusion equation will serve as a good example

$$\frac{\partial y}{\partial t} = \eta \frac{\partial^2 y}{\partial x^2} \quad 3.3.1$$

where  $\eta$  is the diffusion coefficient.

The second derivative may be approximated as [42]

$$\frac{y_{j+1} - 2y_j + y_{j-1}}{(\Delta x)^2} \quad 3.3.2$$

where  $\Delta x$  is the spatial grid spacing (assumed constant), and subscripts refer to spatial grid location.

Writing eqn 3.3.2 symbolically as  $D_j(y)$ , a general form for eqn 3.3.1 is

$$\frac{y_j^{n+1} - y_j^n}{\Delta t} = \eta(\theta D_j(y^n) + (1-\theta)D_j(y^{n+1})) \quad 3.3.3$$

where superscripts refer to temporal grid location,  $\Delta t$  is the temporal grid spacing, and  $0 \leq \theta \leq 1$ .

Setting  $\theta=1$  the right hand side of eqn 3.3.3 involves  $y$  values at the 'old' timestep only and hence eqn 3.3.3 may be trivially advanced in time - this is known as an explicit method. Conversely, setting  $\theta=0$

the right hand side involves  $y$  values at the 'new' timestep only and to time advance eqn 3.3.3 one is forced to solve a coupled set of linear equations for the  $y_j^{n+1}$  - this is known as an implicit method.

At first sight the simplicity of the explicit method would seem to make it the obvious choice. There are however two important criteria which any differencing scheme must satisfy :-

(i) Convergence, which is the property of the difference approximation that it tends to the continuum value uniformly, at any given time as the grid spacings and timestep go to zero. Convergence may be conditional on some relation between grid spacings ( $\Delta x$  and  $\Delta t$  in the example above)

(ii) Stability, which is the property that any given initial conditions yield a solution at a given time which remains uniformly bounded as the timestep goes to zero. Again this may be dependent on relations between grid spacings.

Lax's Equivalence theorem [43] states that stability is a necessary and sufficient condition for convergence. Hence in practice it is only necessary to test for stability.

A Von-Neumann stability analysis shows the explicit method to be stable provided that  $2\eta\Delta t/\Delta x^2 < 1$  [44], whereas the implicit method is unconditionally stable [45]. Hence although the implicit method requires far more computations per timestep, it will in general be more efficient for diffusive problems, since it requires far fewer

timesteps to advance the solution a certain distance in time, than the equivalent explicit calculation.

With  $\theta=0$  eqn 3.3.3 is only first order accurate in time, since the lowest order term in the discretisation error of the time derivative is  $O(\Delta t^2)$ . Setting  $\theta=\frac{1}{2}$  however, renders eqn 3.3.3 second order accurate in time, whilst still preserving the unconditional stability. This is known as a Crank-Nicholson weighting [46].

The solution of the coupled linear equations, which is necessitated by any non explicit method, may be greatly aided by considering their particular form. Defining  $\underline{Y}^n$  as  $[\underline{Y}^n]_j = y_{j+1}^n$  for  $1 \leq j \leq J-2$ , where  $J$  is the total number of spatial mesh points, we may symbolically write our implicit difference system (i.e. eqn 3.3.3 for  $2 \leq j \leq J-1$  and boundary conditions) as

$$\underline{\underline{A}} \underline{Y}^{n+1} = \underline{\underline{B}} \underline{Y}^n \quad 3.3.4$$

where  $\underline{\underline{A}}$  and  $\underline{\underline{B}}$  are  $(J-2) \times (J-2)$  matrices and the boundary conditions have been used to replace  $y_1^{n+1}, y_J^{n+1}, y_1^n$ , and  $y_J^n$ .

Examining eqn 3.3.3 we find that it couples only 3 adjacent spatial mesh points. Accordingly, except for its top and bottom rows,  $\underline{\underline{A}}$  will be non-zero only on the leading diagonal and the diagonals immediately above, and below it. Such a matrix is known as tridiagonal. Simple and efficient algorithms exist for solving tridiagonal systems and their associated boundary conditions. These are discussed in section 3.4.1 for some specific applications. The general problem is dealt with in detail by Richtmyer and Morton [47].

The numerical methods presented so far have been concerned with the solution of equations in one spatial dimension only. Extending these ideas to two or more dimensions leads to certain problems. If we take the two dimensional diffusion equation

$$\frac{\partial y}{\partial t} = \eta \left( \frac{\partial^2 y}{\partial x^2} + \frac{\partial^2 y}{\partial z^2} \right) \quad 3.3.5$$

and apply the Crank-Nicholson weighted differencing scheme in both spatial dimensions we obtain

$$\begin{aligned} \frac{y_{i,j}^{n+1} - y_{i,j}^n}{\Delta t} = \frac{\eta}{2} & \left( \frac{y_{i+1,j}^n - 2y_{i,j}^n + y_{i-1,j}^n}{(\Delta x)^2} + \frac{y_{i,j+1}^n - 2y_{i,j}^n + y_{i,j-1}^n}{(\Delta z)^2} \right. \\ & \left. + \frac{y_{i+1,j}^{n+1} - 2y_{i,j}^{n+1} + y_{i-1,j}^{n+1}}{(\Delta x)^2} + \frac{y_{i,j+1}^{n+1} - 2y_{i,j}^{n+1} + y_{i,j-1}^{n+1}}{(\Delta z)^2} \right) \quad 3.3.6 \end{aligned}$$

where the subscript  $i$  relates to  $x$  grid position and  $j$  to  $z$  grid position. Unfortunately eqn 3.3.6 no longer gives a tridiagonal form and so one is forced to invert a large matrix. Certain methods exist for solving such problems, notably successive over relaxation [48]. The practicality of this method is however, still somewhat questionable for such a large set of equations, as the MHD equations, on a reasonably refined mesh.

These computational difficulties can be overcome by the introduction of multi-step methods. If we advance half a timestep with  $x$  fully implicit and  $z$  fully explicit and the other half timestep with the roles of  $x$  and  $z$  reversed we obtain the following differencing scheme

$$\frac{y_{i,j}^{n+\frac{1}{2}} - y_{i,j}^n}{(\Delta t/2)} = \eta \left( \frac{y_{i+1,j}^{n+\frac{1}{2}} - 2y_{i,j}^{n+\frac{1}{2}} + y_{i-1,j}^{n+\frac{1}{2}}}{(\Delta x)^2} + \frac{y_{i,j+1}^n - 2y_{i,j}^n + y_{i,j-1}^n}{(\Delta z)^2} \right)$$



$$\frac{y_{i,j}^{n+1} - y_{i,j}^{n+\frac{1}{2}}}{(\Delta t/2)} = \eta \left( \frac{y_{i+1,j}^{n+\frac{1}{2}} - 2y_{i,j}^{n+\frac{1}{2}} + y_{i-1,j}^{n+\frac{1}{2}}}{(\Delta x)^2} + \frac{y_{i,j+1}^{n+1} - 2y_{i,j}^{n+1} + y_{i,j-1}^{n+1}}{(\Delta z)^2} \right) \quad 3.3.7$$

This method is aptly known as the alternating direction implicit (ADI) method [49]. It is second order accurate in time and unconditionally stable provided that the equations are linear. However while nonlinear effects introduce some timestep restrictions these are generally far less severe than for explicit methods. The great advantage of the ADI method lies in the fact that one only has to solve a tridiagonal system of equations at each half timestep. This brings the numerical solution of the MHD equations within the potential of modern computers.

#### 3.4 THE m=0 CODE

In this section, details of the application of the the numerical methods of the last section to the particular problem, of solving eqns 3.2.12-3.2.16 are given. The particular algorithm chosen is explained in section 3.4.1. From this algorithm a FORTRAN program "INSTAB" was developed.

Having developed such a large code one of the main problems is to ensure that there are no 'bugs' (errors) in it. Details of the various tests applied to the code are given in section 3.4.2.

### 3.4.1 THE ALGORITHM

The algorithm developed is an extension of the mixed explicit - implicit algorithm developed by Waddell et al [41].

The equations are differenced on a uniform mesh in the r-z plane. The r-mesh has its first point at r=0 and its final point at the wall. The z-mesh must be constructed so as to incorporate the periodicity in z direction. Accordingly the mesh is constructed so that z=0 lies halfway between the first and second mesh point and similarly z=2π/k lies halfway between the last and last but one mesh point. The periodicity requirement then becomes

$$\psi_{i,1} = \psi_{i,J-1}$$

$$\psi_{i,2} = \psi_{i,J} \quad \text{for } 1 \leq i \leq I$$

where I and J are the total number of r and z mesh points respectively.

Writing eqn 3.2.12-3.2.14 symbolically in the form

$$\frac{\partial \psi}{\partial t} = R_{\psi} + Z_{\psi} \quad 3.4.1$$

$$\frac{\partial B_{\theta}}{\partial t} = R_{B_{\theta}} + Z_{B_{\theta}} \quad 3.4.2$$

$$\frac{\partial V_{\theta}}{\partial t} = R_{V_{\theta}} + Z_{V_{\theta}} - \frac{1}{r} \left( V_{\theta} V_r + \frac{B_{\theta}}{r} \frac{\partial \psi}{\partial z} \right) \quad 3.4.3$$

where  $R_{\psi}$  contains the r derivatives of  $\psi$ ,  $Z_{\psi}$  contains the z derivatives of  $\psi$ , and  $R_{B_{\theta}}$  contains the r derivatives of  $B_{\theta}$  and  $V_{\theta}$  etc, and further writing eqn 3.2.15 symbolically

$$\frac{\partial \omega}{\partial t} = f(\psi, B_{\theta}, V_{\theta}, V_r, V_z, \omega)$$

the technique of solution is as follows (superscripts indicate timestep)

The R implicit  $\frac{1}{2}$  timestep

(i) The explicit equation

$$\frac{\omega^{n+\frac{1}{2}} - \omega^n}{(\frac{1}{2}\Delta t)} = f^n$$

is solved for  $\omega^{n+\frac{1}{2}}$ .

(ii) Eqn 3.2.16 is then solved for  $\phi^{n+\frac{1}{2}}$  and hence  $v_r^{n+\frac{1}{2}}$ ,  $v_z^{n+\frac{1}{2}}$  can be obtained

(iii) Next the implicit equation

$$\frac{\psi^{n+\frac{1}{2}} - \psi^n}{(\frac{1}{2}\Delta t)} = R_\psi^{n+\frac{1}{2}} + Z_\psi^n$$

is solved for  $\psi^{n+\frac{1}{2}}$ , where the  $v_r$ ,  $v_z$  are included at  $n+\frac{1}{2}$  in R and at n in the Z terms.

(iv) Finally the coupled implicit equations

$$\frac{B_\theta^{n+\frac{1}{2}} - B_\theta^n}{(\frac{1}{2}\Delta t)} = R_{B_\theta}^{n+\frac{1}{2}} + Z_{B_\theta}^n$$

$$\frac{v_\theta^{n+\frac{1}{2}} - v_\theta^n}{(\frac{1}{2}\Delta t)} = R_{v_\theta}^{n+\frac{1}{2}} + Z_{v_\theta}^n - \frac{1}{r} \left( v_r^{n+\frac{1}{2}} v_\theta^{n+\frac{1}{2}} + \frac{B_\theta^{n+\frac{1}{2}}}{r} \frac{\partial \psi^{n+\frac{1}{2}}}{\partial z} \right)$$

are solved for  $v_\theta^{n+\frac{1}{2}}$ ,  $B_\theta^{n+\frac{1}{2}}$  where  $v_r$ ,  $v_z$ ,  $\psi$  are at  $n+\frac{1}{2}$  in R terms and at n in Z terms.

The Z implicit  $\frac{1}{2}$  timestep

(i) The explicit equation

$$\frac{\omega^{n+1} - \omega^n}{\Delta t} = f^{n+\frac{1}{2}}$$

is solved for  $\omega^{n+1}$ .

(ii) Eqn 3.2.16 is then solved for  $\phi^{n+1}$ , and hence  $V_r^{n+1}$ ,  $V_z^{n+1}$  can be obtained.

(iii) Next the implicit equation

$$\frac{\psi^{n+1} - \psi^{n+\frac{1}{2}}}{(\frac{1}{2}\Delta t)} = R_{\psi}^{n+\frac{1}{2}} + Z_{\psi}^{n+1}$$

is solved for  $\psi^{n+1}$ , where the  $V_r$ ,  $V_z$  are at  $n+\frac{1}{2}$  in R terms and at  $n+1$  in Z terms.

(iv) Finally the coupled implicit equations

$$\frac{B_{\theta}^{n+1} - B_{\theta}^{n+\frac{1}{2}}}{(\frac{1}{2}\Delta t)} = R_{B_{\theta}}^{n+\frac{1}{2}} + Z_{B_{\theta}}^{n+1}$$

$$\frac{V_{\theta}^{n+1} - V_{\theta}^{n+\frac{1}{2}}}{(\frac{1}{2}\Delta t)} = R_{V_{\theta}}^{n+\frac{1}{2}} + Z_{V_{\theta}}^{n+1} - \frac{1}{r} \left( V_r^{n+1} V_{\theta}^{n+1} + \frac{B_{\theta}^{n+1}}{r} \frac{\partial \psi^{n+1}}{\partial z} \right)$$

are solved for  $B_{\theta}^{n+1}$ ,  $V_{\theta}^{n+1}$  where  $V_r$ ,  $V_z$ ,  $\psi$  are at  $n+\frac{1}{2}$  in R terms and at  $n+1$  in Z terms.

Eqn 3.2.16 is solved by a standard Fourier transform method. Using a fast Fourier transform routine [50] the harmonics of  $\omega$  can be obtained.

$$\omega = \sum_{n=0}^{N_{\max}} (A_n(r) \sin nkz + B_n(r) \cos nkz)$$

If we define  $C_n, D_n$  by

$$\phi = \sum_{n=0}^{N_{\max}} (C_n(r) \sin nkz + D_n(r) \cos nkz)$$

then eqn 3.2.16 implies

$$A_n = -\frac{\partial}{\partial r} \left( \frac{1}{r} \frac{\partial C_n}{\partial r} \right) + \frac{n^2 k^2}{r} C_n \quad 3.4.4.(a)$$

$$B_n = -\frac{\partial}{\partial r} \left( \frac{1}{r} \frac{\partial D_n}{\partial r} \right) + \frac{n^2 k^2}{r} D_n \quad 3.4.4.(b)$$

Since  $A_n, B_n$  are known, eqns 3.4.4 represent a system of tridiagonal equations which may be solved for  $C_n, D_n$ . The values of  $\phi$  may now be obtained by use of a fast Fourier transform routine to invert the transform.

The solution of the implicit equations for  $\psi$  varies according to whether the r or z direction is implicit :-

#### R implicit

If we rewrite our difference form for  $\psi$  as (for any j such that  $k \leq j \leq J$ )

$$A_i \psi_{i+1,j}^{n+\frac{1}{2}} + B_i \psi_{i,j}^{n+\frac{1}{2}} + C_i \psi_{i-1,j}^{n+\frac{1}{2}} = D_i \quad 3.4.5$$

and take the boundary conditions (see section 3.2.2) as

$$\psi|_{r=0} = C1 \quad \text{and} \quad \psi|_{r=wall} = C2$$

Then assuming

$$\psi_{i,j}^{n+\frac{1}{2}} = F_i \psi_{i+1,j}^{n+\frac{1}{2}} + G_i \quad 3.4.6$$

and substituting into eqn 3.4.5.

$$A_i \psi_{i+1,j}^{n+\frac{1}{2}} + B_i \psi_{i,j}^{n+\frac{1}{2}} + C_i (F_{i-1} \psi_{i,j}^{n+\frac{1}{2}} + G_{i-1}) = D_i$$

hence

$$\psi_{i,j}^{n+\frac{1}{2}} = \frac{-A_i}{B_i + C_i F_{i-1}} \psi_{i+1,j}^{n+\frac{1}{2}} + \frac{D_i - C_i G_{i-1}}{B_i + C_i F_{i-1}}$$

comparison with eqn 3.4.6 gives

$$F_i = -\frac{A_i}{B_i + C_i F_{i-1}} \quad \text{and} \quad G_i = \frac{D_i - C_i G_{i-1}}{B_i + C_i F_{i-1}} \quad 3.4.7$$

Now the boundary condition at the origin gives

$$F_1 = 0 \quad \text{and} \quad G_1 = C1$$

using eqns 3.4.7 one can then obtain  $F_i, G_i$  for  $2 \leq i \leq I-1$ . Using these values for  $F_i, G_i$ , eqn 3.4.6 and the boundary condition at the wall to initiate the recursion relation, one can obtain  $\psi_{i,j}^{n+\frac{1}{2}}$  for  $1 \leq i \leq I$ .

### Z implicit

The r implicit solution above requires two sweeps of the mesh - one to solve for  $F_i, G_i$  and the other to obtain the solution,  $\psi_{i,j}^{n+\frac{1}{2}}$ . The solution for z implicit is further complicated by the periodic boundary conditions and three sweeps of the mesh are necessitated.

Again defining our difference form as (for any  $i$  such that  $1 \leq i \leq I$ )

$$A_j \psi_{i,j+1}^{n+1} + B_j \psi_{i,j}^{n+1} + C_j \psi_{i,j-1}^{n+1} = D_j \quad 3.4.8$$

and noting the periodic boundary conditions imply

$$\psi_{i,J}^{n+1} = \psi_{i,2}^{n+1} \quad \psi_{i,J-1}^{n+1} = \psi_{i,1}^{n+1}$$

We proceed by assuming

$$\psi_{i,j}^{n+1} = F_j \psi_{i,j+1}^{n+1} + G_j \psi_{i,J-1}^{n+1} + H_j \quad 3.4.9$$

Substituting into eqn 3.4.8 yields

$$\psi_{i,j}^{n+1} = \frac{1}{B_j + C_j F_{j-1}} \left( -A_j \psi_{i,j+1}^{n+1} - C_j G_{j-1} \psi_{i,J-1}^{n+1} + D_j - C_j H_{j-1} \right)$$

comparison with eqn 3.4.9 reveals

$$F_j = \frac{-A_j}{B_j + C_j F_{j-1}} \quad 3.4.10(a)$$

$$G_j = \frac{-C_j G_{j-1}}{B_j + C_j F_{j-1}} \quad 3.4.10(b)$$

$$H_j = \frac{D_j - C_j H_{j-1}}{B_j + C_j F_{j-1}} \quad 3.4.10(c)$$

To start these recursion relations (eqns 3.4.10) off we require a starting condition. This is obtained by application of the boundary conditions to eqn 3.4.9 which yields

$$F_1 = H_1 = 0 \quad \text{and} \quad G_1 = 1$$

If we further assume

$$\psi_{i,j}^{n+1} = T_j \psi_{i,J-1}^{n+1} + S_j \quad 3.4.11$$

then substituting into eqn 3.4.9 we obtain

$$\psi_{i,j}^{n+1} = (F_j T_{j+1} + G_j) \psi_{i,j-1}^{n+1} + F_j S_{j+1} + H_j \quad 3.4.12$$

Comparison with eqn 3.4.11 reveals

$$T_j = F_j T_{j+1} + G_j \quad 3.4.13(a)$$

$$S_j = F_j S_{j+1} + H_j \quad 3.4.13(b)$$

Again we require some initial values for S, T to start these recursion relations - these may trivially be seen to be

$$T_{J-1} = 1 \quad S_{J-1} = 0$$

Applying eqn 3.4.11 we have now expressed all variables in terms of  $\psi_{i,J-1}^{n+1}$ . So to complete the solution it remains to obtain a value for  $\psi_{i,J-1}^{n+1}$ . This may be achieved by applying eqn 3.4.8 at J-1 and using eqn 3.4.11. The result is

$$\psi_{i,J-1}^{n+1} = \frac{D_{J-1} - A_{J-1} S_2 - C_{J-1} S_{J-2}}{A_{J-1} T_2 + B_{J-1} + C_{J-1} T_{J-2}} \quad 3.4.14$$

The implicit solution for  $V_\theta, B_\theta$  is slightly more involved again, since these two equations are coupled, thus necessitating a 2x2 matrix formalism. The tridiagonal solution techniques above carry over in a straightforward manner with matrix inversion and multiplication replacing scalar division and multiplication.



### 3.4.2 TESTING THE CODE

Firstly it is necessary to ensure the code is executing the specified algorithm correctly. At the time of writing, each routine was tested in isolation. In particular each of the tridiagonal inverters was checked to ensure that it really was obtaining the solution of the equations. The  $\phi$  solver was also carefully checked by taking a specified  $V_r$ ,  $V_z$ , working out  $\omega$  from these, solving eqn 3.2.16 for  $\phi$ , and then checking that  $V_r = -\frac{1}{r} \frac{\partial \phi}{\partial z}$ ,  $V_z = \frac{1}{r} \frac{\partial \phi}{\partial r}$ .

Having passed these initial tests the code as a whole was checked for numerical convergence. It is unnecessary to check for timestep convergence as the code contains a routine which repeatedly halves the timestep until a desired degree of convergence is obtained. This timestep checking is performed every 30 or so timesteps, thus ensuring continued timestep convergence.

The r-mesh testing was performed in a straightforward manner, the number of radial mesh points being increased until suitable convergence occurs. It was found that for a magnetic Reynolds number,  $S=1000$ , fifty radial mesh points were sufficient.

Testing the z-mesh presents more of a problem, because the fast Fourier transform routine requires  $2^n$  input data points and so one is not free to vary the number of z-mesh points at will. Instead the actual z length was increased to  $4\pi/k$ , whilst maintaining the number of z-mesh points constant, and two islands instead of the normal one were primed in (see figs 3.4.1 and 3.4.2). The comparison between the growth rate curves for this run and an equivalent one island run shows

the z-mesh convergence to be fairly good (see fig 3.4.3).

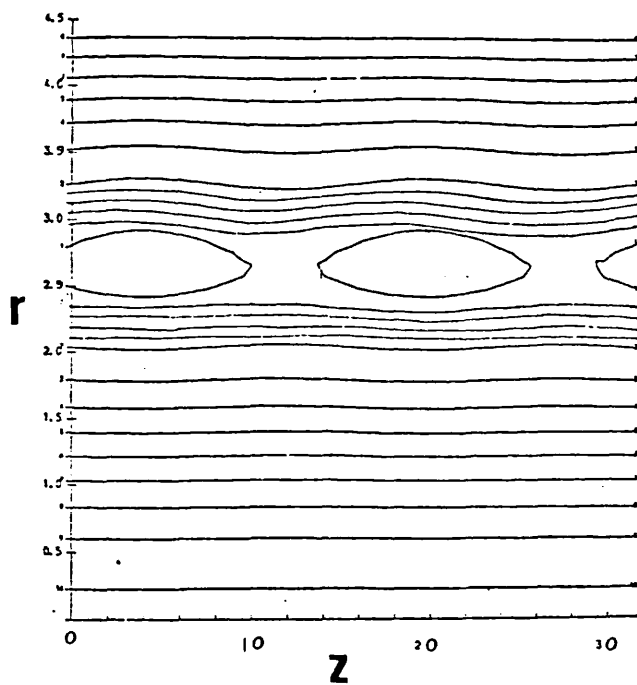
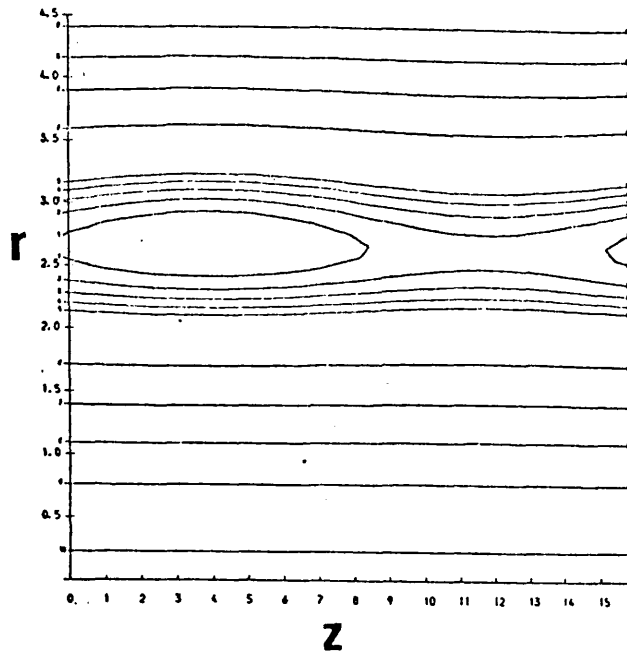


FIG. 3.4.1 and 3.4.2 Comparison of normal island structure (top) and double island structure (bottom) used for mesh testing.

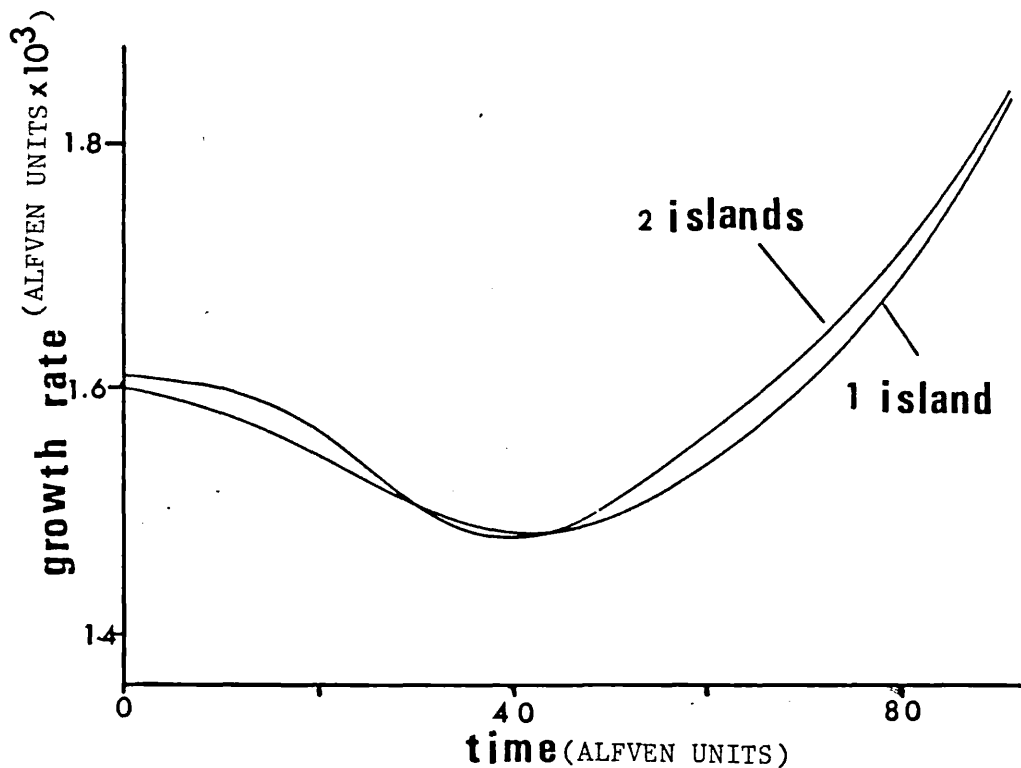


FIG. 3.4.3 Comparison of growth rates between one and two island runs.

Finally it is necessary to check the answers which the code obtains are correct. This is a much more difficult area as no analytic solutions exist to test the code against. However, by priming the code with an equilibrium perturbed by eigenfunctions from a linear code, a certain degree of checking is possible. It is found that if the eigenfunctions are sufficiently small to stay within the linear regime then the growth rates of the linear and the nonlinear codes agree to within 2% over a range of  $500 < S < 5000$ . It must be stressed that this comparison is to the initial growth rates of the nonlinear code, since particularly at lower  $S$  subsequent diffusion of the equilibrium alters the growth rates.

It is also worth noting here that detailed explanations and independent confirmation of results from the code presented in

Chapter 4 serves as an additional validation of the code.

### 3.5 THE FOURIER HARMONIC CODE

Use of the code described in the last section revealed that a more efficient Fourier harmonic formulation was applicable to the  $m=0$  g mode problem. The derivation of the Fourier harmonic equations is described in section 3.5.1 and the numerical algorithm used to solve them is described in section 3.5.2.

#### 3.5.1 FOURIER HARMONIC EQUATIONS

If the linear part of the g mode development is chosen to have:-

$$\psi_i(r, z, t) = \psi_i(r, t) \cos kz$$

$$V_{\theta_i}(r, z, t) = V_{\theta_i}(r, t) \sin kz$$

$$B_{\theta_i}(r, z, t) = B_{\theta_i}(r, t) \cos kz$$

$$\omega_i(r, z, t) = \omega_i(r, t) \sin kz$$

then it is proven in section 3.2.2 that the nonlinear solution will be

$$\psi = \sum_{n=0}^{\infty} \psi_n \cos nkz$$

$$V_{\theta} = V_{\theta_0} + \sum_{n=1}^{\infty} V_{\theta_n} \sin nkz$$

$$B_{\theta} = \sum_{n=0}^{\infty} B_{\theta_n} \cos nkz$$

$$\omega = \omega_0 + \sum_{n=1}^{\infty} \omega_n \sin nkz$$

$$V_r = \sum_{n=1}^{\infty} V_{r_n} \cos nkz; \quad V_z = \sum_{n=1}^{\infty} V_{z_n} \sin nkz$$

Considering the zeroth harmonic of the  $V_\theta$  equation (eqn 3.2.7)

$$\rho_0 \left( \frac{\partial V_{\theta_0}}{\partial t} + \left( V_r \frac{\partial V_\theta}{\partial r} \right)_0 + \frac{(V_\theta V_r)_0}{r} + \left( V_z \frac{\partial V_\theta}{\partial z} \right)_0 \right) = \frac{1}{r} \left( \frac{\partial \psi}{\partial r} \frac{\partial B_\theta}{\partial z} \right)_0 - \frac{1}{r^2} \left( \frac{\partial r B_\theta}{\partial r} \frac{\partial \psi}{\partial z} \right)_0$$

now

3.5.1

$$\begin{aligned} V_\theta V_r &= \left( \sum_{m=1}^{\infty} V_{r_m} \cos mkz \right) \left( V_{\theta_0} + \sum_{n=1}^{\infty} V_{\theta_n} \sin nkz \right) \\ &= V_{\theta_0} \sum_{m=1}^{\infty} V_{r_m} \cos mkz + \frac{1}{2} \sum_{m,n=1}^{\infty} V_{r_m} V_{\theta_n} (\sin(n-m)kz + \sin(n+m)kz) \end{aligned}$$

Hence

$$(V_\theta V_r)_0 = 0$$

Similarly

$$\left( V_r \frac{\partial V_\theta}{\partial r} \right)_0 = \left( V_z \frac{\partial V_\theta}{\partial z} \right)_0 = \left( \frac{\partial \psi}{\partial r} \frac{\partial B_\theta}{\partial z} \right)_0 = \left( \frac{\partial r B_\theta}{\partial r} \frac{\partial \psi}{\partial z} \right)_0 = 0$$

and so eqn 3.5.1 shows  $\frac{\partial V_{\theta_0}}{\partial t} = 0$ . The initial condition that  $V_\theta(r, z, t=0) = 0$  then implies that  $V_{\theta_0} = 0$ . Similar reasoning shows  $\omega_0 = 0$  also. Therefore

if it is chosen to truncate the Fourier series after the first three harmonics, the Fourier components of equation 3.2.12 result in a set of equations for time advancing  $\psi_0, \psi_1, \psi_2$  :-

$$\frac{\partial \psi_0}{\partial t} + \frac{1}{2r} \frac{\partial}{\partial r} r (V_{r_1} \psi_1 + V_{r_2} \psi_2) = \frac{1}{S} \left( \frac{1}{r} \frac{\partial}{\partial r} r \frac{\partial \psi_0}{\partial r} - \frac{2}{r} \frac{\partial \psi_0}{\partial r} \right) \quad 3.5.2(a)$$

$$\begin{aligned} \frac{\partial \psi_1}{\partial t} + \frac{1}{r} \frac{\partial}{\partial r} r (\psi_0 V_{r_1} + \frac{1}{2} (\psi_1 V_{r_2} + \psi_2 V_{r_1})) + k (\psi_0 V_{z_1} + \frac{1}{2} (\psi_1 V_{z_2} - \psi_2 V_{z_1})) \\ = \frac{1}{S} \left( \frac{1}{r} \frac{\partial}{\partial r} r \frac{\partial \psi_1}{\partial r} - k^2 \psi_1 - \frac{2}{r} \frac{\partial \psi_1}{\partial r} \right) \end{aligned} \quad 3.5.2(b)$$

$$\begin{aligned} \frac{\partial \psi_2}{\partial t} + \frac{1}{r} \frac{\partial}{\partial r} r (\psi_0 v_{r2} + \frac{1}{2} \psi_1 v_{r1}) + k(2\psi_0 v_{z2} + \psi_1 v_{z1}) \\ = \frac{1}{S} \left( \frac{1}{r} \frac{\partial}{\partial r} r \frac{\partial \psi_2}{\partial r} - 4k^2 \psi_2 - \frac{2}{r} \frac{\partial \psi_2}{\partial r} \right) \end{aligned} \quad 3.5.2(c)$$

(where the "hats"  $\hat{\phantom{x}}$  have been omitted for simplicity). Similarly the Fourier components of eqns 3.2.13 to 3.2.15 yield equations for time advancing  $B_{\theta_0}, B_{\theta_1}, B_{\theta_2}; v_{\theta_1}, v_{\theta_2}$  and  $\omega_1, \omega_2$ . The set of equations to be solved is closed by the Fourier components of eqn 3.2.16

$$\omega_1 = \frac{k^2 \phi_1}{r} - \frac{\partial}{\partial r} \left( \frac{1}{r} \frac{\partial \phi_1}{\partial r} \right) \quad 3.5.3(a)$$

$$\omega_2 = \frac{4k^2 \phi_2}{r} - \frac{\partial}{\partial r} \left( \frac{1}{r} \frac{\partial \phi_2}{\partial r} \right) \quad 3.5.3(b)$$

The justification for truncating the Fourier series after three terms arises primarily from comparing with results obtained by solving the full set of reduced MHD equations; some comparisons are given in the next section. The physical explanations of the nonlinear g mode behaviour given in the next chapter, also indicate that a small number of Fourier harmonics should resolve the dominant non-linear behaviour. Further, studies using the Oak Ridge Fourier harmonic code RSF have shown that three harmonics can adequately resolve the behaviour of a single helicity tearing mode far into the nonlinear regime [36].

### 3.5.2 NUMERICAL ALGORITHM

The algorithm is broadly similar to that given in section 3.4.1. The Fourier resolution means however that the problem has been reduced from a 2D to a 1D problem. Consequently the ADI time advancement must be replaced by an applicable scheme. In this case a Crank-Nicholson scheme was chosen.

In detail the algorithm chosen is:-

(i) Solve the coupled set of eqns 3.5.2(a),(b), & (c) for  $\psi_0$ ,  $\psi_1$ ,  $\psi_2$  using a Crank-Nicholson weighted differencing scheme, including the  $V_r$ 's and  $V_z$ 's at their "old" values.

(ii) Obtain the time centred value for  $\psi_0$  by taking the average of the "old" and "new"  $\psi_0$  values. Similarly obtain the time centred values for  $\psi_1$ ,  $\psi_2$ .

(iii) Solve the coupled  $B_\theta$ ,  $V_\theta$  equations for  $B_{\theta_0}$ ,  $B_{\theta_1}$ ,  $B_{\theta_2}$ ,  $V_{\theta_1}$ , and  $V_{\theta_2}$  using a Crank-Nicholson weighted differencing scheme. Include the  $V_r$ 's and  $V_z$ 's at their "old" values and the  $\psi$ 's at their time centred values.

(iv) Obtain the time centred values of  $V_\theta$ 's and  $B_\theta$ 's.

(v) Solve the coupled equations for  $\omega_1$  and  $\omega_2$  using a Crank-Nicholson weighted differencing scheme. Including all dependent variables except the  $V_r$ 's and  $V_z$ 's at their time centred values.

(vi) Solve eqns 3.5.3(a) and (b) to obtain the new timestep values for  $\phi_1$ ,  $\phi_2$ . Hence obtain the "new"  $V_{r_1}$ ,  $V_{r_2}$ ,  $V_{z_1}$ , and  $V_{z_2}$ .

All variables have now been time advanced and the algorithm is repeated.

Validation of the code based on the above algorithm was performed by comparing the results with those of the code described in

section 3.4. Defining the percentage difference between the results as  $\int_0^{\text{wall}} |g_n - g_o| dr \times 100 / \int_0^{\text{wall}} g_o dr$  where  $g_n(r)$  is the growth rate from the code described in this section and  $g_o(r)$  is the growth rate from the code described in section 3.4. The percentage error for a case with a magnetic Reynolds number of a 1000 primed such that it is far into the nonlinear regime is 10%, 14% and 6% at 20, 40, and 60 Alfven transit times, respectively.



#### 4.1 INTRODUCTION

In this chapter the results arising from application of the numerical methods of the last chapter to the  $m=0$  g mode in an RFP are discussed.

Firstly in section 4.2 the equilibrium and its tearing mode stability properties are examined in detail. A brief review of the linear stability properties of this model is given in section 4.3. The diagnostic quantities output from the codes are explained in section 4.4 and in section 4.5 the nonlinear results obtained are presented and discussed at length. Finally in section 4.6 an attempt is made to draw some coherent conclusions from section 4.5.

#### 4.2 THE EQUILIBRIUM

The equilibrium used for all the results presented in this chapter is the tearing mode stable (TMS) equilibrium developed by Robinson [7].

If we take the equilibrium equation (eqn 2.3.1)

$$\frac{\partial P}{\partial r} = -B_z \frac{\partial B_z}{\partial r} - \frac{B_\theta}{r} \frac{\partial r B_\theta}{\partial r} \quad 4.2.1$$

and define the pitch,  $\mu(r) = \frac{r B_z}{B_\theta}$  then

$$\frac{dB_\theta}{dr} = B_\theta \frac{(\mu^2/r - \mu\mu' - r + Cr\mu'^2)}{\mu^2 + r^2} \quad 4.2.2$$

where  $C(r) = -\left(\frac{dP}{dr}/rB_z^2\right)\left(\frac{\mu'}{\mu}\right)^2$  is the Suydam parameter ( $C \ll \frac{1}{8}$  being the Suydam stability criterion - eqn 2.3.11)

Specific analytic equilibria can now be obtained by defining functional forms for  $\mu(r)$  and  $C(r)$ . Following Robinson  $C$  is taken to be constant and  $\mu$  is chosen as

$$\mu(r) = 2\left(1 - \frac{r^2}{8} - \frac{r^4}{\lambda}\right) \quad 4.2.3$$

Robinson found  $\lambda=400$  gives optimal tearing mode stability properties and this value is used for the work presented in this chapter. This form for the pitch function has the advantage of implicitly satisfying Robinson's on axis stability criterion [51].

As an added refinement a vacuum region can be included in which  $B_\theta \propto \frac{1}{r}$  and  $B_z = \text{constant}$ . To avoid discontinuities at the plasma vacuum interface a matching zone is necessitated. In this region variables are matched smoothly to each other, in particular  $C$  is taken smoothly to zero with zero gradients at either end. A typical RFP equilibrium given by the TMS model is shown in fig 4.2.1.

It is important for our purposes that the equilibrium be tearing mode stable in order to isolate the nonlinear g mode behaviour. At zero beta using the boundary layer methods of section 2.4.2 a tearing

mode stability criterion can be derived [24]. The result is that for an equilibrium to be tearing mode unstable

$$\Delta' = \frac{\lim_{\epsilon \rightarrow 0} \left( \frac{d\psi}{dr} \Big|_{r_s + \epsilon} - \frac{d\psi}{dr} \Big|_{r_s - \epsilon} \right)}{\psi \Big|_{r_s}} > 0 \quad 4.2.4$$

where  $\psi = \frac{b r^{3/2}}{(m^2 + k^2 r^2)^{1/2}}$  and  $\underline{k} \cdot \underline{B} \Big|_{r_s} = 0$ .

Using an ingenious technique to integrate across the singularity of the ideal MHD equations [52] Robinson has developed a code RCWALL to test for tearing mode stability. This has allowed an exhaustive study of the tearing mode stability properties of the TMS model. The results are summarised for  $C=0.$ ,  $\lambda=400$  and a vacuum radius,  $R_v=4.2$  in fig 4.2.2.

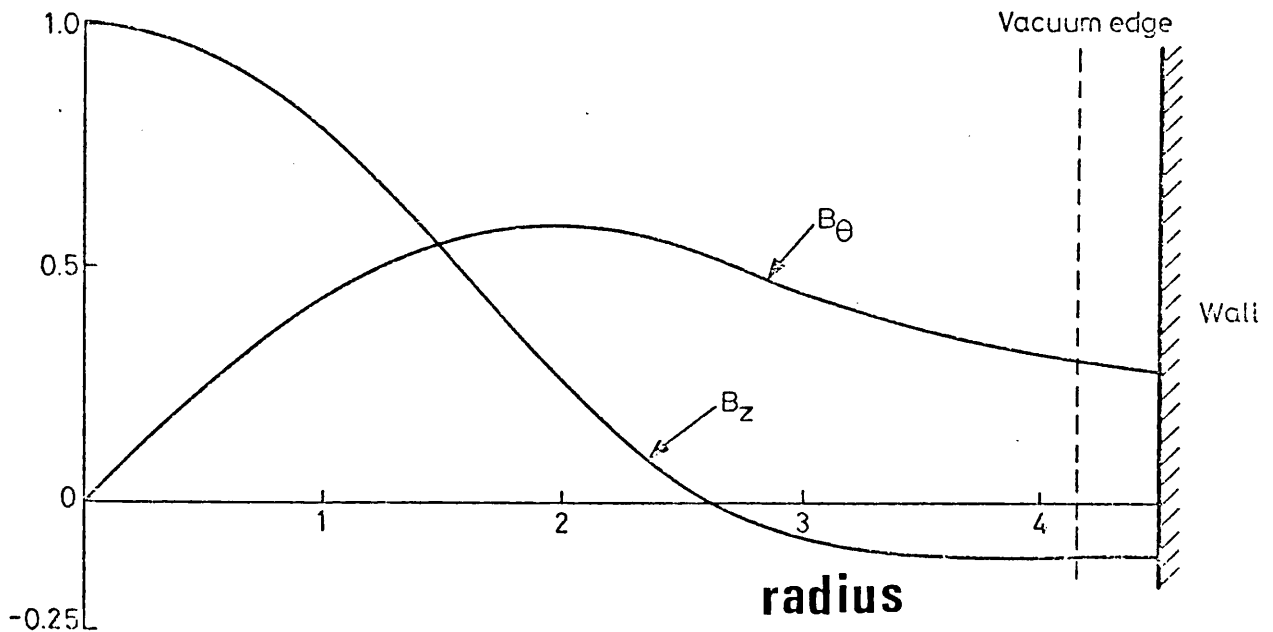


FIG.4.2.1 Tearing mode stable equilibrium with a vacuum edge included.

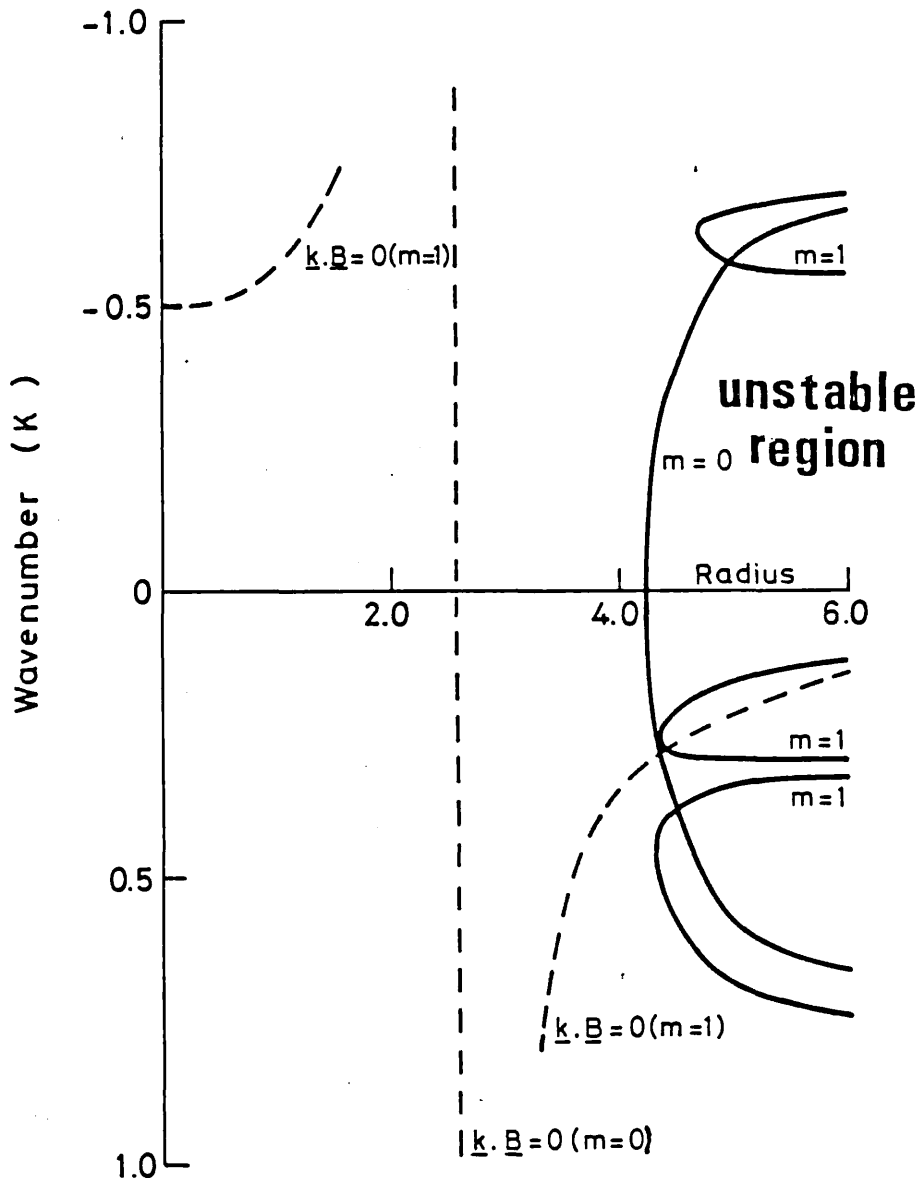


FIG. 4.2.2 Position of wall for marginal tearing mode stability for TMS model to  $m=0$  and  $m=1$  modes.

The  $\Delta'$  analysis can be extended to low beta configurations and a modified stability criterion derived [29]. Unfortunately at the pressures applicable to g mode instability the validity of the  $\Delta'$  analysis becomes dubious, which leaves us in a dilemma over testing our equilibria for tearing mode stability. The  $m=0$  tearing mode however, is very weak and stability should therefore be dominated by the g mode behaviour. In an attempt to satisfy ourselves that our finite beta equilibria are tearing mode stable we have adopted two methods. Both

involve reducing the pressure to zero while maintaining some property of the fields. In the first method we maintain the pitch constant, and in the second we maintain the quantity  $\sigma = \underline{J} \cdot \underline{B} / |\underline{B}|^2$  constant. The second method is probably preferable as it is the gradient of  $\sigma$  which drives the tearing mode. The reduced pressure configurations are then tested for stability using RCWALL. Both methods show all the equilibria used for results presented in this chapter to be tearing mode stable.

#### 4.3 LINEAR RESULTS

In this section previous linear results are very briefly reviewed. These results form the cornerstone of our nonlinear analysis since a linear growth phase precedes the nonlinear phase. Indeed to avoid unnecessary use of computer time the nonlinear code is primed with eigenfunctions from a linear code.

Several linear cylindrical resistive MHD codes have been developed by Robinson, Killeen and co-workers. The majority of this work is detailed in the thesis of Dibiase [38]. The incompressible MHD code, RIP4A, detailed in Dibiase's thesis, is the linear counterpart of our nonlinear  $m=0$  code. RIP4A solves the linearised equations

$$-\rho_0 \frac{\partial}{\partial t} (\nabla^2 \underline{v}_1) = \nabla \times \nabla \times (\underline{B}_0 \cdot \nabla \underline{B}_1 + \underline{B}_1 \cdot \nabla \underline{B}_0) \quad 4.3.1$$

$$\frac{\partial \underline{B}_1}{\partial t} = \nabla \times (\underline{v}_1 \times \underline{B}_0) - \nabla \times (\eta_0 (\nabla \times \underline{B}_1) + \eta_1 (\nabla \times \underline{B}_0)) \quad 4.3.2$$

as an initial value problem for  $V_1$ ,  $B_1$  using a Crank-Nicholson weighted finite difference method.

Using the TMS equilibrium of the previous section for  $R_{wall}=4.5$ ,  $C=0.05$ ,  $m=0$ ,  $k=0.4$  and a magnetic Reynolds number  $S=1000$ , the eigenfunctions shown in fig 4.3.1 are obtained. These eigenfunctions exhibit the odd mode symmetry detailed in section 2.4 and also exhibit very rapid variations in the region of the singular surface, thus vindicating the use of boundary layer techniques. It is of interest to increase  $C$  beyond marginal ideal instability. The resulting eigenfunctions are shown in fig 4.3.2 for a  $C=0.8$ . These show the even mode symmetry characteristic of ideal instabilities,

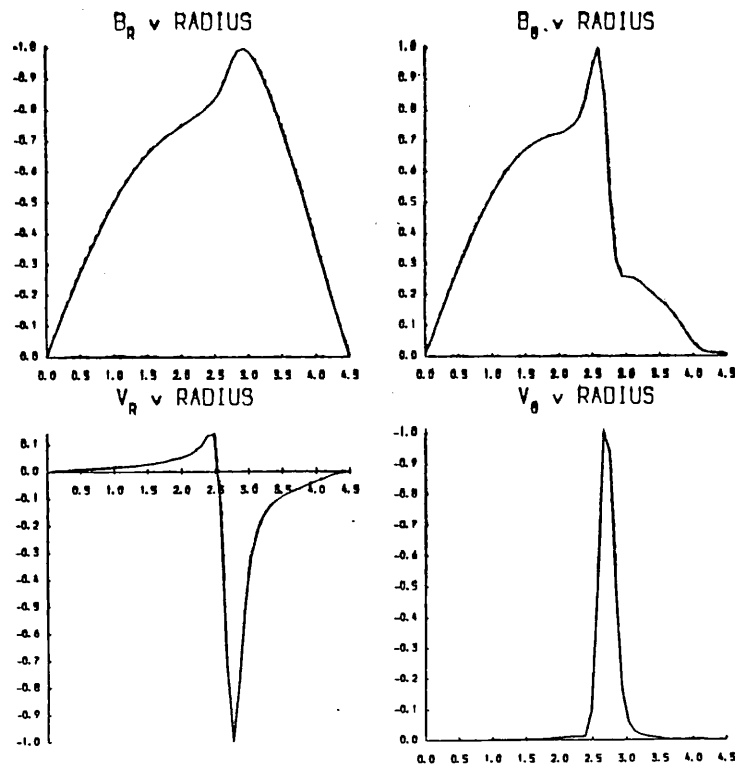


FIG. 4.3.1 Linear eigenfunction for  $C=0.05$  (all magnitudes in arbitrary units). The singular surface is at  $r=2.66$ .

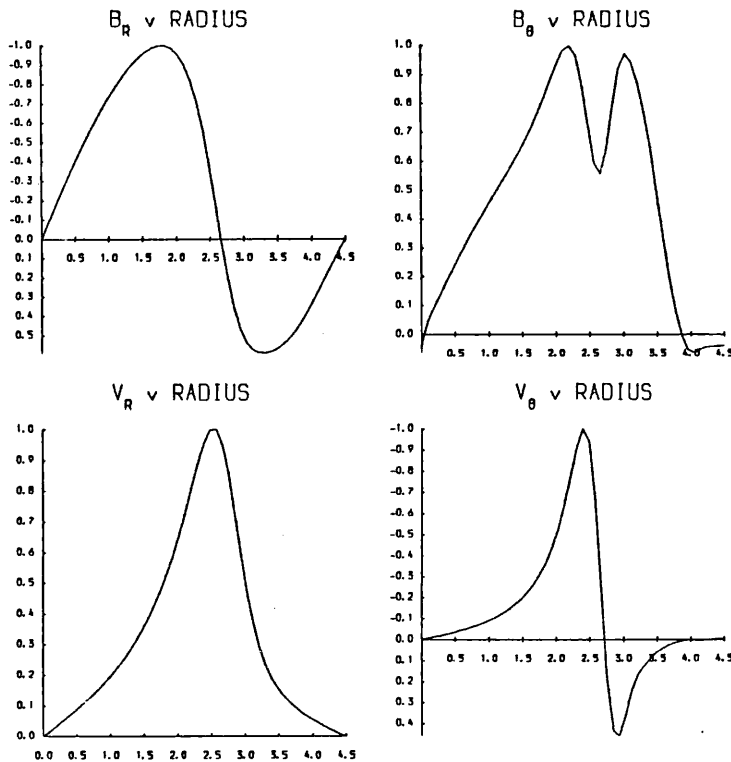


FIG.4.3.2 Linear eigenfunctions for  $C = 0.8$ . (All magnitudes in arbitrary units).

#### 4.4 DIAGNOSTICS FROM THE CODE

Running a large code one is in a similar situation to performing an experiment requiring diagnostics to tell what is happening and more importantly to hopefully explain why it is happening !

Apart from the obvious diagnostics of printing the values of the dependent variables, various other quantities are also output. Following Schnack the primary diagnostic of mode behaviour was taken to be the growth rate of reconnected flux at the singular surface [40]

$$\frac{1}{\psi_R} \left. \frac{\partial \psi_R}{\partial t} \right|_{r_s}$$

where

$$\psi_R(r) = \frac{\text{Max}(\psi(r,z)) - \text{Min}(\psi(r,z))}{k} \quad 0 \leq z \leq \frac{2\pi}{k}$$

Subsequently it was found that the spatial variation of mode growth rate meant that an average growth rate represented a more appropriate diagnostic. The average growth rate is defined as

$$\int_0^{\text{wall}} \frac{\partial \psi_1}{\partial t} dr / \int_0^{\text{wall}} \psi_1 dr$$

where  $\psi_1$  is the first harmonic of  $\psi$ .

In attempting to explain the code results quasi-linear processes similar to those detailed by Rutherford for the tearing mode [34], have been sought. Accordingly the Fourier harmonics of all dependent variables and additionally of the axial and azimuthal currents are calculated. Also since the g mode is pressure driven the pressure and its Fourier components are required. Since the pressure is not time advanced, due to our incompressible formulation, an additional elliptic partial differential equation must be solved to obtain it. Taking the divergence of the equation of motion (eqn 2.2.29) and remembering  $\nabla \cdot \underline{V} = 0$  we obtain

$$\nabla^2 P = \nabla \cdot (\underline{J} \times \underline{B}) - \nabla \cdot (\rho \underline{V} \cdot \nabla \underline{V}) \quad 4.4.1$$

if we now normalise P as  $\hat{P} = 2P/B_0^2$  (see section 3.2.3) then after some tedious algebra we rewrite eqn 4.4.1 in non-dimensional form as

$$\begin{aligned} \frac{1}{2} \nabla^2 (\hat{P} + |\hat{\underline{B}}|^2) &= \left| \frac{\partial \hat{\underline{B}}}{\partial \underline{r}} \right|^2 + \left| \frac{\partial \hat{\underline{B}}}{\partial \underline{z}} \right|^2 - \left| \frac{\partial \underline{V}}{\partial \underline{r}} \right|^2 - \left| \frac{\partial \underline{V}}{\partial \underline{z}} \right|^2 \\ &+ \frac{\hat{\underline{B}}_r^2 + \hat{\underline{B}}_\theta^2 - \hat{\underline{V}}_r^2 - \hat{\underline{V}}_\theta^2}{\hat{r}^2} + |\hat{\underline{\omega}}|^2 - |\hat{\underline{J}}|^2 \end{aligned} \quad 4.4.2$$

Since  $\hat{P} + |\hat{\underline{B}}|^2$  is periodic in the z direction eqn 4.4.2 is solved for  $\hat{P} + |\hat{\underline{B}}|^2$  by a Fourier harmonic method similar to that used in solving for  $\phi$  (see section 3.4.1) and  $\hat{P}$  is then obtained by subtracting  $|\hat{\underline{B}}|^2$ .



#### 4.5 NONLINEAR RESULTS AND DISCUSSION

As mentioned previously the nonlinear code is primed with linear eigenfunctions. A typical island structure and flow pattern resulting from the odd mode resistive eigenfunction is shown in fig 4.5.1. The correct priming level is determined by performing a series of runs at different priming levels to determine the point at which the behaviour becomes significantly nonlinear.

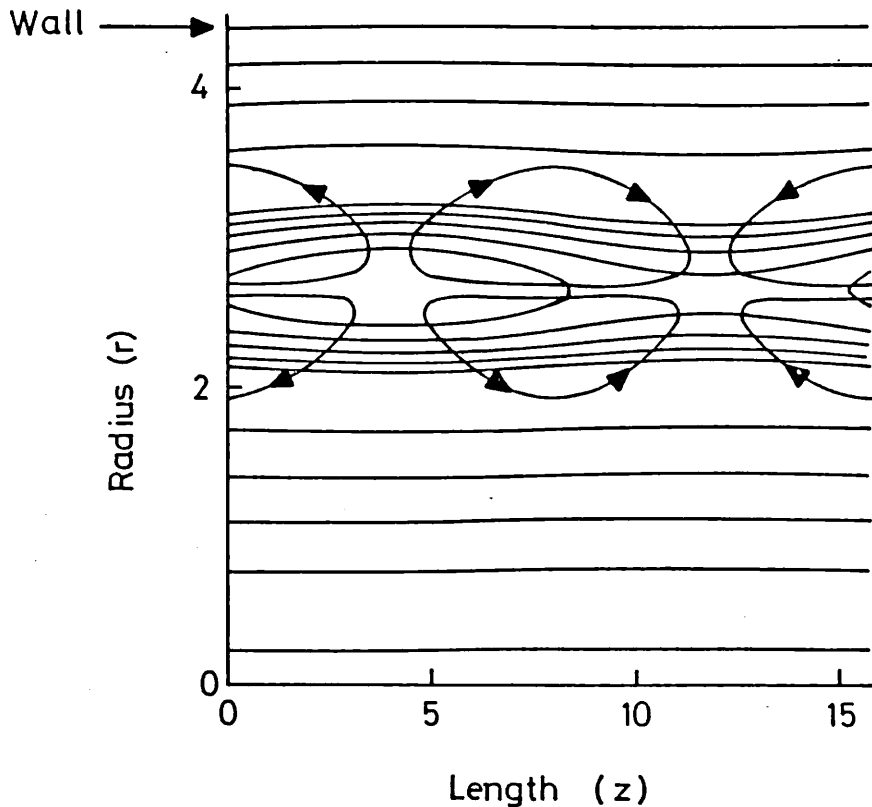


FIG.4.5.1 Typical island structure and velocity flow pattern with which nonlinear run is primed.

Fig 4.5.2. shows the nonlinear development of pressure profile at various times for a run with  $S=10^3$ ,  $C=0.05$ ,  $k=0.4$  and  $R_{wall}=4.5$ ,  $S$  being the magnetic Reynolds number. Two distinct effects are evident in this figure. Firstly the pressure at the singular surface flattens and

secondly the general pressure increases. The pressure flattening at the singular surface,  $r_s$  is an analogue of Rutherford tearing mode saturation [34]. For the tearing mode the driving mechanism is the parallel current gradient and it saturates by flattening the parallel current at its singular surface [34]. For the g mode the driving source is the pressure gradient and as the mode grows the pressure at its singular surface is flattened. The general increase in pressure is caused by ohmic heating which increases the temperature and hence the pressure. Alternatively this pressure rise may be explained by noting that resistive decay of the magnetic field lowers the gross magnetic energy and correspondingly increases the pressure energy, to conserve energy (both views are of course equivalent). This pressure rise mechanism is sometimes known as the overheating effect [53].

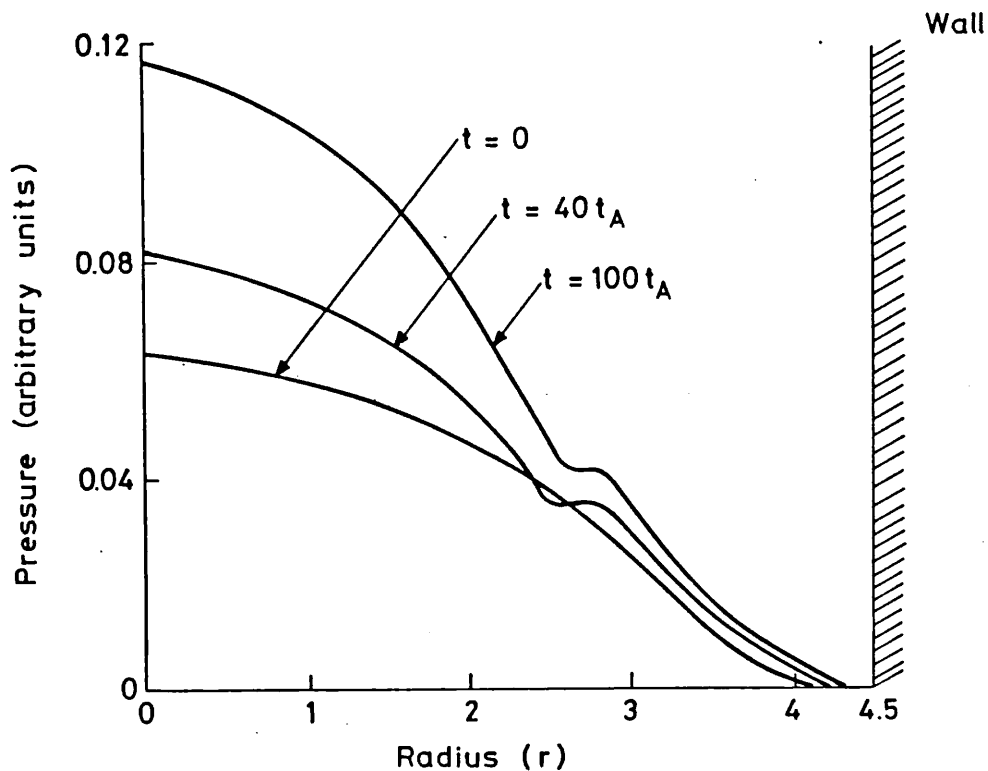


FIG. 4.5.2 Nonlinear development of pressure profile for  $S = 10^3$  case.

The effects of these mechanisms on the growth rate of the g mode

are shown in fig 4.5.3, where the growth rate at the singular surface is plotted against time for runs with  $C=0.05$ ,  $S=10^3$  &  $4 \times 10^3$ , and  $k=0.4$ . The decrease in growth exhibited is due to the pressure flattening. Whilst the subsequent increase in growth may be attributed to the gross pressure rising and thus enhancing the g mode growth rate. The effects of this pressure rise can be seen to be much less marked for the  $S=4 \times 10^3$  run. This is because the increase in central beta due to the ohmic heating scales as  $S^{-1}$ . Fig 4.5.4 shows the increase in central beta for these two cases,  $S=10^3$  and  $4 \times 10^3$ , and confirms the  $S^{-1}$  scaling.

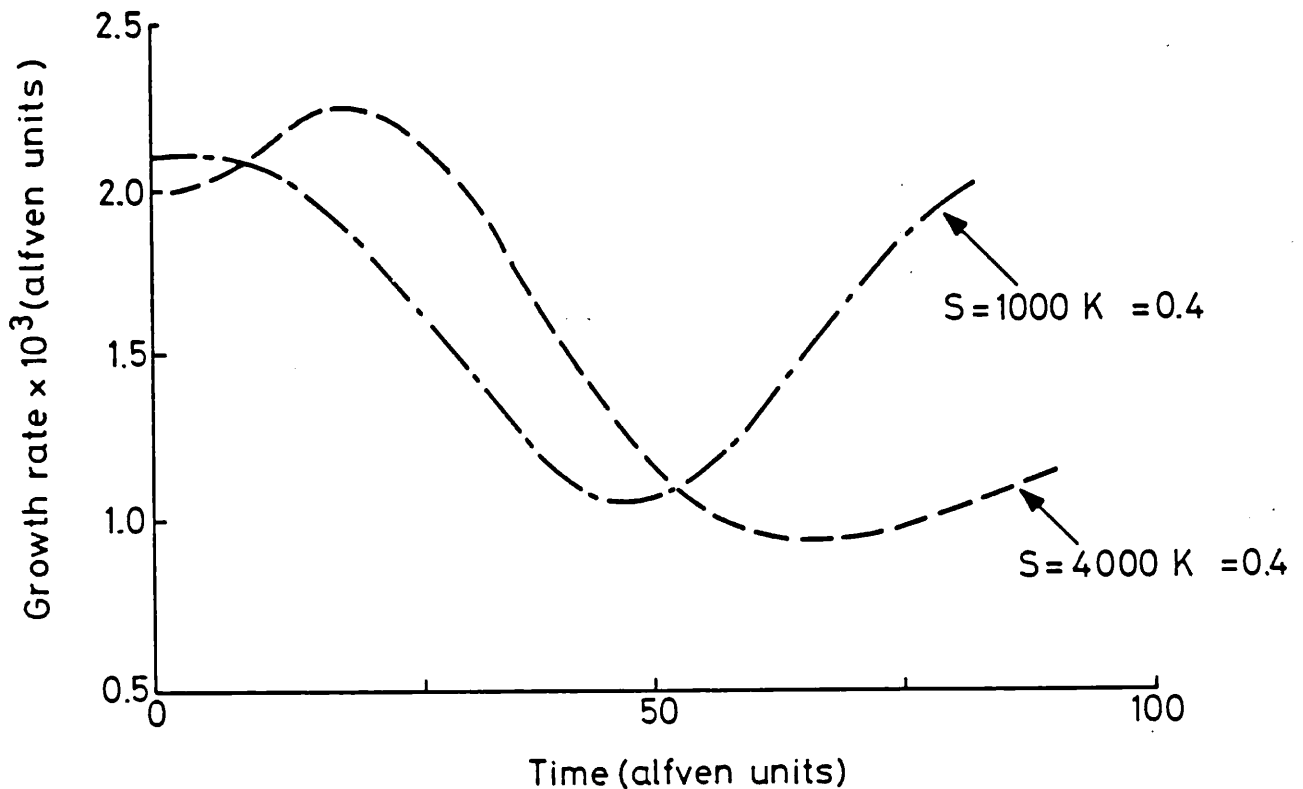


FIG.4.5.3 Nonlinear development of growth rate at the singular surface for  $S=10^3$  and  $4 \times 10^3$ .

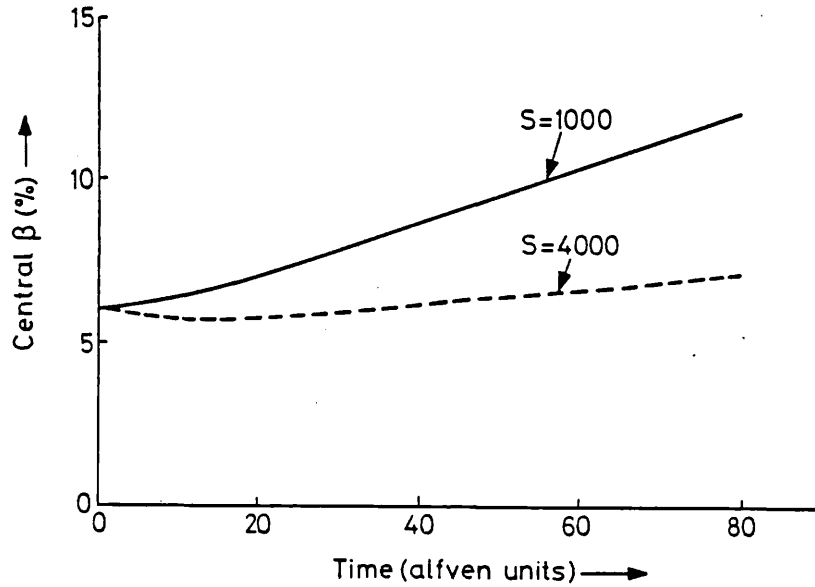


FIG.4.5.4 Increase in central beta for  $S=10^3$  and  $4 \times 10^3$  cases confirming the  $S^{-1}$  scaling.

Examination of the magnitudes of perturbations in the nonlinear runs shows that we are still in a quasi-equilibrium state. Thus

$$\nabla P_0 \cong \underline{J}_0 \times \underline{B}_0 \quad 4.5.1$$

where subscripts zero indicate zeroth harmonics. Near the  $m=0$  surface  $B_{z0}$  by definition must be small, hence the flattening of pressure in this region must be due to modifications to  $J_{z0}$  or  $B_{\theta 0}$ . Again examining the results we find  $J_{z0}$  to be almost totally dominant in the pressure flattening mechanism. Fig 4.5.5 shows  $(\nabla P_0|_{t=16})_r$ ,  $(\underline{J}_0|_{t=16} \times \underline{B}_0|_{t=16})_r$  and  $((0, J_{\theta}|_{t=0}, J_z|_{t=16}) \times \underline{B}_0|_{t=0})_r$  for the  $S=1000$ ,  $k=0.4$  run, examination of this diagram substantiates the statements of this paragraph. Fig 4.5.6 shows the nonlinear variation of  $J_{z0}$  for  $S=10^3$ ,  $k=1.0$ . The decrease in  $J_{z0}$  at  $r_s$ , which gives rise to the pressure flattening, is evident.

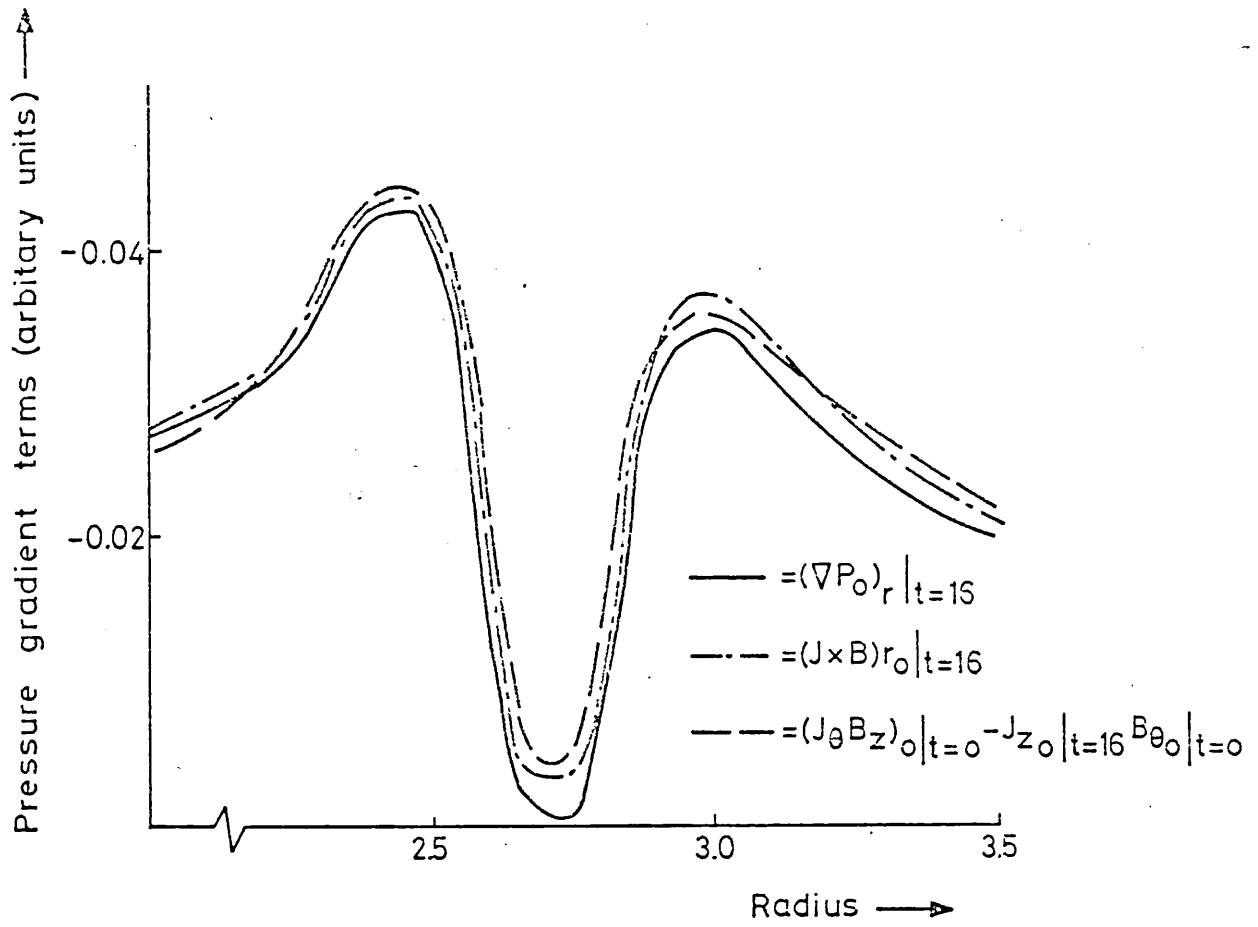


FIG.4.5.5 Comparison of various approximations to the pressure gradient.

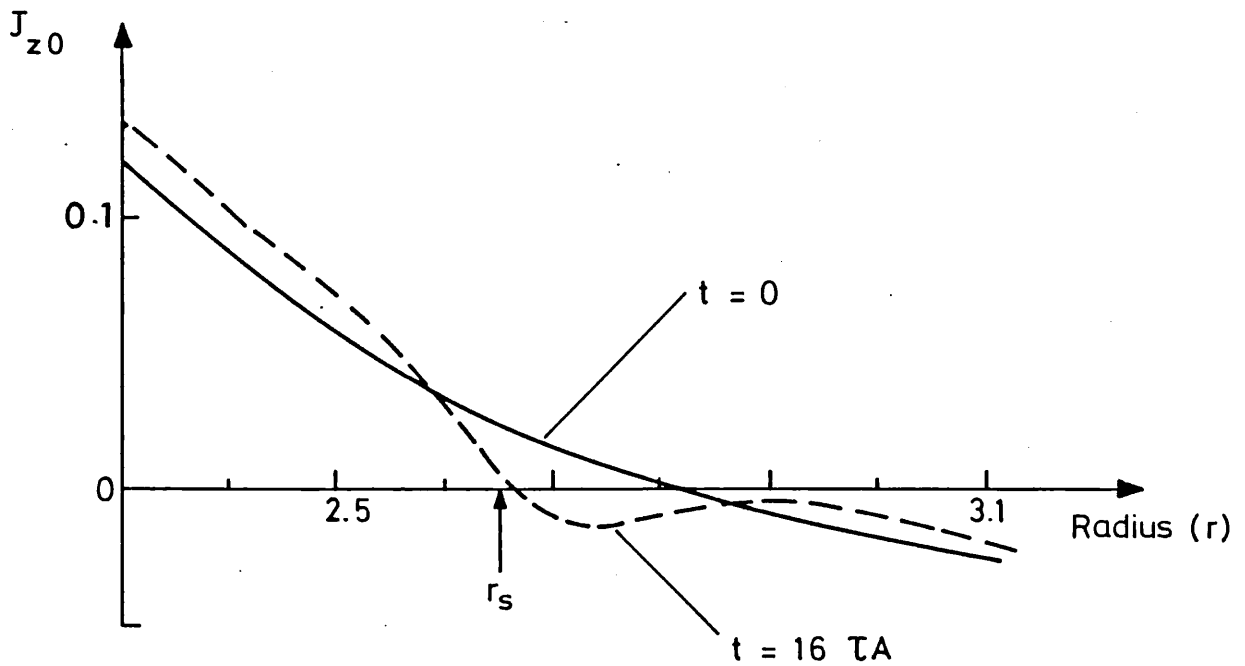


FIG.4.5.6 Nonlinear development of  $J_{z0}$  showing behaviour which accounts for pressure flattening at  $r_s$ .

Using the above knowledge we can obtain an order of magnitude estimate to the saturation width. We have at the singular surface,  $r_s$

$$\eta J_{z_0} = E_{z_0} - (V_{\theta} B_r)_0 \quad 4.5.2$$

since  $V_r|_{r_s} = 0$  (odd mode symmetry - section 2.4.2). It is primarily the  $(V_{\theta} B_r)_0$  term which causes the flattening in the pressure profile at  $r_s$ , since for the range of beta of interest the g mode layer width is less than the resistive skin depth and so  $E$  is able to partially relax resistively (this effect is discussed in more detail below). Hence for  $\frac{\partial P}{\partial r}|_{r_s} = 0$  we must have

$$\eta J_{z_0}|_{\text{orig}} \sim (V_{\theta} B_r)_0 \quad 4.5.3$$

where the subscript `orig` implies the initial equilibrium value. Linearising the  $\theta$ -component of the equation of motion, we have at  $r_s$  that

$$\rho \omega V_{\theta 1} = J_{z_0}|_{\text{orig}} B_{r_1} \quad 4.5.4$$

where  $\omega$  is the linear growth rate and the subscript 1 indicates a linear perturbation term. Eqns 4.5.3 and 4.5.4 then give

$$(V_{\theta} B_r)_0 = \frac{1}{2} V_{\theta 1} B_{r_1} = \frac{1}{2} J_{z_0}|_{\text{orig}} \frac{B_{r_1}^2}{\rho \omega} \sim \eta J_{z_0}|_{\text{orig}}$$

hence

$$\rho \eta \omega \sim \frac{B_{r_1}^2}{2} \quad 4.5.5$$

but from Furth, Killeen and Rosenbluth [23] the resistive layer thickness,  $\ell$ , is given by

$$\ell = \left( \frac{\rho \eta \omega}{k^2 B_{z_0}^2} \right)^{1/4} \quad 4.5.6$$

Using eqn 4.5.5 we find

$$\ell \sim \frac{1}{2}^{1/4} \left( \frac{B_{r1}}{kB'_z} \right)^{1/2} \sim \text{island width} \quad (\text{see eqn 2.4.3}) \quad 4.5.7$$

Hence appreciable pressure flattening at  $r_s$  will occur when the island width and resistive layer thickness are comparable. Fig 4.5.7 shows the level of  $B_{r1}$  such that  $\frac{\partial P}{\partial r} \Big|_{r_s, t=30\tau_A} = 0$  and the corresponding layer thickness plotted against magnetic Reynolds number,  $S$  for  $500 \leq S \leq 50,000$ . The gradients in this graph show the resistive layer thickness decreases as  $S^{-0.22}$  while the radial field perturbation decreases as  $S^{-0.38}$ , which is in good agreement with eqn 4.5.7.

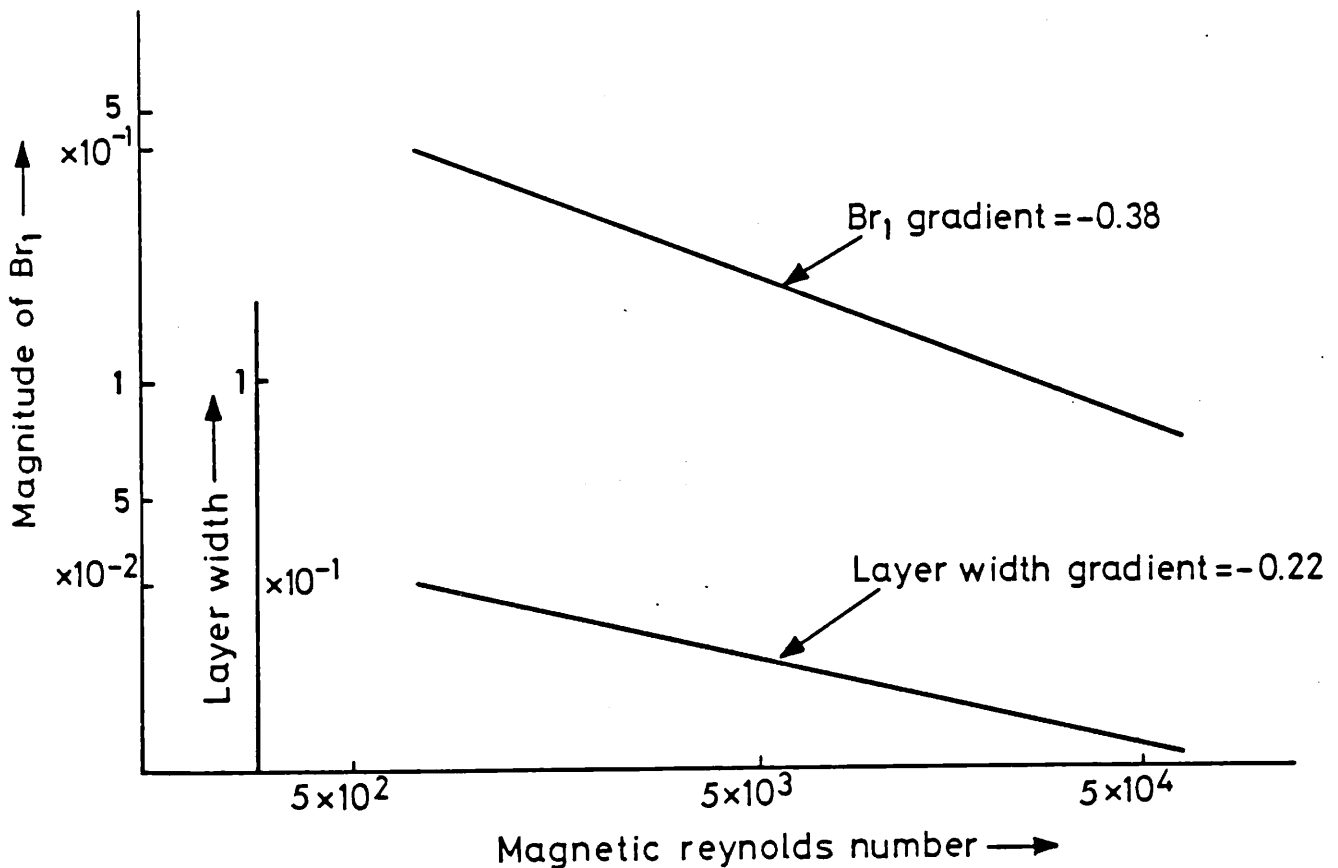


FIG.4.5.7 Comparison of layer width and associated perturbed radial field necessary to cause pressure flattening.

A scaling argument may also be given for the variation of the final nonlinear state with  $S$ . The final state depends on the competition between the pressure flattening and ohmic heating mechanisms and occurs when the rate of increase in driving energy available to the mode from ohmic heating exactly balances the rate of increase of energy in the mode. Let  $E_m$  be the energy in the mode,  $E_D$  be the driving energy and  $\gamma_s$  be the final nonlinear growth rate of  $B_r$ . Then if the resistive layer thickness scales as  $S^{-\alpha}$  we have

$$\frac{\partial E_m}{\partial t} = S^{-\alpha} \frac{\partial E_D}{\partial t} \quad 4.5.8$$

where the factor  $S^{-\alpha}$  on the right hand side occurs because the mode can only draw energy from its immediate vicinity [54]. Now it is shown above that, when pressure flattening is effective, the layer width and island width are comparable hence

$$B_r^{1/2} \propto S^{-\alpha} \quad 4.5.9$$

and so

$$E_m \propto S^{-4\alpha} \quad 4.5.10$$

Therefore in its final nonlinear state

$$\frac{\partial E_m}{\partial t} \propto 2\gamma_s S^{-4\alpha} \quad 4.5.11$$

As mentioned above the ohmic heating rate scales as  $S^{-1}$  and so

$$\frac{\partial E_D}{\partial t} \propto S^{-1} \quad 4.5.12$$

This relation, eqn 4.5.8 and eqn 4.5.11 then imply

$$\gamma_s \propto S^{3\alpha-1} \quad 4.5.13$$

Putting in the numerical value of  $\alpha=0.22$  gives

$$\gamma_s \propto S^{-0.34} \quad 4.5.14$$

However, the results from fig 4.5.7 show that the island width scales



as  $S^{-0.19}$ . Using this value for  $\alpha$  gives

$$\gamma_s \propto S^{-0.43} \quad 4.5.15$$

To investigate the validity of this argument two runs were conducted at much higher  $S$ . Since these runs were to be allowed to evolve far into their nonlinear states the computer time using INSTAB to solve the full set of equations would be prohibitive. Hence the much faster three Fourier harmonic code was used. Fig 4.5.8 shows the average growth rate versus time for runs with  $S=10^4$ ,  $5 \times 10^4$ ,  $k=0.4$  and  $C=0.05$ . It can be seen that the final nonlinear growth rate is essentially static. The scaling implied by these final nonlinear growth rates is  $S^{-0.44}$  which is in good agreement with eqn 4.5.15. Fig 4.5.9 shows the nonlinear development of the various components of the mode energy. It can be seen that the above argument which relies on the mode energy growing at the same rate as the radial field energy is correct.

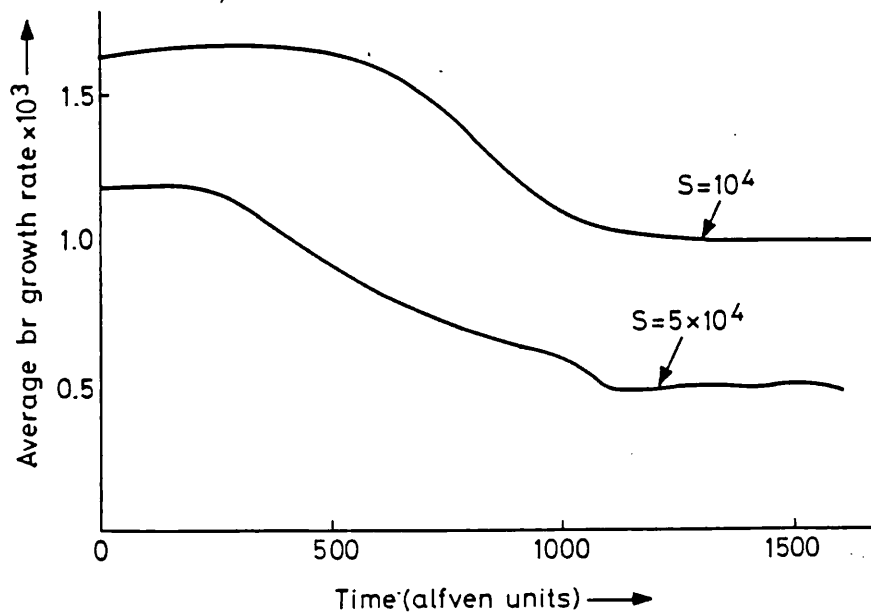


FIG.4.5.8 Average  $b_r$  growth rates against time for  $S=10^4$  and  $5 \times 10^4$  cases.

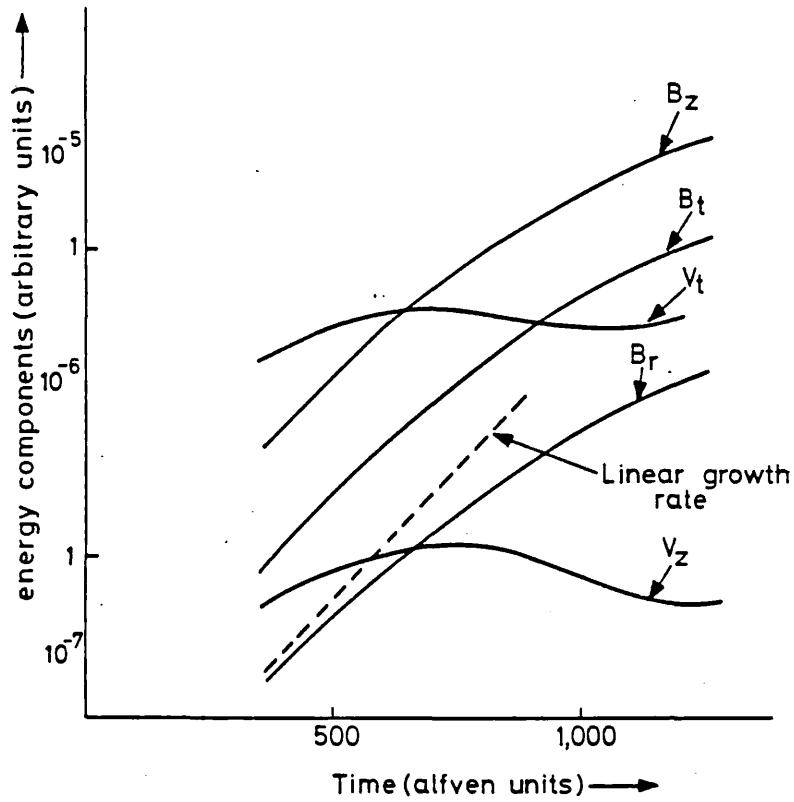


FIG. 4.5.9 First harmonic energy components for  $S=5 \times 10^4$  case ( $V_r$  negligible).

The argument given above, to show that the island width necessary to produce significant pressure flattening scales as the resistive layer width requires that the  $E_{z_0}$  is able to relax resistively. Numerically it is found that the layer width is such that the  $E_{z_0}$  is able to relax resistively but requires a finite penetration time. Fig 4.5.10 shows the various components of the axial Ohm's law for  $S=5 \times 10^4$  at  $655\tau_A$ . The  $E_{z_0}$  can be seen to be only partially able to relax resistively. The effect of this is that the island width must become larger than the layer width before the pressure flattening can occur. The factor between the layer and island width is however practically invariant with  $S$  and so the above island/layer width scaling argument remains valid.

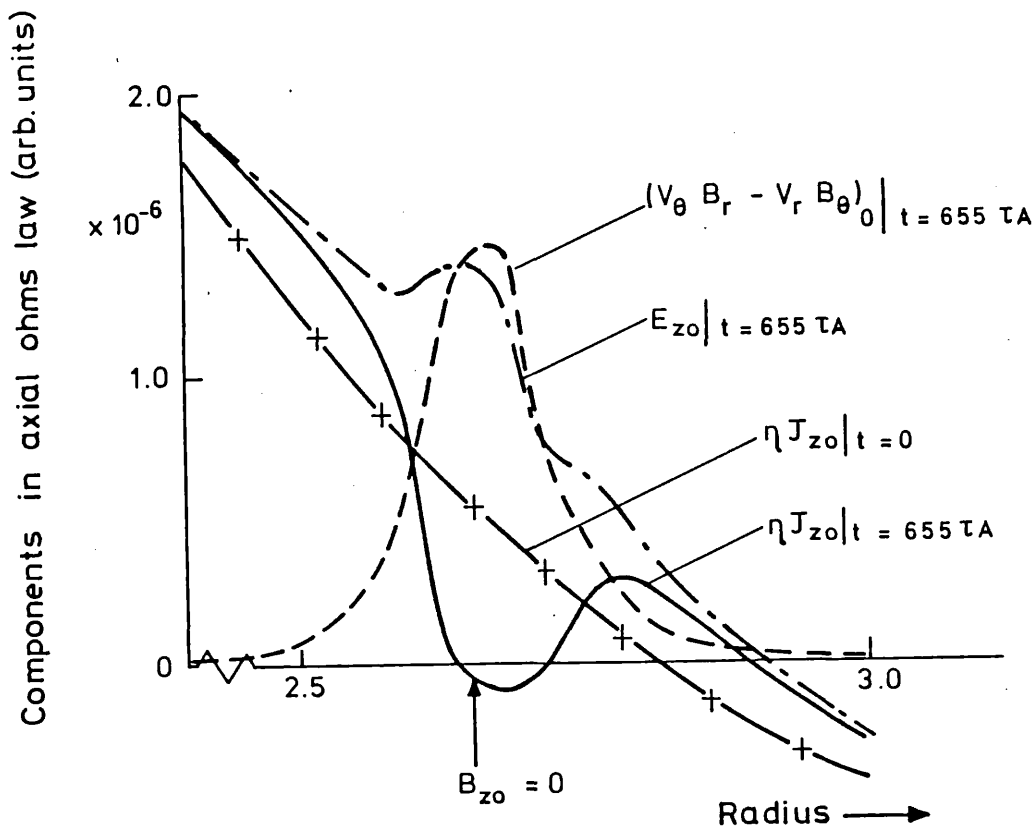


FIG.4.5.10 Nonlinear development of components of axial Ohm's law for  $S=5 \times 10^4$  case.

The variation of growth rate with wavenumber,  $k$  has also been investigated. Fig 4.5.11 shows the growth rate at the singular surface for runs with  $S=10^3$  and  $k=0.4$  and  $1.0$ . It can be seen that the pressure flattening mechanism is more quickly dominated by the overheating effect for the  $k=1.0$  case. A possible explanation of this arises from linear properties of the  $m=0$  g mode. Fig 4.5.12 shows the variation of the linear growth rate with the Suydam parameter,  $C$  for  $k=0.4$  and  $1.0$ . It can be seen that the growth rate of the  $k=1.0$  mode increases significantly faster with pressure than the  $k=0.4$  mode. Hence the mode will be more quickly affected by the overheating effect for the  $k=1.0$  case.

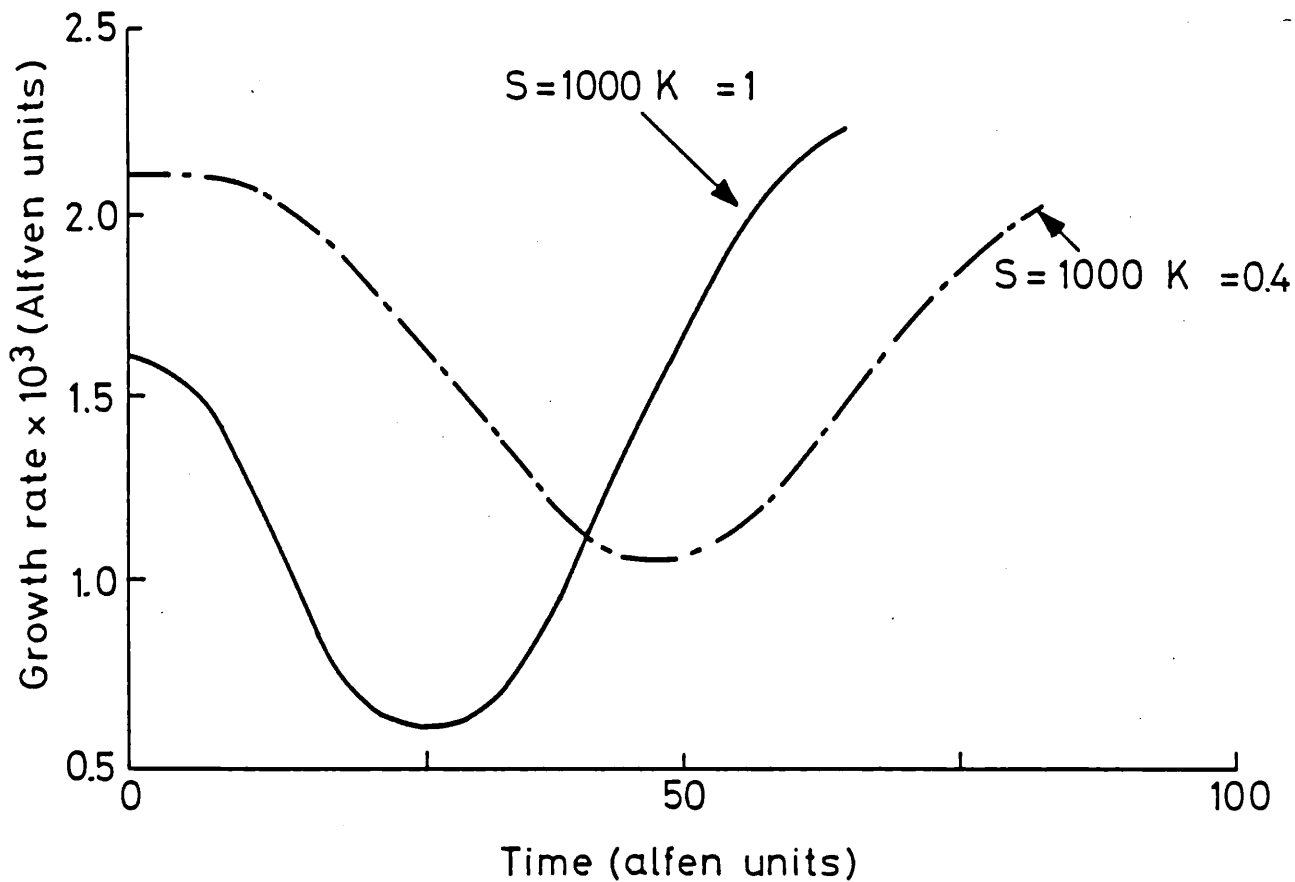


FIG. 4.5.11 Nonlinear development of growth rates at the singular surface for  $k=1.0$  and  $0.4$ .

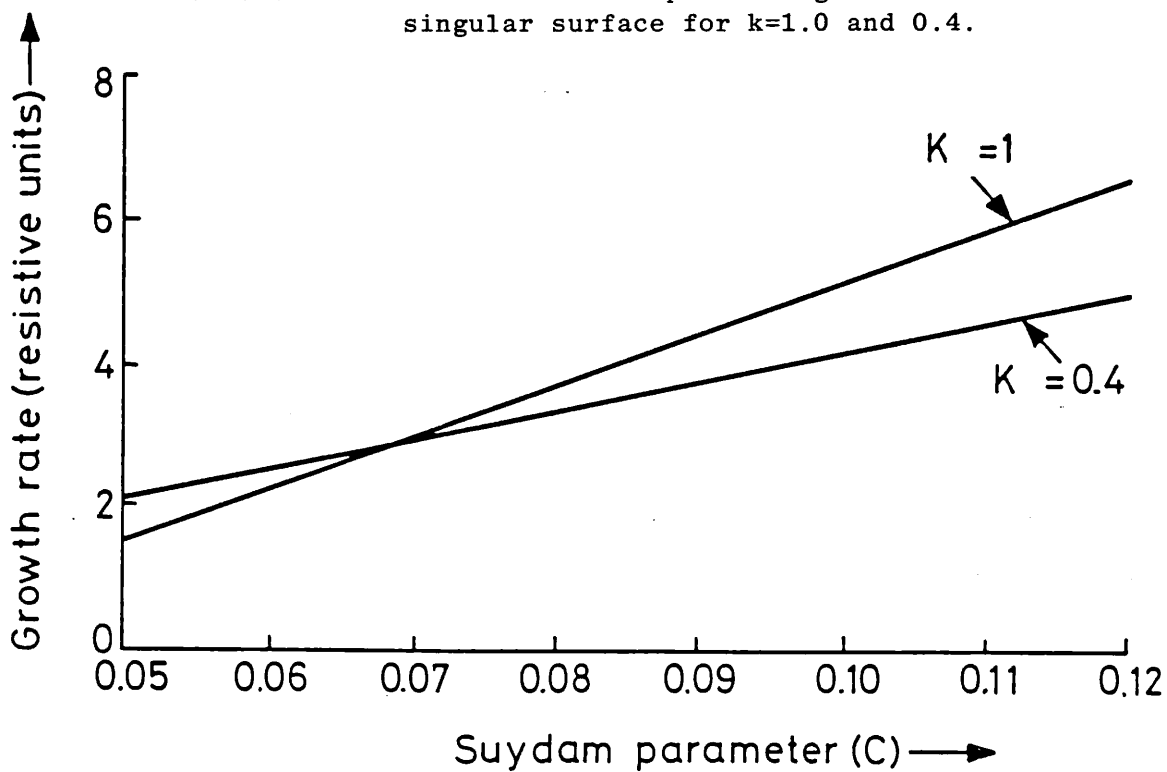


FIG. 4.5.12 Variation of linear growth rate with Suydam parameter for  $k=1.0$  and  $0.4$ .

A second possible explanation for the discrepancies between the  $k=0.4$  and  $1.0$  case may be found by examining the scaling of the resistive layer width with  $k$ . If we take the layer width to scale as  $k^{-\theta}$  and use the above notation for mode energy etc, then

$$\frac{\partial E_m}{\partial t} \propto k^{-\theta} \frac{\partial E_D}{\partial t} \quad 4.5.16$$

then since the island width and layer width in the nonlinear phase of the  $g$  mode have the same  $k$  scaling (eqn4.5.7) we have

$$E_M \propto k^{-4\theta+2} \quad 4.5.17$$

Hence

$$\gamma_s \propto k^{3\theta-2} \quad 4.5.18$$

The analytic values of  $\theta$  are  $\theta=0.33$  for the slow interchange mode and  $\theta=1.0$  for the fast interchange mode [24]. The numerical value  $\theta=0.8$  lies between these two. Using this value we find

$$\gamma_s \propto k^{0.4}$$

for any given  $S$ . Hence the final nonlinear growth rate increases with  $k$ . This may account for the differences between the two curves in fig 4.5.11.

Figs 4.5.13 and 4.5.14 show the time development of the island structure and velocity flow pattern, respectively for the  $S=1000$ ,  $k=0.4$  case. The basic structure of the island and flows can be seen to be unaltered in the nonlinear phase. Following the nonlinear development for times approaching a resistive transit time does reveal significant distortions to the flux surfaces [37]. However for such a large island a mixed helicity simulation is required to produce anything physically meaningful.

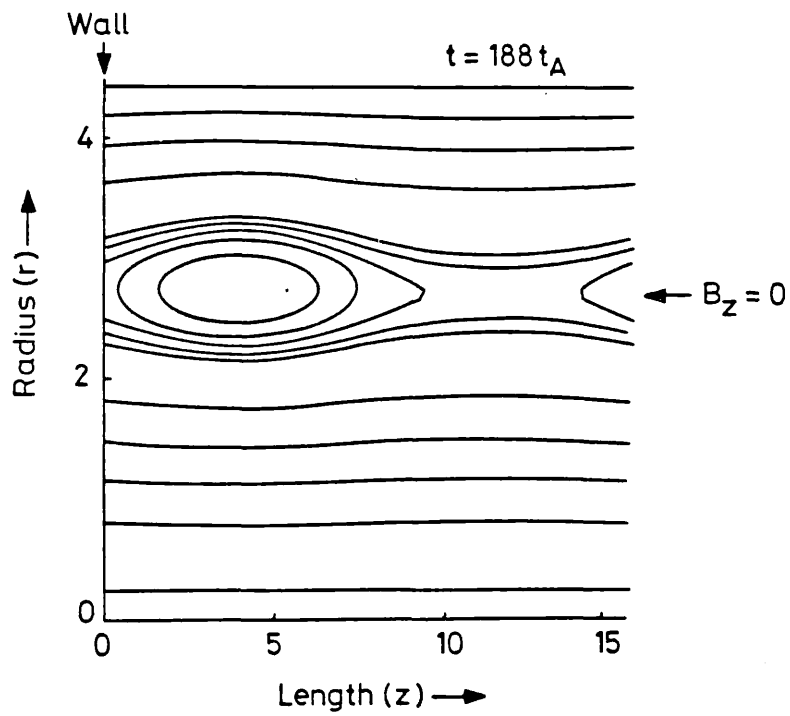
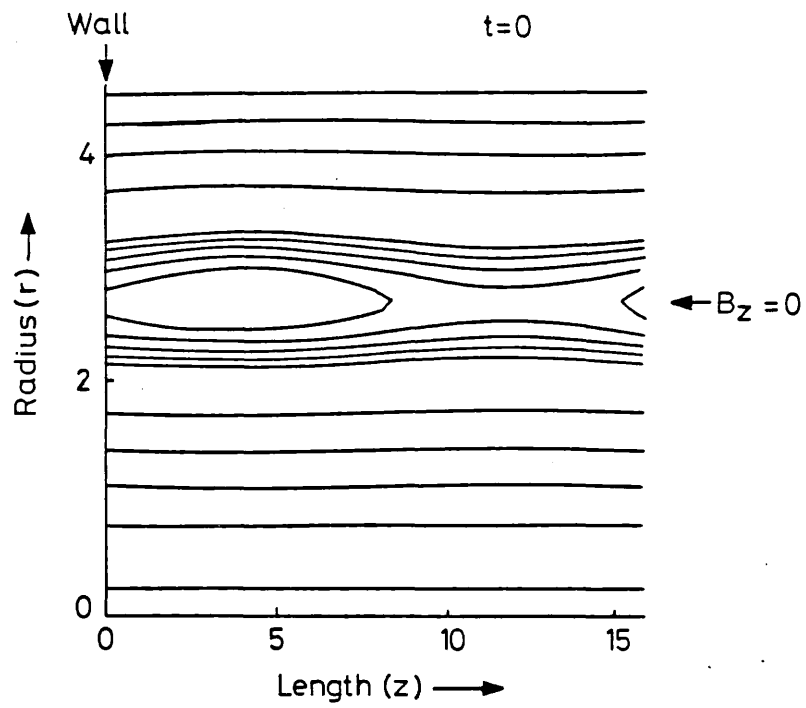


FIG. 4.5.13 Nonlinear development of flux surfaces in  $r, z$  plane.

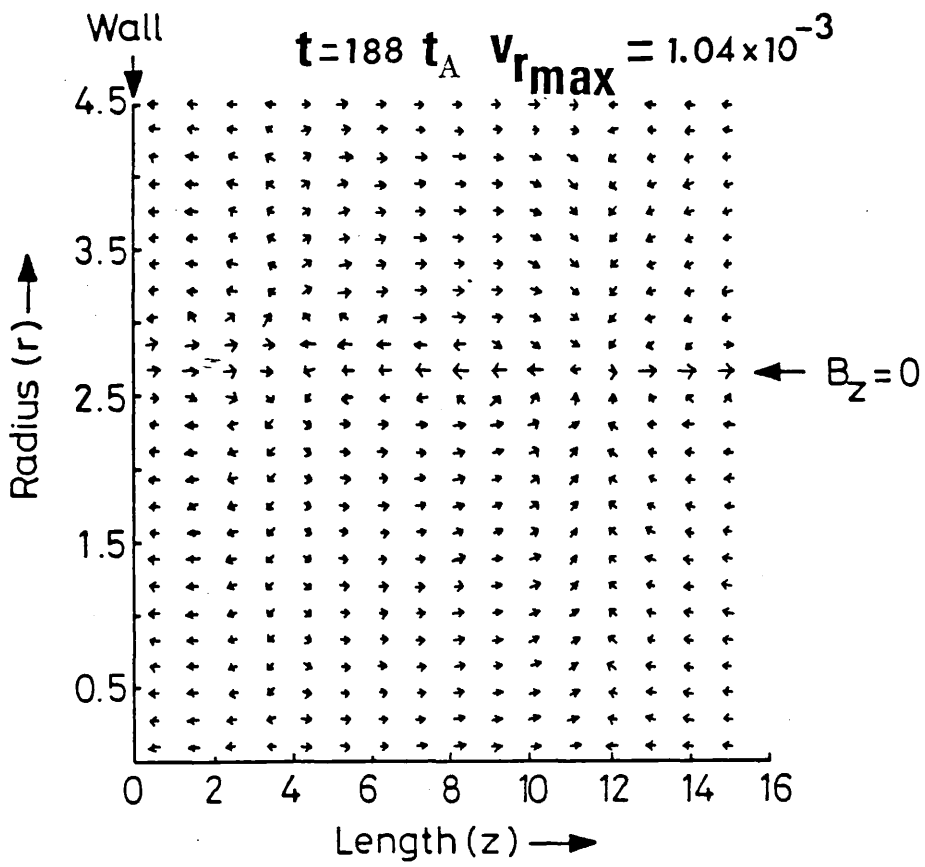
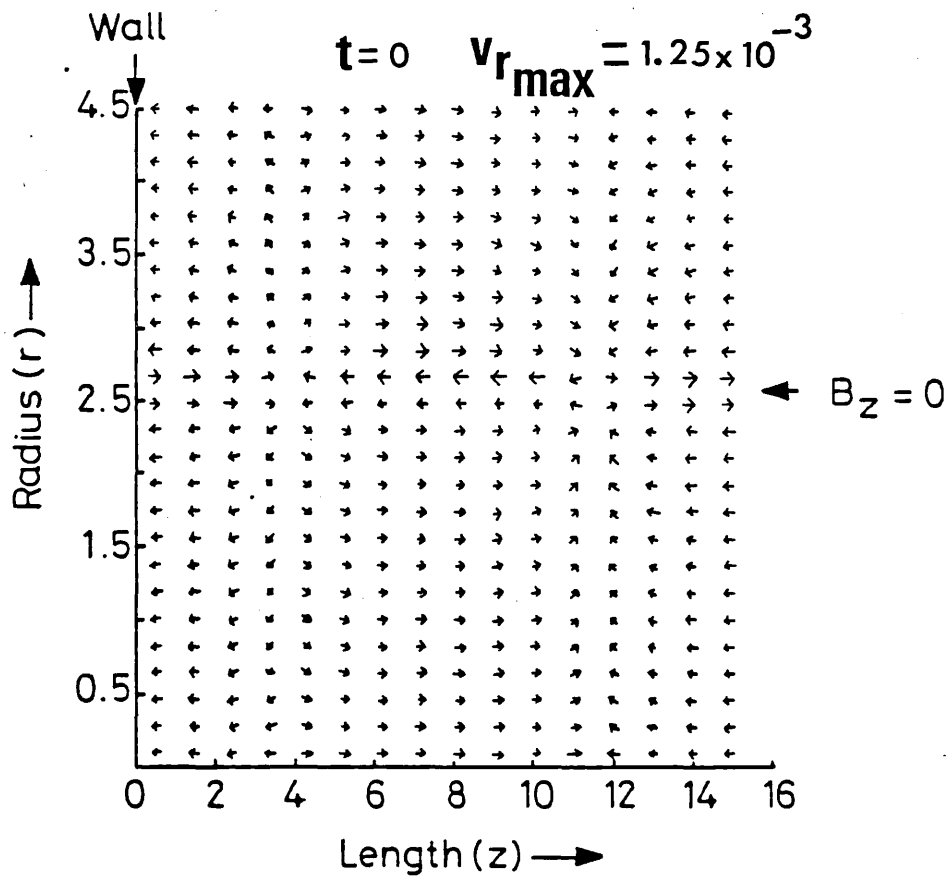


FIG. 4.5.14 Nonlinear development of velocity flows in  $r, z$  plane.

$J_{\theta 0}$  is shown in fig 4.5.15 to exhibit the flattening characteristic of Rutherford saturation [34] for the  $S=10^3$ ,  $k=0.4$  case. Here, however the behaviour is of little consequence as the g mode is driven by perpendicular current (pressure gradient) rather than by parallel current as is the case for the tearing mode.

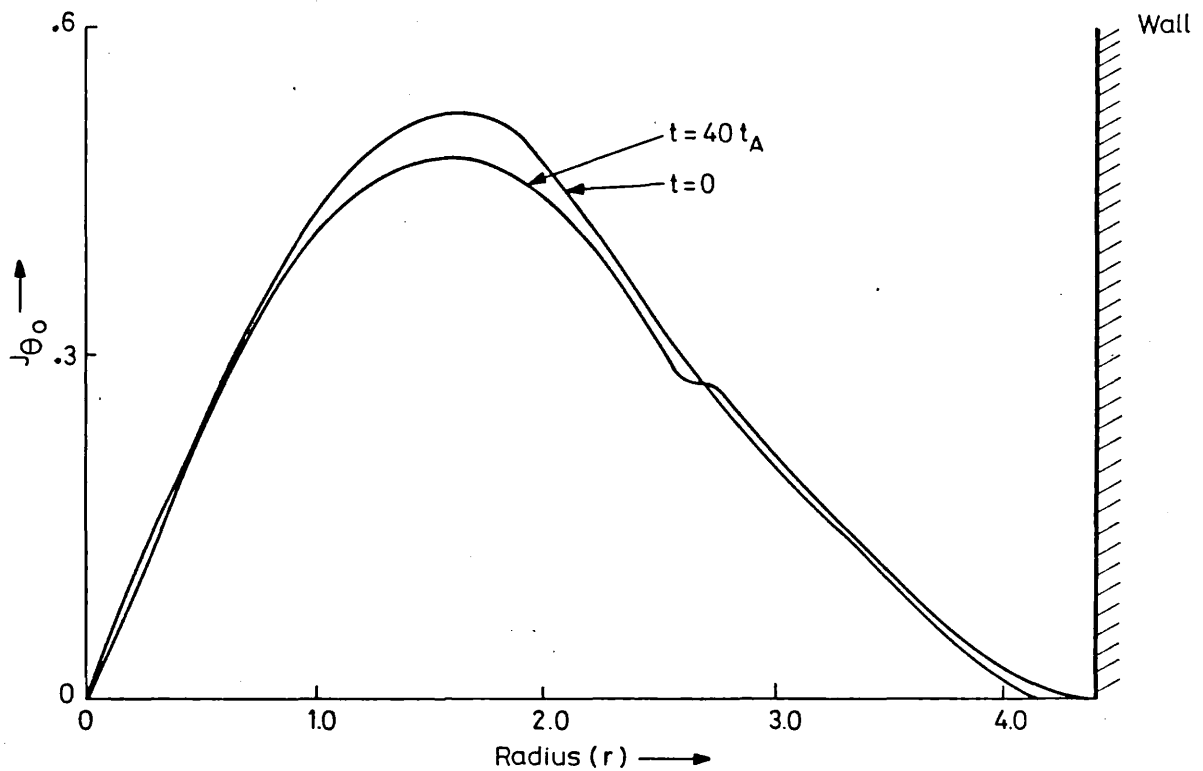


FIG. 4.5.15 Zeroth harmonic of  $J_{\theta}$  at  $t=0$  and  $40 \tau_A$

The linearised  $\theta$ -component of the equation of motion at  $r_s$  is

$$\rho_0 \frac{\partial v_{\theta 1}}{\partial t} = J_{z_0} B_{r_1} \quad 4.5.19$$

Now the pressure flattening corresponds to  $J_{z_0}|_{r_s} = 0$  and hence in the absence of any nonlinear term altering eqn 4.5.19  $v_{\theta}|_{r_s}$  should stop growing as  $J_{z_0}|_{r_s}$  approaches zero. Fig 4.5.16 shows  $(\underline{J}_0 \times \underline{B}_0)|_{r_s}$  as a function of time for the  $S=5 \times 10^4$  case. Fig 4.5.17 shows the first



harmonic of  $V_{\theta}|_{r_s}$  as a function of time for the same case. It can be seen that  $V_{\theta}|_{r_s}$  does indeed stop growing and actually decays. The decay rate of  $V_{\theta}|_{r_s}$  is almost exactly the same as the growth rate of  $\psi$ . Hence  $(V_{\theta}\psi)|_{r_s}$  tends to an approximately time static value as shown in fig 4.5.18. Since it is the  $V_{\theta}B_r (= -k\psi_1 V_{\theta}/r)$  which perturbs the axial Ohm's law and causes the pressure flattening this accounts for the approximately time static final value of  $(\underline{J} \times \underline{B})_r|_{r_s}$ .

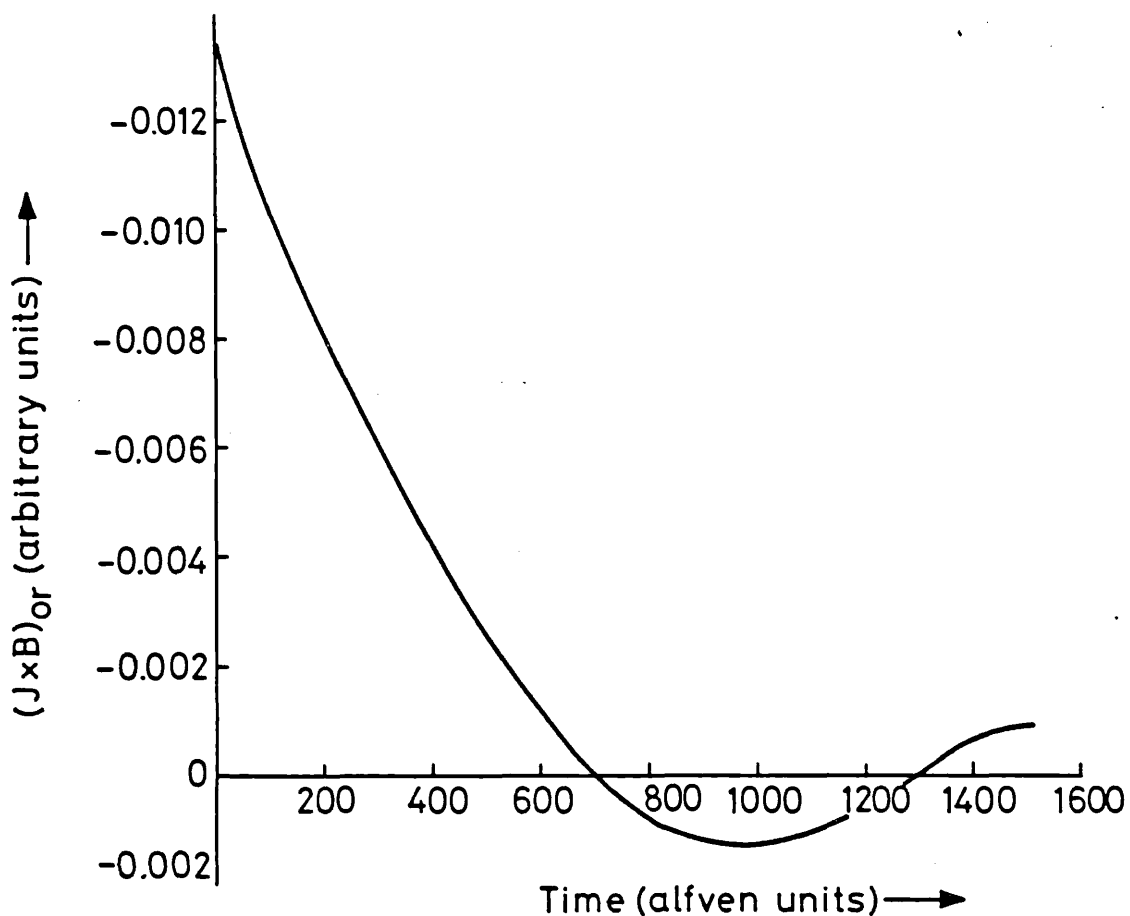


FIG. 4.5.16 Nonlinear behaviour of  $(\underline{J} \times \underline{B})_r|_{r_s}$  for  $S = 5 \times 10^4$  case.

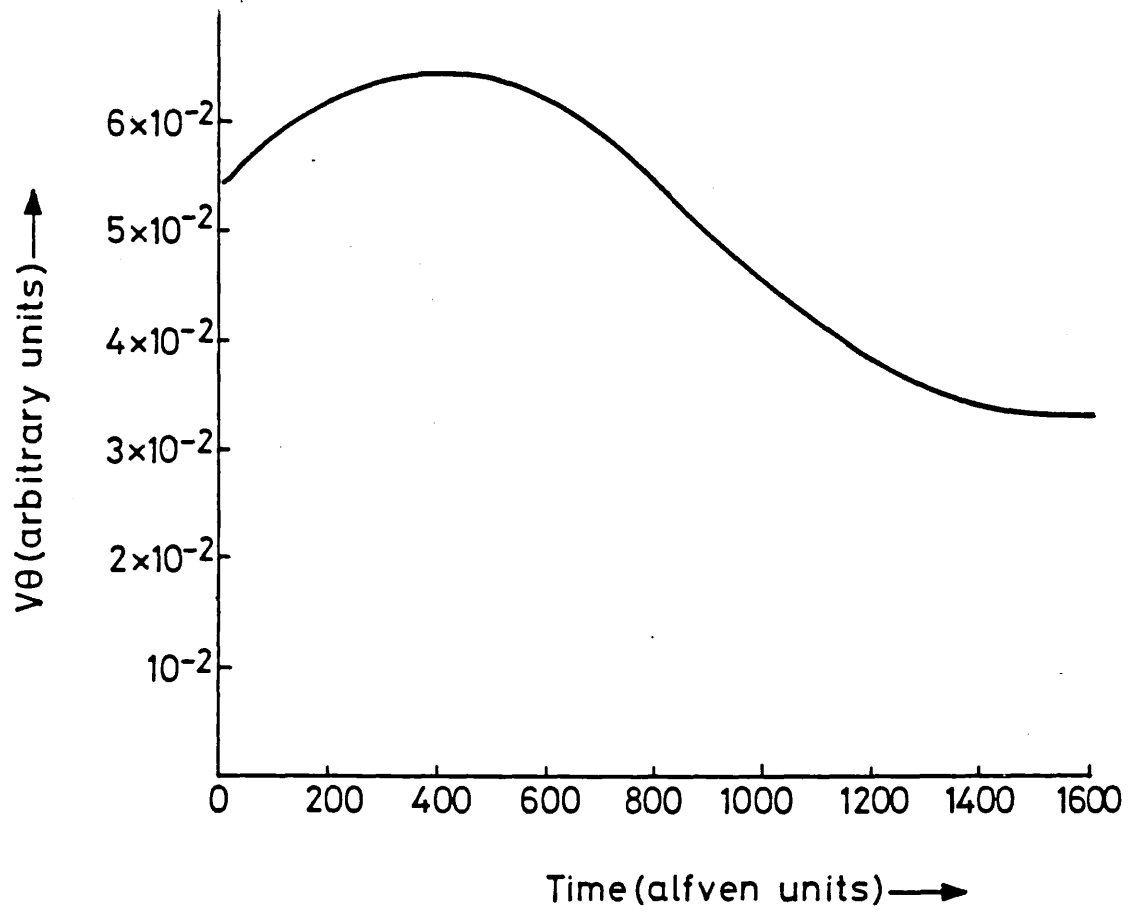


FIG. 4.5.17 First harmonic of  $V_\theta$  v Time for  $S = 5 \times 10^4$  case.

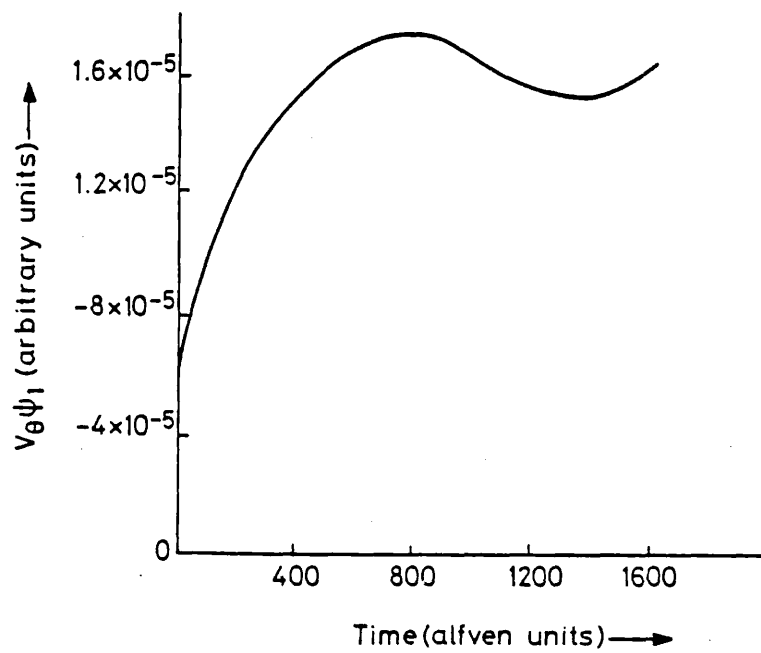


FIG.4.5.18 Nonlinear behaviour of  $V_\theta \psi_1$  for  $S = 5 \times 10^4$  case.

One effect of the presence of the nonlinear  $m=0$  mode is to enhance the pressure gradient to either side of its singular surface. Fig 4.5.19 shows this effect for the  $S=10^3$ ,  $k=1.0$  case. This increase in pressure gradient will enhance the growth of the  $m=1$  modes, which lie to either side of the  $m=0$  mode. Fig 4.5.20 shows the effects on the growth rate, of the  $m=1$  modes, obtained by using a linear code on the evolved  $16 \tau_A$  pressure profile. It can be seen that the growth rates are very much enhanced in the core. This effect may be very important because the  $m=1$ ,  $m=0$  mode interaction leads to ergodic field line behaviour (see chapter 6).

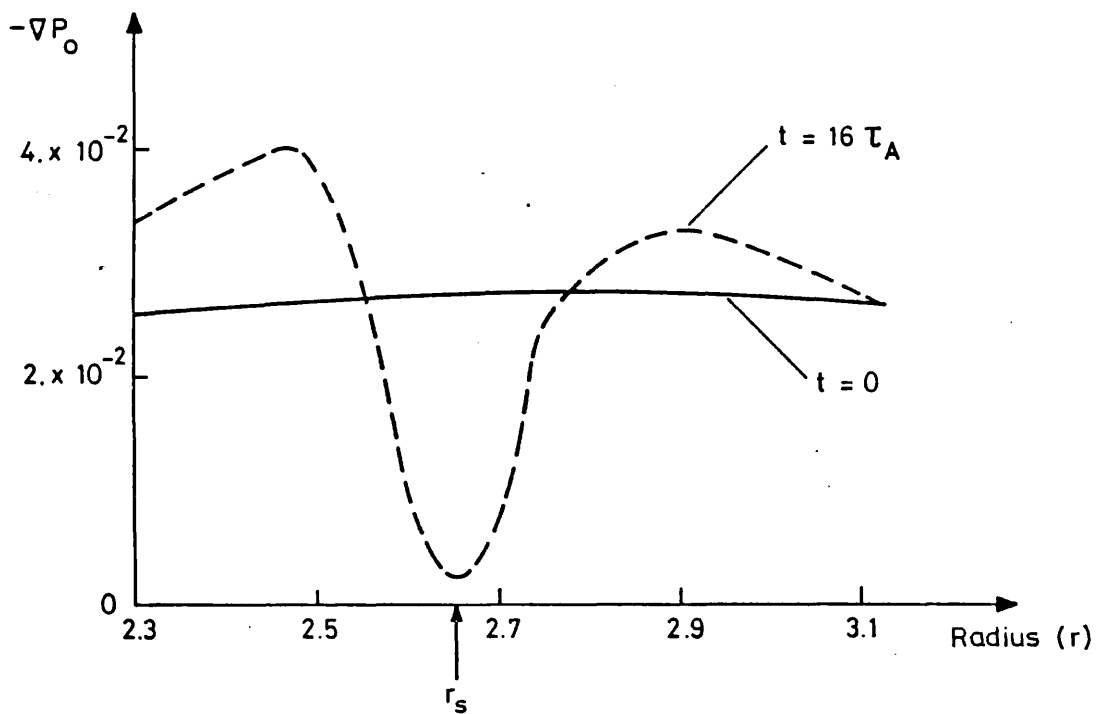


FIG. 4.5.19 Nonlinear development of pressure gradient.

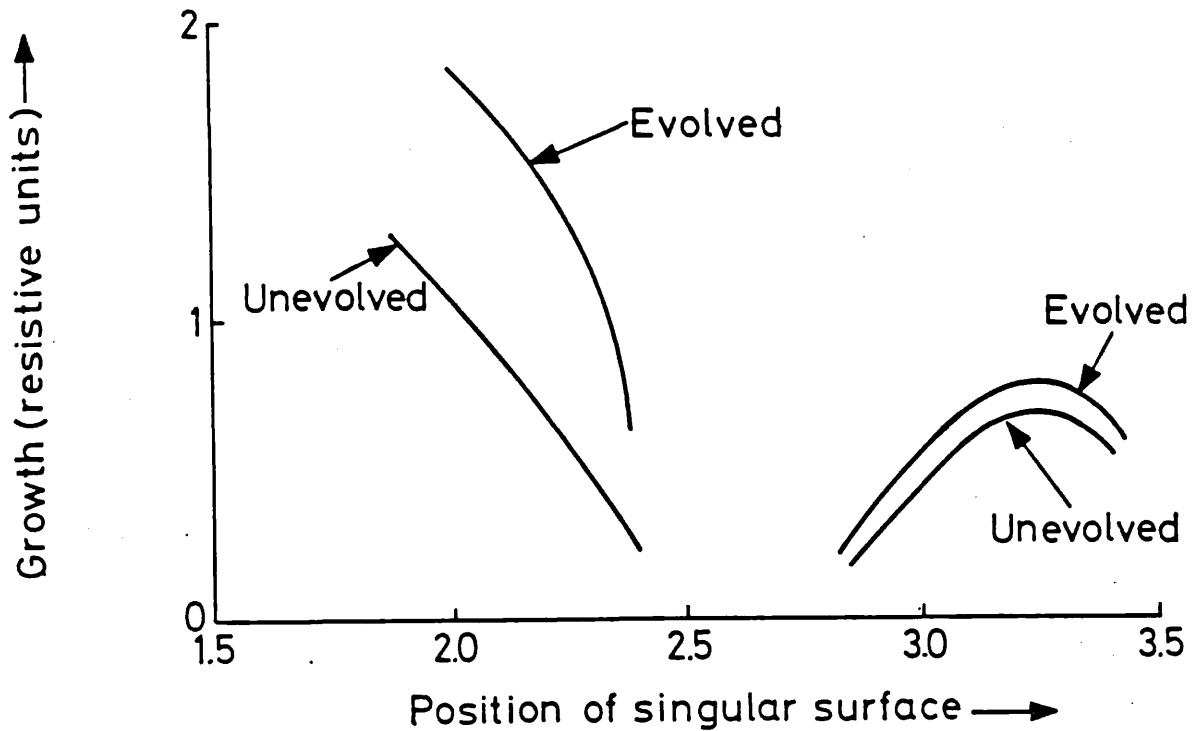


FIG.4.5.20 Effects of  $m=0$  mode on linear  $m=1$  growth rates.

One of the main problems with choosing an incompressible formulation has been the loss of independent control over plasma energy content. While real plasmas have energy loss mechanisms, such as radiation and thermal conduction, the incompressible formulation contains no provision to include these terms. However, by including a non-physical term in the resistive diffusion equation the ohmic heating can be prevented and the loss mechanisms thus approximated. The procedure used is to exactly negate the resistive diffusion of the equilibrium. The modified resistive diffusion equation is

$$\frac{\partial \underline{B}}{\partial t} = \nabla \times (\underline{V} \times \underline{B}) + \eta \nabla^2 \underline{B} - \eta \nabla^2 \underline{B}_0 \Big|_{t=0}$$

This method is only an approximation because in reality the fields

continue to diffuse resistively but the ohmic heating is dissipated. Whereas here the fields do not diffuse resistively and so the ohmic heating never occurs. Using this method the saturation was found to be complete for the  $S=10^3$ ,  $k=0.4$  case, the average growth rate as a function of time is plotted in fig 4.5.21.

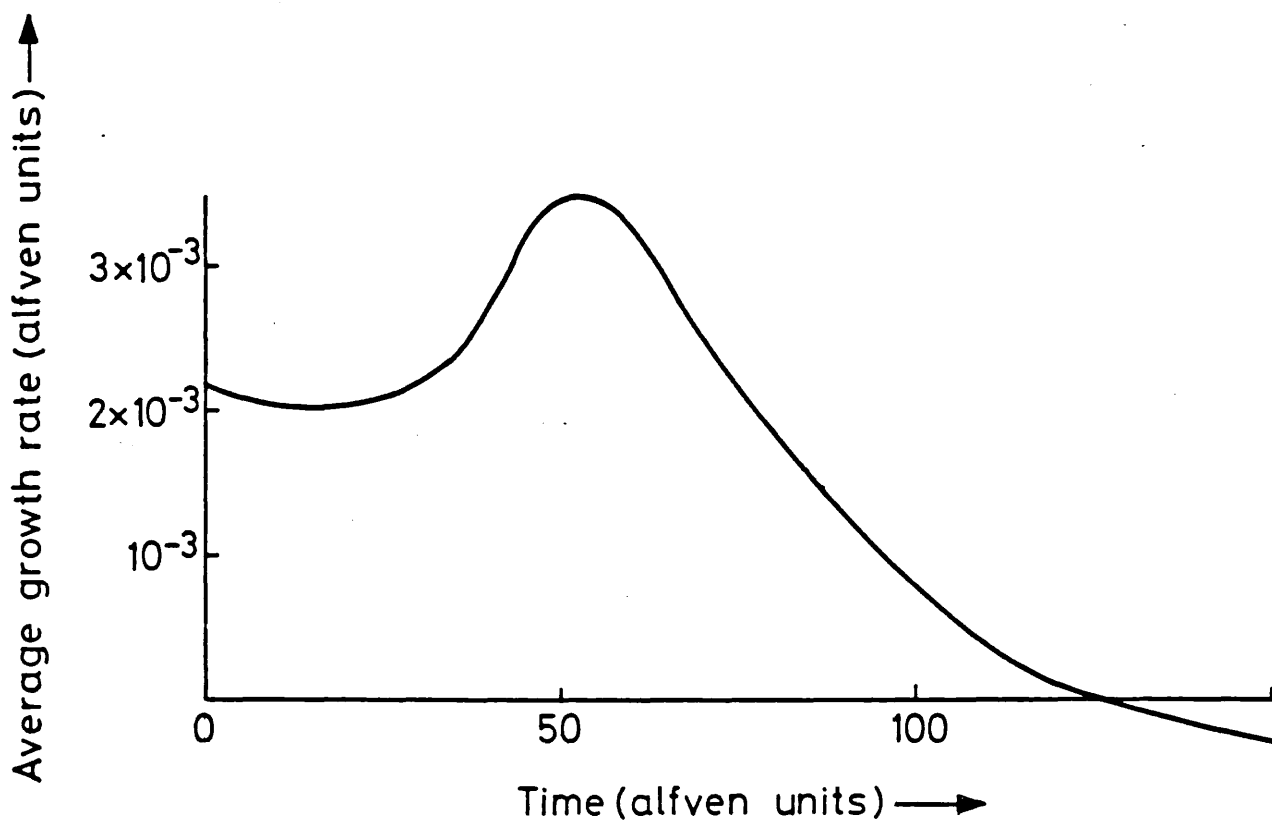


FIG.4.5.21 Average growth rate v Time for case with suppressed ohmic heating.

#### 4.6 CONCLUSIONS

The processes at work in the nonlinear development of the  $m=0$  g mode have been explained. A quasi-linear mechanism has been shown to exist in which the perturbations interact to flatten the equilibrium pressure at  $r_s$  by modifying  $J_z$ . Since the g mode is driven by pressure gradient this flattening of pressure represents a potential saturation mechanism.

This potential saturation mechanism is unfortunately counteracted by increasing pressure resulting from the resistive decay of the equilibrium. The final nonlinear state has been shown to depend on the competition between these two mechanisms, with the final nonlinear growth rate scaling as  $S^{-0.43}$ .

The inclusion of a non-physical term to simulate energy loss processes has shown that the g mode may saturate completely.

Finally it has been shown that the nonlinear  $m=0$  mode linearly destabilises the  $m=1$  modes by increasing the pressure gradient in their vicinity. This effect may be important because of the ergodic field line behaviour which results from the interaction of  $m=0$  and  $m=1$  modes (see chapter 6).

5.1 INTRODUCTION

It was desired to extend the study of the last chapter to include features which could not be added to the existing formalism. The new features were :-

(i) The ability to study modes other than  $m=0$ , particularly the  $m=1$  modes in the core.

(ii) The inclusion of an energy equation into the formalism, to allow independent control over the plasma energy content. This requirement means a compressible formalism must be adopted.

(iii) The possibility of extending the study to mixed helicity interactions between the  $m=0$  and  $m=1$  modes.

Recently the Oak Ridge Group have used a spectral Fourier harmonic method to study the 3D tearing mode [ 8 ]. They have shown the Fourier method to be faster and more accurate than the comparable finite difference method. An extension of this method to the 3D compressible MHD equations would be ideally suited to the above requirements. Such an extension is described in this chapter.

In section 5.2 the particular form chosen for the MHD equations is

discussed. The derivation of the Fourier component equations is explained in section 5.3 and the associated boundary conditions are given in section 5.4. The numerical algorithm used for the solution of the Fourier component equations is explained in section 5.5 and finally in section 5.6 some of the tests applied to the code are given.

## 5.2 THE MHD FORMULATION

The MHD equations may be written :-

$$\frac{\partial \underline{B}}{\partial t} = \nabla \times (\underline{V} \times \underline{B} - \frac{\eta}{s} \nabla \times \underline{B}) \quad 5.2.1$$

$$\frac{\partial \rho \underline{V}}{\partial t} = - \nabla \cdot (\rho \underline{V} \underline{V} - \underline{B} \underline{B} + \frac{1}{2} (P + B^2) \underline{I}) + \hat{\nu}_{||} \nabla_{||}^2 \underline{V} \quad 5.2.2$$

$$\frac{\partial \rho}{\partial t} = - \nabla \cdot (\rho \underline{V}) \quad 5.2.3$$

$$\frac{\partial P}{\partial t} = - \nabla \cdot (P \underline{V}) - (\gamma - 1) P \nabla \cdot \underline{V} + 2(\gamma - 1) \frac{\eta}{s} |\underline{J}|^2 \quad 5.2.4$$

where  $\underline{I}$  denotes the unit dyadic and the normalisations

$$\underline{r}/r_0 \rightarrow \underline{r} \quad t/\tau_H \rightarrow t \quad \underline{B}/B_0 \rightarrow \underline{B}$$

$$\underline{V}\tau_H/r_0 \rightarrow \underline{V} \quad \rho/\rho_0 \rightarrow \rho \quad P/P_0 \rightarrow P$$

$$\eta/\eta_0 \rightarrow \eta \quad \hat{\nu}_{||} = \nu_{||}\tau_H/r_0^2 \rho_0 \text{ and } P_0 = \frac{B_0^2}{2}$$

have been used, the zero subscripted variables being the characteristic value of that variable. The  $\nabla_{||}^2 \underline{V}$  term of eqn 5.2.2 is the parallel



viscosity. Where  $\nabla_{\parallel}^2 \underline{v}$  is defined as [30]

$$\nabla_{\parallel}^2 \underline{v} = \nabla \cdot \underline{T}_{\parallel}$$

and

$$\underline{T}_{\parallel} = -3((\underline{b} \cdot \nabla) \underline{v} \cdot \underline{b} - \underline{v} \cdot (\underline{b} \cdot \nabla) \underline{b}) - \frac{1}{3} \nabla \cdot \underline{v} (\underline{b} \underline{b} - \frac{1}{3} \underline{I})$$

$\underline{b}$  being the local direction of the magnetic field. Braginiskii gives the parallel viscosity coefficient as  $\nu_{\parallel} = .96 \Pi / \nu_{ii}$ , where  $\Pi$  is the ion pressure and  $\nu_{ii}$  is the ion-ion collision frequency [12]. The parallel viscosity is included because it contributes beneficially to numerical stability. Its effects on the physics are negligible for the  $m=0$  mode, however for the  $m=1$  mode it can represent a linear stabilising term [31]. For these reasons the parallel viscosity is only included linearly.

The pressure equation (eqn 5.2.4) is chosen in preference to a full energy equation since the pressure energy of a typical system is much less than the magnetic energy and so rounding errors significantly affect the pressure which may be deduced from the total energy. The pressure equation also directly couples to the  $\nabla p$  term of the equation of motion (eqn 5.2.2), a property which is important for the implicit numerical method used.

### 5.3 THE FOURIER COMPONENT EQUATIONS

In a periodic cylindrical co-ordinate system the variables may be Fourier decomposed in the  $\theta, z$  direction.

eg.

$$B_r(r, \theta, z, t) = \sum_{\substack{-\infty < m < \infty \\ 0 \leq n < \infty}} (B_{r s_{m,n}}(r, t) \sin(m\theta + nkz) + B_{r c_{m,n}}(r, t) \cos(m\theta + nkz)) \quad 5.3.1$$

The summation is for n positive only since the trigonometric identities  $\sin(m\theta - nkz) = -\sin(-m\theta + nkz)$  etc.

serve to render n negative redundant.

To use the Fourier decomposition in a numerical algorithm, the Fourier series must be truncated at some point. For a single helicity simulation in which the first harmonic is dominant, the choice of which modes to include is simple - the higher harmonics decrease in importance and so to the first harmonic and equilibrium, successively higher harmonics are added until convergence occurs. In practice convergence is very rapid with three harmonics giving quantitatively correct answers. For mixed helicity simulations an ordering can generally be found which allows the importance of each mode to be established. eg. If there are two dominant modes m,n and p,q, and m,n is of order  $\epsilon$  and p,q is of order  $\epsilon^2$ , the following ordering tree is obtained :-

$$\begin{aligned} O(1) &:- (0,0) \\ O(\epsilon) &:- (m,n) \\ O(\epsilon^2) &:- (2m,2n), (p,q) \\ O(\epsilon^3) &:- (3m,3n), (p+m, q+n) \end{aligned}$$

etc.

The convergence process can then be performed by including successively higher order modes until convergence occurs.

The convolutions inherent in the nonlinear terms of eqns 5.2.1 - 5.2.4 give rise to coupling between the various Fourier harmonics.

eg.

if  $m_0 = m_1 + m_2$  and  $n_0 = n_1 + n_2$

$$\begin{aligned} &\text{then } b_{r_{s_{m_1, n_1}}} \text{Sin}(m_1 \theta + n_1 k z) V_{\theta_{C_{m_2, n_2}}} \text{Cos}(m_2 \theta + n_2 k z) \\ &= \frac{1}{2} b_{r_{s_{m_1, n_1}}} V_{\theta_{C_{m_2, n_2}}} (\text{Sin}(m_0 \theta + n_0 k z) + \text{Sin}((m_1 - m_2) \theta + (n_1 - n_2) k z)) \end{aligned} \quad 5.3.2$$

and so eqn 5.2.1 couples  $b_{r_{m_0, n_0}}$ ,  $b_{r_{m_1, n_1}}$ , and  $b_{r_{m_2, n_2}}$ .

The dependent variables that are advanced are  $V_r$ ,  $V_{\theta}$ ,  $V_z$ ,  $B_r$ ,  $B_{\theta}$ ,  $P$  and  $\rho$ .  $B_z$  has been removed from the set by using the Maxwell equation  $\nabla \cdot \underline{B} = 0$  to give

$$B_{z_{s_{m, n}}} = - \frac{1}{nk} \left( \frac{1}{r} \frac{\partial}{\partial r} (r B_{r_{C_{m, n}}}) + \frac{m}{r} B_{\theta_{s_{m, n}}} \right) \quad 5.3.3(a)$$

$$B_{z_{C_{m, n}}} = \frac{1}{nk} \left( \frac{1}{r} \frac{\partial}{\partial r} (r B_{r_{s_{m, n}}}) - \frac{m}{r} B_{\theta_{C_{m, n}}} \right) \quad 5.3.3(b)$$

A special case arises when  $n=0$  and eqns 5.3.3 cannot be used. A particularly important example of this is the equilibrium ( $m=n=0$ ). A special set of equations is solved for the equilibrium; these are discussed below. The case  $m \neq 0$  and  $n=0$  has not yet been implemented in the algorithm described here. However this would be a straightforward task with  $B_{\theta}$  instead of  $B_z$  being made redundant by using  $\nabla \cdot \underline{B} = 0$ .

Using  $S_{m, n}^{p, q}(AB)$  to denote the  $\text{Sin}(m\theta + nkz)$  part of the convolution of  $(A - pA_0)$  and  $(B - qB_0)$ , where  $A_0 = A_{C_{0, 0}}$  (ie.  $A_0$  is the equilibrium harmonic) and defining  $C_{m, n}^{p, q}(AB)$  similarly to be the cosine phased part, the equations to be solved for a particular  $m, n$  mode pair

are :-

$$\begin{aligned} \frac{\partial B_{r_{s_{m,n}}}}{\partial t} &= - \left( \frac{m}{r} B_{\theta_o} + nk B_{z_o} \right) V_{r_{C_{m,n}}} - \frac{\eta}{s} \left( \frac{m^2}{r^2} + n^2 k^2 \right) B_{r_{s_{m,n}}} \\ &+ \frac{\eta}{s} \frac{m}{r^2} \frac{\partial}{\partial r} \left( r B_{\theta_{C_{m,n}}} \right) + \frac{\eta}{s} \frac{\partial}{\partial r} \left( \frac{1}{r} \frac{\partial r}{\partial r} B_{r_{s_{m,n}}} - \frac{m}{r} B_{\theta_{C_{m,n}}} \right) \\ &- \frac{m}{r} (C_{m,n}^{0,1} (V_r B_\theta) - C_{m,n}^{0,0} (V_\theta B_r)) + nk (C_{m,n}^{0,0} (V_z B_r) - C_{m,n}^{0,1} (V_r B_z)) \end{aligned} \quad 5.3.4$$

$$\begin{aligned} \frac{\partial (\rho_o V_{r_{C_{m,n}}})}{\partial t} &= - \frac{1}{2r} \frac{\partial (r P_{C_{m,n}})}{\partial r} - \frac{1}{r} \frac{\partial}{\partial r} r \left( B_{\theta_o} B_{\theta_{C_{m,n}}} + \frac{B_{z_o}}{nk} \left( \frac{1}{r} \frac{\partial}{\partial r} r B_{r_{s_{m,n}}} - \frac{m}{r} B_{\theta_{C_{m,n}}} \right) \right) \\ &+ \left( \frac{m}{r} B_{\theta_o} + nk B_{z_o} \right) B_{r_{s_{m,n}}} + \frac{1}{r} \left( \frac{P_{C_{m,n}}}{2} + B_{z_o} B_{z_{C_{m,n}}} - E_{\theta_o} B_{\theta_{C_{m,n}}} \right) - \frac{\partial}{\partial t} (C_{m,n}^{1,0} (\rho V_r)) \\ &- \frac{1}{r} \frac{\partial}{\partial r} r (C_{m,n}^{0,0} (\rho V_r^2) - \frac{1}{2} C_{m,n}^{0,0} (B_r^2) + \frac{1}{2} C_{m,n}^{1,1} (B_\theta^2) + \frac{1}{2} C_{m,n}^{1,1} (B_z^2)) \\ &- \frac{m}{r} (S_{m,n}^{0,0} (\rho V_\theta V_r) - S_{m,n}^{1,0} (B_\theta B_r)) - nk (S_{m,n}^{0,0} (\rho V_z V_r) - S_{m,n}^{1,0} (B_z B_r)) \\ &+ \frac{1}{r} (C_{m,n}^{0,0} (\rho V_\theta^2) - \frac{1}{2} C_{m,n}^{1,1} (B_\theta^2) + \frac{1}{2} C_{m,n}^{0,0} (B_r^2) + \frac{1}{2} C_{m,n}^{1,1} (B_z^2)) \end{aligned} \quad 5.3.5$$

$$\begin{aligned} \frac{\partial P_{C_{m,n}}}{\partial t} &= - \frac{1}{r} \frac{\partial}{\partial r} (r P_o V_{r_{C_{m,n}}}) - \left( \frac{m}{r} V_{\theta_{s_{m,n}}} + nk z V_{z_{s_{m,n}}} \right) P_o \gamma + (1-\gamma) \frac{P_o}{r} \frac{\partial}{\partial r} (r V_{r_{C_{m,n}}}) \\ &+ \frac{4\eta}{s} (\gamma-1) \frac{\partial B_{z_o}}{\partial r} \left( \frac{\partial B_{z_{C_{m,n}}}}{\partial r} - nk B_{r_{s_{m,n}}} \right) \\ &+ \frac{4\eta}{s} (\gamma-1) \frac{1}{r} \frac{\partial}{\partial r} (r B_{\theta_o}) \left( \frac{1}{r} \frac{\partial}{\partial r} (r B_{\theta_{C_{m,n}}}) - \frac{m}{r} B_{r_{s_{m,n}}} \right) - \frac{1}{r} \frac{\partial}{\partial r} (r C_{m,n}^{1,0} (P V_r)) \\ &- \frac{m}{r} S_{m,n}^{1,0} (P V_\theta) - nk S_{m,n}^{1,0} (P V_z) - (\gamma-1) C_{m,n}^{1,0} (P \nabla \cdot \underline{V}) \\ &+ \frac{2\eta}{s} (\gamma-1) (C_{m,n}^{0,0} (J_r^2) + C_{m,n}^{1,1} (J_\theta^2) + C_{m,n}^{1,1} (J_z^2)) \end{aligned} \quad 5.3.6$$

$$\frac{\partial \rho C_{m,n}}{\partial t} = -\frac{1}{r} \frac{\partial}{\partial r} (r C_{m,n}^{0,0}(\rho V_r)) - \frac{m}{r} S_{m,n}^{0,0}(\rho V_\theta) - nk S_{m,n}^{0,0}(\rho V_z) \quad 5.3.7$$

(for simplicity only the r components of eqns 5.2.1 and 5.2.2 are given and the parallel viscosity terms are not included)

where the conventions  $S_{m,n}^{0,0}(A^2) = S_{m,n}^{0,0}(AA)$ , and if  $D = BC$  then  $S_{m,n}^{0,0}(ABC) = S_{m,n}^{0,0}(AD)$  etc. are assumed and the resistivity is taken to be a function of r and t only. The reason for separating the equations into the form linearised equation + nonlinear convolution terms will become apparent when the numerical algorithm is explained in section 5.5. A similar set of equations exist for the opposite phasing ie.  $B_r, V_\theta, V_z$  cosine phased and  $V_r, B_\theta, B_z, \rho, P$  sine phased.

It is a well known property of the linearised MHD equations that unless special effects such as finite Larmor radius terms are included, no coupling occurs between the two phases of any given Fourier harmonic [38]. Therefore only one phase need be solved for each harmonic. This property also extends to the nonlinear MHD equations as may be demonstrated using proofs similar to those of sections 3.2.2 and 3.5.1. For example if  $B_r$  is chosen to be wholly sine phased ie.

$$B_r = \sum_{m,n} B_r S_{m,n} \sin(m\theta + nkz)$$

and  $V_\theta, V_z$  are also sine phased, whilst  $V_r, B_\theta, B_z, P$  and  $\rho$  are chosen to be wholly cosine phased. Then the nonlinear terms of the  $B_r$  equation give rise to no opposite phasing

eg.

$$\begin{aligned}
\frac{1}{r} \frac{\partial}{\partial \theta} (V_r B_\theta) &= \frac{1}{r} \frac{\partial}{\partial \theta} \left( \sum_{m,n} V_r C_{m,n} \cos(m\theta + nkz) \sum_{p,q} B_\theta C_{p,q} \cos(p\theta + qkz) \right) \\
&= \frac{1}{2r} \frac{\partial}{\partial \theta} \left( \sum_{\substack{m,n \\ p,q}} V_r C_{m,n} B_\theta C_{p,q} (\cos((m+p)\theta + k(n+q)z) + \cos((m-p)\theta + k(n-q)z)) \right) \\
&= -\frac{1}{2r} \sum_{\substack{m,n \\ p,q}} (m+p) V_r C_{m,n} B_\theta C_{p,q} \sin((m+p)\theta + k(n+q)z) \\
&\quad - \frac{1}{2r} \sum_{\substack{m,n \\ p,q}} (m-p) V_r C_{m,n} B_\theta C_{p,q} \sin((m-p)\theta + k(n-q)z)
\end{aligned}$$

All the other dependent variables can also be shown to retain their initial pure phasing. For a 2D situation in which the first harmonic is dominant and generates all the higher harmonics the above proof shows only one phase need be solved for each harmonic. For a 3D mixed helicity case the situation is less clear. However generally two harmonics of different helicity will be dominant and generate all other harmonics for a 3D case. If this is the case then both harmonics can be taken to have the same phase, since a  $\theta$ ,  $z$  origin can always be defined to achieve this

eg.

if the harmonics are  $m_1, n_1$  and  $m_2, n_2$  and they are sine and cosine phased in a particular frame of reference then defining a new origin by  $\theta' = \theta - a$ ,  $z' = z - b$  where  $a, b$  are the solutions of

$$(m_1 a + n_1 k b) = 2\pi$$

$$(m_2 a + n_2 k b) = \pi/2$$

renders both harmonics sine phased in the  $\theta'$ ,  $z'$  frame of reference. Hence for most 3D cases only one phase need be solved for each harmonic. The ability to solve for both phases is however retained in

the algorithm described in section 5.5 to allow any 3D problem to be solved.

Another consequence of the "pure" phasing property is that only the cosine phased terms can possess non zero equilibrium components. Hence the only equilibrium quantities which need be time advanced are  $B_\theta$ ,  $B_z$ ,  $v_r$ ,  $\rho$ , and  $P$ . The equilibrium equations are

$$\frac{\partial B_\theta}{\partial t} = -\frac{\partial}{\partial r}(v_r B_\theta) + \frac{1}{S} \frac{\partial}{\partial r} \frac{\eta}{r} \frac{\partial}{\partial r}(r B_\theta) - \frac{\partial}{\partial r}(C_{0,0}^{1,1}(v_r B_\theta) - C_{0,0}^{1,1}(v_\theta B_r)) \quad 5.3.8$$

$$\frac{\partial B_z}{\partial t} = -\frac{1}{r} \frac{\partial}{\partial r}(r B_z v_r) + \frac{1}{S r} \frac{\partial}{\partial r} \left( r \eta \frac{\partial B_z}{\partial r} \right) + \frac{1}{r} \frac{\partial}{\partial r} (C_{0,0}^{1,1}(v_z B_r) - C_{0,0}^{1,1}(v_r B_z)) \quad 5.3.9$$

$$\begin{aligned} \frac{\partial(\rho v_r)}{\partial t} &= -\frac{1}{r} \frac{\partial}{\partial r} (r \rho v_r^2) - \frac{1}{2r} \frac{\partial}{\partial r} r (P_\theta + B_\theta^2 + B_z^2) \\ &+ \frac{1}{2r} (P_\theta - B_\theta^2 + B_z^2) - \frac{\partial}{\partial t} C_{0,0}^{1,1}(\rho v_r) \\ &- \frac{1}{r} \frac{\partial}{\partial r} r \left( (C_{0,0}^{0,0}(\rho v_r^2) - \rho v_r^2) + \frac{1}{2} (-C_{0,0}^{1,1}(B_r^2) + C_{0,0}^{1,1}(B_\theta^2) + C_{0,0}^{1,1}(B_z^2)) \right) \\ &+ \frac{1}{r} (C_{0,0}^{0,0}(\rho v_\theta^2) + \frac{1}{2} (C_{0,0}^{1,1}(B_r^2) - C_{0,0}^{1,1}(B_\theta^2) + C_{0,0}^{1,1}(B_z^2))) \end{aligned} \quad 5.3.10$$

$$\frac{\partial \rho}{\partial t} = -\frac{1}{r} \frac{\partial}{\partial r} r (C_{0,0}^{0,0}(\rho v_r)) \quad 5.3.11$$

$$\begin{aligned} \frac{\partial P}{\partial t} &= -\frac{1}{r} \frac{\partial}{\partial r} (r P v_r) - (\gamma-1) \frac{P}{r} \frac{\partial}{\partial r} r v_r + 2(\gamma-1) \frac{\eta}{S} (J_\theta^2 + J_z^2) \\ &- \frac{1}{r} \frac{\partial}{\partial r} r C_{0,0}^{1,1}(P v_r) - (\gamma-1) C_{0,0}^{1,1}(P v \cdot \underline{v}) \\ &+ 2(\gamma-1) \frac{\eta}{S} (C_{0,0}^{1,1}(J_r^2) + C_{0,0}^{1,1}(J_\theta^2) + C_{0,0}^{1,1}(J_z^2)) \end{aligned} \quad 5.3.12$$

## 5.4 BOUNDARY CONDITIONS

One problem with developing a code which uses finite difference methods in all three spatial dimensions is that of finding consistent boundary conditions. Often numerical smoothing has to be used at the boundaries. However, the Fourier decomposition performed here allows different boundary conditions to be specified for each Fourier component. The boundary conditions chosen are those used by Dibiase for his compressible linear code [38] :-

At the origin (r=0)

The boundary conditions at the origin arise from symmetry considerations and vary according to the particular harmonic :-

Equilibrium

$$\frac{\partial \rho_0}{\partial r} = \frac{\partial B_{z_0}}{\partial r} = \frac{\partial P_0}{\partial r} = 0$$

$$B_{\theta_0} = V_{r_0} = 0$$

m=0 n≠0

$$B_{r_{0,n}} = B_{\theta_{0,n}} = V_{r_{0,n}} = V_{\theta_{0,n}} = 0$$

$$\frac{\partial V_{z_{0,n}}}{\partial r} = \frac{\partial P_{0,n}}{\partial r} = \frac{\partial \rho_{0,n}}{\partial r} = 0$$

m=1

$$V_{z_{1,n}} = P_{1,n} = \rho_{1,n} = 0$$

$$\frac{\partial B_{r_{1,n}}}{\partial r} = \frac{\partial B_{\theta_{1,n}}}{\partial r} = \frac{\partial V_{r_{1,n}}}{\partial r} = \frac{\partial V_{\theta_{1,n}}}{\partial r} = 0$$



m>2

$$B_{r_{m,n}} = B_{\theta_{m,n}} = V_{r_{m,n}} = V_{\theta_{m,n}} = V_{z_{m,n}} = P_{m,n} = \rho_{m,n} = 0$$

At the wall

Again the boundary conditions are dependent on the particular harmonic :-

Equilibrium

The wall is assumed non-porous and so

$$V_{r_0} = 0$$

It is also assumed that the equilibrium current at the wall is maintained constant

$$\frac{\partial J_{\theta_0}}{\partial t} = \frac{\partial J_{z_0}}{\partial t} = 0$$

The equilibrium boundary conditions at the wall are therefore

$$V_{r_0} = \frac{\partial}{\partial t} \left( \frac{\partial}{\partial r} (r B_{\theta_0}) \right) = \frac{\partial}{\partial t} \left( \frac{\partial B_{z_0}}{\partial r} \right) = \frac{\partial \rho_0}{\partial r} = \frac{\partial P_0}{\partial r} = 0$$

All other harmonics (m,n)

Taking the wall to be perfectly conducting and non-porous yields

$$V_{r_{m,n}} = B_{r_{m,n}} = 0$$

If the perturbed radial current is assumed to vanish at the wall then

$$\frac{m}{r} B_{z_{s_{m,n}}} = nk B_{\theta_{s_{m,n}}} \quad \text{and} \quad \frac{m}{r} B_{z_{c_{m,n}}} = nk B_{\theta_{c_{m,n}}}$$

Combining this with the Maxwell relation  $\nabla \cdot \underline{B} = 0$  yields, at the wall,

$$B_{\theta_{c_{m,n}}} = \frac{m R_{\text{wall}}}{m^2 + n^2 k^2 R_{\text{wall}}^2} \frac{\partial B_{r_{s_{m,n}}}}{\partial r}$$

and

$$B_{\theta s_{m,n}} = \frac{-mR_{\text{wall}}}{m^2 + n^2 k^2 R_{\text{wall}}^2} \frac{\partial B_r C_{m,n}}{\partial r}$$

(where  $R_{\text{wall}} = r|_{\text{wall}}$ )

Robinson has also derived similar boundary conditions for  $V_{\theta}$ ,  $V_z$  [38]

$$V_{\theta C_{m,n}} = \frac{mR_{\text{wall}}}{m^2 + n^2 k^2 R_{\text{wall}}^2} \frac{\partial v_r s_{m,n}}{\partial r}$$

$$V_{\theta s_{m,n}} = \frac{-mR_{\text{wall}}}{m^2 + n^2 k^2 R_{\text{wall}}^2} \frac{\partial v_r C_{m,n}}{\partial r}$$

and  $V_{z_{m,n}} = R_{\text{wall}} \frac{nk}{m} V_{\theta_{m,n}}$

The final boundary conditions required are taken to be

$$P_{m,n} = \rho_{m,n} = 0$$

## 5.5 NUMERICAL ALGORITHM

It is desirable because of numerical stability problems resulting from the resistive diffusion and sound wave terms to solve eqns 5.3.4 - 5.3.6 implicitly. However the harmonic couplings inherent in the nonlinear terms would require the inversion of a lot of matrices of size (no. harmonics x no. dependent variables), in order to solve using the standard tri-diagonal method (section 3.4.1). The inversion of such matrices is computationally impractical and so a compromise must be found. If the convolution terms in eqns 5.3.4 - 5.3.7 are

ignored then the linear problem solved by Dibiase is obtained for each particular harmonic [38], and an implicit method is immediately applicable. Hence a compromise which achieves the required stability properties whilst remaining computationally practical can be achieved by solving implicitly for the linearised part of each harmonic and including the convolution coupling terms explicitly.

The main problem with such a formulation is the  $\frac{\partial}{\partial t}(C_{m,n}^{1,0}(\rho V_r))$  term of eqn 5.3.5 and the similar terms of the  $V_\theta$  and  $V_z$  equations. These terms require the "new" values of the  $\rho$ ,  $\underline{V}$  harmonics and cannot therefore be included explicitly, yet to include them implicitly would cause the harmonics to couple, which as explained above must be avoided. An iteration process has therefore been used to include these momentum time derivatives. Firstly this iteration method will be detailed for a single helicity situation. In this case the first harmonic will be the fastest growing mode of that helicity and the higher harmonics will be predominantly perturbed by this mode. Hence if an ordering  $\epsilon$  is attributed to the first harmonic then the second harmonic will be of order  $\epsilon^2$ , the third harmonic will be of order  $\epsilon^3$ , etc. Also the equilibrium radial flow,  $V_{r_0}$  which is perturbed by the first harmonic is of order  $\epsilon^2$  and so :-

For the zeroth harmonic (equilibrium)

$$0 \left\{ \left( \frac{\partial \rho V}{\partial t} \right)_0 \right\} \sim \epsilon^2 \frac{\partial}{\partial t} \left( \rho_0 V_0 + \frac{1}{2} \rho_1 V_1 \right) + \epsilon^4 \frac{\partial}{\partial t} \left( \frac{1}{2} \rho_2 V_2 \right) + \dots$$

For the first harmonic

$$0 \left\{ \left( \frac{\partial \rho V}{\partial t} \right)_1 \right\} \sim \epsilon \frac{\partial}{\partial t} \left( \rho_0 V_1 \right) + \epsilon^3 \frac{\partial}{\partial t} \left( \rho_1 V_0 \pm \frac{1}{2} \rho_1 V_2 \pm \frac{1}{2} \rho_2 V_1 \right) + \dots$$

For the second harmonic

$$O \left\{ \left( \frac{\partial \rho \underline{v}}{\partial t} \right)_2 \right\} \sim \epsilon^2 \frac{\partial}{\partial t} \left( \rho_0 \underline{v}_2 \pm \frac{1}{2} \rho_1 \underline{v}_1 \right) + \epsilon^4 \frac{\partial}{\partial t} \left( \rho_2 \underline{v}_0 \pm \frac{1}{2} \rho_3 \underline{v}_1 \pm \frac{1}{2} \rho_1 \underline{v}_3 \right) + \dots$$

For the third harmonic

$$O \left\{ \left( \frac{\partial \rho \underline{v}}{\partial t} \right)_3 \right\} \sim \epsilon^3 \frac{\partial}{\partial t} \left( \rho_0 \underline{v}_3 \pm \frac{1}{2} \rho_1 \underline{v}_2 \pm \frac{1}{2} \rho_2 \underline{v}_1 \right) + \dots$$

etc.

where the subscripts denote the harmonics and the arbitrary signs occurring in the harmonic convolutions terms must be resolved for each particular harmonic and component. Hence if the first harmonic is solved for initially with only the  $\frac{\partial \rho_0 \underline{v}_1}{\partial t}$  term of the momentum time derivative included the error will be small,  $O(\epsilon^2)$ . Then solve for the zeroth and second harmonics with just the order  $\epsilon^2$  terms included (NB that  $\frac{\partial}{\partial t}(\rho_1 \underline{v}_1)$  is now known). Then solve for the third harmonic with just the terms of order  $\epsilon^3$  included, etc. Solving in this manner reduces the error in including the  $\left( \frac{\partial \rho \underline{v}}{\partial t} - \frac{\partial \rho_0 \underline{v}_n}{\partial t} \right)_n$  term explicitly to order  $\epsilon^2 O \left( \frac{\partial \rho \underline{v}}{\partial t} \right)_n$  for the nth harmonic. Hence a good first "guess" to the solution at the new timestep can be obtained. The iteration process then proceeds in the normal manner with the previous iteration values being used to evaluate  $\left( \frac{\partial \rho \underline{v}}{\partial t} - \frac{\partial \rho_0 \underline{v}_n}{\partial t} \right)_n$ . The iteration is repeated until a desired degree of convergence is obtained.

The application of this hierarchical ordering method to a mixed helicity problem requires that an ordering be found. Generally as explained above in mixed helicity simulations two modes of different helicity dominate and generate all the other harmonics. The orderings of these two dominant modes then generate the hierarchical solution

order, necessary to produce the initial solution for the iteration process. It is conceivable that some mixed helicity problems may have no evident ordering, however such problems are not considered here.

In fact it was found that assuming  $\rho$  to be a function of  $r$  only has little effect on the g mode; a comparison between two runs one time advancing  $\rho$  and the other taking  $\rho = \rho(r)$ , is given in the next chapter. Since taking a static density profile circumvents all the above problems associated with the momentum time derivatives, the iteration is no longer necessitated and so the code runs two to three times faster. For this reason the majority of runs described in the next chapter take the density as a static profile.

The algorithm used is given as a flow diagram in fig 5.4.1.



The adaptation of this algorithm to solve for static density profiles requires that only the  $\underline{V}$ ,  $\underline{B}$ ,  $P$  solution need be performed since the iteration is no longer necessary.

Eqns 5.3.4 - 5.3.7 are differenced using centred finite differences in the  $r$  direction and a Crank-Nicholson weighting for the implicit part of the time advancement scheme. The implicit solution of eqns 5.2.4 - 5.3.6 together with the associated equations for  $V_\theta$ ,  $V_z$  and  $B_\theta$  produces a block tri-diagonal form which is solved using the methods described in section 3.4.1. The equilibrium equations (eqns 5.3.8 - 5.3.12) are also differenced and solved in this manner. The implicit nonlinear terms of the equilibrium equations such as  $\frac{\partial}{\partial r}(V_r B_\theta)$  of eqn 5.3.8 are included in the temporal differencing as  $\frac{1}{2} \frac{\partial}{\partial r}(V_{r_o}^n B_{\theta_o}^{n+1} + V_{r_o}^{n+1} B_{\theta_o}^n)$  for advancing from timestep  $n$  to  $n+1$ . Such terms are time centred and are therefore not Crank-Nicholson weighted.

Since the convolutions represent one of the most time consuming parts of the algorithm they must be optimised as much as possible. To achieve this an array INDEX is used where

INDEX(n,1)= Poloidal mode number of  $n^{\text{th}}$  harmonic

INDEX(n,2)= Toroidal mode number of  $n^{\text{th}}$  harmonic

and at the start of the calculation an array INDEX1 is set up, where

INDEX1(p,q,1)=  $n$  if INDEX(p,1)+INDEX(q,1)=INDEX(n,1)

and INDEX(p,2)+INDEX(q,2)=INDEX(n,2)

or= 0 if the additive part of the convolution does not

produce a result in INDEX.

and if  $I_{\text{sign}} = \text{Sign}(\text{INDEX}(p,2) - \text{INDEX}(q,2))$  then

$\text{INDEX1}(p,q,2) = n$  if  $I_{\text{sign}} \times (\text{INDEX}(p,1) - \text{INDEX}(q,1)) = \text{INDEX}(n,1)$

and  $|\text{INDEX}(p,2) - \text{INDEX}(q,2)| = \text{INDEX}(n,2)$

or  $= 0$  if the subtractive part of the convolution does not produce a result in INDEX.

Having set up INDEX1 the convolutions can then be performed very efficiently since the result of every possible convolution of harmonics that produces a result in INDEX is stored in INDEX1.

## 5.6 TESTING THE CODE

The 3D Fourier harmonic code was tested in a similar manner to the 2D codes (see section 3.4). Each of the tridiagonal solvers was tested in isolation to ensure it was solving correctly and the convolution routines were checked against simple analytically evaluated convolutions.

The code as a whole was checked for convergence. The  $r$  mesh convergence checking was performed in the usual manner by repeatedly refining the mesh until convergence occurs. For the range of magnetic Reynolds number of interest ( $10^3$  to  $10^4$ ), 100 radial mesh points were found to be sufficient. The code is run by initially advancing only the first harmonic until settled linear eigenfunctions result. These linear eigenfunctions are then used after suitable rescaling to prime the nonlinear run. The timestep convergence checking for the linear



phase is performed by repeatedly halving the timestep until the eigenvalue growth rate converges. For the nonlinear phase of the run the code chooses its own timestep by repeatedly halving the timestep until a desired degree of convergence occurs. This timestep checking is repeated every 30 timesteps thus ensuring continued convergence. Convergence in the Fourier resolution must be checked for each case by increasing the number of Fourier harmonics until the solution converges.

Although the MHD equations implicitly conserve energy, the code itself will not conserve energy exactly. This is because the pressure equation and not the energy equation is time advanced, and also because the discretisation method is not compatible with energy conservation. However the code must still conserve energy to a good approximation. This is found to be the case - for a long simulation of 1000 Alfvén transit times the total energy decreased by 0.06% whilst over the same period a 4% exchange of energy between the magnetic and pressure energy occurred. This high degree of energy conservation serves as a valuable validation of the code.

The code was also checked in its linear phase against existing linear codes. The linear code RESTAB developed by Dibiase [38] closely approximates the code described here, except that it solves the temperature instead of the pressure equation. For this reason and because the derivatives of equilibrium quantities are obtained analytically in Dibiase's code instead of numerically as they must for the 3D code, slight discrepancies between the answers of the two codes are to be expected. Fig 5.6.1 shows the growth rates obtained from the two codes, for a range of  $k$  at a magnetic Reynolds number,  $S=1344$  with

$m=0$ . Fig 5.6.2 shows comparisons over a range of  $S$  with  $k=0.2$  and  $m=0$ . Although the growth rates do not coincide exactly for these cases, the discrepancies are small enough to be accounted for by the reasons described above. The larger discrepancies occurring in both cases, when the layer width becomes narrower and the differences between the two codes more significant. Therefore these results also serve to validate the code.

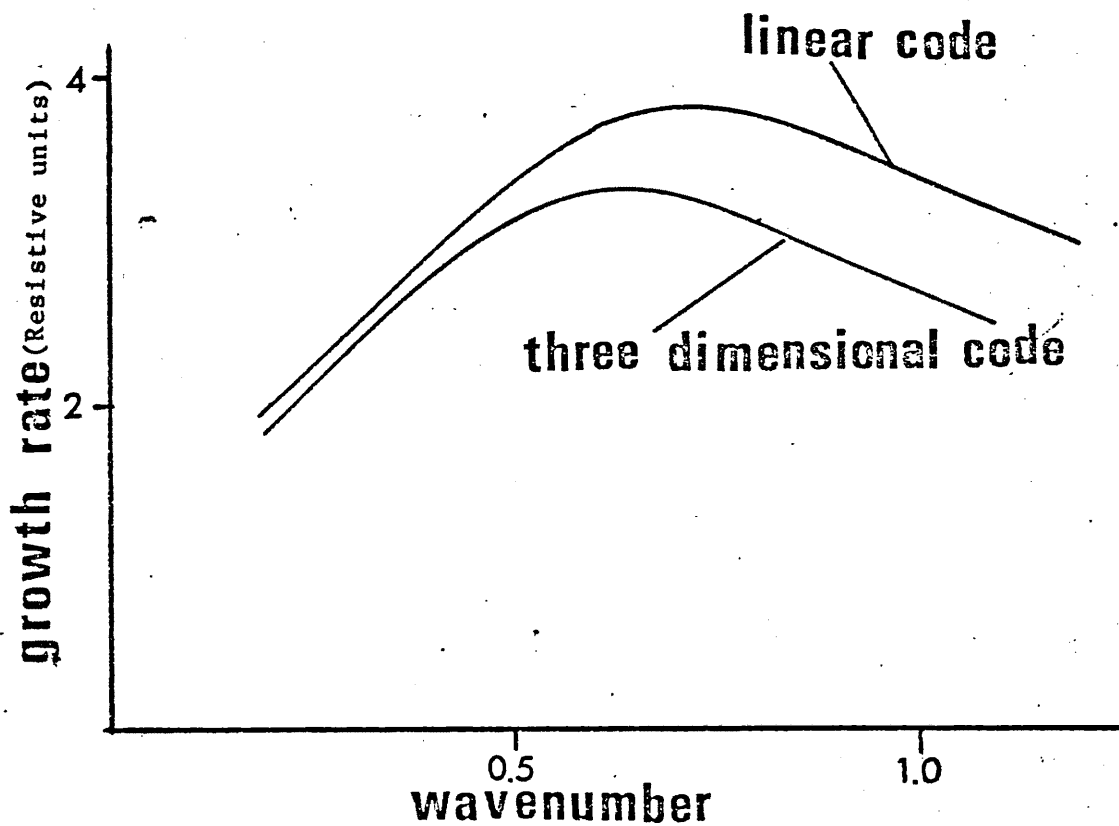


FIG. 5.6.1 Comparison of growth rates for linear code and Fourier harmonic code over a range of wavenumbers.

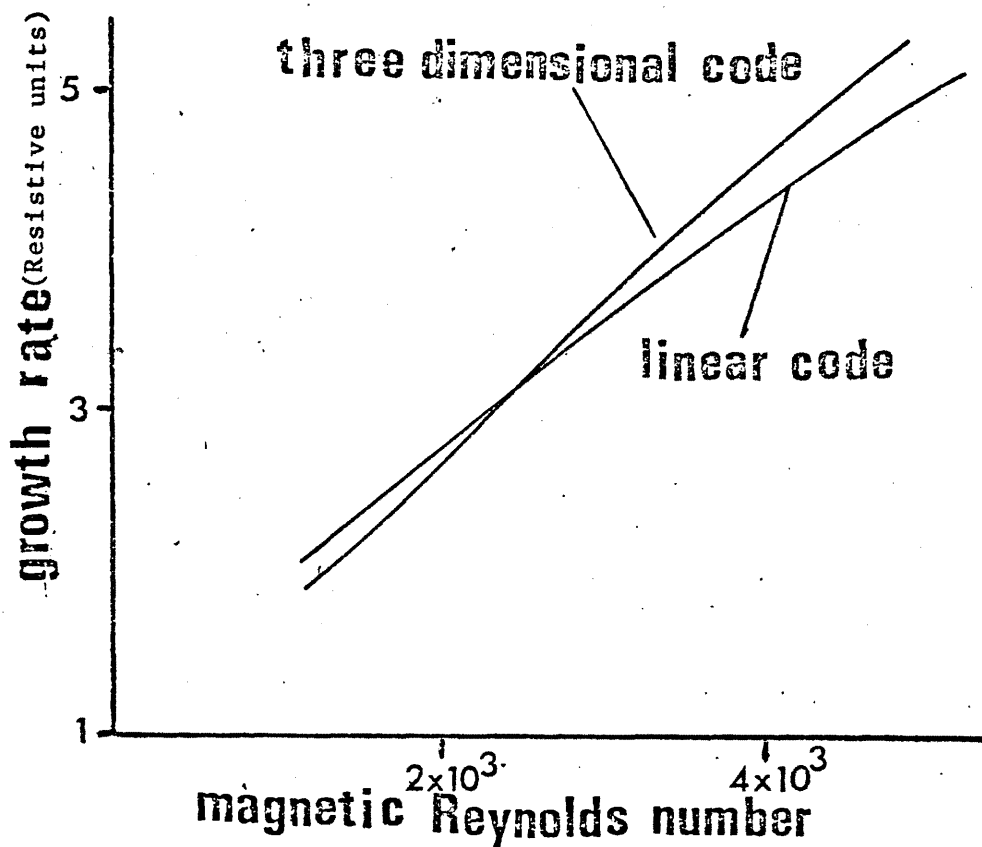


FIG. 5.6.2 Comparison over a range of S.

Checking of the code in the nonlinear phase is achieved by comparing the results against those obtained by using the 2D incompressible codes of chapters 3 and 4. Since they are based on an incompressible formulation whilst the present formulation is compressible, exact quantitative agreement cannot be expected. However qualitative agreement is found on comparing the results and dominant nonlinear mechanisms given in chapter 4 and chapter 6.

6.1 INTRODUCTION

In this chapter further nonlinear g mode results, arising from use of the Fourier harmonic code described in chapter 5 are presented. Firstly in section 6.2 the effects of compressibility and energy losses are examined for the single helicity  $m=0$  mode. The single helicity  $m=1$  mode is briefly discussed in section 6.3 and in section 6.4 mixed helicity interactions between the  $m=0$  and  $m=1$  modes are examined. Such mixed helicity interactions are found to lead to ergodic (random) field line behaviour in the reverse field pinch. This ergodic behaviour and its relation to experimentally observed phenomena is discussed in section 6.5. Finally in section 6.6 the results of this chapter are reviewed and conclusions drawn.

6.2  $m=0$  MODE RESULTS

The Fourier harmonic code may be run as a linear code by simply time advancing only one harmonic. For such a run the code is primed with noise and the solution followed until settled linear eigenfunctions result. These eigenfunctions are then rescaled to a magnitude just sufficient to precipitate nonlinear behaviour, and used as initial conditions for the nonlinear run.

The  $m=0$  mode case which is studied for all the results presented in this section is  $S=10^4$ ,  $k=0.4$ , and  $C=0.05$ . This case is discussed in the incompressible limit in chapter 4. Firstly with a Fourier harmonic code it is necessary to determine how many harmonics must be included to obtain a convergent solution. As has been discussed in chapter 5 if an order  $\epsilon$  is attributed to the first harmonic  $m,n$  (say) then the following ordering is obtained :-

- $O(1)$ :- Equilibrium
- $O(\epsilon)$ :-  $m,n$
- $O(\epsilon^2)$ :-  $2m,2n$
- $O(\epsilon^3)$ :-  $3m,3n$  etc.

Fig 6.2.1 shows a comparison between the average  $b_r$  growth rate  $(\int_0^{R_{wall}} \frac{\partial b_r}{\partial t} dr / \int_0^{R_{wall}} b_r dr)$  for cases with the first three and five harmonics included. This favourable comparison is in accordance with that given in chapter 3 between solving the full set of reduced  $m=0$  mode equations and the results obtained by solving for only the first three Fourier harmonics of that set.

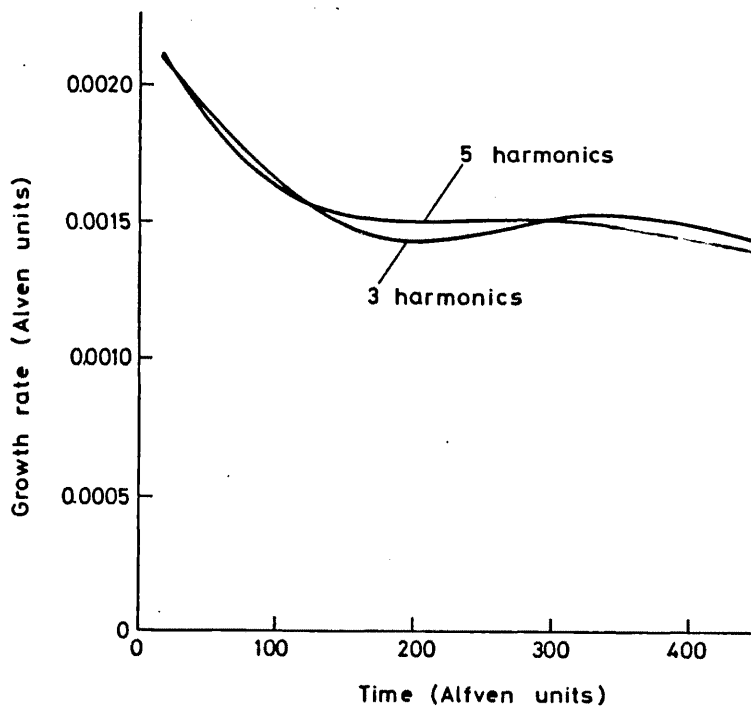


Fig 6.2.1 Fourier harmonic convergence test for  $m=0$  mode. Average  $B_r$  growth rates for 3 and 5 harmonics.

As mentioned in chapter 5 a comparison has been made between a case for which  $\rho(r)=1$  for all  $r$  and  $t$ , and a case in which the density is time advanced. Fig 6.2.2 shows the average  $b_r$  growth rate for these two cases. It can be seen that the assumption of a static density profile has little effect on the nonlinear behaviour of the g mode. This assumption does however save a considerable amount of computer time and will thus be used for the remainder of the results described in this chapter.

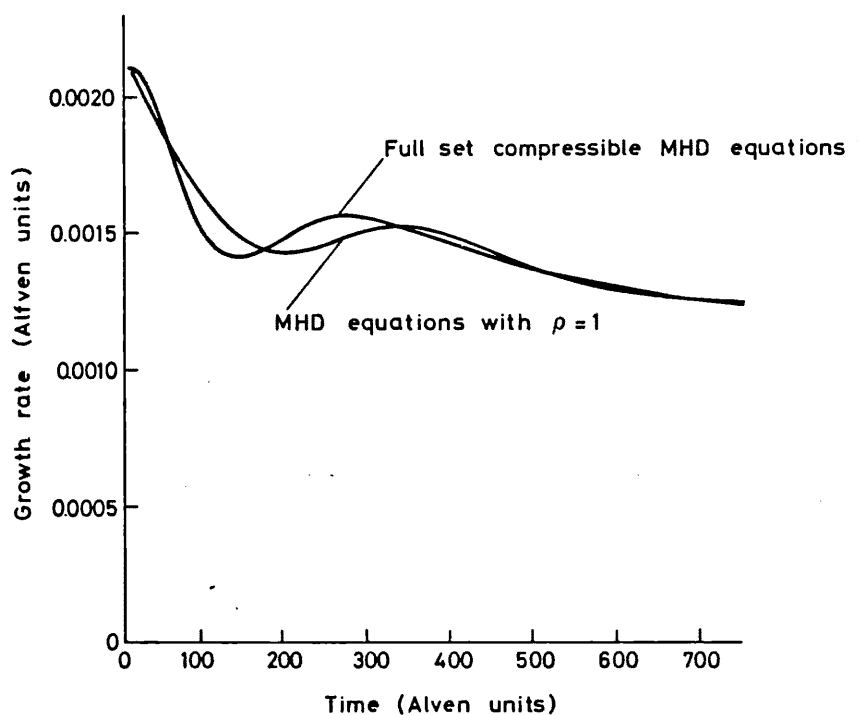


Fig 6.2.2 Average  $b_r$  growth rate for cases in which  $\rho$  is time advanced and  $\rho = \rho(r)$ .

It has been shown in chapter 4 that ohmic heating plays an important role in the nonlinear development of the g mode. The Fourier code contains an energy equation and energy loss terms can thus be included in the formulation. The exact nature of the anomalous loss processes in the pinch is however not well understood and so they are included by

means of a simple approximation. It is assumed that a thermal equilibrium exists and that the ohmic heating is exactly balanced by the energy loss terms. This approximation may be simply achieved by removing the ohmic heating terms from the equilibrium pressure equation. Fig 6.2.3 shows the effect on the average  $b_r$  growth rate of removing the ohmic heating terms.

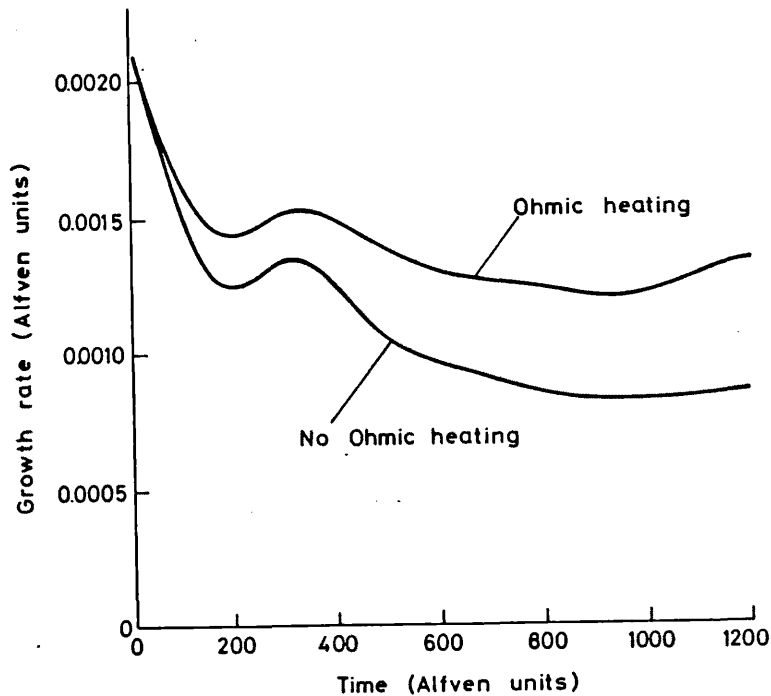


Fig 6.2.3 Effect of removing ohmic heating terms on average  $b_r$  growth rate for  $m=0$  mode.

It can be seen that the saturation is still not complete even when the ohmic heating terms are removed. This is probably because the resistive diffusion of the equilibrium still continues to cause the shear to decrease and thus the Suydam driving term,  $C$ , to increase. Fig 6.2.4 shows this effect for the no ohmic heating case.

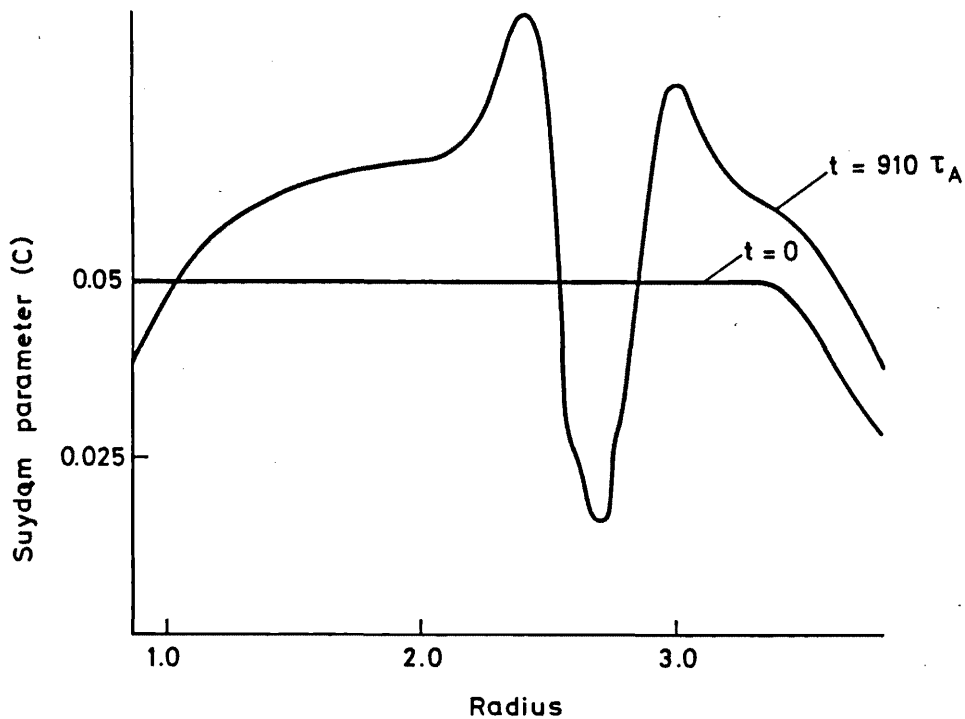


Fig 6.2.4 Nonlinear development of Suydam parameter for no ohmic heating case.

Finally it is of interest to examine the time development of the various energies in the system. The time development of magnetic, pressure and total energies are shown in figs 6.2.5 & 6.2.6 for the ohmic and no ohmic heating cases, respectively. The ohmically heated case (fig 6.2.5) exhibits the interchange of magnetic and pressure energy which is caused by resistive decay and ohmic heating. The total energy which can be seen to remain almost constant in this case. As mentioned in chapter 5 this serves as a valuable validation of the code. For the case in which no ohmic heating is included (fig 6.2.6) the pressure can be seen to be approximately constant in time which is accord with the removal of heating terms. The magnetic and total energies can be seen to decay at the same rate due to the simulated energy loss processes.



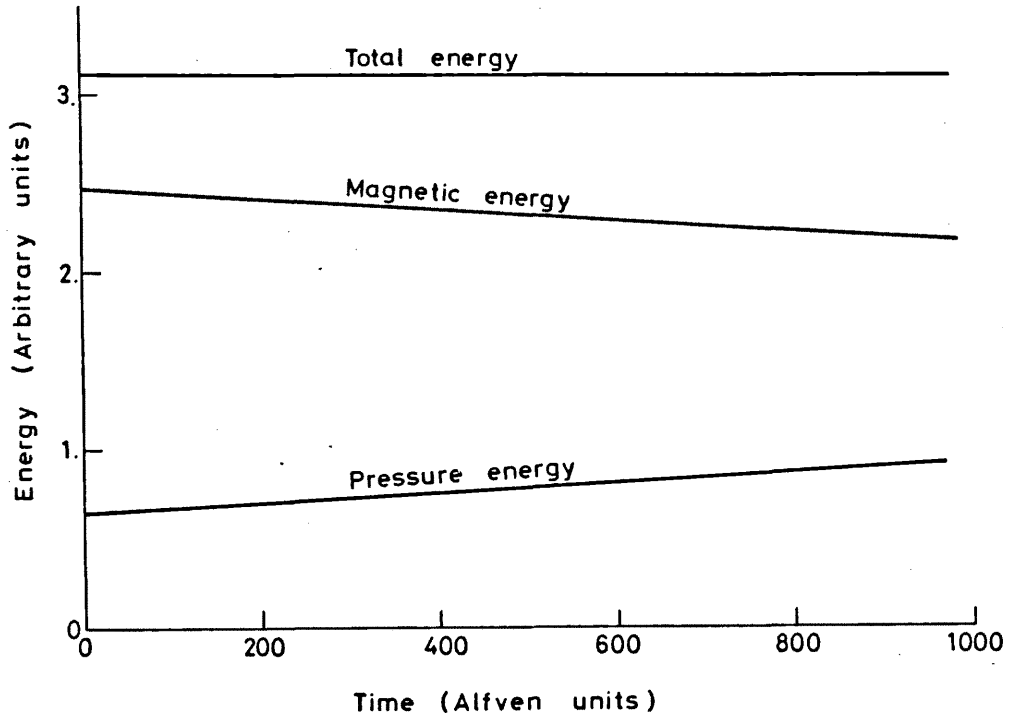


Fig 6.2.5 Nonlinear development of energy components for ohmically heated case.

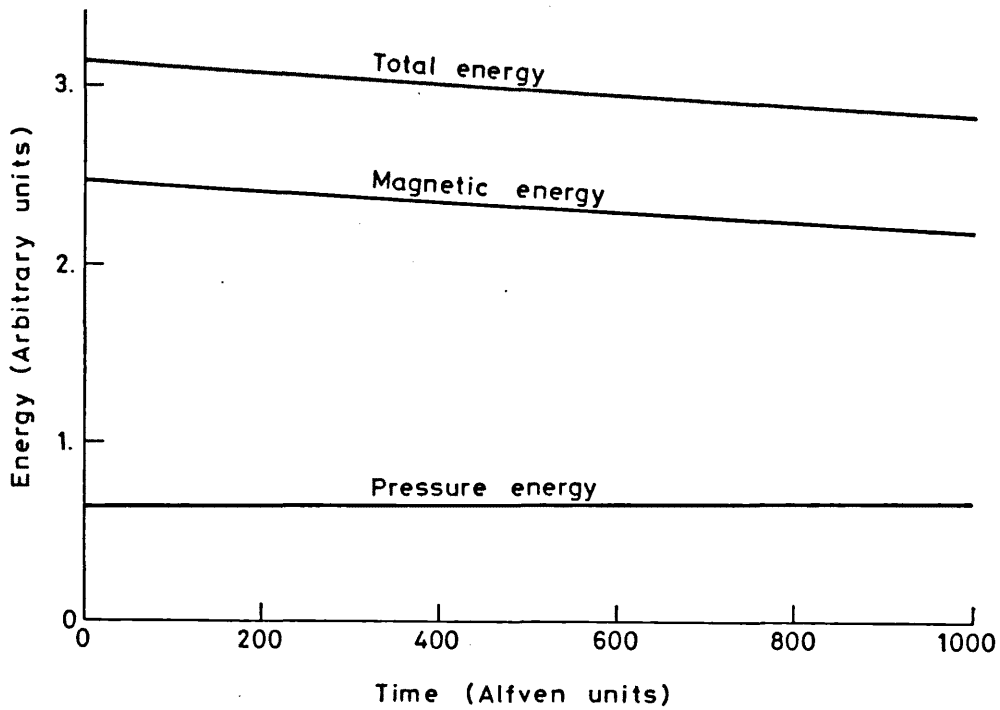


Fig 6.2.6 Nonlinear development of energy components for non ohmically heated case.

### 6.3 m=1 MODE RESULTS

The single helicity  $m=1$  mode has been very briefly examined. The reasons for not examining it in more detail are explained in section 6.5 where it is shown that ergodic behaviour occurs long before the  $m=1$  modes reach a width sufficient to precipitate two dimensional nonlinear behaviour. Fig 6.3.1 shows a comparison for an  $m=1$  mode of average  $b_r$  growth rate between an ohmically heated and a non ohmically heated case. This  $m=1$  mode occurs just inside the field null ( $nk=1.6$ ) and the case considered has a magnetic Reynolds number  $S=10^4$  and a Suydam value,  $C=0.05$ .

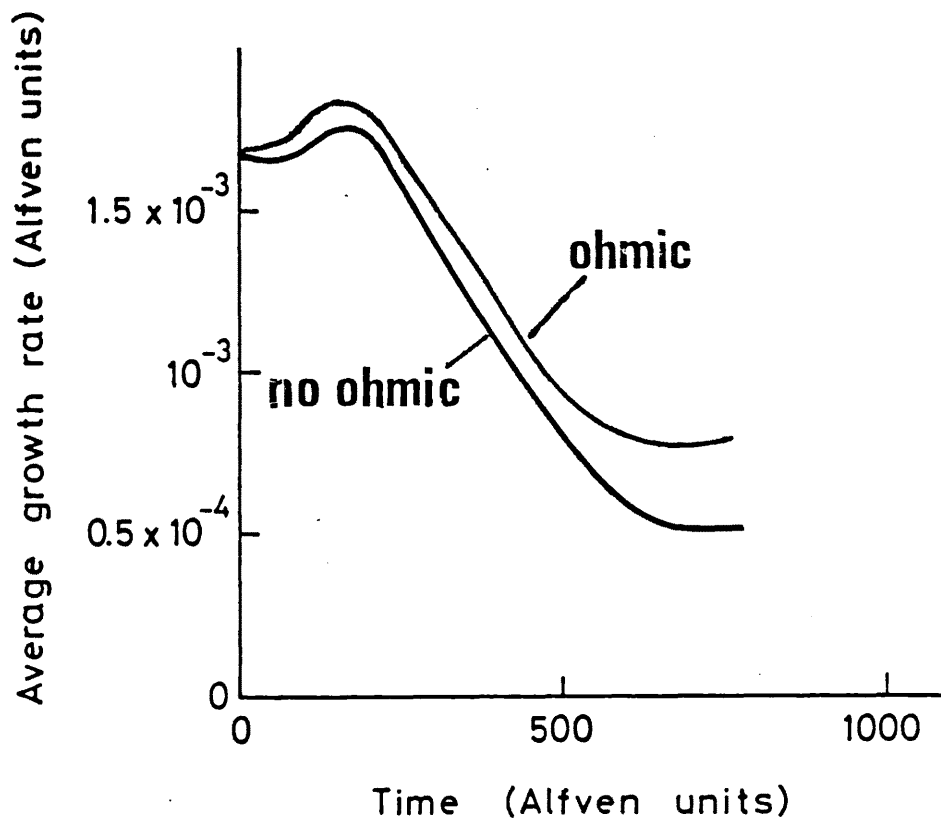


Fig 6.3.1 Comparison of  $b_r$  average growth rates for  $m=1$  mode cases with and without ohmic heating.

Fig 6.3.2 shows the nonlinear development of the equilibrium pressure

gradient for the non ohmically heated case and exhibits the characteristic pressure flattening at the  $m=1$  rational surface. Thus the nonlinear behaviour of the  $m=1$  mode is dominated by the same pressure flattening and ohmic heating mechanisms as the  $m=0$  mode.

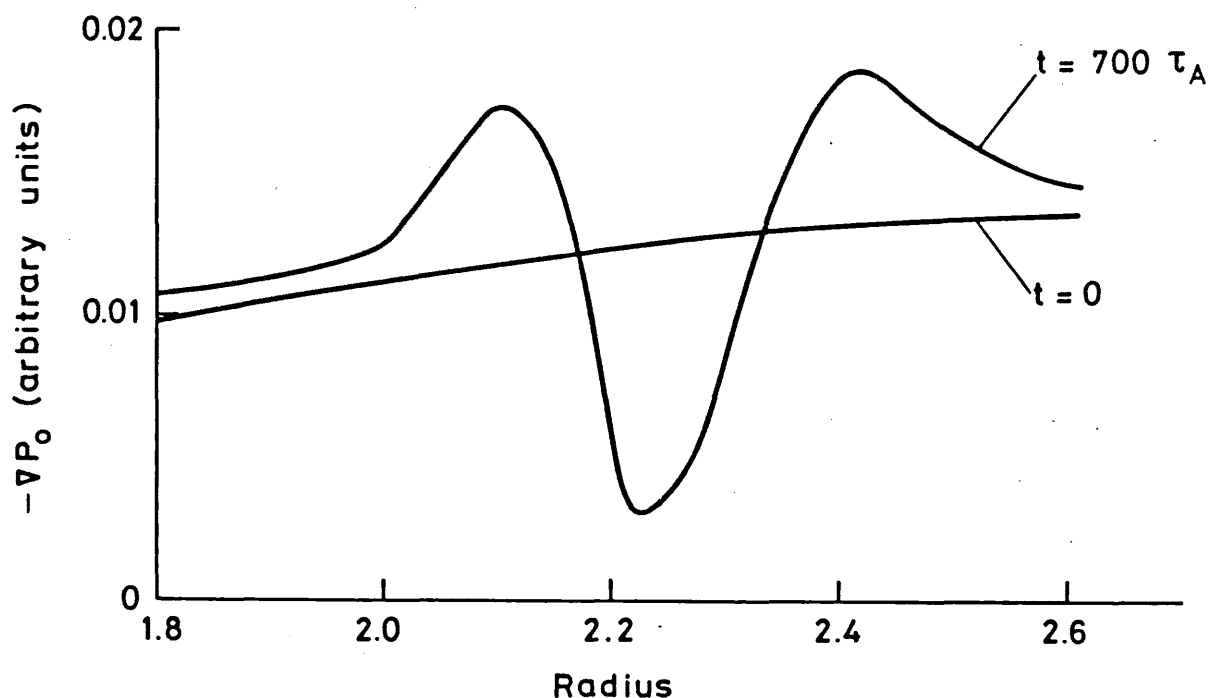


Fig 6.3.2 Nonlinear development of pressure gradient for  $m=1$  mode with no ohmic heating.

#### 6.4 MIXED HELICITY RESULTS

The mixed helicity interactions between an  $m=0$  and a nearby  $m=1$  mode has been studied, for a case in which the ohmic heating terms have been removed from the equilibrium pressure equation (see section 6.2). Only six harmonics are included in this simulation. They are :-

Equilibrium, (0,6) , (0,12)  
 (-1,16) , (-2,32) , (-1,22)

with an axial wavenumber  $k=0.1$ , a magnetic Reynolds number,  $S=10^4$  and a

Suydam value,  $C=0.05$ . The truncation at such a small number of harmonics has not been verified by increasing the number of harmonics but may in part be justified by comparison with the Oak Ridge work [36]. They find using a similar Fourier code to study the (2,1), (3,2) tearing mode interaction that 6 harmonics produce qualitatively correct answers [55].

Fig 6.4.1 shows the nonlinear development of the various island widths.

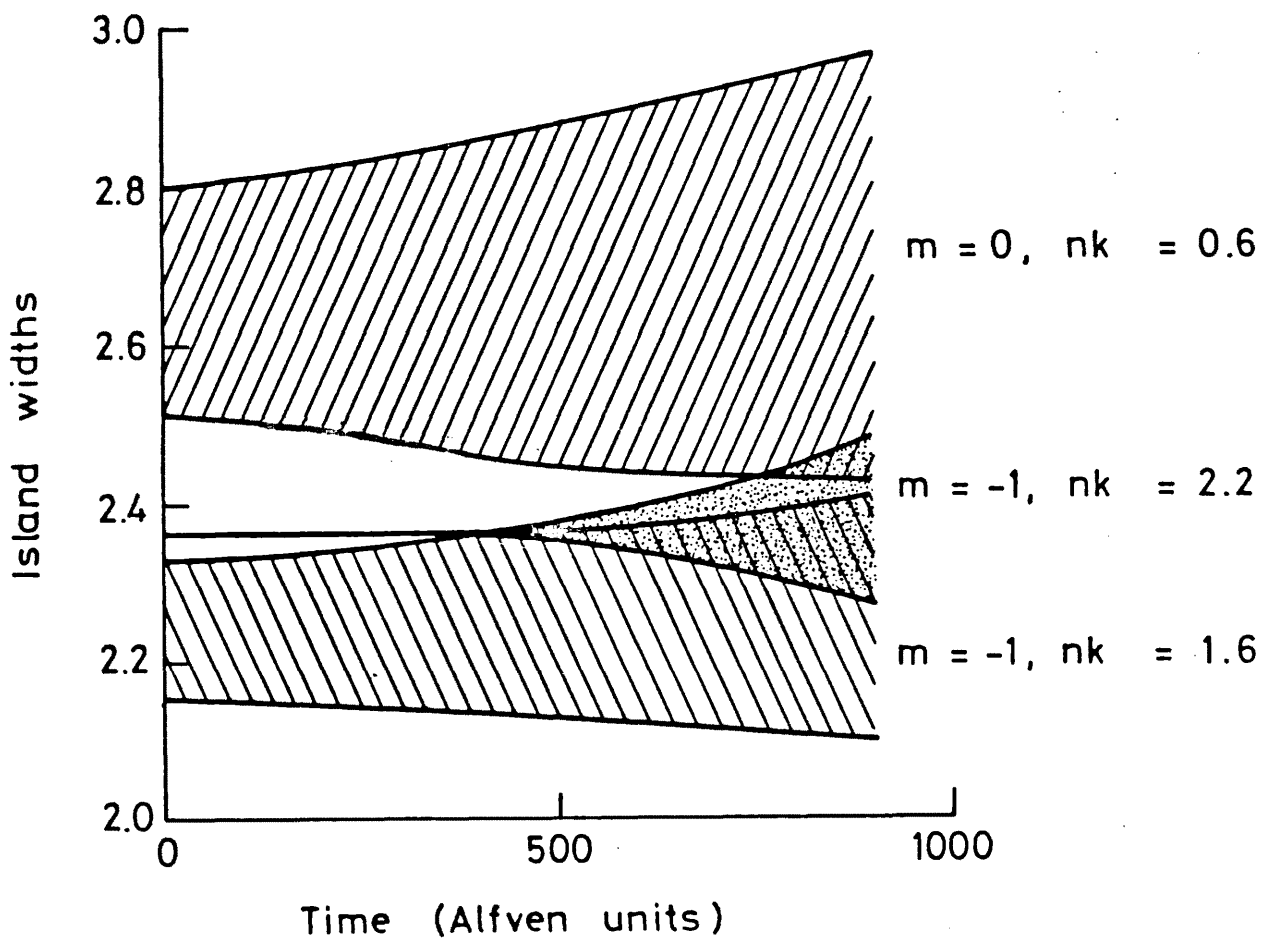


Fig 6.4.1 Nonlinear development of island widths for the various helicities included in the mixed helicity run.

It can be seen that when the  $m=-1$ ,  $nk=1.6$  island touches the rational surface of the 'cross talk' harmonic ( $m=-1$ ,  $nk=2.2$ ), that the cross talk harmonic grows very rapidly. The effect of this is to destabilise the  $m=-1$ ,  $nk=1.6$  mode (fig 6.4.2) but there is a negligible effect to the  $m=0$ ,  $nk=0.6$  mode (fig 6.4.3). This is analogous to the tearing mode case mentioned above where the (5,3) mode grows very rapidly and destabilises the (3,2) mode [55].

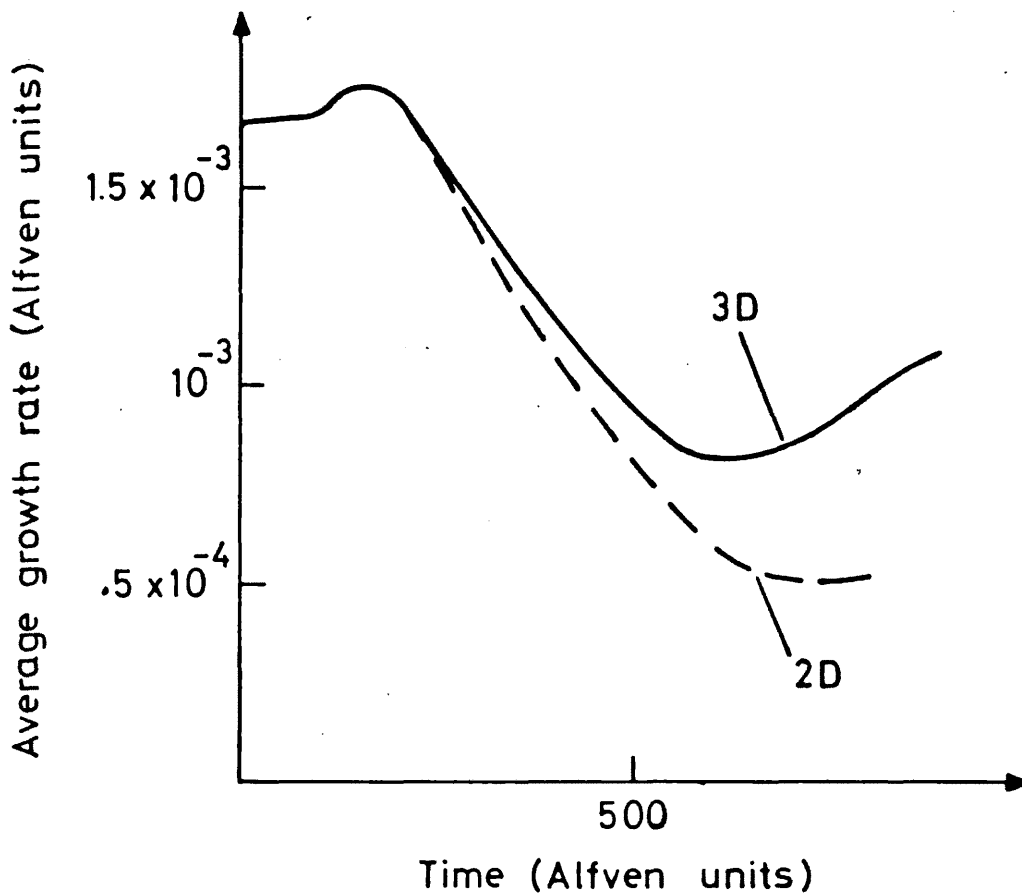


Fig 6.4.2 Comparison of single helicity and mixed helicity average growth rate for  $m=-1$ ,  $nk=1.6$  mode.

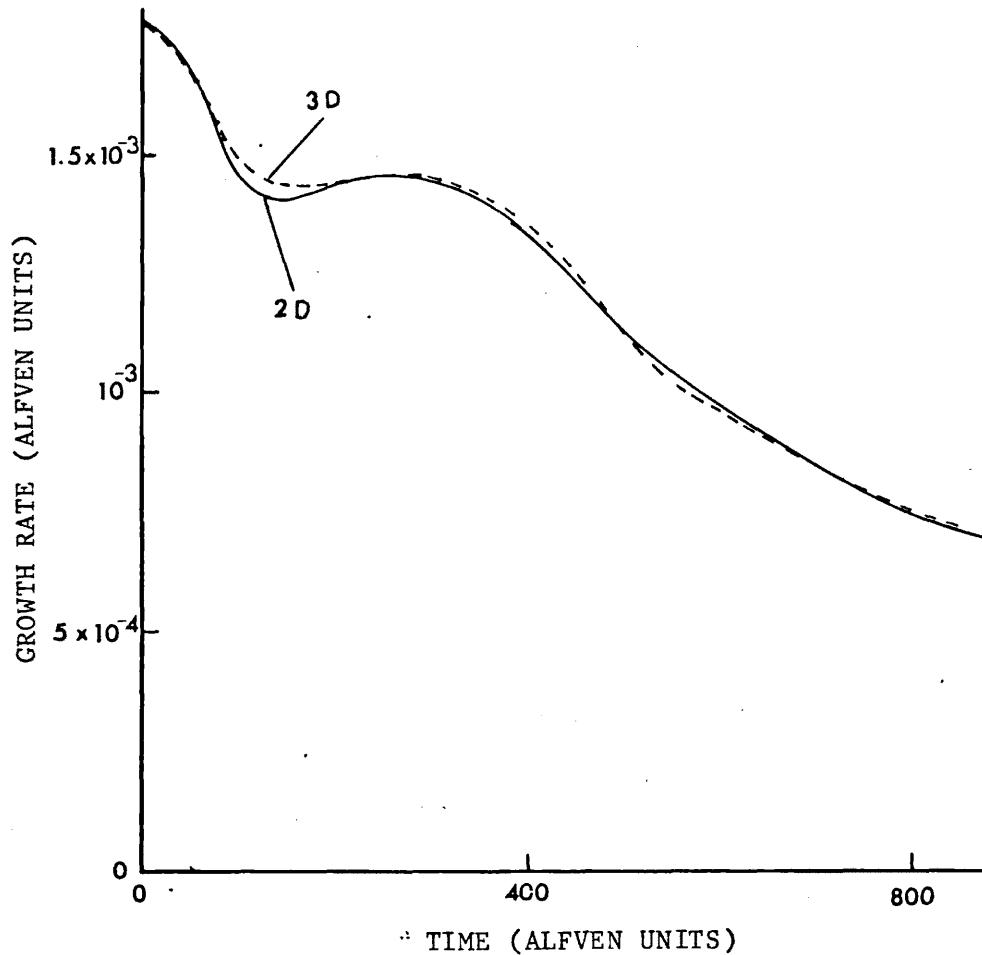


Fig 6.4.3 Comparison of single helicity and mixed helicity average growth rate for  $m=0$ ,  $nk=0.6$  mode.

The two modes which are primed in,  $m=0$ ,  $nk=0.6$  and  $m=-1$ ,  $nk=1.6$  give rise to the normal pressure flattening at their singular surfaces. This effect is shown in fig 6.4.4 where the pressure gradient is plotted for  $t=607 \tau_A$ .

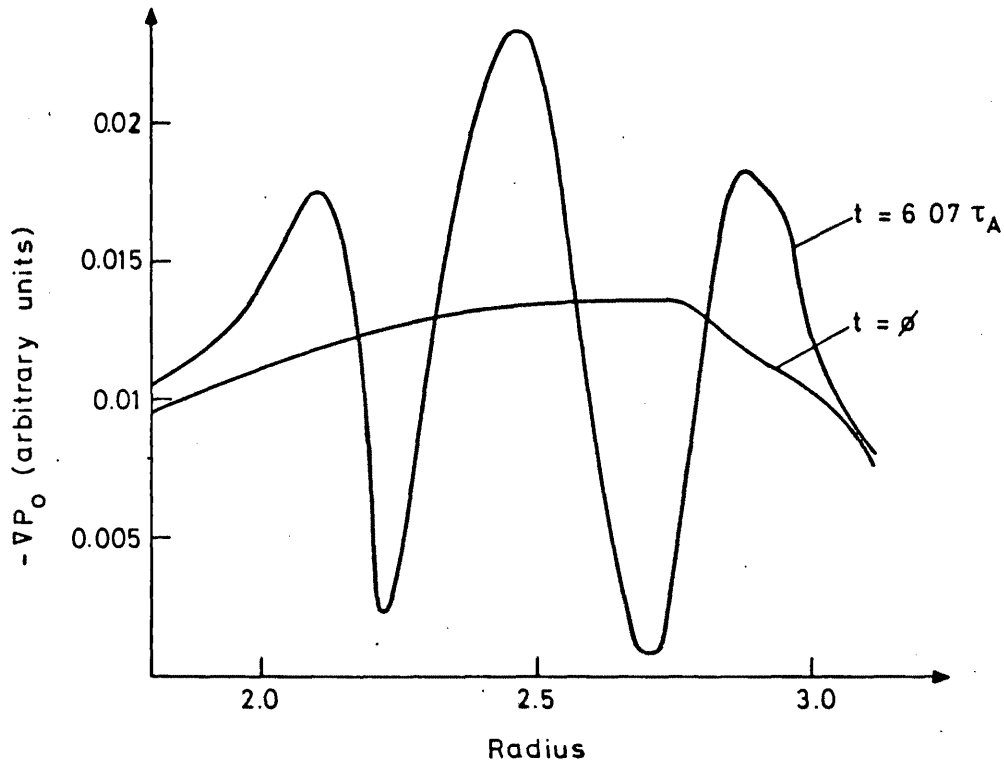


Fig 6.4.4 Nonlinear development of pressure gradient for mixed helicity run.

As will be discussed in the next section, when islands of differing helicity touch, ergodic behaviour occurs. Fig 6.4.5 shows the intersections of field lines with the  $r, z$  plane at the start ( $t=0$ ) and end ( $t=880\tau_A$ ) of this mixed helicity simulation (for clarity only the region between  $z=0$  and  $\pi/k$  is plotted). These results are obtained using a field line tracing code, which is also discussed in the next section, and each different symbol plotted represents a distinct field line. At the start of the calculation the three  $m=0$  islands occurring about  $r=2.66$  are clearly visible whilst the eight  $m=1$  islands occurring about  $r=2.23$  may be just distinguished. Also it is evident that closed flux surfaces exist between the  $m=0$  and  $m=1$  modes at  $t=0$ . However at the end of the calculation ( $t=880\tau_A$ ) one field line can be seen to ergodically traverse the entire region. This stochastic behaviour gives rise to greatly enhanced radial electron transport and will be discussed in detail in the next section.

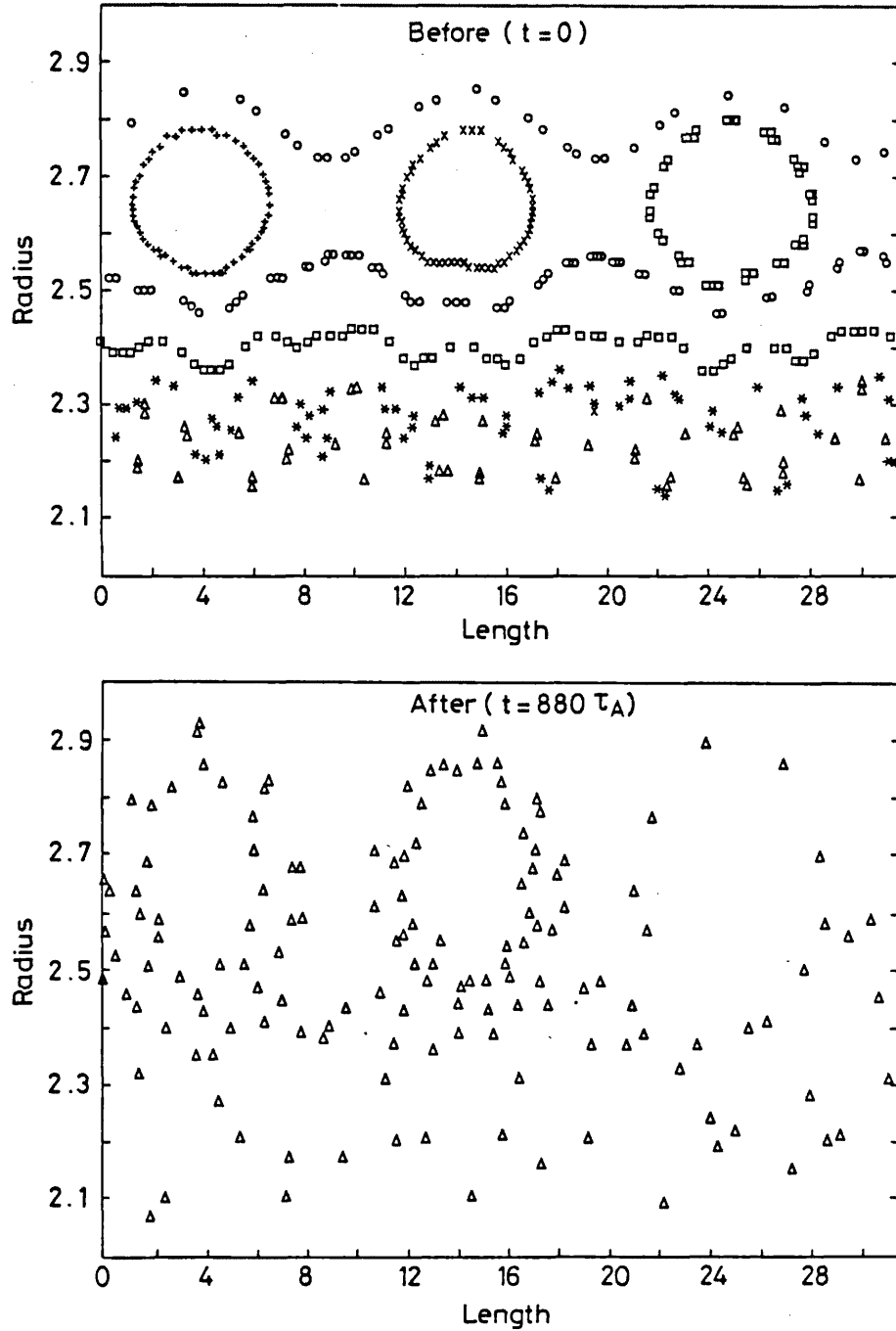


Fig 6.4.5 Field line intersections with  $r,z$  plane for mixed helicity run at  $t=0$  and  $t=880 \tau_A$ .



## 6.5 ERGODICITY

The majority of studies in this section have involved the use of a field line tracing code which is discussed in section 6.5.1. The basic nature of ergodity and its occurrence in the reverse field pinch are examined in section 6.5.2 and finally possible explanations for some experimental results are given in section 6.5.3.

### 6.5.1 THE FIELD LINE TRACING CODE

The field line tracing code used is a modified version of the Culham code TORFLD [56]. As the name implies TORFLD is designed to follow field lines in toroidal geometry, whereas for the present application it was required to follow field lines in a periodic cylindrical system. To achieve this the variables in the cylindrical co-ordinates  $r, \theta, z$ , are converted into cartesian  $x, y, z$ . The problem then reduces to solving the field line trajectory equations

$$\frac{dx}{dS} = \frac{B_x}{|B|}, \quad \frac{dy}{dS} = \frac{B_y}{|B|}, \quad \frac{dz}{dS} = \frac{B_z}{|B|},$$

where  $S$ , the independent variable, is distance along the field line. These equations are integrated using an eighth order accurate method given by Butcher [57]. The output from this code is most conveniently given in graphical form showing the intersections of the field line being followed with a particular plane. In considering field line behaviour near the field reversal point ( $B_z=0$ ) it is most informative to plot field line intersections with an  $r,z$  plane ( $\theta=\text{constant}$ ). Such a representation is used for all field line plots given in this chapter.

### 6.5.2 ERGODIC BEHAVIOUR IN THE RFP

Ergodic field line behaviour occurs when two or more islands of differing helicity overlap. Defining the quantity  $\lambda$  by

$$\lambda = \frac{1}{2} \frac{W_{m,n} + W_{m',n'}}{|r_{m,n} - r_{m',n'}|} \quad 6.5.1$$

where  $W_{m,n}$  is the width of the  $m,n$  island and  $r_{m,n}, r_{m',n'}$  are two neighbouring rational surfaces, ergodicity is found for  $\lambda \geq 1$  [58]. To verify this numerically the interaction of an  $m=0, n=1$  and an  $m=-1, n=4$  set of islands was examined. Fig 6.5.1 shows the field line intersections with the  $r,z$  plane for  $\lambda=0.79, 1.0,$  and  $1.14$  (from top to bottom). The  $m=0$  island is clearly visible in all three cases, whilst the  $m=1$  islands are most easily distinguished for the  $\lambda=1.0$  case (fig 6.5.1(b)). For the  $\lambda=0.79$  case (fig 6.5.1(a)) a closed flux surface denoted by 'x' is clearly evident between the  $m=0$  and  $m=1$  islands. For the  $\lambda=1.0$  case (fig 6.5.1(b)) the flux surface between the  $m=0$  and  $m=1$  islands has been destroyed, whilst for the  $\lambda=1.14$  case (fig 6.5.1(c)) all the  $m=1$  surfaces have been destroyed. Thus the onset of ergodicity when  $\lambda \approx 1$  has been verified.

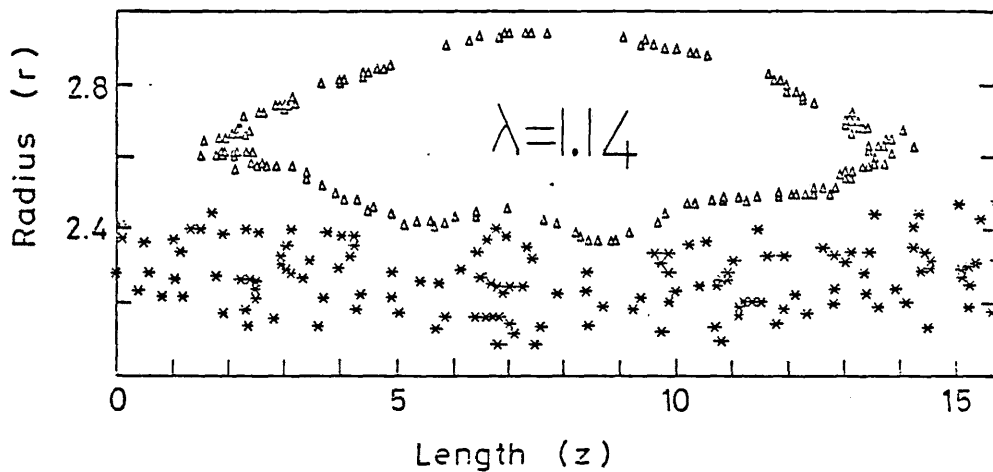
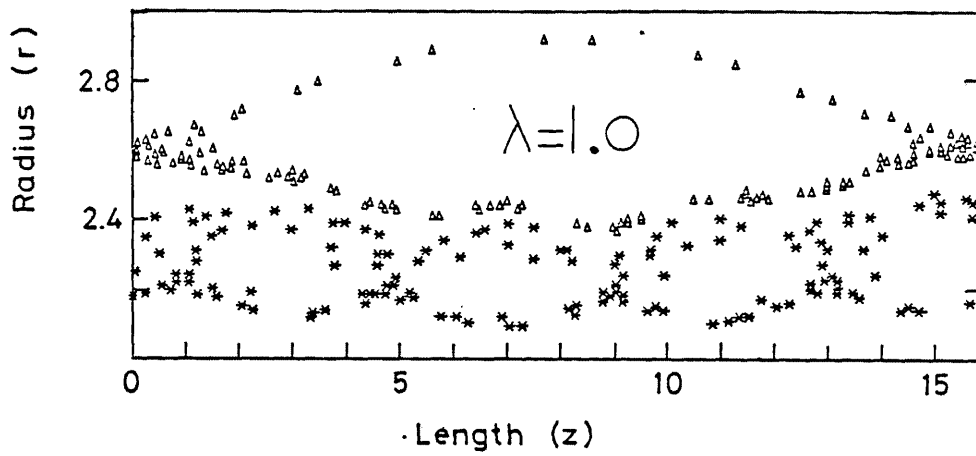
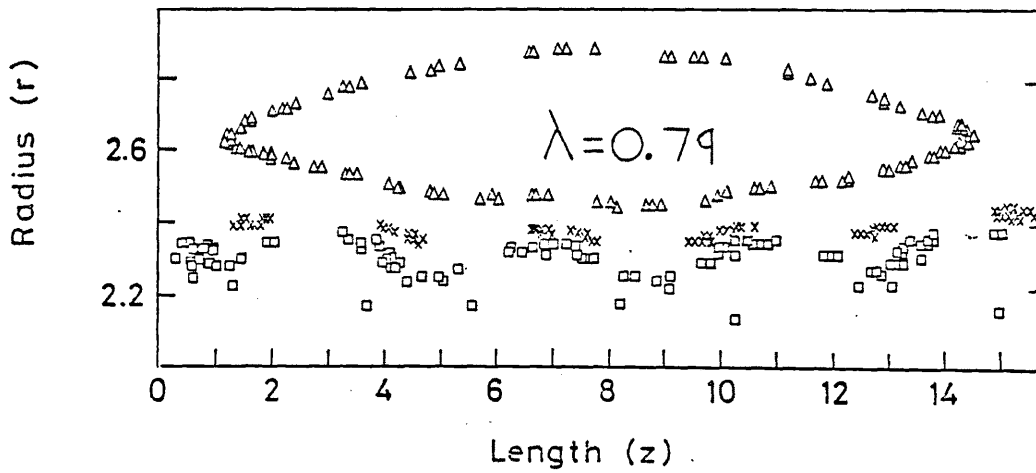


Fig 6.5.1 (a),(b),(c) Interaction of two differing helicities illustrating the onset of ergodic behaviour when  $\lambda$  exceeds approximately 1.

The width of a magnetic island is given by (section 2.4.1)

$$4 \left( \frac{r}{m} \frac{B_r}{B_\theta} \left| \frac{d\mu}{dr} \right| \right)^{\frac{1}{2}} \quad (m \neq 0) \quad 6.5.2$$

whilst the distance between two neighbouring rational surfaces of toroidal mode numbers  $n_1$  and  $n_1+1$ , and poloidal mode number  $m_1$  is

$$\frac{m_1 \left( \frac{1}{n_1} - \frac{1}{n_1+1} \right)}{k \left| \frac{d\mu}{dr} \right|} \quad 6.5.3$$

where  $\mu = rB_z/B_\theta$  is the pitch of the equilibrium field. Using eqns 6.5.2 and 6.5.3 together with the condition that neighbouring islands of poloidal mode number  $m_1$  do not touch (ie  $\lambda < 1$ ), yields the inequality

$$m_1^3 \frac{\left( \frac{1}{n_1} - \frac{1}{n_1+1} \right)^2}{16K^2 \mu r} > \frac{B_r}{B_\theta} \quad 6.5.4$$

The bound imposed by this inequality for the tearing mode stable equilibrium with  $m=1$  and an aspect ratio  $a/R = \frac{1}{4}$  (ie.  $k=0.07$ ) is shown in fig 6.5.2. Also plotted in this figure is the magnitude that  $B_r/B_\theta$  must attain before appreciable quasi-linear pressure flattening will occur for a magnetic Reynolds number,  $S=10^4$ , and a central beta of 5%. It can be seen particularly in the vicinity of the field reversal point ( $r=2.66$ ) that several orders of magnitude difference exist between the two curves. Hence for contemporary reverse field pinches the g mode is still in its linear phase when it precipitates ergodic behaviour.

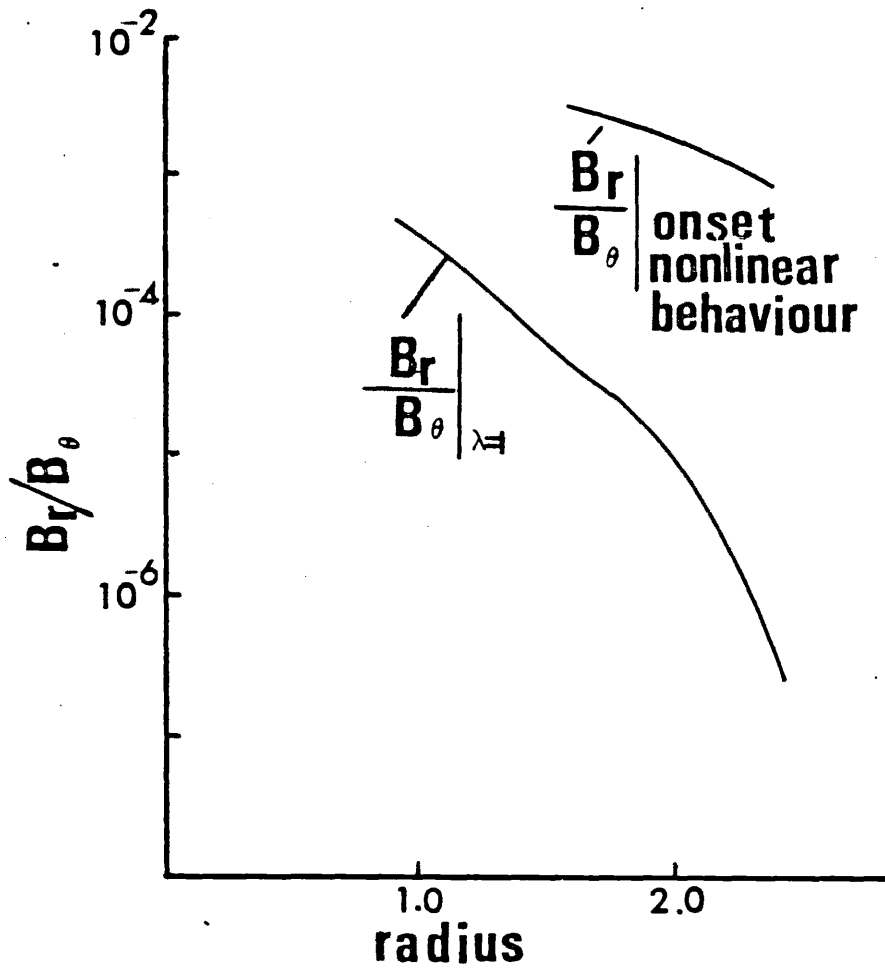


Fig 6.5.2 Bound imposed by eqn 6.5.4 and typical saturation width for  $m=1$  mode at  $S=10^4$ ,  $\beta_0=5\%$ .

The above considerations are optimistic in that they consider only the  $m=1$  modes. In practice even at a modest magnetic Reynolds number,  $S=10^4$  and a central beta of 5%, the  $m=2$  and  $m=3$  modes are unstable in the core. Fig 6.5.3 shows the linear growth rates (resistive units) as a function of  $-nk/m$  for this case. The region  $-nk/m=0.5$  to 1.0 corresponds to modes with singular surfaces near  $r=0$  which are unstable but are numerically very difficult to resolve. Fig 6.5.4 shows the variation of singular surface radius with  $-nk/m$ . Reference to figs 6.5.3 and 6.5.4 shows that for  $S=10^4$  and  $\beta_0=5\%$ , almost the entire core region is unstable.

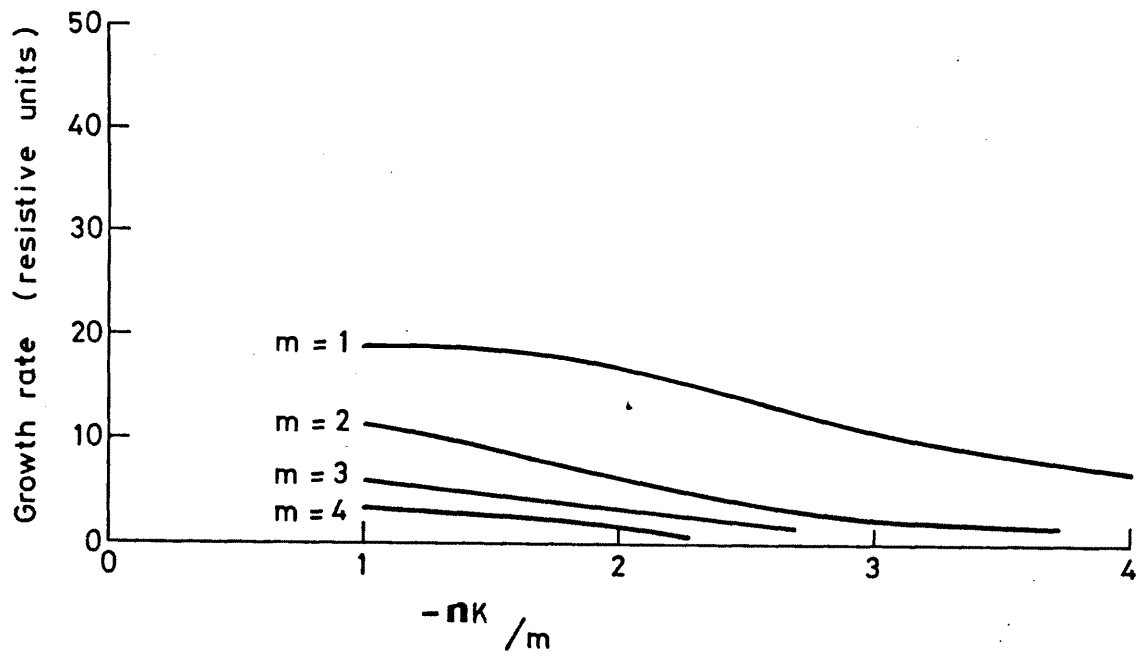


Fig 6.5.3 Variation of linear growth rate with  $-nk/m$ .

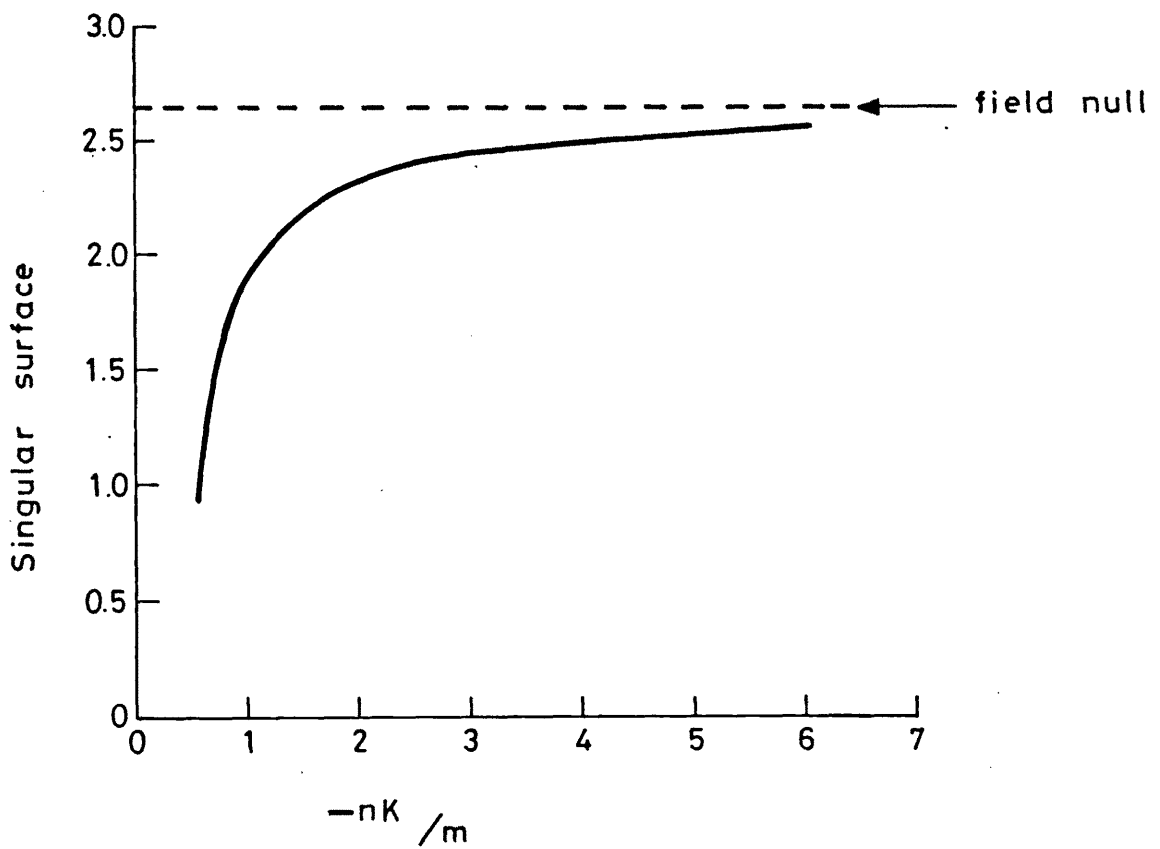


Fig 6.5.4 Singular surface position as a function of  $-nk/m$ .

To avoid ergodicity some nonlinear process will have to halt the rapid linear g mode growth before the islands of various helicities touch. In fact it is known from the results in this chapter and those of chapter 4 that the g mode does not saturate completely. However it is certainly sufficient to use the scalings for  $B_r$  at the onset of nonlinear behaviour to demonstrate that ergodicity occurs in the RFP, since such scalings represent an optimistic view of the  $B_r$  scalings. Also it is known from the results given in chapter 4 that the island width at the onset of nonlinear behaviour scales as the resistive layer width. Hence the philosophy adopted in all scaling arguments to determine whether ergodicity occurs is that the island widths scale as their resistive layer widths.

It is evident from examining fig 6.5.2 that the  $B_r/B_\theta$  at the onset of nonlinear behaviour exceeds the  $B_r/B_\theta$  required to give  $\lambda=1$  by at least 100 over a large region of the core for  $S=10^4$  and a central beta of 5%. Now from chapter 4 it is known that  $B_r$  at the onset of nonlinear behaviour scales as  $S^{-0.38}$  so to render the  $B_r/B_\theta$  at the onset of nonlinear behaviour equal in magnitude to the  $B_r/B_\theta$  for  $\lambda=1$  would require  $S > 1.8 \times 10^9$ . This estimate is optimistic because only the overlap of the  $m=1$  modes has been considered, whereas in practice many other poloidal mode numbers are unstable. Fig 6.5.5 shows the linear growth rates (resistive units) of g modes with  $m=1$  to 7 at a point within the field null, whose singular surface is given by  $nk/m=-2$  for an equilibrium central  $\beta_0$  of 5%.

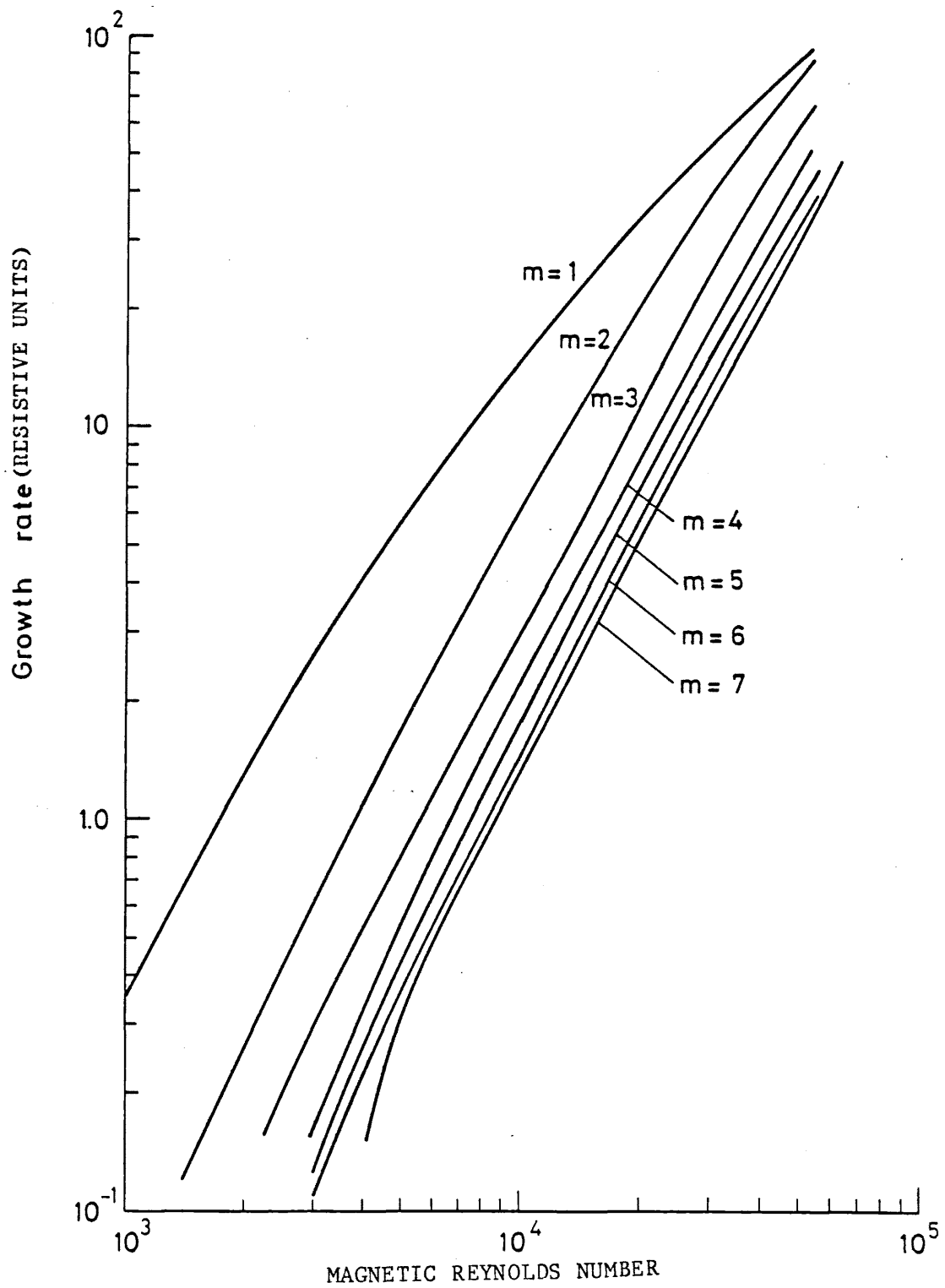


Fig 6.5.5 Linear growth rates for  $m=1$  to 7 and  $nk/m=-2$  as a function of magnetic Reynolds number.



Examining fig 6.5.5 it is evident that increasingly high poloidal mode numbers are destabilised in the core as the magnetic Reynolds number increases. Although it is likely that finite Larmor radius effects will eventually limit the unstable poloidal mode numbers [59].

To quantify the ergodic behaviour with varying  $m$  it is necessary to make some assumption about the variation of  $B_r$  with  $m$ . It is assumed that  $B_r$  is invariant of  $m$  at a given helicity, an assumption which will be discussed later. Now the number of rational surfaces increases as  $\pi m^2/9$  for  $m > 2$  [60]. So considering two neighbouring  $m=1$  surfaces  $r_{1,n}$ ,  $r_{1,n+1}$ , if  $T_s$  is the total number of surfaces between these limits and  $M$  is the maximum unstable poloidal mode number, the number of rational surfaces with poloidal mode number  $m_2$  ( $1 \leq m_2 \leq M$ ) is given by

$$\left(\frac{T_s}{\pi M^2}\right) \left(\frac{\pi}{9} m_2^2 - \frac{\pi}{9} (m_2 - 1)^2\right) = \frac{T_s}{M^2} (2m_2 - 1) = a(2m_2 - 1) \quad 6.5.5$$

Since  $T_s \propto M^2$  and therefore  $T_s = aM^2$ .

Hence the distance occupied by the islands with poloidal mode number  $m_2$ , between  $r_{1,n}$  and  $r_{1,n+1}$  is given by

$$a(2m_2 - 1) \left( \frac{1}{2} \frac{(r_{1,n} + r_{1,n+1})}{m_2} \frac{B_r}{B_\theta} \left| \frac{\mu}{\mu'} \right| \right)^{\frac{1}{2}} \quad 6.5.6$$

So the condition that  $\lambda < 1$  in this region is

$$r_{1,n+1} - r_{1,n} > \frac{4a}{\sqrt{2}} \sum_{m_2=1}^M \left( \frac{B_r}{B_\theta} \left| \frac{\mu}{\mu'} \right| (r_{1,n} + r_{1,n+1}) \right)^{\frac{1}{2}} \left( 2m_2^{\frac{1}{2}} - \frac{1}{m_2^{\frac{1}{2}}} \right)$$

or

$$\frac{B_r}{B_\theta} < \left| \frac{\mu'}{\mu} \right| \frac{1}{8a^2} \frac{(r_{1,n+1} - r_{1,n})^2}{(r_{1,n} + r_{1,n+1})} \frac{1}{\left( \sum_{m_2=1}^M \left( 2m_2^{\frac{1}{2}} - \frac{1}{m_2^{\frac{1}{2}}} \right) \right)^2} \quad 6.5.7$$

Evaluating the sum  $\sum_{m=1}^M \left( 2m^{\frac{1}{2}} - \frac{1}{m^{\frac{1}{2}}} \right)$  numerically

shows it to increase at least as fast as  $M^{+0.55}$  for  $M < 30$ . To examine whether the ergodic behaviour becomes better or worse with  $S$  it is necessary to understand the variation of the various quantities in eqn 6.5.7 with  $S$  :-

(i) A scaling of maximum unstable poloidal mode number with  $S$  may be inferred from fig 6.5.5. A plot of  $m$  against the  $S$  at which it attains a growth of 0.4 is given in fig 6.5.6 for the case  $-nk/m=2$ . Also plotted in this figure is the curve for modes outside the field null with  $nk/m=1$  and  $\beta_0=10\%$  when they attain a growth of 1.0. Since below a certain growth rate the modes will not be significant these curves may be interpreted as giving the scaling of maximum unstable poloidal mode number with  $S$ . The scaling given by these curves is  $M \propto S^{0.72}$  for low  $M$  numbers.

(ii) The scaling of  $B_r/B_\theta$  as  $S^{-0.38}$  has already been explained above.

It is also necessary to justify the assumption that  $B_r$  is invariant of  $m$  at a given helicity. Again the philosophy explained above, that at

best  $B_r$  will scale as the layer width is used. It is found numerically that the layer width at a given helicity varies as  $m^{-0.5}$  and since the layer width at the onset of nonlinear behaviour scales as the island width (chapter 4) this implies that  $B_r$  is invariant of  $m$  because the island width formula (eqn 6.5.2) also contains an  $m^{-0.5}$ . Applying these  $S$  scalings to eqn 6.5.7 shows the LHS to decrease as  $S^{-0.38}$  whilst the RHS decreases as  $S^{-0.79}$ , hence ergodicity will always occur in the pinch.

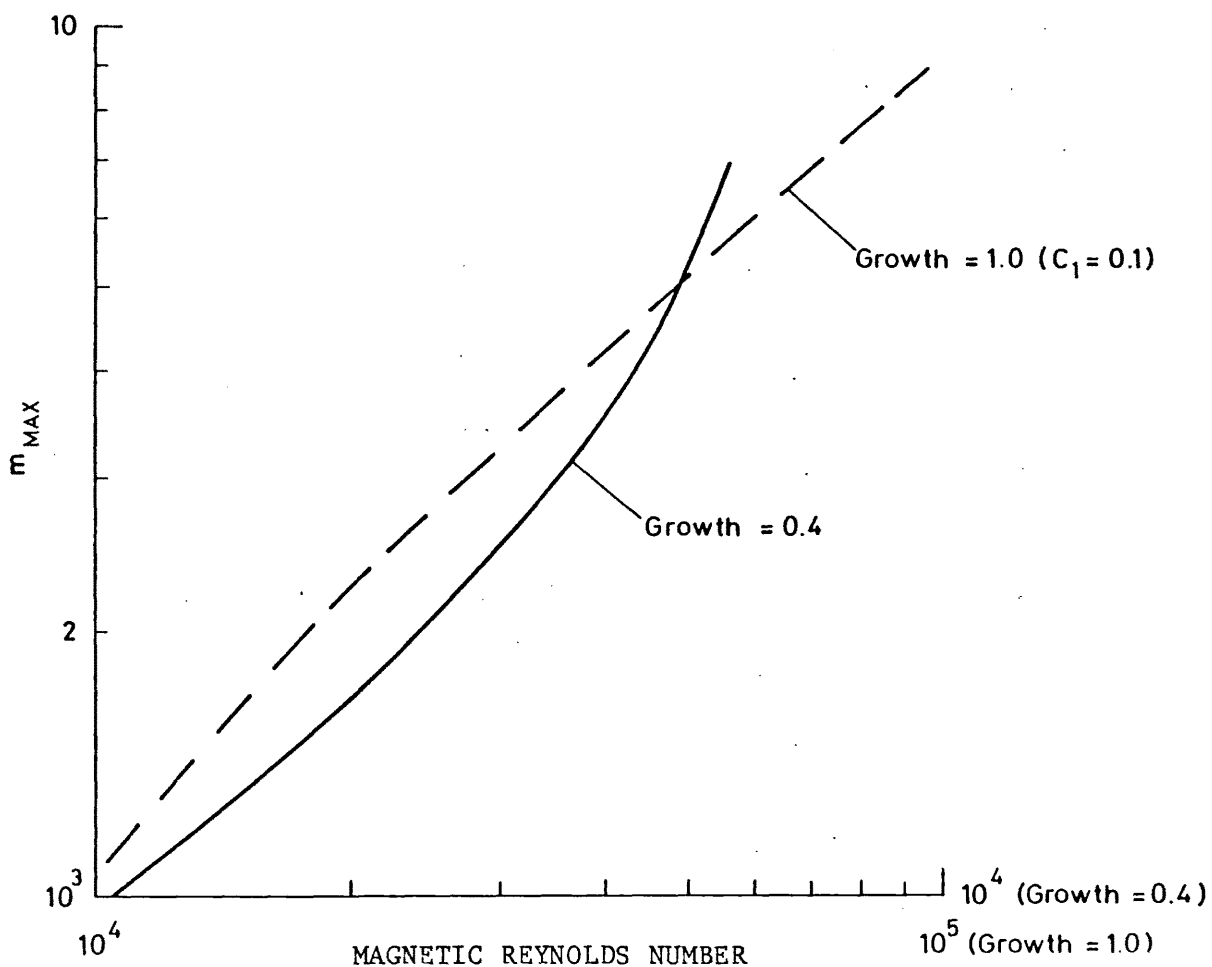


Fig 6.5.6 Value of magnetic Reynolds number at which given poloidal mode number attains indicated growth rate (in resistive units).

To study the relationship of this theory to experimental situations requires a knowledge of the effects of ergodicity on the perpendicular electron transport. This topic has been studied in some detail by Rechester and Rosenbluth [61], and their results will now be reviewed.

The ergodic behaviour may be quantified in terms of a diffusion coefficient,  $D_{st}$ , for the field lines [62]

$$D_{st} = \frac{\text{Mean square radial displacement of field line}}{2 \times \text{dist. travelled along field line}} \quad 6.5.8$$

The enhanced electron diffusion which this field line diffusion causes is governed by whether the plasma is in the collisional or collisionless regime. A collisionless plasma, with respect to ergodicity, is defined as one for which the electron mean free path,  $\delta$ , is greater than the characteristic length over which neighbouring field lines diverge from each other,  $L_c$ . Formally the correlation length,  $L_c$  is defined as

$$1/L_c = \lim_{\ell \rightarrow \infty} \lim_{d(0) \rightarrow 0} \left( \frac{1}{\ell} \log_e \frac{d(\ell)}{d(0)} \right) \quad 6.5.9$$

where  $d(\ell)$  is the distance between two field lines as a function of the distance travelled along them,  $\ell$ . As the name implies in the collisionless regime collisions are unimportant because the electron is displaced a significant radial (perpendicular) distance between collisions by the ergodic wandering of the field lines. Hence the enhanced electron diffusion in the collisionless regime is simply governed by the velocity at which electrons travel along the field lines. The enhanced electron diffusion,  $\chi_{\perp \text{eff}}$ , is thus

$$\chi_{\perp \text{eff}} = D_{st} v_{\parallel} \quad 6.5.10$$

where  $v_{\parallel}$  is the parallel electron thermal velocity. In the collisional

regime the role of the collisions must be taken into account. The collisions themselves give rise to radial transport but they also inhibit the passage of electrons along the field lines. Rechester and Rosenbluth give the following formula for the enhanced electron transport in the collisional regime [61] :-

$$\chi_{\text{leff}} = D_{\text{st}} \chi_{\parallel} / \left( L_c \log_e \left( (r/mL_c) \left( \frac{\chi_{\parallel}}{\chi_{\perp}} \right)^{\frac{1}{2}} \right) \right) \quad \delta \ll L_c \quad 6.5.11$$

where  $\chi_{\parallel}$  is the parallel electron conductivity,  $\chi_{\perp}$  is the perpendicular electron conductivity and  $m$  is the poloidal mode number. Transition regimes have been identified by various authors for the region where  $\delta \cong L_c$  [63].

### 6.5.3 ERGODICITY AND EXPERIMENT

Some typical results from the Culham reverse field pinch experiment, HBTX1A [64], will now be presented.

Fig 6.5.7 shows the average electron number density [65]. This shows two distinct features :-

(i) A rapid decrease in density between  $t=0.5\text{mS}$  and  $1.25\text{mS}$ . This phenomenon is known as pump out.

(ii) A quieter period during which the density decreases less rapidly between  $t=1.25\text{mS}$  and  $2.0\text{mS}$ . This part of the discharge is known as the quiescent phase.

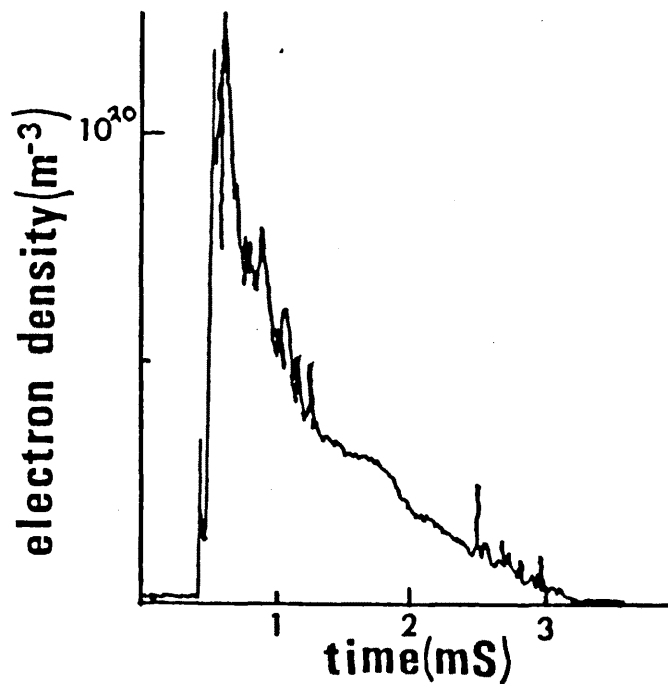


Fig 6.5.7 Average line of sight electron density for shot of HBTX1A.

Figs 6.5.8 and 6.5.9 show respectively, the total toroidal current and electron temperature for the same shot of HBTX1A [65]. The electron temperature is derived from the resistance using the assumptions that  $Z_{\text{eff}}=2$  and the Coulomb logarithm is 13. The electron energy confinement time for this shot during the quiescent phase is approximately  $80 \mu\text{s}$ .

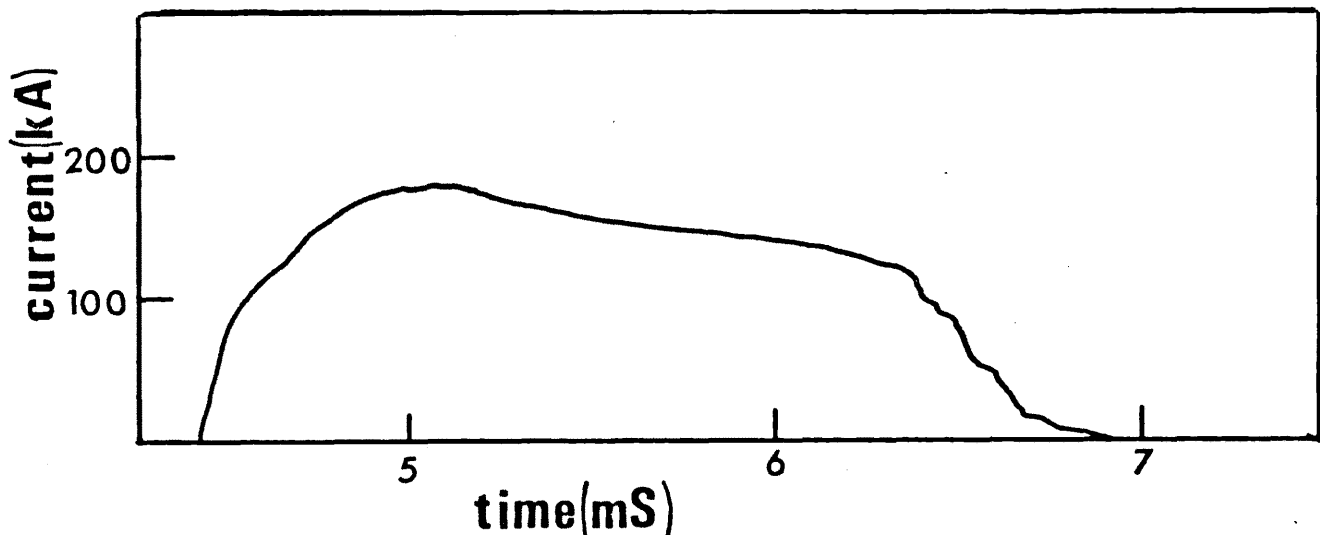


Fig 6.5.8 Toroidal current for typical shot of HBTX1A.

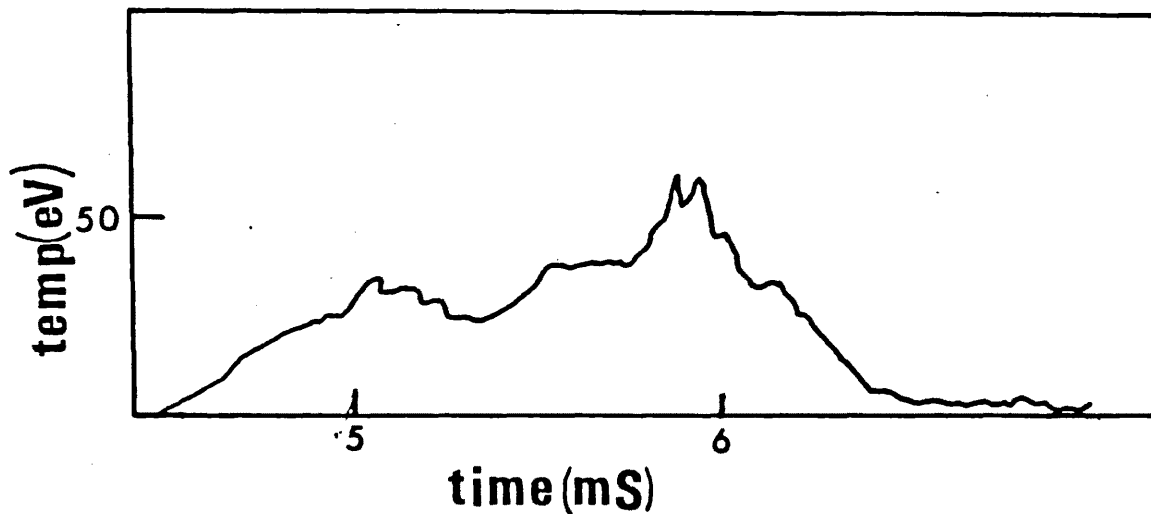


Fig 6.5.9 Electron temperature derived from resistance for same shot as Fig 6.5.8.

To relate the g mode and ergodicity theory of this thesis to the above experimental observations the effect of perturbing the TMS equilibrium with a series of g modes has been examined. For the TMS model with an axial wavenumber,  $k=0.07$ , which corresponds to an aspect ratio of  $a/R=1/4$ , there are at least 50 unstable  $m=1$  modes of distinct helicities and nearly as many  $m=2$  and 3 modes. It would obviously be a huge task to try and include all 150 modes in a field line tracing calculation and would also require prohibitive amounts of computer time and disc space. Therefore in the calculation presented here the number of modes is severely limited by including only the  $m=1$  modes in the core and also by choosing  $k=0.2$  (which corresponds to an aspect ratio  $a/R=1./1.31$ ). Hence the results presented in this section should be regarded as giving qualitative explanations of RFP behaviour. Quantitatively the results will be optimistic because far too few modes have been included.

The linear eigenfunctions used to perturb the TMS model and their magnitudes are given in Table 6.5.1. These magnitudes are chosen as "typical widths" at which significant nonlinear behaviour occurs for an ohmically heated case with  $S=10^4$  and  $\beta_0=5\%$ . Since the ergodicity gives rise to energy losses it is possible that it may be more consistent to include the modes at the slightly smaller "typical widths" of a non ohmically heated case. To establish whether or not this view is correct will require a detailed study of the interaction of the g modes and enhanced transport they produce. In any case the effect of including the modes at slightly too large a magnitude is more than offset by the limited number of modes included.

m	$nK_z$	Singular Radius	$\left. \frac{B_r}{ B } \right _{r=\text{Singular Radius}}$
- 1	2	2.32	0.14%
- 1	1.8	2.27	0.17%
- 1	1.6	2.22	0.21%
- 1	1.4	2.15	0.27%
- 1	1.2	2.07	0.35%
- 1	1.0	1.92	0.46%
- 1	0.8	1.67	0.51%
0	0.4	2.66	0.28%

Table 6.5.1  $B_r/B$  perturbations to TMS model for fig 6.5.10

The intersection of the field lines with the  $r,z$  plane are shown in fig 6.5.10. The two  $m=0$  islands bounded by a closed flux surface at  $r=3.0$  are clearly visible. In the core however the  $m=1$  surfaces have been totally destroyed as can be seen from the field lines which wander



ergodically. In this ergodic region a field line diffusion coefficient may be estimated. Fig 6.5.11 shows the order of intersections with  $r, z$  of an ergodic field line whose start co-ordinate is  $r=2.2, z=1.5, \theta=0$ . Analysing a large number of such field line trajectories with varying start co-ordinates gives an average value for  $D_{st}$

$$D_{st} = 4.9 \times 10^{-4} \quad 6.5.12$$

It must be remembered that  $D_{st}$  is dimensional and its magnitude is therefore dependent on the normalisations of the TMS model. For HBTX1A which has a minor radius of 26 cm

$$D_{st} = 3.3 \times 10^{-3} \text{ cm}$$

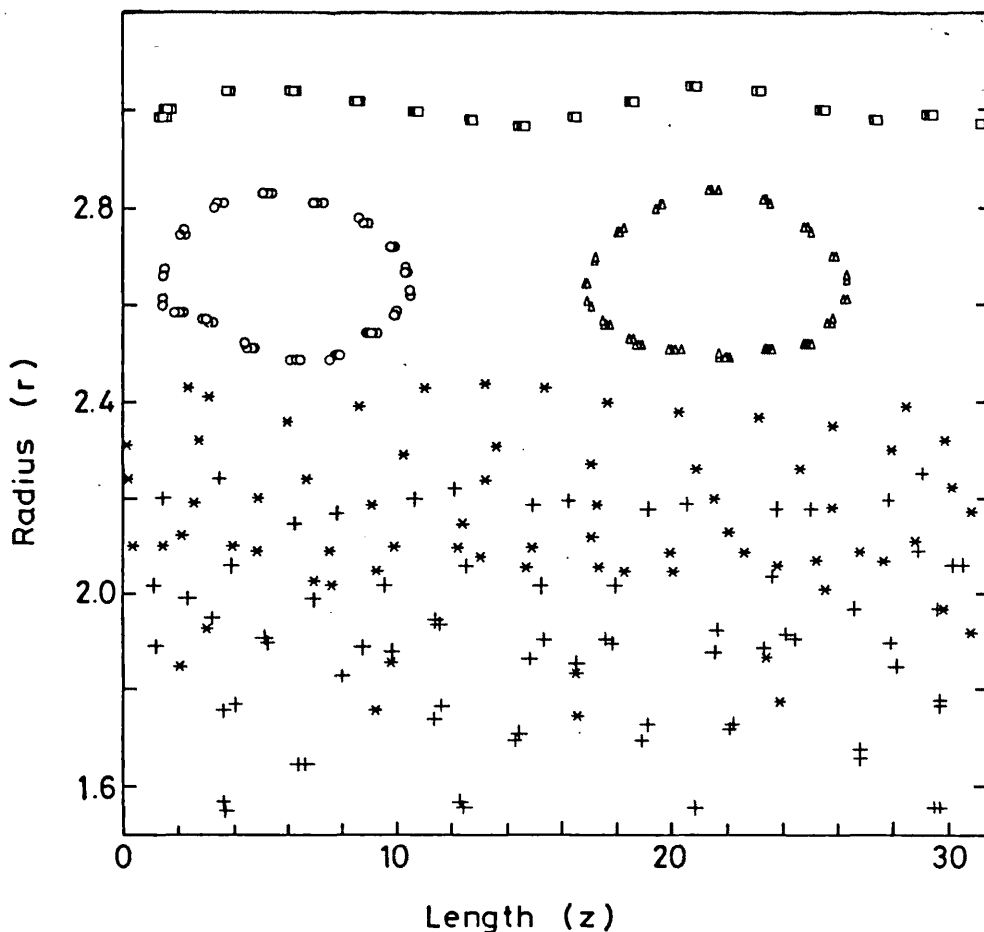


Fig 6.5.10 Field line intersections with the  $r, z$  plane for TMS model perturbed by fields in Table 6.5.1.

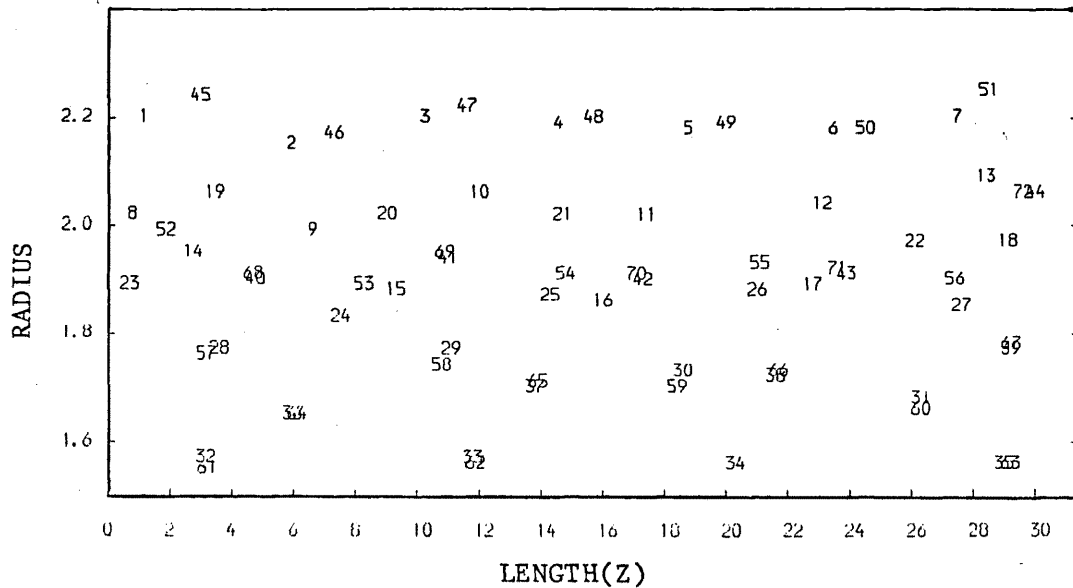


Fig 6.5.11 Order of intersections of a field line with the r,z plane for same case as Fig 6.5.10.

For a machine with the dimensions of HBTX1A and  $n = 3 \times 10^{13} \text{ cm}^{-3}$  and  $T = 60 \text{ eV}$  the parallel electron thermal velocity is  $2.64 \times 10^8 \text{ cms}^{-1}$  and hence in the collisionless limit (eqn 6.5.10)

$$\chi_{\perp \text{eff}} = 8.7 \times 10^5 \text{ cm}^2 \text{ s}^{-1}$$

Using the Rechester and Rosenbluth expression for the correlation length,  $L_c$  [66]

$$L_c = 2.8 \times \left( \frac{\mu^2}{a\mu} \right)^{2/3} \left/ \left( \frac{\pi R}{a^2} \sum_{m,n} |m b_{r_{m,n}}|^2 \delta \left( n + \frac{m}{k\mu} \right) \right)^{1/3} \right. \quad 6.5.13$$

(where  $\mu$  is the pitch (section 4.2) and "a" is the plasma minor radius) it is found that  $L_c = 60 \text{ cm}$  for HBTX1A. Hence in the collisional limit (eqn 6.5.11)

$$\chi_{\perp \text{eff}} = 4.7 \times 10^5 \text{ cm}^2 \text{ s}^{-1}$$

It must be remembered that these formulae for  $\chi_{\perp \text{eff}}$  are dimensional and relate to a machine with a minor radius of 26 cm.

Assuming a Bessel function model the energy confinement time is given by [67]

$$\tau_E = \frac{a^2}{5.8 \chi_{\perp \text{eff}}}$$

For the Culham RFP experiment HBTX1A, this gives

$$\tau_E = \begin{cases} 130 \mu\text{s} & \text{(collisionless)} \\ 248 \mu\text{s} & \text{(collisional)} \end{cases}$$

The mean free path for HBTX1A with  $n=3 \times 10^{13} \text{cm}^{-3}$  and  $T=60 \text{eV}$  is approximately 40 cm. Hence  $L_c \sim \delta$  in this case and so the collisional and collisionless values are of the same magnitude.

This ergodic theory may also account for the particle confinement times in the RFP and the phenomenon of pump out. Particle losses require that the ions also move along the field lines. But the ion velocity is limited to some fraction of the ion sound speed, by the development of shocks if the ions try to exceed the sound speed. Also it must be remembered that the ion Larmor radius is much larger than that of an electron at the same temperature. The effect of a large Larmor orbit is to average out the fine scale ergodic behaviour and so particles with large gyroradii are much less affected by ergodicity. However it is likely in contemporary RFP's that the equipartition time is such that the ions remain much colder than the electrons and their gyroradii therefore remain small.

Examining the field line tracing results relating to the perturbed fields given in Table 6.5.1 and assuming the same degree of ergodicity to exist across the entire pinch, shows that on average a field line requires 82 transits to move from  $r=0$  to the wall. Hence for HBTX1A a

rough estimate of the transit time of an ion from the centre to the wall is

$$\frac{\text{Dist travelled}}{V_c} = 82 \times \frac{((26\pi)^2 + (80\pi)^2)^{\frac{1}{2}}}{V_c} = 1.5 \text{ ms}$$

where  $V_c$  is the ion sound speed and the electron temperature is taken to be 100eV. During the pump out phase the observed fluctuations are much greater than those given in table 6.5.1 and so the particle loss rate which scales as the square of the fluctuation level [61], will be correspondingly higher. Hence this theory accounts for the very rapid particle loss rates during pump out and the somewhat slower loss rates during quiescence.

## 6.6 CONCLUSIONS

It has been shown that including the effects of compressibility does not alter the nonlinear mechanisms given in chapter 4, for the  $m=0$  g mode. Simulating an energy loss process by removing the ohmic heating terms has been shown to make a disappointingly small improvement to the final nonlinear growth rate of the  $m=0$  g mode. This is because resistive diffusion of the magnetic fields still causes the Suydam driving term to increase to either side of the g modes rational surface.

The  $m=1$  g mode in the core, has also been examined and is found to possess the same nonlinear behaviour as the  $m=0$  g mode.

The mixed helicity interaction between an  $m=0$  mode and a nearby  $m=1$  mode in the core has been shown to cause the "cross talk" harmonic to grow very rapidly. This rapid growth in turn destabilises the  $m=1$  mode in the core. The interaction of these rapidly growing modes, of differing helicities, is shown to give rise to ergodic field line behaviour.

A criterion for the onset of ergodic behaviour is given and using this it is proven that ergodic behaviour will always occur in the reverse field pinch. The relationship between this ergodic behaviour and enhanced electron transport is explained in terms of the theory given by Rechester and Rosenbluth [61]. This theory is shown to be capable of explaining the energy confinement times found in contemporary reverse field pinch experiments. Finally an explanation for the phenomenon of pump out, due to ergodic field line behaviour, has been given.

7.1 SUMMARY OF THESIS AND CONCLUSIONS

A primarily numerical investigation has been made of the nonlinear  $g$  mode in the reverse field pinch. Three major computer codes have been developed to aid in this investigation. The first two codes, which are detailed in chapter 3, solve the reduced two dimensional  $m=0$  mode equations. One of the codes solves the full set of reduced  $m=0$  mode equations, whilst the other solves for only the first three Fourier harmonics of the reduced set of equations. Both codes include the resistive diffusion terms implicitly and so avoid excessively strict timestep restrictions. The third and most powerful code developed solves the full set of compressible resistive MHD equations using a spectral Fourier harmonic method. Details of this code are given in chapter 5.

Using these codes an extensive study has been made of the  $m=0$   $g$  mode, which occurs in the RFP about the toroidal field reversal point. A quasi-linear mechanism has been found in which the  $m=0$   $g$  mode acts to flatten the pressure in the vicinity of its singular surface. A scaling argument is given in chapter 4 to explain this mechanism and the variation of its onset with magnetic Reynolds number. This pressure flattening is analogous to the Rutherford tearing mode saturation mechanism, in which the tearing mode saturates by flattening the current gradient in the vicinity of its singular surface.

Unfortunately the potential saturation effects of the pressure flattening are counteracted by ohmic heating and resistive decay of the shear, which both act to increase the Suydam parameter that is the driving term for the g mode. The balance between these competing mechanisms determines the final nonlinear state of the g mode. Another scaling argument is given in chapter 4 to explain this facet of the nonlinear g mode behaviour. Good agreement is found between the predictions this argument gives for the variation of final nonlinear growth rate with magnetic Reynolds number, and those found computationally. Using the spectral Fourier harmonic code an energy loss process has been simulated by removing the ohmic heating terms from the equilibrium pressure equation. The effect of this is to lower the final nonlinear growth rate of the g mode relative to the equivalent ohmically heated case, but a total saturation is still inhibited by resistive decay of the shear. Details of these results are given in chapter 6.

The nonlinear properties of the  $m=1$  g mode are also examined in chapter 6. A comparison is made between an ohmically heated case and a non ohmically heated case, for an  $m=1$  mode which has its singular surface to the inside of the field null. The nonlinear mechanisms which dominate the  $m=0$  mode are also found to apply to the  $m=1$  mode.

As a prelude to a fully three dimensional calculation, the mixed helicity interaction between an  $m=1$  mode, in the core, and an  $m=0$  mode has been examined. Only six modes are included in this simulation since work by the Oak Ridge group has indicated that this is sufficient to give qualitatively correct answers. It is found that mode-mode coupling dominates the mixed helicity interactions with the "cross talk

harmonic" growing very rapidly when its singular surface touches the  $m=1$  mode. This rapid growth has the effect of destabilising the  $m=1$  mode but has a negligible effect on the  $m=0$  mode. Ergodic field line behaviour occurs when these rapidly growing islands of differing helicity overlap. As a result of ergodicity enhanced electron transport occurs and the effects of this on energy containment must be taken into account before a fully self consistent three dimensional calculation can be made.

Finally, in chapter 6, the topic of ergodicity is examined in some detail. The simple resonance overlapping criterion for the onset of ergodicity is verified numerically for magnetic islands in the RFP. Using this criterion and the scalings for the onset of nonlinear g mode behaviour given in chapter 4, it is proven that ergodicity will always occur in the RFP. The theory of Rechester and Rosenbluth is used to quantify the enhanced electron transport which arises due to ergodicity. The energy confinement times associated with this enhanced transport are found to be consistent with contemporary experimental RFP results. The experimental phenomenon of pump out is also explained as a consequence of ergodicity.

## 7.2 FUTURE WORK

The most important effect omitted from the two dimensional nonlinear g mode studies of chapters 4 and 6, is that of parallel thermal conductivity. This would have the effect of enhancing transport around the island flux surfaces and thus flattening the



temperature profile somewhat in the vicinity of the mode. In considering the effect of this on the pressure gradient it must be remembered that it is probable in the RFP that the majority of the pressure gradient is supported by the density gradient. However parallel thermal conductivity would undoubtedly lower the final nonlinear growth rate of the g mode. The reason it has not yet been implemented is because of the numerical difficulties in doing so :-

(i) The parallel thermal conductivity is approximately  $10^7$  times greater than the perpendicular conductivity and so any small numerical errors in including it would erroneously enhance the perpendicular transport.

(ii) The magnitude of the parallel thermal conductivity also produces a much stiffer numerical problem in the RFP, than that imposed by the magnetic Reynolds number timescales. Thus the inclusion of parallel thermal conductivity would probably impose stricter timestep limitations.

A possible solution to these problems is to use a quasi-linear expression for the enhanced radial conductivity due to parallel thermal conductivity. This would overcome the above objections but is not wholly satisfactory because it is only quasi-linear.

The mixed helicity studies of the g mode are obviously far from complete. However before a full simulation of the RFP can be made the enhanced transport processes must be understood in detail. A start has been made in this direction with the study of ergodic transport in the RFP. However it is totally impractical to use the field line tracing

code after every timestep of the mixed helicity code to determine the new transport coefficients. A possible compromise may be to use the field tracing code to provide exact quantitative expressions for the enhanced transport as a function of the number of unstable modes and their magnitudes. If this could be achieved then it should be possible to theoretically predict temperature, density and beta limits in the reverse field pinch.

#### REFERENCES

- [1] J.D. Lawson, Proc. Roy Soc. (London), B70, p6, (1957).
- [2] L.A. Artsimovich, Nucl. Fusion, 12, p215, (1972).
- [3] H.A.B. Bodin and A.A. Newton, Nucl. Fusion, 19, p489, (1979).
- [4] T.H. Stix, Phys. Rev. Lett., 30, p833, (1973).
- [5] B.V. Waddell, B. Carreras, H.R. Hicks, J.A. Holmes, and D.K. Lee, Phys. Rev. Lett., 41, p1386, (1978).
- [6] D.C. Robinson, Controlled Nuclear Fusion and Plasma Physics (Proc. 8th Europ. Conf. Prague), Vol 1, Czechoslovak Academy sciences, p78, (1977).
- [7] D.C. Robinson, Nucl. Fusion, 18, p939, (1978).
- [8] H.R. Hicks, B. Carreras, J.A. Holmes, D.K. Lee, and B.V. Waddell, Oak Ridge Nat. Lab. report ORNL/TM-7132, (1979).
- [9] J.A. Stratton, Electromagnetic theory, (Mc Graw Hill), ppl-6, (1941).
- [10] D.S. Jones, The Theory of Electromagnetism, (Pergamon press), p134, (1941).
- [11] M.G. Haines, Plasma Physics (Notes from Culham Summer School), (Inst. of Physics), p177, (1974).
- [12] S.I. Braginskii, Reviews of Plasma Physics, (Ed. M.A. Leontovich), Consultants Bureau New York, p205, (1965).
- [13] W.M. Tang, Nucl. Fusion, 18, p1089, (1978).
- [14] G. Bateman, MHD Instabilities, (Massachusetts Inst. Tech.), p89, (1978).
- [15] J.W. Connor, R.J. Hastie, and J.B. Taylor, Phys. Rev. Lett., 40, p399, (1979).
- [16] I.B. Bernstein, E.A. Frieman, M.D. Kruskal and R.M. Kulsrud, Proc. Roy. Soc., A244, p17, (1958).
- [17] H.P. Furth, J. Killeen, M.N. Rosenbluth, and B. Coppi, Culham IAEA Conf. 1, ppl03-126, (1965).
- [18] W.A. Newcomb, Annals of Physics, 10, p232, (1960).
- [19] V.D. Shafranov, Zh. Tech. Fiz., 40, p241, (1970).
- [20] B.R. Suydam, Proc. UN Conf. on Peaceful Uses of Atomic Energy, 2nd Geneva, Vol 31, (1958).

- [21] G.A. Sawyer, P.L. Scott, and T.F. Stratton, Phys. Fluids, 2, p47, (1958).
- [22] F.F. Cap, Handbook of Plasma Instabilities, (Academic Press), Vol 1, P287, (1976).
- [23] H.P. Furth, J. Killeen, and M.N. Rosenbluth, Phys Fluids, 6, p459 (1963).
- [24] B. Coppi, J.M. Greene, and J.L. Johnson, Nucl. Fusion, 6, p101, (1966).
- [25] G. Bateman, and R.N. Morris, "Effect of a localised magnetic perturbation on magnetic islands in a cylindrical plasma", Report from School of Nuclear Eng. Georgia Inst. of Tech., (1980).
- [26] J.M. Finn, Nucl. Fusion, 15, p854, (1975).
- [27] P. Lorrain, and D. Corson, Electromagnetic Fields and Waves, (W.H. Freeman and Co.), p477, (1970).
- [28] J.L. Johnson, J.M. Greene, and B. Coppi, Phys. Fluids, 6, p1169, (1963).
- [29] A.H. Glasser, J.M. Greene, and J.L. Johnson, Phys. Fluids, 18, p875, (1975).
- [30] R.J. Hosking, and G.M. Marinoff, Plasma Phys., 15, p327, (1973).
- [31] R.J. Hosking and D.C. Robinson. 9th Euro. Conf, on Controlled Fusion and Plasma Physics, Oxford, BP6, p61, (1979).
- [32] B. Coppi, and M.N. Rosenbluth, Plasma Physics and Controlled Nuclear Fusion Research, Vol. 1, p617, (1966).
- [33] D. Drobott, S.C. Prager, and J.B. Taylor, Phys. Fluids, 20, p1850, (1977).
- [34] P.H. Rutherford, Phys. Fluids, 16, p1903, (1973).
- [35] R.B. White, D.A. Monticello, M.N. Rosenbluth, and B.V. Waddell, Phys. Fluids, 20, p800, (1977).
- [36] B. Carreras, H.R. Hicks, J.A. Holmes, and B.V. Waddell, Oak Ridge Nat. Lab. Report ORNL/TM-7161, (1980).
- [37] D.D. Schnack, J. Killeen, and R.A. Gerwin, Lawrence Livermore Lab. preprint UCRL-84301, (1980).
- [38] J. Dibiase, PhD thesis, Univ. Calif. report UCRL-51591, (1974).
- [39] P. Lorrain and D. Corson, Electromagnetic Fields and Waves, (W.H. Freeman and Co.), p140, (1970).
- [40] D.D. Schnack. PhD Thesis, Univ. of Calif. report UCRL-52399, (1978).
- [41] B.V. Waddell, M.N. Rosenbluth, D.A. Monticello, R.B. White, and B.

- Carreras, (Theoretical and Comp. Plasma Physics ITCP College), p79, (1977).
- [42] G.D. Smith, Numerical Soln. of Partial Diff. Eqns., (Oxford Math. Handbooks), p6, (1969).
- [43] R.D. Richtmyer and K.W. Morton, Difference Methods for Initial Value Problems, (Wiley and sons), p45, (1967).
- [44] R.D. Richtmyer and K.W. Morton, Difference Methods for Initial Value Problems, (Wiley and sons), p71, (1967)
- [45] R.D. Richtmyer and K.W. Morton, Difference Methods for Initial Value Problems, (Wiley and sons), p18, (1967)
- [46] J. Crank and P. Nicholson, Proc. Camb. Phil. Soc., 43, p50, (1947).
- [47] R.D. Richtmyer and K.W. Morton, Difference Methods for Initial Value Problems, (Wiley and sons), p198, (1967)
- [48] G.D. Smith, Numerical Soln. of Partial Diff. Eqns., (Oxford Math. Handbooks), p29, (1969).
- [49] D.W. Peaceman and H.H. Rachford, SIAM Journal, 3, p28, (1955).
- [50] NAG Library routine C06AAF, Numerical Algorithms Group Oxford.
- [51] D.C. Robinson, Plasma Physics, 13, p439, (1971).
- [52] R.W. Hamming, Numerical Methods for Scientists and Engineers, (Mc Graw Hill), p344, (1962).
- [53] E.P. Butt and R.S. Pease, Culham Lab. Report CLM-R30, (1963).
- [54] E.A. Alder, R.M. Kulsrud, and R.B. White, Phys. Fluids, 23, p1375, (1980).
- [55] B.A. Carreras, M.N. Rosenbluth, and H.R. Hicks, Oak Ridge Nat. Lab. Report ORNL/TM-7520, (1980).
- [56] T.J. Martin, Culham Lab. report CLM-PDN 2/73, (1973).
- [57] J.C. Butcher, JACM, 14, p84, (1967).
- [58] G.M. Zaslavsky and B.V. Chirikov, USP. Fiz. Nauk., 14, p195, (1972).
- [59] Dr R.J. Hastie, private communication.
- [60] G.H. Hardy and E.M. Wright, Theory of Numbers, (Oxford Clarendon press), p268, (1962).
- [61] A.B. Rechester and M.N. Rosenbluth, Phys. Rev. Lett., 40, p38, (1978).
- [62] J.R. Jokipii and E.N. Parker, Astrophysical Jnl., 155, p773, (1969).

- [63] J.A. Krommes, R.G. Kleva, and C. Oberman, Princeton Lab. Report PPPL-1389, (1978).
- [64] P.G. Carolan et al, 10th Europ. Conf. on Controlled Fusion and Plasma Physics, Moscow, L2, (1981).
- [65] M.R.C Watts, private communication.
- [66] A.B. Rechester, M.N. Rosenbluth, and R.B. White, Phys. Rev. Lett., 42, p1247, (1979).
- [67] K. Miyamoto, "Plasma Physics for Nuclear Fusion", (M.I.T. Press), p198, (1978).

APENDIX OF PUBLISHED PAPERS

Paper 1

The Nonlinear g Mode in the Reverse Field Pinch  
T.C. Hender and D.C. Robinson  
Nucl. Fusion, 21, p755, (1981).

Paper 2

The Nonlinear g Mode  
T.C. Hender and D.C. Robinson  
Proceedings 10th European Conference on Controlled Fusion and Plasma  
Physics, Vol 1, L-11, (1981).

Paper 3

Local Heating and Current Investigations on TOSCA  
M.W. Alcock, T. Edlington, P.A. Gaisford, T.C. Hender, B. Lloyd, and  
D.C. Robinson  
Proceedings 10th European Conference on Controlled Fusion and Plasma  
Physics, Vol 1, H-15, (1981).

Paper 4

Linear and Nonlinear Resistive Instability Studies  
T.C. Hender and D.C. Robinson  
Proceedings of the Workshop on Computational MHD Models of the  
Behaviour of Magnetically Confined Plasmas, Wildhaus, (1981).

## LETTERS

### THE NON-LINEAR 'g'-MODE IN THE REVERSE-FIELD PINCH

T.C. HENDER\*, D. C. ROBINSON (Culham Laboratory, Abingdon, Oxon, (Euratom/UKAEA Fusion Association), United Kindom)

**ABSTRACT.** The non-linear development of the  $m=0$  resistive 'g' mode has been studied in the reverse-field pinch. A saturation process is shown to exist in which the perturbations cause a quasi-linear flattening of the equilibrium pressure near the  $m=0$  resonant surface. The mechanism for this flattening is discussed.

#### 1. INTRODUCTION

The reverse-field pinch [1] and the Spheromak [2] have adverse curvature and as a consequence are unstable to the resistive interchange or 'g'-mode. It is, therefore, particularly important to investigate the non-linear consequences of this mode. A numerical code has been developed to time-advance a reduced set of MHD equations.

It is known from previous work that while 'g'-modes with azimuthal mode number,  $m \geq 1$  may be stabilized by finite-Larmor-radius effects, the relatively long-wavelength  $m=0$  mode is unlikely to be stabilized [3]. Further, we know from the work of Schnack [4] that the  $m=0$  mode may continue to grow far into the non-linear regime. This provides our motivation for choosing to study the non-linear development of the  $m=0$  'g'-mode. This mode occurs about the point at which the longitudinal field reverses and is driven by the pressure gradient. To simplify the problem further we have assumed the plasma to be incompressible. This has the numerical advantage of precluding magneto-sonic waves which can lead to severe time-step restrictions.

#### 2. EQUATIONS

We choose to study the 'g'-mode in periodic cylindrical geometry. This means that the 'g'-mode is driven 'correctly' by the interaction of pressure and curvature rather than by a fictitious 'g'-term [5] which is needed in slab geometry. The incompressibility

condition then allows us to define magnetic and velocity stream functions. Using these the resistive MHD-equations can be reduced, for the  $m=0$  mode, to the two-dimensional form:

$$\frac{\partial \psi}{\partial t} + V_r \frac{\partial \psi}{\partial r} + V_z \frac{\partial \psi}{\partial z} = \eta \left( r \frac{\partial}{\partial r} \left[ \frac{1}{r} \frac{\partial \psi}{\partial r} \right] + \frac{\partial^2 \psi}{\partial z^2} \right) \quad (1)$$

$$\frac{\partial B_\theta}{\partial t} = \frac{\partial}{\partial z} \left( \frac{V_\theta}{r} \frac{\partial \psi}{\partial r} - V_z B_\theta \right) - \frac{\partial}{\partial r} \left( V_r B_\theta + \frac{V_\theta}{r} \frac{\partial \psi}{\partial z} \right) + \eta (\nabla^2 \bar{B})_\theta \quad (2)$$

$$\rho \left( \frac{\partial V_\theta}{\partial t} + (\bar{V} \cdot \nabla \bar{V})_\theta \right) = \frac{1}{r} \frac{\partial \psi}{\partial r} \frac{\partial B_\theta}{\partial z} - \frac{1}{r^2} \frac{\partial r B_\theta}{\partial r} \frac{\partial \psi}{\partial z} \quad (3)$$

where

$$V_r = -\frac{1}{r} \frac{\partial \phi}{\partial z}, \quad V_z = \frac{1}{r} \frac{\partial \phi}{\partial r}$$

and

$$B_r = -\frac{1}{r} \frac{\partial \phi}{\partial z}, \quad B_z = \frac{1}{r} \frac{\partial \psi}{\partial r}$$

$\eta$  is the resistivity,  $V$  the fluid velocity,  $B$  the magnetic field and  $J$  the current.

Defining the vorticity  $\omega = (\nabla \times \bar{V})_\theta$

$$\rho \left( \frac{\partial \omega}{\partial t} + \frac{\partial}{\partial r} (V_r \omega) + \frac{\partial}{\partial z} (V_z \omega) \right) = \frac{\partial}{\partial r} (B_r J_\theta) + \frac{\partial}{\partial z} (B_z J_\theta) + \frac{1}{r} \left( \rho \frac{\partial V_\theta^2}{\partial z} - \frac{\partial B_\theta^2}{\partial z} \right) \quad (4)$$

and the system is closed by the relation

$$\omega = -\frac{1}{r} \frac{\partial^2 \phi}{\partial z^2} - \frac{\partial}{\partial r} \left( \frac{1}{r} \frac{\partial \phi}{\partial r} \right) \quad (5)$$

\* Royal Holloway College, University of London.



## LETTERS

These equations are numerically advanced in time by a mixed ADI/explicit algorithm similar to that used by Waddell et al. [6].

### 3. EQUILIBRIUM

The investigations have been conducted using the Tearing Mode Stable (TMS) equilibria [7]. This is an analytic reverse-field-pinch model for which the pitch,  $P(r)$ , and the Suydam value,  $C$ , are specified ( $C = -(dp/dr)/rB_z^2[(dP/dr)/P]^2 \leq 1/8$  is the Suydam stability criterion, where  $p$  is the plasma pressure). As a further refinement, a vacuum region is included in which  $B_z = \text{const}$ , and  $B_\theta \propto 1/r$ . To avoid discontinuities at the vacuum-plasma interface a matching zone is necessary. In this region variables are matched smoothly to each other, in particular  $C$  is taken gradually to zero with zero gradients at both ends of the matching zone. In most of our runs we have taken the pitch in the core of the plasma as  $P(r) = 2(1 - r^2/8 - r^4/400)$ , where the radius is defined such that the longitudinal field and current on axis are unity.

The tearing-mode stability properties of the TMS model have been exhaustively studied by Robinson [7]. It is important for our purposes that the equilibrium be tearing-mode stable, in order to isolate the non-linear 'g'-mode behaviour. The  $m=0$  tearing mode is, however, very weak for this configuration, even if wall stabilization is not effective, and the stability should, therefore, be dominated by the 'g'-mode behaviour. This property is fortunate since in testing for tearing-mode stability at finite beta we are left in the dilemma that the  $\Delta'$  criterion [8] does not apply whenever the 'g'-mode is dominant, in such a high- $\beta$  configuration. In an attempt to satisfy ourselves that our finite-beta equilibria are tearing-mode stable, we have adopted two methods. Both involve reducing the pressure to zero while maintaining some property of the fields. In the first method, we maintain the pitch constant, and in the second we maintain the quantity  $\sigma = \mathbf{j} \cdot \mathbf{B} / |\mathbf{B}|^2$  constant. The second is probably preferable as it is the gradient of  $\sigma$  which drives the tearing mode. The reduced-pressure configurations are tested for stability using a precise value of  $\Delta'$  obtained from the code, RCWALL, which is based upon the method developed by Robinson [7].

### 4. RESULTS AND DISCUSSION

The code is run by priming with linear eigenmodes from the code RIP4A [9]. It was found in all cases

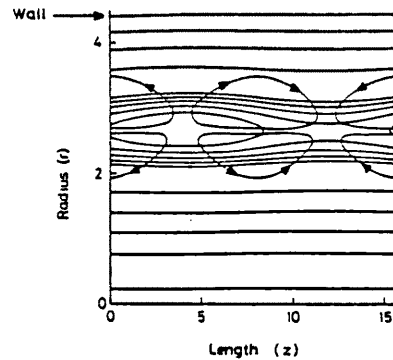


FIG. 1. Magnetic fields and velocity flows (arrowed lines) with which non-linear run is primed.

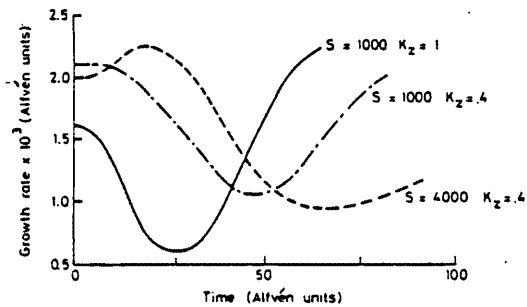


FIG. 2. Growth rate curves for reconnected flux at the singular surface. All three curves are for TMS equilibrium with a Suydam value,  $C = 0.05$ .

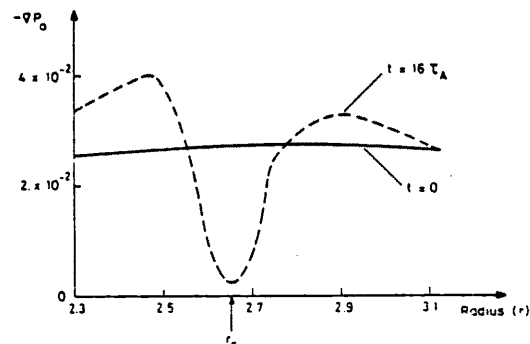


FIG. 3. Non-linear development of zeroth harmonic of pressure gradient for  $S = 1000$ ,  $C = 0.05$  and  $K_z = 1.0$ .

attempted, that if the non-linear code was primed with sufficiently small eigenmodes to keep it in the linear regime then it produces growth rates to within 2% of those of RIP4A. A typical magnetic-island structure and velocity flow pattern, with which the non-linear run is started, are shown in Fig. 1.

The growth rate defined as  $(1/\psi)(\partial\psi/\partial t)$  at the singular surface is shown for three full non-linear runs in Fig. 2. They are for  $S = 1000$  and  $4000$ , with  $K_z = 0.4$ ,  $C = 0.05$  and for  $S = 1000$ ,  $C = 0.05$  and  $K_z = 1.0$  (where  $S$  is the magnetic Reynolds number). All three curves exhibit similar behaviour: a marked decrease in growth followed by an increase. The decrease in growth is caused by quasi-linear flattening of the zeroth-harmonic of pressure, in the region of the singular surface. This is shown for the  $C = 0.05$ ,  $S = 1000$ ,  $K_z = 1.0$  case in Fig. 3. The increasing-growth-rate phase corresponds to resistive diffusion of the magnetic fields, which increase the average beta and drive the 'g'-mode more unstable again.

The differences between the growth rate-curves allows us to deduce some important properties of these modes. For the  $S = 4000$ ,  $K_z = 0.4$  case, it is seen that the growth rate increases much more slowly after turning, than the corresponding  $S = 1000$  case. This is because the increase in pressure due to the resistive evolution of the equilibrium is slower for the  $S = 4000$  case. The different times to the turning points for the  $K_z = 0.4$  and  $K_z = 1.0$ ,  $S = 1000$ , cases follow from a linear-stability analysis of the equilibrium: it is found that the growth rate of the  $K_z = 1.0$  mode increases much faster with pressure than does the  $K_z = 0.4$  case. Thus the decrease in pressure gradient, at the singular surface, is more quickly counteracted by the increase in pressure in the  $K_z = 1.0$  case.

Examination of the magnitudes of the perturbations in the non-linear runs shows that we are still in a quasi-equilibrium state. Thus

$$\nabla p_0 \cong \bar{J}_0 \times \bar{B}_0 \quad (6)$$

where subscripts zero indicate zeroth harmonics. Now near the  $m = 0$  surface,  $B_{z0}$  must, by definition, be small. Hence, the flattening of the pressure near the singular surface can almost totally be accounted for by quasi-linear modifications to the  $J_{z0}$ . This can easily be demonstrated to be correct: by simply altering the  $J_{z0}$  to that at a given timestep while maintaining  $J_{\theta 0}$ ,  $B_{\theta 0}$  and  $B_{z0}$  at their original values we obtain an almost exact fit to the pressure gradient in the region of singular surface at that timestep.

Using this knowledge, we can obtain an order-of-magnitude estimate to the saturation width. We have at the singular surface,  $r_s$ ,

$$\eta J_{z0} = E_{z0} - (V_{\theta} B_r)_0 \quad (7)$$

since  $V_r|_{r_s} = 0$ . For the range of betas of interest the 'g'-mode-layer thickness is less than the resistive-skin depth, and so  $E_{z0}$  is able to partially relax resistively. Hence it is primarily the  $(V_{\theta} B_r)_0$  term which causes the saturation process:

$$\eta J_{z0}|_{\text{orig}} \sim (V_{\theta} B_r)_0 \quad (8)$$

where the subscript 'orig' implies the initial equilibrium value. Now, at  $r_s$ , from linear stability theory

$$\rho \omega V_{\theta 1} = J_{z0}|_{\text{orig}} B_{r1} \quad (9)$$

where  $\omega$  is the linear growth rate and the subscript 1 indicates a linear perturbation term. Equations (8) and (9) then give

$$(V_{\theta} B_r)_0 = \frac{1}{2} V_{\theta 1} B_{r1} = \frac{1}{2} J_{z0}|_{\text{orig}} \frac{B_{r1}^2}{\rho \omega} \sim \eta J_{z0}|_{\text{orig}}$$

Hence,

$$\rho \eta \omega \sim \frac{B_{r1}^2}{2} \quad (10)$$

but from Furth, Killeen and Rosenbluth [5] the resistive-layer thickness,  $\ell$ , is given by

$$\ell = \left( \frac{\rho \eta \omega}{K_z^2 (B_{z0}')^2} \right)^{1/4} \quad (11)$$

Using (10) this then gives

$$\ell \sim \frac{1}{2^{1/4}} \left( \frac{B_{r1}}{K_z (B_{z0}')^2} \right)^{1/2} \sim \text{island width.} \quad (12)$$

Hence, we can expect appreciable saturation by pressure flattening when the island width is comparable to the resistive-layer thickness. This is indeed found to be the case in our non-linear calculations. A somewhat similar situation prevails when considering the non-linear behaviour of the tearing mode [10]. Our calculations show that the resistive-layer thickness decreases as  $S^{-0.22}$  for values of  $S$  up to  $5 \times 10^4$  and the radial field perturbation decreases as  $S^{-0.39}$ . This is to be compared with the predictions from Eq.(11)

## LETTERS

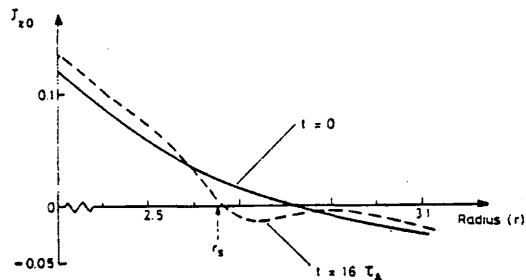


FIG. 4. Non-linear development of zeroth harmonic of axial current for  $S = 1000$ ,  $C = 0.05$  and  $K_T = 0.4$ .

for a pure resistive 'g'-mode and from Eq.(12) that the field perturbation decreases as  $S^{-0.67}$ .

We have also modified the equilibrium profiles in the linear code, RIP4A, to match the pressure profiles at various times of the non-linear evolution. The linear code then gives growth rates to within 5% of the corresponding non-linear calculation. Hence, we conclude that we are dealing with a quasi-linear phenomenon in which the dominant effect is that of perturbations on their own equilibrium. The quasi-linear modification to  $J_{z0}$  is shown in Fig.4.

## 5. CONCLUSIONS

The decrease in growth rate has been shown to be due to the quasi-linear modification to the axial current,  $J_{z0}$ . The effect of this on the growth of the linear perturbations can be seen with reference to Eq.(9). Setting  $J_{z0}|_{r_s}$  equal to zero (which is equivalent to flattening the pressure at  $r_s$ ) essentially stops the growth of the azimuthal velocity perturbations,  $V_\theta$ , at  $r_s$ . This is found to be the case on detailed examination of the results from the non-linear calculations. The coupling between the radial-field perturbations and the azimuthal velocity has been broken, and so the exponential linear growth will cease.

The increase in growth rates caused by resistive diffusion of the equilibrium reflects an unfortunate facet of our reduced MHD formalism. By using an incompressible formalism we lose independent control

of the plasma energy content, which could have been used to control the diffusive rise in pressure. The inclusion of more physical effects such as parallel thermal conduction, to control this pressure rise, would allow the saturation process to continue. This view is confirmed by the difference between the  $S = 1000$  and the  $S = 4000$  mode evolution.

In re-distributing the pressure to achieve the flattening at the singular surface, the  $m = 0$  mode increases the pressure gradient markedly in the core of the plasma and to some extent in the outer regions of the plasma, Fig.3. This effect is further enhanced by resistive diffusion. We have examined the linear effect of this on the  $m = 1$  modes in the core and find that their growth rate increases considerably. This could be an important effect, but we have not yet examined the non-linear effects of the  $m = 1$  and  $m = 0$  mode interaction, which would require a three-dimensional calculation.

## REFERENCES

- [1] BODIN, H.A.B., NEWTON, A.A., Nucl. Fusion 20 (1980) 1255.
- [2] ROSENBLUTH, M.N., BUSSAC, M., Nucl. Fusion 19 (1979) 489.
- [3] HOSKING, R.J., ROBINSON, D.C., in Controlled Fusion and Plasma Physics (Proc. 9th Europ. Conf. Oxford, 1979) BP6 61.
- [4] SCHNACK, D.D., KILLEEN, J., Nucl. Fusion 19 (1979) 877; SCHNACK, D.D., KILLEEN, J., GERWIN, R.A., The Non-Linear Evolution of Resistive Interchange Modes in a Reversed-Field Pinch (submitted to Nucl. Fusion).
- [5] FURTH, H.P., KILLEEN, J., ROSENBLUTH, M.N., Phys. Fluids 6 (1963) 459.
- [6] WADDELL, B., ROSENBLUTH, M.N., MONTICELLO, D.A., WHITE, R.B., CARRERAS, B., in Theoretical and Computational Plasma Physics (Proc. ICTP College, Trieste, 1977), IAEA, Vienna (1978) 79.
- [7] ROBINSON, D.C., Nucl. Fusion 18 (1978) 939.
- [8] COPPI, B., GREENE, J.M., JOHNSON, J.L., Nucl. Fusion 6 (1966) 101.
- [9] KILLEEN, J., in Physics of Hot Plasmas (RYE, B.J., TAYLOR, J.C., Eds), Plenum Press, New York (1970) 202; ROBINSON, D.C., CROW, J.E., FURZER, A.S., DIBIASE, J.A., KILLEEN, J., to be published in Plasma Physics.
- [10] RUTHERFORD, P.H., Phys. Fluids 16 (1973) 1903.

(Manuscript received 6 January 1981)

Final manuscript received 21 April 1981)

Contribution for the 10th EPS Moscow Conf. Sept. 1981

THE NONLINEAR 'g' MODE

T C Hender\* and D C Robinson  
Culham Laboratory, Abingdon, Oxon, OX14 3DB, UK  
(Euratom/UKAEA Fusion Association)

\*Royal Holloway College, University of London

ABSTRACT The nonlinear properties of the  $m=0$  resistive 'g' mode have been studied for a wide range of magnetic Reynolds numbers. A quasi-linear saturation mechanism has been found in which the pressure in the vicinity of the singular surface is flattened. This saturation is however counteracted by overheating of the plasma. The  $m=1$  mode in the core of the plasma has also been investigated and similar mechanisms prevail. A field line tracing code has been used to study the existence of magnetic surfaces when  $m=0$  and  $m=1$  modes interact. Ergodic field line behaviour has been found for parameters typical of contemporary reverse field pinches.

INTRODUCTION In both the RFP and spheromak the most dangerous instability is the 'g' mode. It is therefore important to understand its nonlinear behaviour.

To study the  $m=0$  mode a simplified formalism is chosen; a periodic cylindrical system is assumed, a 2D approximation made ( $\frac{\partial}{\partial z} \equiv 0$ ), and the plasma is assumed to be incompressible. This allows the introduction of a flux function and a velocity stream function. The resulting equations are similar to the reduced tearing mode equations and an extension of the algorithm of Waddell et al<sup>[1]</sup> is used to solve them. Recently a mixed helicity code has been developed. A spectral method similar to the Oak Ridge code RSF<sup>[2]</sup> is used to solve the full set of compressible resistive MHD equations. This code has been used to make a study of the single helicity  $m=1$  mode.

RESULTS AND DISCUSSION The equilibrium chosen for the study is the tearing mode stable equilibrium developed by Robinson<sup>[3]</sup>. This RFP equilibrium is stable to all ideal MHD instabilities and to tearing modes. To model experimental conditions more realistically this equilibrium

includes a vacuum region between the plasma and the wall.

The non-linear results for the  $m=0$  mode show the dominant nonlinear process to be the modification of the axial current,  $J_{z0}$ . Figure 1 shows the alteration to  $\eta J_{z0}$  for a

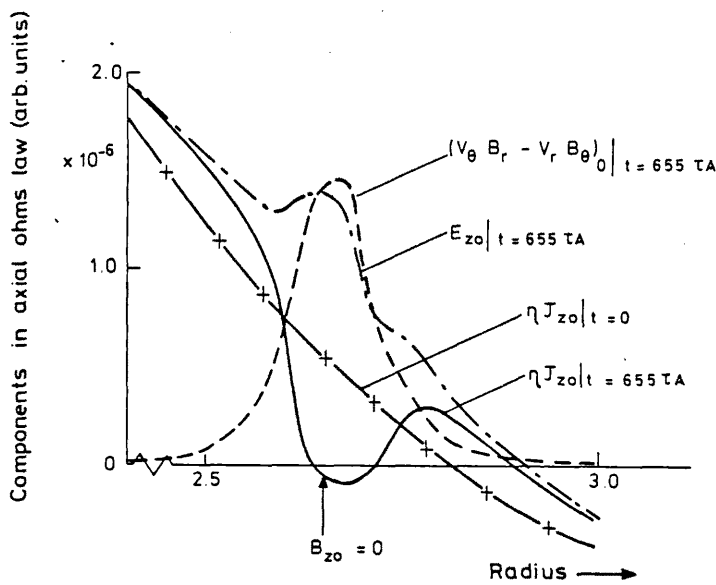


Fig.1 Components of Ohm's law at 655 Alfvén transit times for the  $m=0$  'g' mode.

case with a magnetic Reynolds number,  $S = 5 \times 10^4$  ( $\eta$  being the plasma resistivity). The displacement of  $E_{z0}$  and  $\eta J_{z0}$  to larger radii is due to resistive diffusion while the behaviour in the vicinity of the singular surface is due to the quasi-linear perturbation  $(\mathbf{V}_1 \times \mathbf{B}_1)_{z0}$ , to Ohm's law. The modification to  $J_{z0}$  near the singular surface causes a flattening of the equilibrium pressure in this region, and since the 'g' mode is driven by pressure gradient, represents a quasi-linear saturation mechanism. However the resistive diffusion of the equilibrium results in ohmic heating increasing the gross pressure and thus counteracting the saturation process. The nonlinear behaviour observed depends on the competition between these two mechanisms; our calculations indicate that the  $S$  scaling of these two effects causes the saturation mechanism to become increasingly dominant at high  $S$ . However at  $S \sim 5 \times 10^4$  the growth rate is only reduced to 40% of its linear value. It is likely that by introducing physical energy loss mechanisms (thermal conductivity, radiation etc) the saturation may be comp-

plete. Within the incompressible formalism used for the  $m=0$  code this energy loss process can be represented by introducing a non-physical term in the resistive diffusion equation to stop the fields resistively decaying. With this term present saturation is obtained for  $S=1000$ .

The nonlinear behaviour of the  $m=0$  leads to an enhancement of the pressure gradient in the vicinity of the  $m=1$  surfaces. Figure 2 shows the pressure gradient resulting from the

presence of an  $m=0$  mode for  $S=1000$ . The positions of some of the  $m=1$  surfaces are also recorded on Fig.2. The effect on the linear growth rates of the  $m=1$  modes due to the alterations to the pressure profile have been investigated. In the centre of the plasma the growth rates can double. The nonlinear behaviour of a single helicity  $m=1$  mode is found to be dominated by the same mechanisms as for the  $m=0$  mode.

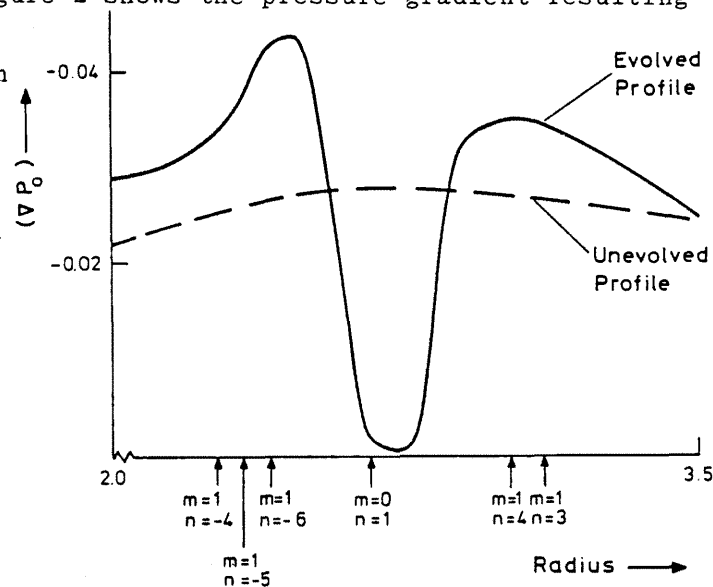


Fig.2 Evolved pressure profile in the region of  $B_z=0$

file have been investigated. In the centre of the plasma the growth rates can double. The nonlinear behaviour of a single helicity  $m=1$  mode is found to be dominated by the same mechanisms as for the  $m=0$  mode.

To assist in a mixed helicity study a field line tracing code has been used to study the result of the interaction between the  $m=0$  mode and the  $m=1, n=4$  mode in the core of the plasma. A linear code is used to produce the perturbations to the magnetic fields and they are introduced at the smallest amplitude at which saturation is likely to occur; the results are therefore optimistic. At low magnetic Reynolds numbers ergodic field line behaviour is found. Figure 3 shows the intersection of two different field lines with the  $\theta=0$  plane, for  $S=5000$  and a central beta of 5%. The closed

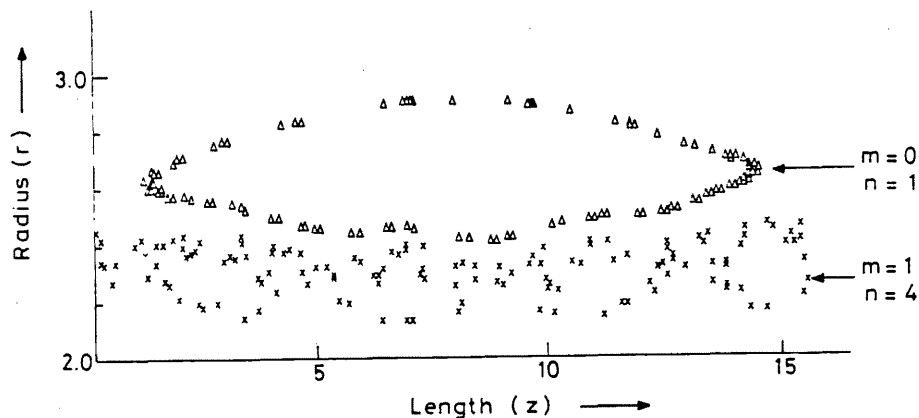


Fig.3 Magnetic surfaces in the  $r$ - $z$  plane with  $m=0$  and  $m=1$  modes present.

surface of the large  $m=0$  island can be seen while field lines forming the  $m=1$  islands experience ergodic behaviour between the two surfaces. At higher  $S$  the surfaces become closed if only the two island structures are considered. However increasing  $S$  causes the  $m=1$  (and  $m=2$ ) modes in the core with  $n > 4$  ( $n > 8$ ) to become destabilised and so the surfaces do not close. The effect of this non-closure on energy containment is being investigated.

CONCLUSIONS The nonlinear behaviour of the  $m=0$  mode exhibits a quasi-linear saturation mechanism. This saturation may be prevented by overheating of the plasma.

The  $m=1$  mode possesses a similar nonlinear behaviour. The  $m=1$  modes are linearly destabilised by the presence of the  $m=0$  mode.

The interaction between the  $m=0$  and  $m=1$  modes leads to ergodic field line behaviour.

REFERENCES

- [1] WADDELL B, ROSENBLUTH M N and MONTICELLO D A, WHITE R B, CARRERAS B, "Nonlinear Numerical Algorithms", ITCP College (1977) 79.
- [2] HICKS R, CARRERAS B, HOLMES J et al, Oak Ridge National Laboratory Report ORNL/TM7132, 1979.
- [3] ROBINSON D C, Nuclear Fusion, 18 (1978) 939.

LOCAL HEATING AND CURRENT DRIVE INVESTIGATIONS ON TOSCA

M W Alcock, T Edlington, P A Gaisford\*, T C Hender\*,  
B Lloyd\*\* and D C Robinson

Culham Laboratory, Abingdon, Oxon, OX14 3DB, UK  
(Euratom/UKAEA Fusion Association)

\*Royal Holloway College, University of London

\*\*University of Oxford.

ABSTRACT ECRH experiments at the second harmonic show local heating when the cyclotron resonance is on the outer flux surfaces. Above a critical power level this induces continuous  $m=1$  activity in the heating zone. The local heat conduction coefficient is close to the INTOR value and the parallel heat conduction may be anomalous. Attempts to detect a wave driven current using a variable angled antenna ( $\pm 50^\circ$ ) indicates that the current is less than 3A/kW in the plasmas used in these investigations.

INTRODUCTION The resonance zone width for ECRH is generally much less than the plasma radius and localised heat-

$$\bar{n}_e = 7.5 \times 10^{18} \text{ m}^{-3}$$

$$P_{rf} = 50 \text{ kW}$$

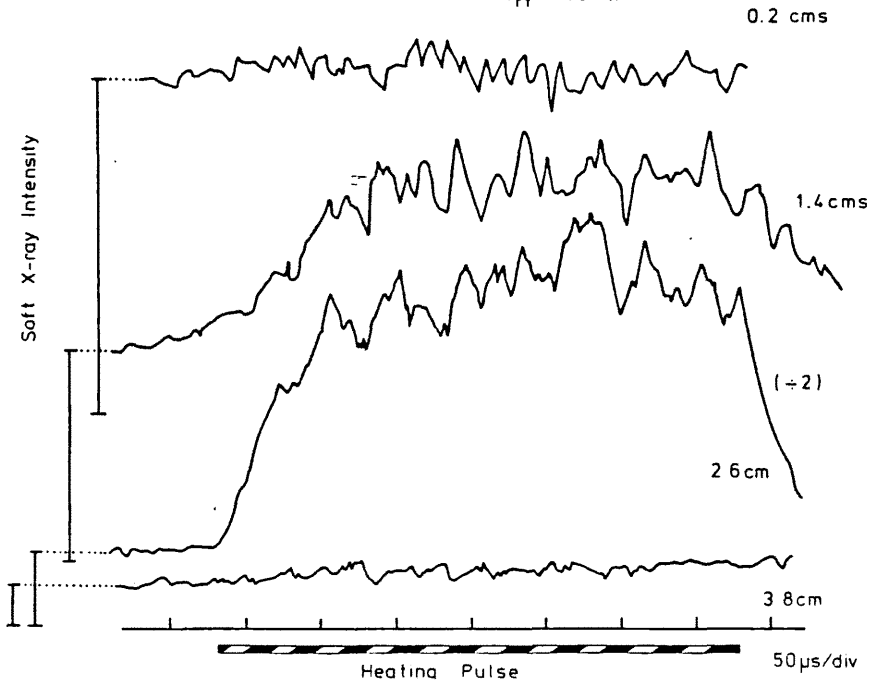


Fig.1 Soft X-ray emission from four radii during the heating pulse.



ing is possible in an optically thick plasma, when the directionality of the injected radiation is controlled. This is important for current profile and instability control and heat conduction studies. Even in an optically thin plasma when one must take account of reflections there is a geometrical effect<sup>[1]</sup> which permits strong local maxima in the heating profile thus allowing such investigations in small tokamaks. Theory<sup>[2]</sup> also indicates that cyclotron waves should be suitable for generating a current if the absorption is predominantly on one side of the resonance which is possible for the X-mode in a small tokamak at sufficiently high temperatures with the waves launched preferentially in one direction.

LOCAL HEATING EXPERIMENTS The soft X-ray emission observed vertically from a seven channel diode array indicates that strong local heating occurs close to the cyclotron resonance both above and below the X-mode cut-off provided the resonance is on the outside of the magnetic surfaces. The emission associated with four different radii during the heating pulse is shown in Fig.1. The signal saturates in some 50 $\mu$ s and falls with a similar time constant. In the high temperature zone continuous fluctuations in the region of 50kHz are produced provided the input power is above some threshold dependent on the initial value of  $q$ . These fluctuations appear to be continuous  $m=1$  activity associated with local heating and current concentration producing a small region with  $q < 1$ . These discharges have  $q_a \sim 7$  and before heating  $q(0) \lesssim 2$ . The new magnetic axis is thus close to the heating zone. Evidently the transport processes in this case do not permit sawtooth activity. The width of the heating zone is typically 20mm at a particular toroidal field. If the toroidal field is varied then heating is detected at a particular radius if the resonance zone moves approximately 30mm, - Fig.2. The existence of two sustained temperature maxima and the absence of a peak on the opposite side of the magnetic surface indicates the 2-D nature of the heat conduction process in the tokamak. We have used a 2D

anisotropic heat conduction and field diffusion code with a local heating source to simulate this behaviour. The experimental results can be reproduced by reducing the parallel heat conduction by 100 x as shown in Fig.3.

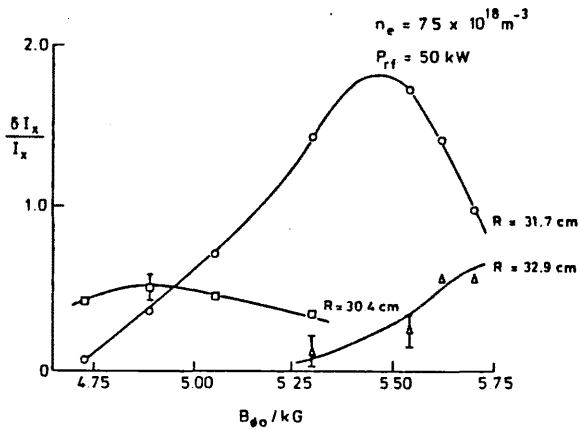


Fig.2 Variation of soft X-ray emission at three-radial positions with toroidal field.

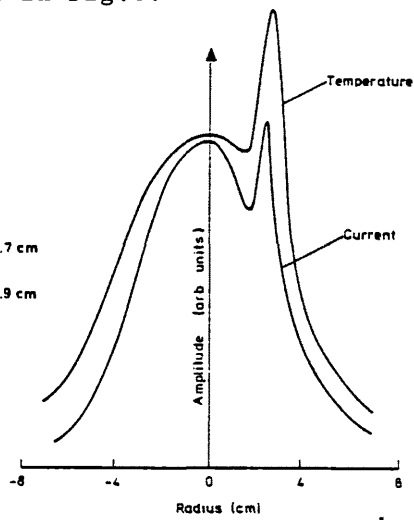


Fig.3 Temperature and current profile associated with anomalous parallel heat conduction.

From the heating and decay times and the width of the heating zone we obtain a local average heat conduction coefficient of  $0.5 \text{ m}^2 \text{ s}^{-1}$  in the hot core of the plasma which is about six times smaller than the average INTOR value. An alternative explanation for the failure of the temperature to be uniform on a magnetic surface is that the ECRH produces perpendicular runaway and electrons with energies of  $\sim 3 \text{ keV}$  become trapped with large banana orbits of width  $\sim 1\text{-}2 \text{ cm}$ , which is in accord with the observed absence of local heating on the high field side of the plasma. No evidence for this non-thermal perpendicular electron distribution has however been obtained.

CURRENT DRIVE EXPERIMENTS Theoretical ray tracing and absorption calculations for the X-mode in TOSCA at a central density of  $4.5 \times 10^{18} \text{ m}^{-3}$  and temperatures of  $600 \text{ eV}$  indicate that a net current of some  $30 \text{ A/kW}$  should be produced. The calculations suggest that the optimum angle of injection is less than  $14^\circ$  and that although the single pass absorption

can be quite high (80%) the local current produced on one side of the resonant layer is approximately cancelled by that on the opposite side of the layer. This should produce a substantial change in the current profile and is likely to excite mode activity. The directed antenna in the experiments produces its power in two lobes (normally at  $\pm 20^\circ$ ), at  $+8^\circ$  and  $+48^\circ$  and can be rotated so that one lobe should be efficient for current drive.

Typical discharge waveforms for such an experiment are shown in Fig.4. The heating is not as efficient as for the usual  $\pm 20^\circ$  antenna and in general the soft X-ray emission is not fully sustained throughout the heating pulse. In both directions, the plasma current increases by typically 10% associated with the decrease in inductance, and resistance but there is a difference in the two directions of up to 300 amps for 100 kW input. As with the perpendicular antennae the high power ECRH does not produce run-away discharges.

**CONCLUSIONS** The local heating on the outer flux surfaces may be associated with anomalous parallel heat conduction or with the presence of perpendicular electron runaway leading to a build up trapped electrons. The efficiency for current drive in these experiments appears to be low, possibly because the single pass absorption is low.

**REFERENCES**

- [1] FIELDING P J, Culham Laboratory Report, CLM-P615 (1980).
- [2] CORDEY J G et al, Culham Laboratory Report, CLM-P636 (1981)

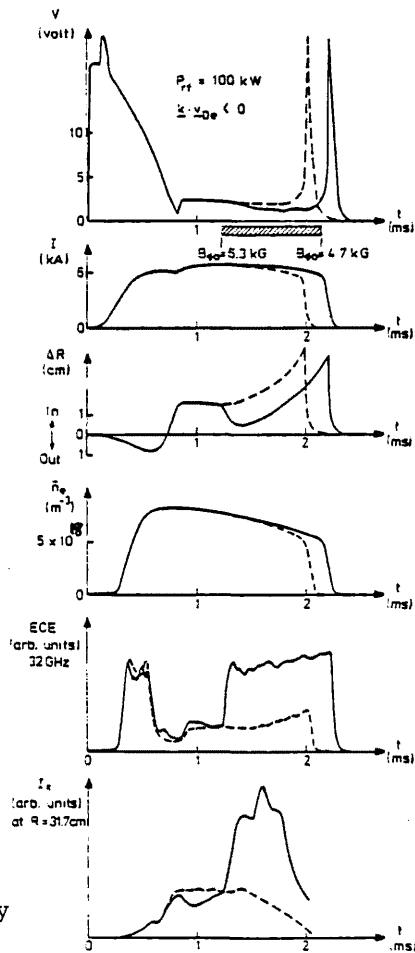


Fig.4 Discharge waveforms for a directed antenna.

*Contribution for the Workshop on Computational MHD Models of the Behaviour of Magnetically Confined Plasmas, Wildhaus, Switzerland, 9-11 September 1981.*

## LINEAR AND NONLINEAR RESISTIVE INSTABILITY STUDIES

T C Hender\* and D C Robinson  
Culham Laboratory, Abingdon, Oxon, OX14 3DB, UK  
(Euratom/UKAEA Fusion Association)

\*Royal Holloway College, University of London

### ABSTRACT

The linear stability properties of the resistive 'g' mode are examined. The effects of including a full stress tensor have been examined for this mode. The nonlinear 'g' mode has also been examined and a potential saturation mechanism identified. The results of 2D calculations for the  $m=0$  and  $m=1$  'g' modes in the reverse field pinch (RFP) are presented. Ergodic field line behaviour is found as a result of the interaction of mixed helicity 'g' modes.

### 1 INTRODUCTION

Both the RFP<sup>[1]</sup> and Spheromak<sup>[2]</sup> are unstable to the resistive interchange or 'g' mode. It is therefore important to investigate this mode both linearly and nonlinearly.

The linear studies have been conducted using implicit codes developed by Robinson, Killeen and co-workers<sup>[3]</sup>. The most recent of these codes includes the effects of compressibility, isotropic resistivity, Hall term, anisotropic thermal conductivity, and the full stress tensor<sup>[4]</sup>, i.e. anisotropic viscosity and finite Larmor radius terms.

The nonlinear studies, initially concentrated on the  $m=0$  'g' mode which occurs about the toroidal field reversal point in the RFP. Basically because this mode is of long wavelength and not readily stabilised by other physical effects apart from very low  $\beta$  ( $< 1\%$ ). Recently the  $m=1$  mode has also been investigated and (possible) ergodic interactions between the  $m=0$  and  $m=1$  modes have been exhibited using a field line tracing code.

### 2 LINEAR STUDIES

The linear codes vary in complexity from an incompressible resistive code, RIPPLE4A<sup>[3]</sup>, to the most recent compressible code,

GNSTAB, described in the introduction. All these codes solve the MHD equations in a periodic cylindrical system and employ the same implicit formalism, solving the resulting tri-diagonal equations in the normal manner<sup>[5]</sup>. The codes are written such that the implicit weighting factor may be easily varied but are generally run using a Crank-Nicholson weighting. GNSTAB solves 7 complex partial differential equations for the different perturbed physical quantities.

The RFP studies are conducted using the tearing mode stable (TMS) equilibrium developed by Robinson<sup>[6]</sup>. The TMS model is defined by specifying a pitch function  $P(r)$ . A pressure gradient is introduced into the TMS model so that it satisfies the Suydam criterion everywhere with

$$C = -\frac{dp}{dr} / rB_z^2 \left( \frac{dP}{dr} / P \right)^2 < \frac{1}{8}$$

$p$  being the plasma pressure. To match experimental conditions a vacuum region is also included in which  $B_z = \text{const.}$ ,  $B_\theta \propto 1/r$  and  $dp/dr = 0$ . At zero beta this model is stable to all ideal and tearing modes<sup>[6]</sup>. A typical TMS reverse field pinch equilibrium, for  $P(r) = 2(1-r^2/8-r^4/400)$  and  $C=0.05$ , is shown in Fig.1. Such configurations have been demonstrated numerically to be stable to ideal modes for central beta values of up to 17% ( $\beta_0 < 0.5$ ).

The variation of linear growth rate with magnetic Reynolds number,  $S$  has been examined for a large range of poloidal mode numbers,  $m$ . The most unstable  $m$  is found to increase with  $S$ . At low  $S$  however resistive dissipation is found to have a marked effect so that the  $m=9$  mode is stable for  $S < 3 \times 10^3$  and  $C = 0.1$ . These results are summarised in Fig.2. For large values of  $S$  ( $\sim 10^6$ ) the high  $m$  modes have a very localised structure and a very fine mesh is required in the region of their singular surfaces: this is achieved by concentrating the computational domain on the singular surface and applying suitably modified boundary conditions.

The resistive layer thickness for the 'g' mode is found to scale approximately as  $S^{-1/4}$  (this is to be compared with the analytic scaling of  $S^{-1/3}$ <sup>[7]</sup>). This variation with  $S$  is much the same if one includes anisotropic viscosity and heat conduction though the resistive layer thickness is larger and the growth rate is reduced a little as shown in Fig.3.

It has been demonstrated that only the local pressure gradient gives rise to the growth. By increasing the value of  $C$  locally the ideal MHD Suydam mode eventually dominates. This occurs, for  $S=45,000$ , when the pressure gradient exceeds the Suydam limit by four times.

When the resistive layer thickness is comparable to the ion collisionless skin depth, the inclusion of the Hall effect and magnetic viscosity or finite Larmor radius terms is necessary. It should be noted that these equations do not reduce simply to those of slab geometry and curvature effects dominate. In particular the parallel viscosity survives in leading order with a term which is zero in slab geometry. Inclusion of the Hall effect alone makes the interchanges more unstable but the resistive layer thickness is then limited by approximately the ion collisionless skin depth,  $c/\omega_{pi}$ , or ion Larmor radius,  $r_{Li}$ , ( $r_{Li} \sim \beta^{1/2} c/\omega_{pi}$ ). Figure 4 shows the results of including all the finite Larmor radius terms for two values of axial wavenumber,  $K$ , for the  $m=0$  mode as a function of  $c/\omega_{pi}$  - the ion collisionless skin depth. A rapid reduction in growth is observed for the short wavelength  $m=0$  mode and this is also observed for  $m=2$  modes. The long wavelength  $m=0$  mode has its growth rate reduced somewhat but remains strongly unstable at this beta value.

At low values of beta, i.e. central values of  $\beta \leq 4\%$ , the parallel viscosity is found to have a stabilising effect and gives rise to a critical local pressure gradient depending on the shear. However, the region of strong shear where the field reverses, has essentially zero critical pressure gradient as the parallel viscosity does not stabilise the  $m=0$  mode. This gives rise to a critical pressure profile for the RFP with an average value of beta of  $10\%$  [8].

### 3 NONLINEAR $m=0$ STUDIES

The initial nonlinear 'g' mode studies concentrated on the  $m=0$  mode in a periodic cylindrical system. This mode was thought to be the most interesting because of its long wavelength nature and the failure of parallel viscosity<sup>[8]</sup> to stabilise the mode.

Making the approximation of incompressibility the 2D resistive MHD equations for the  $m=0$  mode are simplified by the introduction of a flux function,  $\psi$ , and velocity stream function,  $\phi$ <sup>[9]</sup>. The

equations obtained are similar to the reduced tearing mode equations [10], except that the components of velocity and magnetic field perpendicular to the island plane ( $r, z$ ) are retained (i.e.  $V_\theta$  and  $B_\theta$ ): this is because an ordering of the type used for tokamak problems [10] cannot be introduced for the pinch. These reduced equations are solved using an algorithm similar to that of Waddell et al [11].  $\psi, V_\theta, B_\theta$  are time advanced using an ADI scheme, whilst the  $\theta$ -component of vorticity ( $\omega$ ) is time advanced explicitly. The velocity stream function being obtained by solving

$$\omega = -\frac{\partial}{\partial r}\left(\frac{1}{r}\frac{\partial\phi}{\partial r}\right) - \frac{1}{r}\frac{\partial^2\phi}{\partial z^2} \quad (1)$$

A second code based on a Fourier resolution technique was also written to solve the reduced  $m=0$  mode equations. This code solves for the first three harmonics (i.e. the equilibrium,  $e^{ik_z z}, e^{2ik_z z}$ , where  $k_z = 1/R$ ) using a technique broadly similar to that above. However since the equations have now been reduced to a larger set of 1D equations, by the Fourier resolution, a Crank-Nicholson scheme is used for the implicit time advancement. The truncation of the Fourier series after three terms is justified by comparing the results of the ADI and Fourier codes. Very good quantitative agreement is found between the two codes, the Fourier code having the advantage that it runs approximately six times faster.

Figure 5 shows the nonlinear development of the equilibrium pressure for a run with a magnetic Reynolds number,  $S=10^3$  and  $C=0.05, K_z=0.4$ . Two distinct features are evident in this figure:

- (i) A general increase in pressure with time. This is due to ohmic heating; or equivalently to the resistive decay of magnetic energy and the corresponding increase in pressure energy necessary to conserve energy.
- (ii) A flattening of the pressure in the vicinity of the singular surface. This is a quasi-linear effect of the  $m=0$  mode on its equilibrium [9].

Since increasing the pressure gradient, increases,  $C$ , (i) represents a destabilising effect whilst (ii) represents a possible

saturation mechanism. Thus it is the competition between (i) and (ii) which determines the final nonlinear state. Balancing these two mechanisms analytically indicates that the final nonlinear growth rate should decrease with increasing S. Figure 6 shows the average growth rate of the first harmonic of  $b_r$ ,

$$\int_0^{\text{wall}} \frac{\partial b_{r1}}{\partial t} dr / \int_0^{\text{wall}} b_{r1} dr$$

as a function of time for runs with  $S=10^4$  and  $5 \times 10^4$ ,  $C=0.05$ . The S scaling implied by the final nonlinear growth in these two runs is  $S^{-0.44}$ .

#### 4 NONLINEAR m=1 STUDIES

In order to study modes other than  $m=0$  a new formalism and code were required. To attain independent control over the plasma energy a compressible formulation containing an energy equation was adopted. Also it was required that the new code be capable of studying mixed helicity problems. To satisfy these requirements a spectral code was written to solve the compressible resistive MHD equations.

In a periodic cylindrical system the dependent MHD variables may be Fourier analysed in the  $\theta, z$  directions e.g.

$$B_r = \sum_{\substack{-\infty < m < \infty \\ 0 < n < \infty}} (B_{rS_{m,n}} \sin(m\theta + nK_z z) + B_{rC_{m,n}} \cos(m\theta + nK_z z))$$

Of course in practice only a finite number of harmonics can be included.

It is desirable to time advance the Fourier component equations implicitly to avoid timestep restrictions; however the nonlinear convolution terms cause all the harmonics to couple and renders a totally implicit solution impractical. A compromise is thus used. The MHD equations may be written in the form:



'Linearised part' + Nonlinear convolution terms

$$\text{e.g. } \frac{\partial B_r}{\partial t} = \underbrace{(\nabla \times (\underline{v}_{m,n} \times \underline{B}_0))_r - (\nabla \times (\eta \nabla \times \underline{B}_{m,n}))_r}_{\text{Linearised part}} + \underbrace{(\nabla \times (\underline{v} \times (\underline{B} - \underline{B}_0)))_{m,n}}_{\text{Nonlinear part}}_r$$

where for simplicity the resistivity,  $\eta$ , is assumed to have the functional form  $\eta = \eta(r, t)$ .

Ignoring the nonlinear terms yields the standard 1D linearised equations for each harmonic, which may be solved implicitly in the normal manner. Thus the solution technique used is to solve for each separate harmonic implicitly with the nonlinear convolution terms included explicitly. This method achieves the required numerical stability whilst remaining computationally practical.

The 2D  $m=0$  results obtained are in good agreement with those of the previous section (small differences in growth rate occur because of the compressibility). To simulate an energy loss process the ohmic heating term was removed from the energy equation: the saturation of the mode was still not complete however because resistive diffusion of the fields caused the shear to decrease (and thus  $C$ , the driving term, to increase).

Figure 7 shows the nonlinear behaviour of an  $m=1$  mode just inside the field null ( $nK_z=1.6$ ) at  $S=10^4$  and  $C=0.05$ , the ohmic heating term again being removed. The decrease in growth is caused by the same pressure flattening mechanism as that for the  $m=0$  mode.

## 5 ERGODIC BEHAVIOUR

To study ergodic behaviour a field tracing code has been used to display magnetic surfaces for the TMS equilibrium perturbed by suitably scaled eigenfunctions. The above studies indicate that the island width at the onset of nonlinear behaviour scales as the resistive layer width<sup>[9]</sup>. The exact nonlinear behaviour of the 'g' mode depends on the energy losses (radiation, conduction) from the pinch. However by including the linear eigenfunctions at a level just sufficient to precipitate nonlinear behaviour optimistic estimates of the ergodic behaviour can be obtained. The results

are optimistic in that the modes will have to be at least as great in magnitude before 2D saturation will occur.

Figure 8 shows the intersections of several field lines with the  $r, z$  plane for a case with  $S=10^4$ ,  $\beta_0=5\%$  and  $K_z=0.2$ . The magnetic fields for this case are obtained by perturbing the TMS equilibrium by suitably scaled linear eigenfunctions. The modes included and their magnitudes are given in Table 1. The two  $m=0$  islands bounded by a closed flux surface at  $r=3.0$  are clearly visible. In the core however the  $m=1$  surfaces have been destroyed as can be seen by the field lines denoted by "\*" and "+" which wander ergodically. Estimates of the field line diffusion coefficient,  $D_{st}$  [12] have been made using the field line tracing results. Using the Rechester and Rosenbluth expression for the enhanced electron diffusion in the collisionless limit [13]

$$D = D_{st} V_{||}$$

(where  $V_{||}$  is the electron thermal velocity) anomalous values several orders of magnitude greater than the classical value are found.

## 6 CONCLUSIONS AND DISCUSSION

The linear 'g' mode has been examined for a large range of poloidal mode numbers and magnetic Reynolds numbers. At low  $S$  it is found that resistive dissipative effects cause marked departures from analytic results [7]. It has been demonstrated that the FLR effects are of little importance for the long wavelength modes, which are generally the fastest growing modes. The parallel viscosity has been found to be a more important effect providing a marked stabilisation to the  $m=1$ , although having little effect on the  $m=0$  mode.

The nonlinear behaviour of the 'g' mode has been found to depend on the competition between the stabilising effect of the quasi-linear pressure flattening and the destabilising effects arising from the resistive evolution of the equilibrium. Removing the ohmic heating has been shown to improve matters although the decrease in shear still inhibits a total saturation process. The inclusion of parallel thermal conductivity into the calculation has not yet been attempted. This may represent a stabilising factor because of its

ability to greatly enhance conduction across the island flux surfaces and thus to lower the temperature gradient in the vicinity of the mode. It must be remembered however that the pressure gradient is also supported by the density gradient which is much less affected by the conduction along field lines.

Introducing the 'g' mode eigenfunctions at typical levels indicated by the 2D nonlinear calculations has been shown to give rise to ergodic field line behaviour. The field line tracing calculations allow the stochastic diffusivity to be estimated but the effects of this on the energy containment time will require a 1D equilibrium simulation.

Finally it must be stressed that these field line tracing calculations only represent a first approximation. No attempt has been made to include a nonlinearly evolved equilibrium nor have the second order currents been included. Indeed the final resolution of the problem cannot be achieved until a fully self consistent 3D calculation is made.

TABLE 1

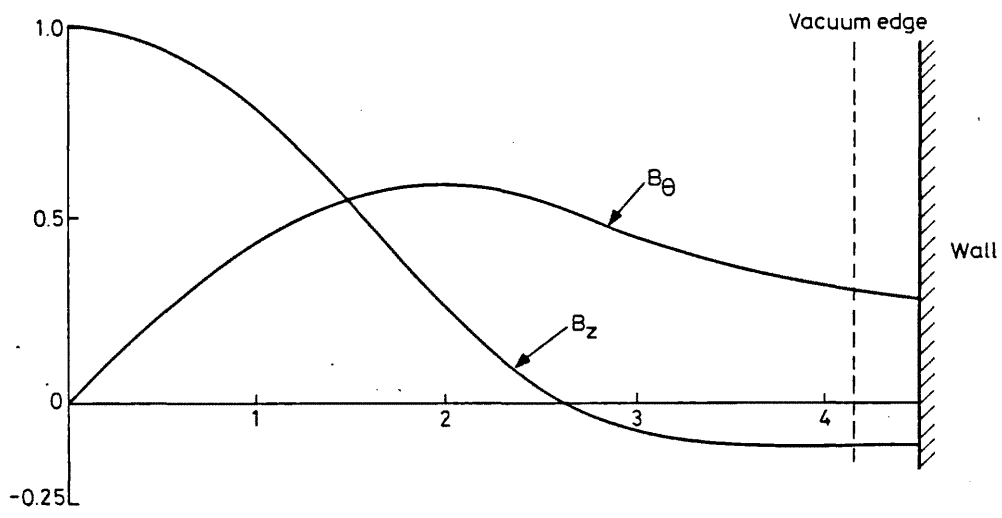
m	nK <sub>z</sub>	Singular Radius :	$\frac{\delta B_r}{ B } \Big _{r = \text{Singular Radius}}$
- 1	2	2.32	0.14%
- 1	1.8	2.27	0.17%
- 1	1.6	2.22	0.21%
- 1	1.4	2.15	0.27%
- 1	1.2	2.07	0.35%
- 1	1.0	1.92	0.46%
- 1	0.8	1.67	0.51%
0	0.4	2.66	0.28%

## REFERENCES

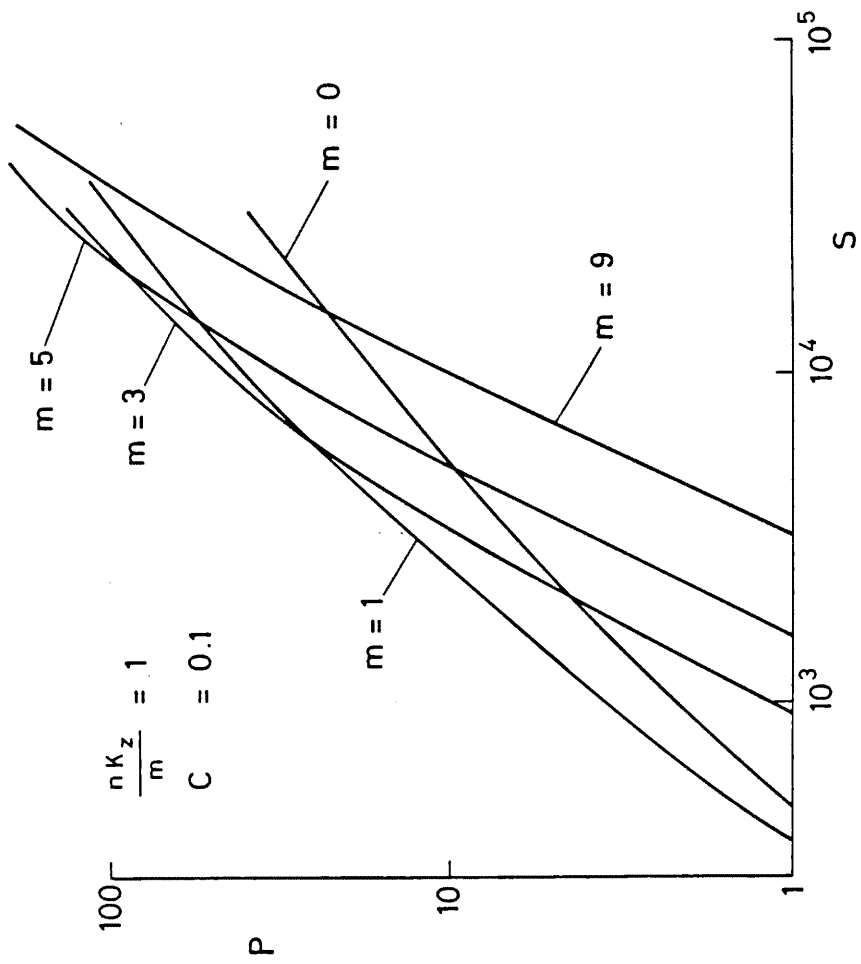
- [1] Bodin H A B and Newton A A, Nuclear Fusion 20 (1980) 1255.
- [2] Rosenbluth M N, Bussac M, Nuclear Fusion 19 (1979) 489.
- [3] Killeen J, in Physics of Hot Plasmas (Rye B J, Taylor J C, Editors) Plenum Press, New York (1970) 202; Robinson D C, Crow J E, Furzer A S, Dibiase J A, Killeen J, to be published in Plasma Physics.
- [4] Braginskii S I, (1965) Reviews of Plasma Physics (ed. M A Leontovich) Vol.1 p 205.
- [5] Richmyer R D and Morton K W. Difference methods for initial value problems (Interscience, John Wiley and Sons, Inc. New York, 1967) 2nd Edition.
- [6] Robinson D C, Nuclear Fusion 18 (1978) 939.
- [7] Coppi B, Greene JM and Johnson JL, Nuclear Fusion 6 (1966) 101.
- [8] Hosking R and Robinson D C, Proc. of 9th Euro. Conf. on Controlled Fusion and Plasma Physics, Oxford 1979, BP6
- [9] Hender T C and Robinson D C, Nuclear Fusion 21 No.6 (1981) 755.
- [10] Rosenbluth M N, Monticello D A, Strauss H, White R B, Phys. Fluids 19 (1976) 1987.
- [11] Waddell B, Rosenbluth M N, Monticello D A, White R B, Carreras B in Theoretical and Computational Plasma Physics, (Proc. ICTP College, Trieste, 1977) IAEA Vienna, (1978) 79.
- [12] Jokipii J R and Parker E N, Astrophysical Journal Vol.155 (1969) 773.
- [13] Rechester A B and Rosenbluth M N, Phys.Rev.Lett. (1978) 40 38.

#### FIGURE CAPTIONS

- Fig.1 Typical TMS reverse field pinch equilibrium for a Suydam value,  $C=0.05$  and a vacuum radius of 4.2.
- Fig.2 Growth rate in resistive units,  $p v$  Magnetic Reynolds number  $S$ , for various poloidal mode numbers  $m$  with  $nK_z/m=1$  and a Suydam value  $C=0.1$ .
- Fig.3 Comparison of growth rates (resistive units) between incompressible case and compressible case for a range of magnetic Reynolds number  $S$  with  $m=0$ ,  $nK_z=0.4$  and  $C=0.1$ .
- Fig.4 Layer widths,  $\Delta$  (upper two curves) and growth rates,  $p$  (lower two curves) in resistive units as a function of ion collisionless skin depth,  $c/\omega_{pi}$ , for  $m=0$ ,  $S=5000$  and axial wavenumbers  $K=0.4$  and 2.0.
- Fig.5 Nonlinear development of equilibrium pressure profile for  $m=0$  mode with,  $nK_z=0.4$ , a magnetic Reynolds number  $S = 10^3$  and a Suydam value,  $C=0.05$ .
- Fig.6 Average growth rates (Alfven units) for  $m=0$  mode with  $nK_z=0.4$ , a Suydam value,  $C=0.05$  and magnetic Reynolds numbers,  $S=10^4$  and  $5 \times 10^4$ .
- Fig.7 Average growth rate (Alfven units) for  $m=1$  mode, just inside field null ( $nK_z=1.6$ ) with a magnetic Reynolds number  $S=10^4$  and a Suydam value  $C=0.05$ .
- Fig.8 Intersection of five field lines with  $(r,z)$  plane for TMS equilibrium perturbed by modes given in Table 1.

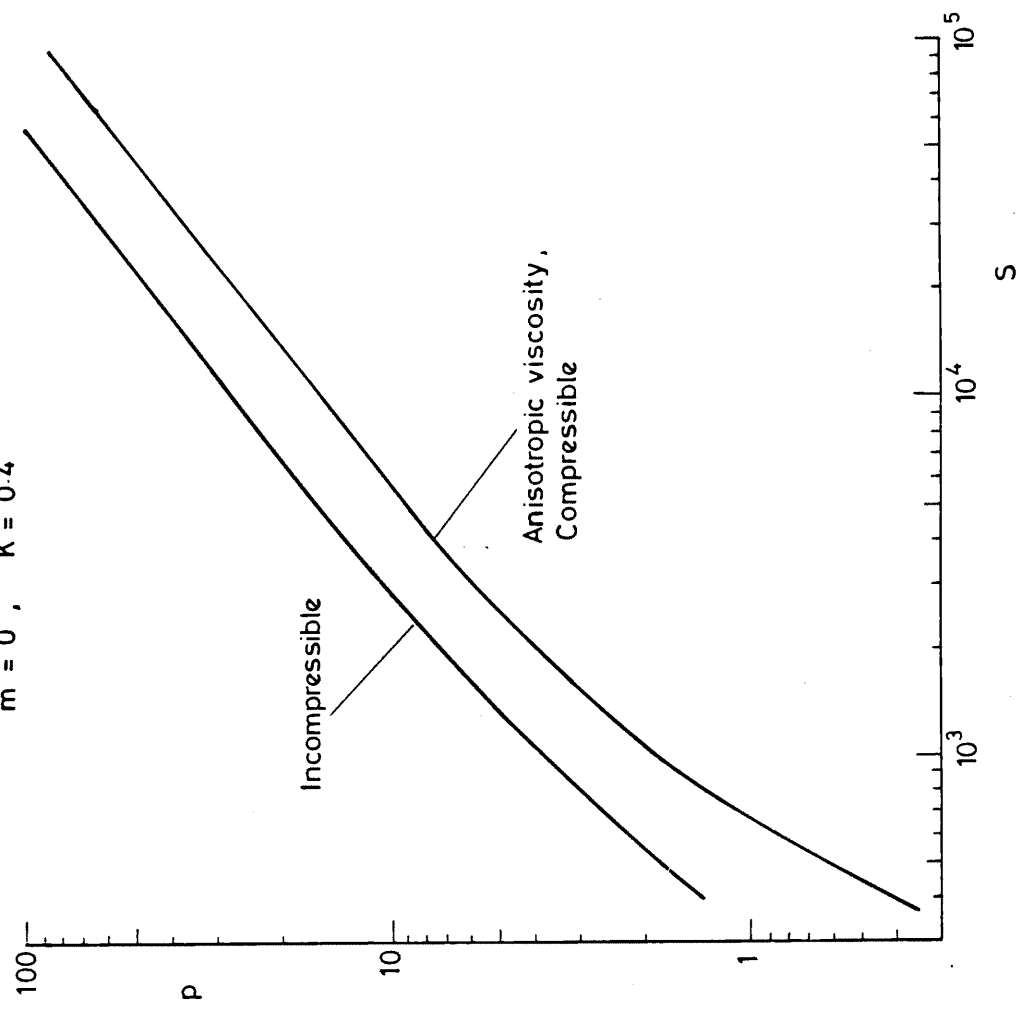


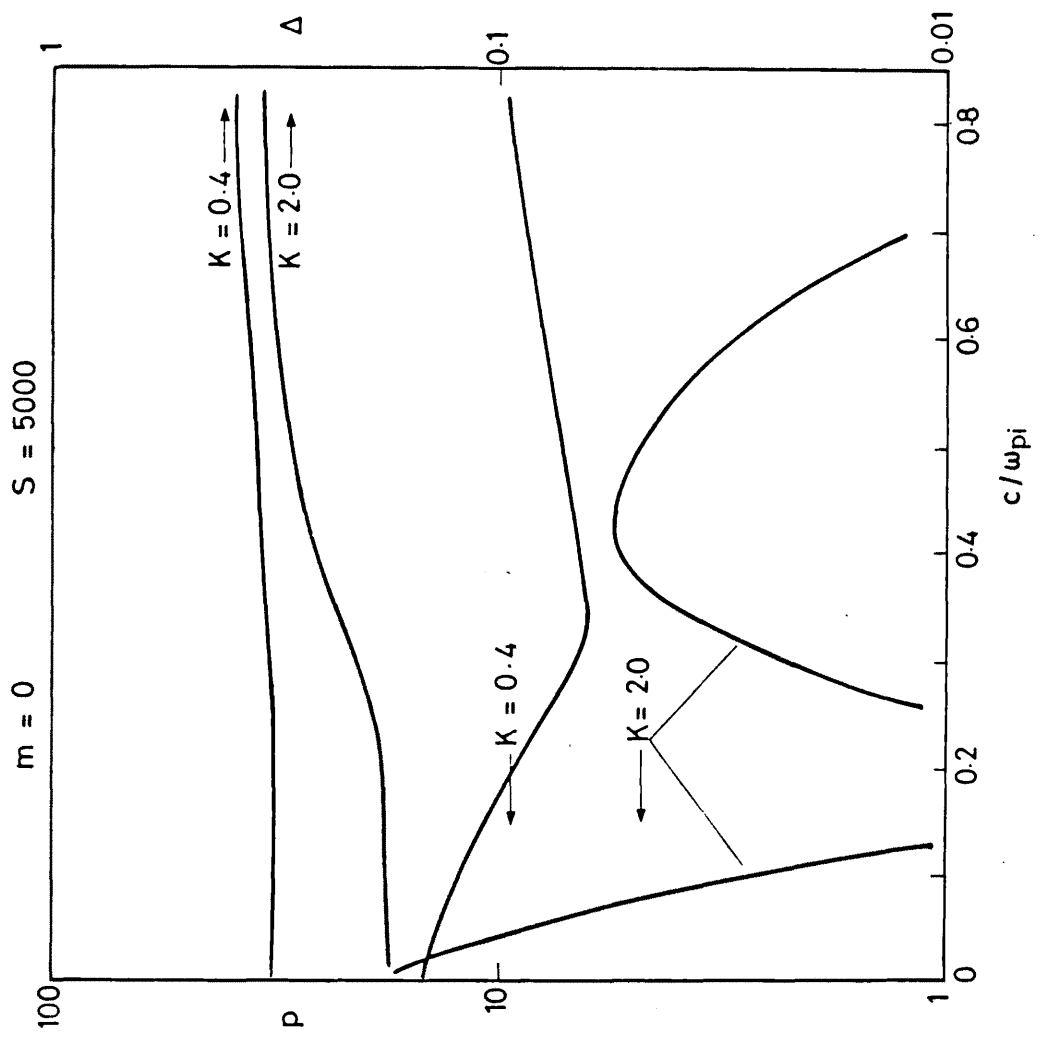
Pitch and pressure model equilibrium

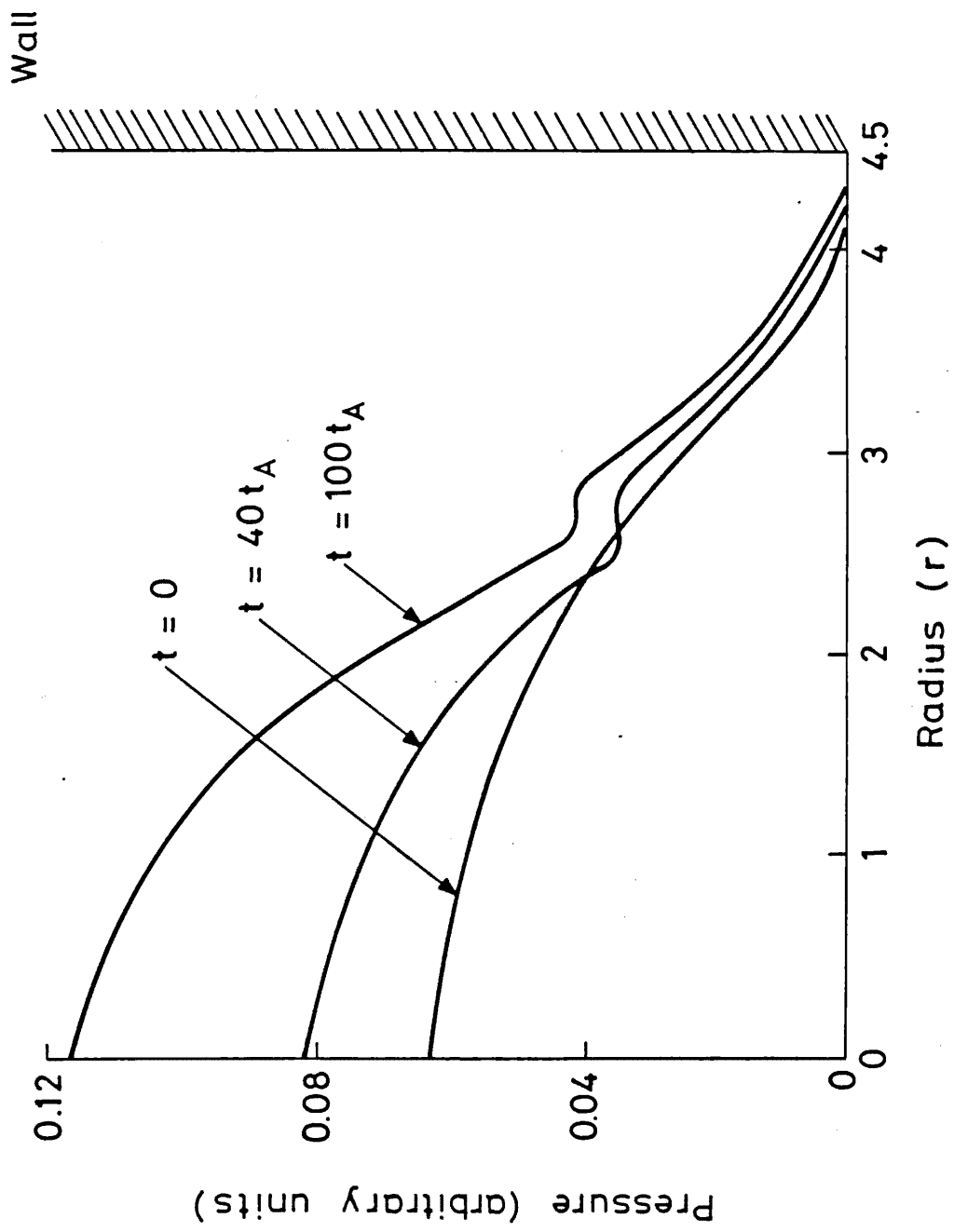


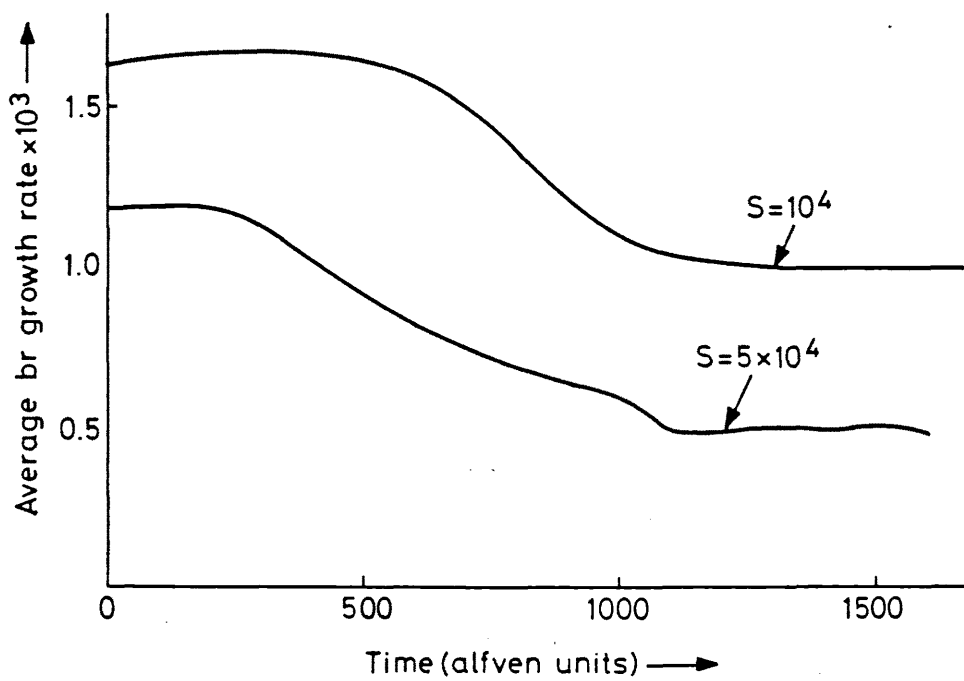


$m = 0, K = 0.4$



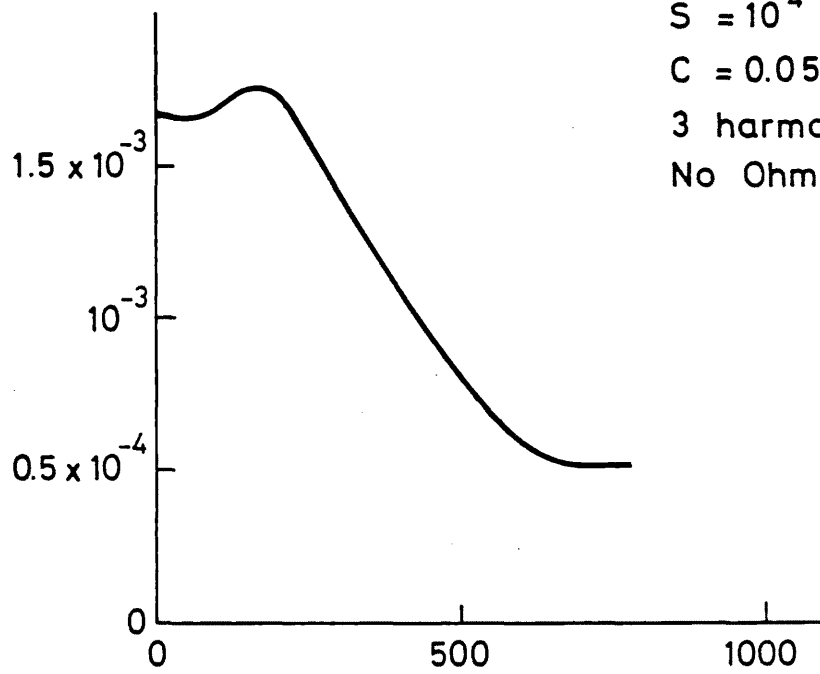






Growth rate v time for  $S=10^4$  and  $5 \times 10^4$  cases.

Average growth rate (Alfven units)



$S = 10^4$

$C = 0.05$

3 harmonics

No Ohmic heating

Time (Alfven units)

